Progress Towards High Power, High Brightness Microchip Lasers: Multi-Watt Operation using Diamond Heatspreaders

Rolf Birch

A thesis presented in fulfilment of the requirements for the degree of Doctor of Philosophy to the University of Strathclyde, Department of Physics

2011

Copyright

Abstract

The microchip laser – a sub-millimetre thick slice of laser gain material onto which cavity mirrors are directly coated – offers a robust, compact laser design; however, this design both inhibits heat removal and is sensitive to thermally induced distortions. This limits power scaling and degrades beam quality at higher powers. This thesis describes progress towards achieving a high power, high brightness microchip laser using diamond heatspreaders.

Diamond, silicon carbide (SiC) and sapphire heatspreaders are examined in a selection of doped-dielectric microchip lasers using finite element analysis (FEA). This suggests that diamond is the heatspreader of choice for most applications. The role of gain material thickness with respect to temperature gradients within Nd:YVO_4, Nd:$GdVO_4$ and Yb:KYW microchip lasers incorporating diamond heatspreaders is explored. Operation in the thin-disk regime is predicted to provide improved thermal management. At lower thicknesses, diamond is likely to outperform SiC at reducing thermal lensing and improving the overlap between the pump and fundamental cavity modes. This offers the potential for better beam quality.

The same heatspreader materials examined using FEA are also investigated experimentally in extended cavity and quasi-microchip Nd:YVO_4 lasers. It is found that diamond gives rise to the best performance. The performance of Nd:$GdVO_4$ and a 1060nm semiconductor disk laser in an extended cavity format incorporating an intra-cavity diamond heatspreader is compared with that of Nd:YVO_4. Finally, initial characterisation of a Yb:KYW extended cavity laser is presented.

Over 3W of output power is achieved using Nd:YVO_4 microchip lasers in novel configurations incorporating intra and extra-cavity diamond heatspreaders. Routes to achieving higher brightness are discussed.

Finally, thoughts are given on how to best achieve high brightness, high power microchip lasers in the future by moving to smaller gain thicknesses and using Yb:KYW which is well suited to efficient operation in this configuration.

Contents

1. Introduction

1.1 Microchip lasers

At their simplest, microchip lasers comprise of a thin slice of gain material that possesses plane-plane parallel facets onto which dielectric mirror coatings are deposited to form a cavity which can be optically pumped, typically by a diode laser [1]. This type of configuration offers a compact, robust laser with the potential for mass production [2]. Single frequency operation can readily be achieved and Q-switched operation is possible with the addition of a second crystal providing saturable absorption. Microchip lasers have been used for a number of different applications including use in range finders, materials processing, LIDAR [3], supercontinuum generation [4], and remote sensing [5].

The microchip laser concept was introduced in 1989 separately by Dixon [6] and by Zayhowski and Mooradian [1]. In both cases, the gain medium was based upon neodymium-doped materials operating in the 1µm wavelength region. The basic set-up of a simple end-pumped microchip laser can be seen in figure 1.1. The microchip is usually optically pumped with a low brightness diode laser whereby the pump optics are chosen to produce a pump spot of a pre-determined radius upon the gain material. The gain material can be edge-cooled by mounting on a heatsink to provide a measure of thermal management. The mirror coating nearest the pump source will be coated for high reflectivity at the laser wavelength and high transmission at the pump wavelength; the other mirror will be partially transmissive at the laser wavelength, acting as an output coupler.

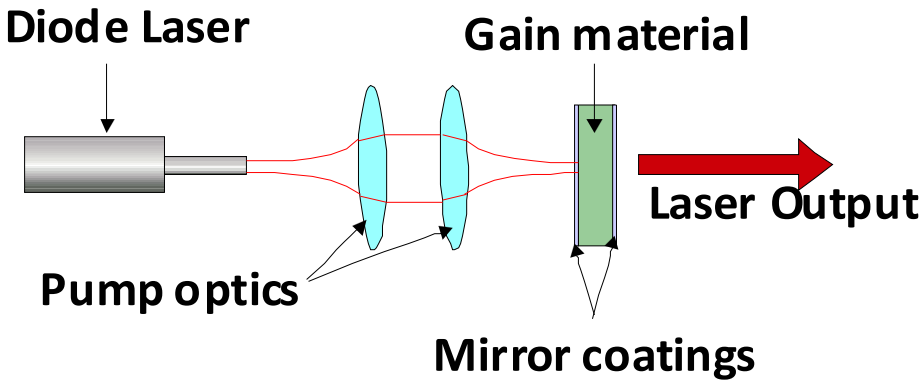

Figure 1.1.i *Schematic diagram of a microchip laser. The gain material is generally less than 1mm thick.*

The microchip shown figure 1.1.i can be termed a monolithic device due to the single element within the cavity i.e. the gain material, with no air gaps present in the device. A microchip cavity containing more than one element – but with no air-gaps between them – will be termed a quasi-monolithic device for the purposes of this thesis. Non-linear and saturable absorbing crystals (or semiconductor saturable absorbing mirrors (SESAMS)) can be included in the cavity to provide frequency doubling and passive Q-switched operation [7]. The semiconductor disk laser (SDL) format [8] has also been employed in a microchip format [9] and can be engineered to offer a wide range of wavelengths.

1.2 Guiding mechanisms in microchip lasers

The plane-plane cavity arrangement of the unpumped microchip laser might initially seem an odd choice from the point of view of cavity stability; however there are a number of mechanisms that contribute to a guided transverse mode in a pumped microchip laser as shown in figure 1.2. The diagram displays an end-pumped microchip laser being pumped by a beam with a Gaussian profile (figure. 1.2.i part **A)**. The effect of the incident pump power upon the surface of the gain material is to cause bulging due to thermal expansion (fig 1.2, part **B)**, effectively leading to curved cavity mirrors which act to stabilise the cavity and

confine the mode. In addition, the thermo-optic coefficient, *dn/dT* plays a role in mode guiding. As heat is deposited in the gain medium via optical pumping, it will diffuse away from the centre of the beam leading to a radially symmetric temperature distribution [10]. This results in a thermally-induced refractive index variation across the pumped region, also known as a thermal lens. This produces a positive contribution to cavity stability for materials with a positive *dn/dT* and a negative contribution for materials with a negative *dn/dT* [11].

In quasi-three level gain media an additional form of guidance takes place called aperture guiding. Due to the proximity of the lower laser level population to the ground state, the lower laser level can be thermally populated and absorption at the laser wavelength can occur [12]. At higher pump powers where the populations of the ground and lower laser levels are reduced, such absorption primarily takes place in the un-pumped material around the pumped region (as approximated by the dashed lines either side of the beam propagating through the gain region in figure 1.2.i part **B**) and hence in the wings of the laser mode. These absorption losses effectively act like a spatial aperture which contributes to mode guiding [13].

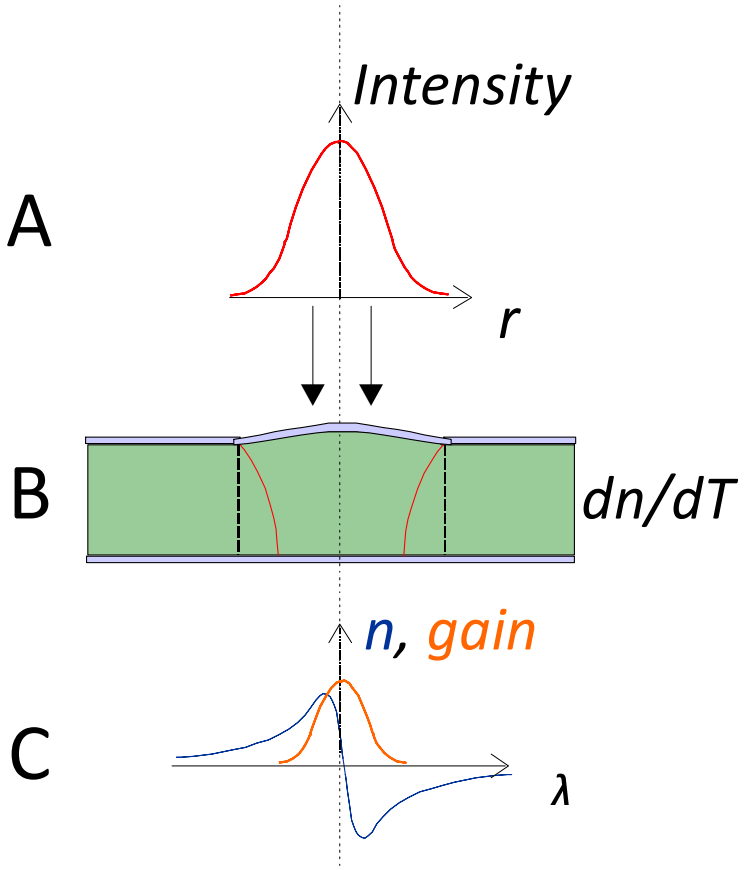

Figure 1.2.i *Diagram of guiding mechanisms in an end-pumped solid state microchip laser.*

Aperture guiding in quasi-three level materials is related to another similar guiding process called gain guiding. The gain profile, as shown in figure 1.2.i part **C,** is derived from a spatially varying population inversion profile which itself is dependent upon the pump profile. This means that more gain is available for the centre of the beam and less for the wings which acts to guide the cavity mode [14].

There is a second gain-related guiding effect known as gain-related index guiding whereby the refractive index experienced by the laser mode is modified as a function of the detuning of the laser wavelength from the peak of the gain and of the level of the saturated population inversion. In section **C** of figure 1.2.i, a plot of the refractive index and gain

against operating wavelength can be seen. Depending on the sign of the detuning and whether the saturated gain increases or decrease across the radial extent of the laser mode, guiding or anti-guiding can result [15].

For different laser materials, different guiding effects play the more predominant role dependant on certain material parameters. Zayhowski reported on the predominant guiding mechanism in Nd:YAG being that of the thermally induced distributed lens [10]. Thermal effects are the predominant guiding process in Nd:YVO_4 above threshold; however, the fundamental cavity mode is modified by gain-related guiding mechanisms, in particular gain-related index guiding as reported by Kemp *et al* [16]. In the case of lithium neodymium tetraphosphate (LNP), the thermo-optic coefficient *dn/dT* is negative unlike Nd:YAG which leads to the thermal lens providing a negative contribution to the guided mode. The two guiding processes that do provide cavity stability for microchip lasers incorporating LNP are gain guiding and surface deformation. MacKinnon and Sinclair determined that surface deformation was the predominant guiding process [11]. For Yb:YAG, a quasi-three level gain material, Fan investigated the dominant guiding mechanism and found it to be aperture guiding which he postulated would be the dominant guiding mechanism for other quasi-three level microchip lasers [13].

1.3 Q-switching in microchip lasers

Since the inception of the microchip laser concept in 1989, research has focussed on a number of different areas. Q-switching is one area that has been heavily investigated. Q-switched operation in microchip lasers can be classed either as active or passive where active Q-switching involves the modulation of the intracavity losses through means of an active control element [17]. This is usually achieved by means of an intracavity electro-optical element to control the losses within the laser cavity in order to produce high intensity pulses. In 1999, Zayhowski used an intracavity electrically modulated slice of lithium tantalate with optical coatings at the lasing wavelength of the Nd:YVO_4 microchip

laser to act as a tuneable Fabry-Perot etalon and hence a loss modulator. This generated actively Q-switched pulses of 115ps at a repetition rate of 1kHz and a peak power of 80kW. To-date these are still the shortest pulses produced by an actively Q-switched microchip laser. By increasing the reflectivities of the etalon mirrors, Zayhowski was able to reduce the threshold of the laser in order to increase its repetition rate to 2.25MHz with a pulse duration of 8.8ns and a peak power of 16W [2].

There are drawbacks to active Q-switching in microchip lasers due to the fact the electro-optic modulators run at high voltages and tend to be expensive and complex. Passive Q-switching involving the use of saturable absorbers presents a more attractive method to achieve shorter pulses in a less complex and more compact system. The basic idea behind passive Q-switching is to use a material which can absorb at the lasing wavelength causing intracavity loss but which suffers significant ground state depletion at high optical intensities where bleaching occurs leading to a rapid decrease in cavity loss causing pulsed operation. Examples of doped-dielectric saturable absorbers include Cr:YAG for operation in the 1µm wavelength region and V:YAG for the eye-safe 1.3µm region [18]. Using a Cr:YAG saturable absorber combined with a Nd:YVO_4 gain medium, Zayhowski achieved pulses of 218ps with peak powers of 18kW [2]. Sphühler *et al* used SESAM technology in a diode-pumped Nd:YVO_4 microchip cavity to produce pulses as short as 37ps at a peak power of 1.4kW, the shortest pulses achieved in a Q-switched system with no extra-cavity pulse shortening components [7]. The advantages of using SESAMs as opposed to doped dielectric saturable absorbers are that they allow for smaller cavity lengths (and hence shorter pulses) due to their much shorter physical length (a few micrometeres within the cavity) and that they can be engineered to operate at a large range of wavelengths

The shortest active and passive Q-switched pulses have not been bettered in well over a decade. The designs of these microchip lasers, however, have drawbacks in the sense that the actively Q-switched set-ups are expensive and complex whilst the SESAM set up used by Sphühler possessed a low optical damage threshold. Progress has been made in terms of the

optimisation of the SESAM approach; in 2007 Nodop *et al* utilised an optically transparent spin-on-glass glue to provide optical bonding of an InGaAs-GaAs SESAM to the gain material to ensure a much better contact than that achieved by Sphühler; the thickness of the SESAM-Nd:YVO_4 gap was estimated to be less than a few hundred nanometres. The pulse duration, repetition rate and peak power measured was 50ps, 40 kHz and 20kW respectively using 1W of input power. A second SESAM was examined and achieved 110ps, 166 kHz and 6kW [19].

There has been recent interest in pulse durations of tens to hundreds of picoseconds. Such pulse durations are shorter than the thermal diffusion time in materials subjected to laser processing. This leads to a much smaller heat affected zone around the area of the material on which the laser is incident and hence more precise processing [20]. Whilst mode-locked lasers are more than capable of operating in this pulse duration regime and below [21], they are alignment sensitive, expensive and complex. The latest Q-switched, quasi-monolithic lasers offer a more rugged, simpler and less expensive solution and there has been progress in developing Q-switched laser systems that offer pulse durations in the sub 30ps regime [22, 23]. The pulses produced however, are as a result of pulse shortening techniques which shorten the pulse of a Q-switched microchip laser that would produce pulse durations on the order of a few picoseconds. In [23] the advances lay not so much in the Q-switching technique but in the post processing of the pulse where photonic crystal fibre amplifiers have been used to boost energy levels and provide self-phase modulation which acts to spread the pulse duration which is then shortened by a diffraction grating compressor. This results in a Q-switched system that retains some of the advantages of a microchip lasers in terms of robustness and cost effectiveness when compared to a mode-locked equivalent.

Whilst Q-switched microchip laser systems produce high peak powers that can range into the Mega-Watt regime even in the UV [24], the continuous wave (CW) output powers of lasers struggle to achieve multi-watt operation whilst retaining high brightness. Indeed whilst there are microchip lasers that are reported to achieve high CW powers such as

16.8W from a Nd:YVO_4 microchip laser with M^2 of 11-14 [25] and 414W with an M^2 of 130 from a Yb:YAG microchip laser [26], they are not microchip lasers in the strictest sense but *quasi-microchip lasers*. In the terminology used in this thesis a microchip laser consists of a monolithic or quasi-monolithic device with no air-gaps present and the mirror coatings are deposited on the outer element(s) so that the cavity is of fixed length. A quasi-microchip laser is defined, for the purposes of this thesis, as a microchip laser which has a discrete output-coupling mirror separated from the gain material by an air gap; quite frequently this is simply an ordinary output coupler that completes the cavity. Essentially the quasi-microchip is a conventional 2-mirror laser configuration. Whilst not "true" microchip lasers according to the definition presented above, these devices are useful to optimise key parameters for use in future microchip laser work as seen in chapter three.

There has been work on high powered CW microchip devices that do adhere to the microchip laser definition, however, and output powers range from 9.7W and 10W for Nd:$LuVO_4$ [27] and Nd:$GdVO_4$ [28] respectively. Whilst beam brightness was not quantified in these papers, the beam brightness was measured for a set-up similar to the latter paper in Chapter 6 and was found to be multi-mode. To the best of the author's knowledge there have been no reports of multi-watt, microchip lasers with near diffraction limited beam quality. The highest output power achieved in a microchip laser with near diffraction limited beam quality is believed to be 730mW in a Nd:YVO_4 quasi-monolithic microchip laser where the M^2 was reported to be better than 1.15 [29]

Achieving higher average output powers whilst retaining beam quality can be a challenging task for all diode-pumped solid-state lasers [30] but is more difficult for microchip lasers. The fundamental cavity mode radius of a conventional cavity with air-gaps can be controlled through cavity design allowing for flexible optimisation of the cavity/pump mode overlap. In microchip lasers, however, the fundamental cavity mode radius is controlled by the thermal lens; as the absorbed power increases, the thermal lens focal length decreases, causing the fundamental cavity mode radius to shrink. Typical fundamental cavity mode radii of

microchip lasers are of a similar size, or smaller than the pump spot radii [10, 16]. This leads to oscillation of higher order transverse modes that serve to cause deterioration in beam quality. At higher absorbed powers crystal fracture may even occur and so thermal management, and management of the thermal lens in particular, is vital if the output power of microchip lasers is to be increased other than at the expense of beam quality. The next section will discuss some of the approaches used to for power and brightness scaling in solid-state lasers and how these might be applied to microchip lasers. In this thesis, brightness is defined by equation 1.3.i where *B* is the brightness, *P* is the output power, λ is the laser wavelength and M_x^2 and M_y^2 are the M^2 parameters in the x and y axes respectively [31].

$$B = \frac{4P}{\lambda^2 M_x^2 M_y^2} \qquad \text{Eq. 1.3.i}$$

1.4 Thermal management concepts

In order to power scale microchip lasers the detrimental effects of heat generated in the laser medium due to optical pumping must be mitigated. Indeed, this need to provide good thermal management is a requirement for power scaling of all solid-state lasers and there have been several designs that have made important inroads into the power scaling issue such as thin-disk, slab, long rod and fibre lasers [32-38].

1.4.a Disk Lasers

Disk Lasers tackle the issue of heat management through the geometry of the gain crystal [39]; aggressive face-cooling can be achieved by adopting a gain material that is thin in one dimension and cooling through one of the resulting large faces: a so-called thin-disk laser. This class of laser encompasses not only solid-state gain material but also semiconductor gain material in the form of *Semiconductor Disk Lasers* (SDLs) [40]. First reported in 1994 [39], the key concept behind the thin-disk laser is in the geometry of the gain medium and

the pump profile: the axial dimension of the disk being small relative to the transverse dimension of the pumped region, whilst a top-hat pump beam is required to encourage axial heat flow. The resulting thin slice of gain medium presents a large surface area for diode-pumping and for cooling. The cooled face is coated to be highly reflecting at the pump and laser wavelengths, forming one mirror of a laser cavity.

The main limitations to power scaling in diode-pumped solid-state lasers arise from the deposition of heat through the pumping process. The flow of heat through the medium to the heatsink gives rise to temperature gradients, and hence changes in the refractive index through the thermo-optic effect, leading to thermal lensing [41]. In an edge-cooled laser rod where the heat flow is predominantly radial in the gain medium, this gives rise to predominantly radial temperature gradients and hence strong thermal lensing which complicates cavity design. In end-pumped configurations, this strong thermal lensing is typically accompanied by strong aberrations to the thermal lens due to the radial non-uniformity of the pump.

Unlike the end-pumped rod, the geometry of the thin-disk encourages axial heat due to the geometry and the use of a flat-top pump profile, thus reducing the effects of thermal lensing dramatically since radial temperature gradients within the pumped region are negligible. Cooling one face of the disk aggressively, however, causes a large temperature differential between the cooled and uncooled faces. This produces a mechanical deformation of the crystal resulting in a curvature of each face; the cooled face will curve away from the heatsink acting like a diverging mirror whilst the uncooled face will curve to act like a converging lens. An exaggerated schematic of this effect is displayed in figure 1.4.a.i.

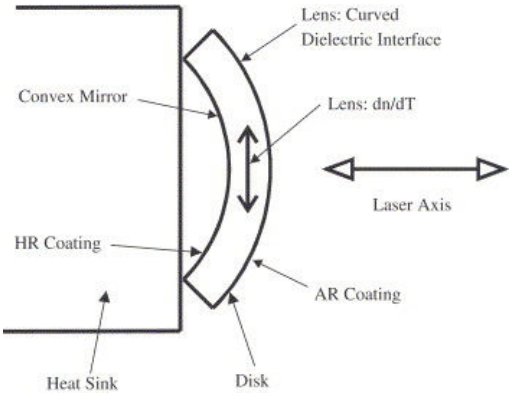

Figure 1.4.a.i *Schematic diagram of the bowing of thin-disk connected to a heatsink [31].*

The defocusing effects caused by the deformation of the cooled face are partly cancelled out by the curvature of the uncooled face but ultimately the laser resonator mode will be affected, impacting on the ability to power-scale. The deformation also causes mechanical stresses in the gain medium which in due course will lead to material fracture at high enough pump powers [31].

Whilst the thin disk approach offers a very attractive approach to power scaling in solid-state lasers, the thinness required of the gain medium makes it challenging to absorb as much pump light as possible in a microchip laser. In solid-state lasers, multiple pump reflections can be re-imaged onto the gain material allowing for more pump to be absorbed [39]; however, this makes set-ups more bulky and complex which runs contrary to some of the attractive qualities that a microchip laser seeks to achieve. An alternative approach to thermal management is to look at using heatspreaders instead.

1.4.b Heatspreader Contacting

Finite element modelling and previous experiments have indicated that the use of low-loss heatspreaders that are transparent at the pumping and lasing wavelengths can reduce the temperature gradients within the gain material caused by the optical pumping process [42].

One of the practical challenges for this approach is to attach the heatspreader to the gain material and achieve an effective thermal contact that is robust under optical pumping.

A number of different techniques have been used to obtain a good thermal contact between two materials, such as soldering, pressure-induced-bonding and mechanical pressing. Soldering is commonly used to bond heat sinks to semiconductor lasers [43]; however, the opacity of solder means it can't be used to bond intracavity surfaces. In 1999 Bewley and co-workers adopted a pressure-based approach by positioning a diamond heatspreader directly up against the epitaxial side of a mid-IR Sb-based semiconductor laser [44]. Initially, the air film between the two surfaces exhibited Newton's rings, indicating a poorly contacted interface, but changed to a uniform black appearance at higher pressures, indicating the mechanical contact. In the same year, Liao and co-workers used a sapphire-Nd:YVO_4 pressure set-up that provided thermal contact but also importantly provided a means to alleviate thermal stresses, compensating for the associated thermal lensing and achieving output powers of up to 19W with an M^2 of 1.3 using contact pressures of 700MPa [45]. Although these results are impressive, the mechanical requirements as seen in figure 1.4.b.i do not lend themselves to the development of compact, robust microchip lasers.

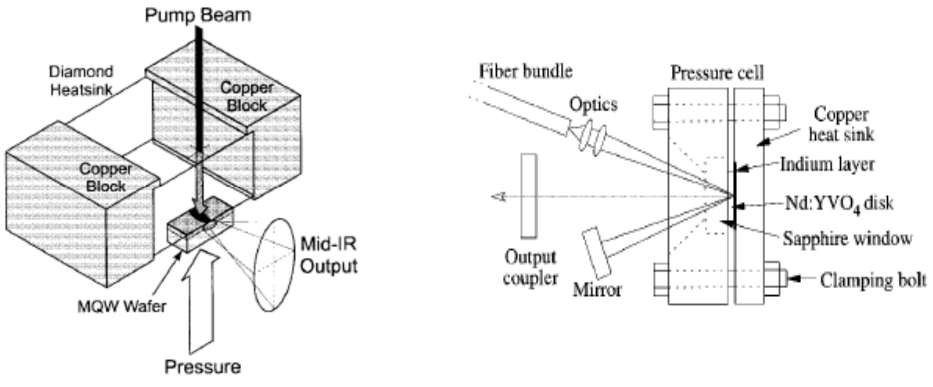

a) b)

Figure 1.4.b.i *Set-ups demonstrating a) diamond-pressure-bonding and b) mechanical pressing of sapphire to Nd:YVO_4 [44, 45].*

Another approach to establishing good contact between heatspreader and gain material was initially discussed in 1990 by E. Yablonovitch and co-workers who bonded 1500Å thick GaAs thin films to substrates such as Si, sapphire and diamond [46]. They named this bonding “Van der Waals” (VDW) bonding due to the fact that the bonding process was presumed to be due to the interfacial forces involved. The VDW bonding used de-ionized (DI) water as a contact between the film and substrate surfaces, the surface tension pulling the surfaces into much closer proximity. As pressure was applied, the DI water was squeezed out and any excess water remaining between the two surfaces evaporated. After a period of approximately two hours the bond was formed. The team used transmission electron microscopy to observe the various thicknesses of the GaAs – Substrate VDW bond and found that the separation between the two surfaces ranged from 20Å to 100Å using silicon and GaAs substrates.

The work done on bonding by Yablonovitch and co-workers was expanded upon by Liau in 2000 [47]. Liau used thicker materials than Yablonovitch *et al* in his investigations such as wafer couples of GaP, GaAs, InP, Si and sapphire. He used the term “liquid capillarity” instead of VDW bonding to label the process. The dimensions of the wafer surfaces ranged from 0.5 - 5cm in diameter and methanol was used as the contacting liquid rather than DI water. Having prepared the surfaces by a cleaning process and positioned one on top of the other, interference fringes were seen. As the methanol and a little pressure was applied, the two surfaces came into closer contact and the interference fringes were seen to disappear indicating a separation of the two surfaces of about ¼ of the visible wavelength, corresponding in this case to a separation of ~1000Å. After approximately 30 minutes, the methanol had been squeezed out by the surfaces coming into contact more closely; evanescent-wave tunnelling was used to show that the air gap between the wafers was roughly 15Å. Bonded Si/(InGaAs/InP) wafers were subjected to heat treatment at temperatures of 500°C and were found to have remained bonded despite the thermal stresses that arose due to differential thermal expansion.

In 2002 Alford *et al* used liquid capillarity to bond a 2mm thick, uncoated 10mm diameter window of sapphire to an InGaAs VECSEL as shown in figure 1.4.b.ii. 1.5W of CW output power was demonstrated, as opposed to a maximum output power of 300mW without the presence of a sapphire heatspreader [48]. The first use of a diamond heatspreader bonded to a SDL using liquid capillarity was reported by Hopkins *et al* in 2004 [49]. Using a GaInNAs SDL structure, >0.6W at a wavelength of 1.3µm was achieved at an incident pump power of 9W.

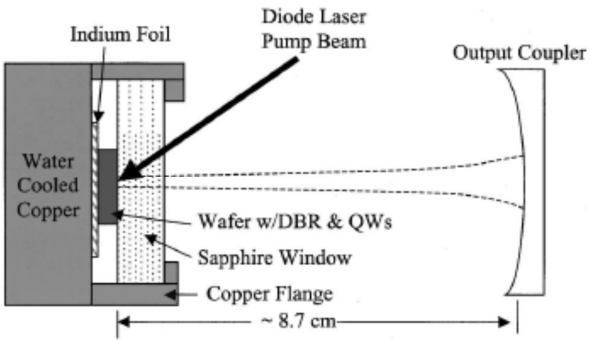

Figure 1.4.b.ii *VECSEL cavity incorporating sapphire heatspreader [48]*

The potential for mass production of semiconductor-heatspreader composites using the liquid capillarity method was demonstrated in 2004 by Hastie [50]. A GaAs wafer was bonded to a 0.36mm wafer of SiC for use as a heatspreader. The wafer was diced by a computer controlled 255nm Cu-vapour laser, at a pulse width of 30ns, repetition rate of 6 kHz and an average power of 660mW. On completion of the dicing process, the bond between the SiC heatspreader and the GaAs wafer of each diced sample remained intact. This is an example of how the heatspreader approach could be adapted to mass production of microchip lasers.

A demonstration of the effectiveness of heatspreaders in the power scaling role was demonstrated by Millar *et al* in 2009 by examining Nd:YVO_4 and Nd:$GdVO_4$ in a three mirror

cavity, double pump pass configuration incorporating an intracavity diamond heatspreader [51]. For a fixed incident power of 25W, a 0.5mm thick a-cut 1 atm. % doped $Nd:YVO_4$ set-up achieved a pump power limited output power of 7.6W whilst 4.4W was achieved using the same parameters without a diamond heatspreader. Increasing the input power further caused the crystal without a heatspreader to fracture. The 25W diode laser pump source was replaced with a 90W source and it was found that a maximum output power achieved by the $Nd:YVO_4$ set-up including the diamond heatspreader was 25.7W at an absorbed power of 49.5W. The output decreased beyond 49.5W absorbed power until crystal fracture occurred at 55W. The diamond heatspreader approach proved to be effective at providing suitable thermal management. In terms of brightness scaling, for an absorbed pump power of 46W, the M^2 was measured to be 44 and 29 in the horizontal and vertical axes respectively. This shows that whilst power scaling has been achieved using the heatspreader approach, further work is required on ensuring good brightness scaling which must be taken into consideration when employing heatspreaders in the microchip format.

1.4.c The function of a heatspreader

The function of a heatspreader, which is bonded to the laser gain material, is to alter the path of the heat flow within the gain material, especially for a face-cooled thin material [42, 52]. Without a heatspreader in place, the heat within a gain region will flow through the gain region to the heatsink, increasing the thermal impedance of the laser structure and leading to higher thermal gradients and temperature rises within the gain. By using a heatspreader in addition to the heat sink, the heat flow is directed through the heatspreader and flows back to the heat sink or through the gain material but over a much larger area than the pump spot size. This reduces the thermal impedance and lowers the temperature rise within the gain material for a given pump power [52]. By ensuring that the heat flow distance through the lower thermally conductive gain region into the higher thermally conducting heatspreader is minimised, the thermal resistance is minimised also. This means that materials with high thermal conductivities and optical transparency at the pump and laser wavelengths are optimal for the heatspreading role. Finite element simulations of the temperature rise and heat flow within a 1060nm SDL can be seen in

figure 1.4.c.i where sapphire, silicon carbide and diamond heatspreaders are modelled. As can be seen, the heat flow around the pumped region is predominantly out of the gain region and into the heatspreader.

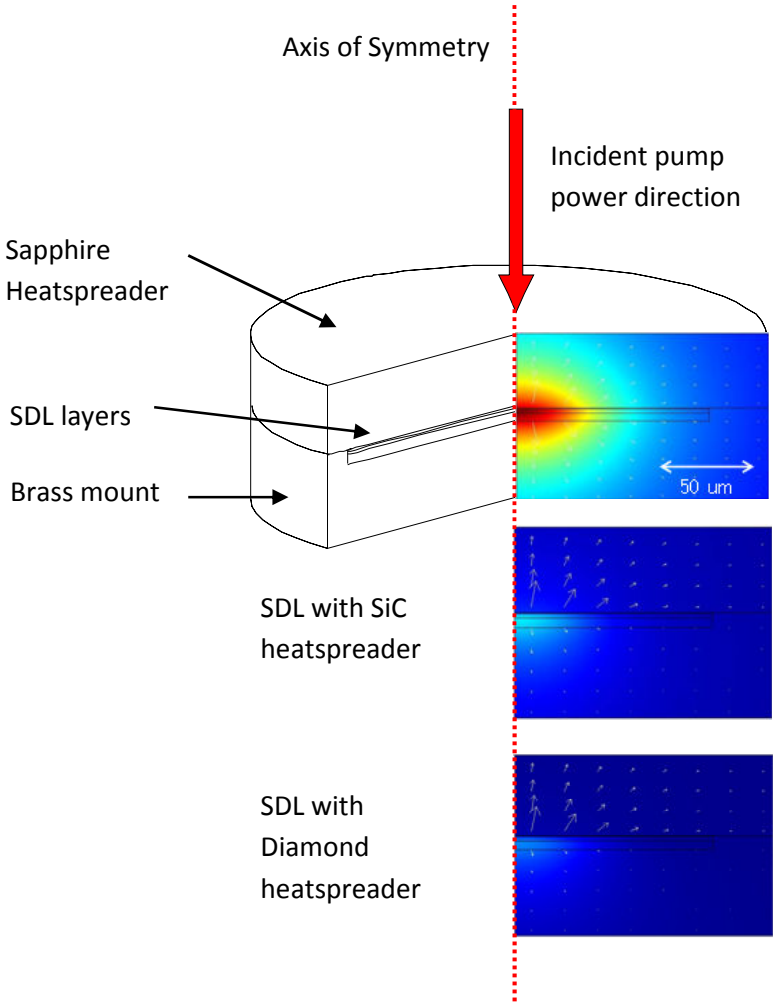

Figure 1.4.c.i: *2-D axially symmetric finite element simulations of heat flow and temperature rise around the pumped region in a 1060nm semiconductor disk laser for different heatspreader materials: sapphire, silicon carbide and diamond [52, 53]. The dashed line represents the line of symmetry. An incident pump power of 10W and a pump spot radius of 50µm are assumed. For the higher thermal conductivity heatspreader materials, the heat extraction is dominated by heat flow through the heatspreader. The colour map represents the temperature rise and the arrows indicated the size and direction of the heat flux. The FEA maps are scaled up for display purposes.*

If axial heat flow can be ensured in the laser gain material by reducing the thickness of the gain below the pump spot radius then the higher thermal conductivity of the heatspreader serves to minimise the axial thermal gradients that lead to thermal lensing. When moving towards thin gain media from rod-like dimensions, however, mechanical deformation becomes more significant and as noted by Giesen and Speiser, it is the most significant source of "thermal lensing" in the thin disk laser [36]. Another function of the heatspreader is to minimise the thermally induced mechanical deformation of the gain material [42] as shown by Weber *et al* [54].

To achieve good performance, a heatspreader should be transparent at the pump and laser wavelengths and have low optical loss. To reduce temperature gradients within the gain region, a heatspreader should possess high thermal conductivity whilst to reduce thermally-induced mechanical deformation, a rigid heatspreader is preferable. In table 1.4.i, the thermal and mechanical properties of three heatspreaders are compared alongside Nd:YAG, a common laser material. All of the heatspreaders possess a higher thermal conductivity than Nd:YAG and so make them promising candidates as heatspreader. The rigidity (represented by a high Young's modulus) and high tensile strength of diamond also have the potential to be useful properties in the context of a heatspreader.

Material	Thermal Conductivity (W/(m.K))	Young's Modulus (GPa)	Thermal Expansion Coefficient ($x10^{-6}$ K^{-1})	Thermo-optical Coefficient ($x10^{-6}$ K^{-1})	Tensile Strength (MPa)	Approximate cost of heatspreader (£)
Diamond	2000 [55]	1100 [55]	1.0 [55]	9.6 [55]	2860 [55]	1000
SiC	490 [56]	393 [57]	4.5 [58]	36 [59]	~1000 [60]	160*
Sapphire	34 [55]	344 [55]	5.3 [55]	12 [55]	400 [55]	30
YAG	12.9 [42]	282 [42]	8 [42]	7.3 [42]	200 [41]	-

Table 1.4.i *A comparison of the properties of candidate heatspreader materials with Nd:YAG – an archetypal solid-state laser material. The costing of the diamond, SiC, and sapphire heatspreaders are sourced from Element 6, TankeBlue, and Optosigma respectively.*This is the approximate price for a 2 inch wafer.*

A cursory glance at table 1.4.i suggests that the thermal and mechanical properties of diamond surpass those of sapphire and SiC and thus would make for an excellent heatspreader. Until recently, however, the use of diamond as a intracavity heatspreader has been restricted by the cost and poor optical quality of early diamond material [61-63]. Over the past three years, the growth of high optical quality synthetic single crystal diamond using chemical vapour deposition (CVD) techniques has been achieved [55, 64, 65]. The principle source of optical absorption in diamond stems from nitrogen purities within the diamond; by using high-purity source gases, this absorption can be minimised. Spatially varying birefringence is also an issue in diamond which is caused by local strains introduced by the dislocation density; this can be minimised by growing the diamond on a single crystal diamond substrate that has very few surface imperfections. The minimisation of spatially varying birefringence and optical loss within the latest single crystal CVD diamond has led to the material being commercially available, making synthetic diamond a very promising candidate for use in the heatspreading role. This has allowed the opportunity to explore the use of diamond as a heatspreader in a doped-dielectric microchip laser environment for the first time in this thesis and to test whether the extreme properties of diamond can be fully exploited.

1.5 Goals of this thesis

As discussed previously in this chapter, progress in developing multi-watt microchip lasers with good beam quality has been limited. Challenges include providing effective thermal management and ensuring a good fundamental cavity/pump mode overlap for high beam quality. Once these challenges are met, the end result could be adapted to provide the functionality associated with current microchip lasers, for example Q-switching to potentially provide sub-nanosecond, mJ pulses at high repetition rates. This thesis will present work done by the author towards the goal of a multi-watt, high brightness microchip lasers using a heatspreader approach.

This thesis comprises six chapters, the first and sixth chapters being this introductory chapter and the conclusions chapter. Finite element modelling of potential microchip laser configurations will be presented in chapter two of this thesis. Through use of computer modelling, key design parameters are deduced for employment in experimental conditions. The third chapter covers research into the optimum heatspreader for use in Nd:YVO_4 microchip lasers, examining the use of sapphire, silicon carbide and synthetic diamond. The fourth chapter investigates the use of different gain media, comparing Nd:YVO_4 to Nd:$GdVO_4$ and a 1060nm semiconductor disk laser material in three-mirror format to assess their suitability as gain media for employment in future microchip designs. Early progress in examining 10 atm. % doped Yb:KYW is also presented. Finally, chapter 5 will discuss beam brightness investigation of the multi-watt microchip laser reported by Liao *et al* [28] and will examine diode-pumped Nd:YVO_4 microchip lasers that include intracavity and extracavity diamond heatspreaders in different configurations.

1.6 References

[1] J. J. Zayhowski and A. Mooradian, "Single-frequency microchip Nd lasers," *Optics Letters*, vol. 14, pp. 24-26, 1989.

[2] J. J. Zayhowski, "Microchip Lasers," *Optical Materials*, vol. 11, pp. 255-267, 1999

[3] E. Molva, "Microchip lasers and their applications in optical microsystems," *Optical Materials*, vol. 11, pp. 289-299, 1999

[4] J. M. Stone and J. C. Knight, "Visibly “white” light generation in uniform photonic crystal fiber using a microchip laser," *Optical Express*, vol. 16, pp. 2670-2675, 2008

[5] J. J. Zayhowski, "Passively *Q*-switched Nd:YAG microchip lasers and applications," *Journal of Alloys and Compounds,* vol. 16, pp. 393-400, 2000

[6] G. J. Dixon, L. S. Lingvay, and R. H. Jarman, "Properties of Close Coupled Monolithic, Lithium Neodymium, Tetraphosphate Lasers," Proc. SPIE 1104, vol. 107, 1989.

[7] G. J. Spühler, R. Paschotta, R. Fluck, B. Braun, M. Moser, G. Zhang, E. Gini, and U. Keller, "Experimentally confirmed design guidelines for passively Q-switched microchip lasers using semiconductor saturable absorbers," *Journal of the Optical Society of America B*, vol. 16, pp. 376-388, 1999

[8] A. C. Tropper, H. D. Foreman, A. Garnache, K. G. Wilcox, and S. H. Hoogland, "Vertical-external-cavity semiconductor lasers," *Journal of Physics D: Applied Physics*, vol. 39, pp. R74-R85, 2004.

[9] J. E. Hastie, J. M. Hopkins, C. W. Jeon, S. Calvez, D. Burns, M. D. Dawson, R. Abram, E. Riis, A. I. Ferguson, W. J. Alford, T. D. Raymond, and A. A. Allerman, "Microchip vertical external cavity surface emitting lasers," *Electronics Letters*, vol. 39, pp. 1324-1326, 2003.

[10] J. J. Zayhowski, "Thermal Guiding in Microchip Lasers," *Advanced Solid State Lasers*, vol. 6, paper DPL3, 1999

[11] N. MacKinnon and B. D. Sinclair, "Pump power induced cavity stability in lithium neodymium tetraphosphate (LNP) microchip lasers," *Optical Communications,* vol. 94, pp. 281-288, 1992

[12] W. F. Krupke, "Ytterbium solid-state lasers - The first decade," *IEEE Journal of Selected Topics in Quantum Electronics*, vol. 6, pp. 1287-1296, 2000.

[13] T. Y. Fan, "Aperture guiding in quasi-three-level lasers," *Optics Letters*, vol. 19, pp. 554-556, 1994.

[14] B. D. Sinclair, "Frequency-doubled microchip lasers", *Optical Materials*, vol. 11, pp. 217-233, 1999

[15] A. J. Kemp, "The Physics of Microchip Lasers: Spatial and Spectral Selectivity Mechanisms " Ph.D. Thesis: University of St Andrews, 1999.

[16] A. J. Kemp, R. S. Conroy, G. J. Friel, and B. D. Sinclair, "Guiding Effects in Nd:YVO_4 Microchip Lasers Operating Well Above Threshold," *IEEE Journal of Quantum Electronics*, vol. 35, pp. 675-681, 1999.

[17] J. J. Zayhowski, "Q-switched operation of microchip lasers," *Optics Letters*, vol. 16, pp. 575-577, 1999

[18] A. M. Malyarevich, I. A. Denisov, K. V. Yumashev, V. P. Mikhailov, R. S. Conroy and B. D. Sinclair, " V:YAG – a new passive Q-switch for diode-pumped solid-state lasers," *Applied Physics B*, vol. 67, pp. 555-558, 1998.

[19] D. Nodop, J. Limpert, R. Hohmuth, W. Richter, M. Guina, and A. Tünnermann, "High-pulse-energy passively Q-switched quasi-monolithic microchip lasers operating in the sub-100-ps pulse regime," *Optics Letters*, vol. 32, pp. 2115-2117 2007

[20] P. P. Pronko, S. K. Dutta, D. Du, R. K. Singh,"Thermophysical effects in laser processing of materials with picosecond and femtosecond pulses," Journal of *Applied Physics,* vol. 78, pp. 6233-6240, 1995.

[21] T. Südmeyer, C. R. E. Baer, C. Kränkel, C. J. Saraceno, O. H. Heckl, M. Golling, R. Peters, K. Petermann, G. Huber, and U. Keller, "Power-Scaling of Femtosecond Thin Disk Lasers," *Advanced Solid-State Photonics*, paper ATuC1, 2011

[22] F. Doutre, D. Pagnoux, V. Couderc, A. Tonello, and A. Jalocha, "30 ps pulses source based on a fiber-coupled passively q-switched microchip laser," *Optics & Laser Technology*, Vol. 44, pp. 145-147, 2012

[23] A. Steinmetz, D. Nodop, T. Eidam, J. Limpert, and A. Tünnermann, "High Pulse Energy Sub-10 ps Pulses from Compressed Passively Q-Switched Laser," *Advanced Solid-State Photonics*, paper ATuD5, 2011.

[24] R. Bhandari and T. Taira, "Megawatt Level UV Output from <110> Cr4+:YAG Passively Q-Switched Microchip Laser," *Nonlinear Optics: Materials, Fundamentals and Applications*, paper NME2, 2011.

[25] T. Suzudo, M. Hiroi, Y. Higashi, Y. Satoh, Y. Sato, H. Ishizuki, T. Taira, and Y. Furukawa, "9.6-W cw Green Output from Diode Edge-Pumped Composite Vanadate Microchip Laser with Small Packaged Volume," *Advanced Solid-State Photonics*, paper WD4, 2008.

[26] M. Tsunekane, and T. Taira, "High Power operation of diode edge pumped composite all-ceramic Yb:$Y_3Al_5O_{12}$ microchip laser," *Applied Physics Letters*, vol. 90, pp. 1–3, 2007.

[27] Z. Wang, H. Zhang, F. Xu, D. Hu, X. Xu, J. and Z. Shao "High-power, continuous-wave Nd:$LuVO_4$ microchip lasers" *Laser Physics Letters*, vol. 5, pp. 25-28, 2008.

[28] M. Liao, R. Lan, Z. Wang, H. Zhang, J. Wang, X. Hou and X. Xu "10W continuous-wave Nd:$GdVO_4$ microchip laser" *Laser Physics Letters*, vol. 7, pp. 503-505, 2008.

[29] Y. Ma, L. Wu, H. Wu, W. Chen, Y. Wang, and S. Gu, "Single-longitudinal mode Nd:YVO_4 microchip laser with orthogonal-polarization bidirectional traveling-waves mode," *Optical Express*, vol. 16, pp. 18702-18713, 2008

[30] W. A. Clarkson, "Thermal effects and their mitigation in end-pumped solid-state lasers," *Journal of Physics D-Applied Physics*, vol. 34, pp. 2381-2395, 2001.

[31] A. J. Kemp, G. J. Valentine, and D. Burns, "Progress towards high-power, high-brightness neodymium-based thin-disk lasers," *Progress in Quantum Electronics*, vol. 28, pp. 305-344, 2004

[32] A. Tunnermann, H. Zellmer, W. Schone, A. Giesen, and K. Contag, "New Concepts for Diode-Pumped Solid-State Lasers," in *High Power Diode Lasers*, vol. 78, *Topics in Applied Physics*, R. Diehl, Ed. Berlin Heidelberg: Springer-Verlag, 2000, pp. 369-408.

[33] J. M. Eggleston, T. J. Kane, K. Kuhn, J. Unternahrer, and R. L. Byer, "The Slab Geometry Laser .1. Theory," *IEEE Journal of Quantum Electronics*, vol. 20, pp. 289-301, 1984.

[34] T. J. Kane, J. M. Eggleston, and R. L. Byer, "The Slab Geometry Laser .2. Thermal Effects in a Finite Slab," *IEEE Journal of Quantum Electronics*, vol. 21, pp. 1195-1210, 1985.

[35] E. C. Honea, R. J. Beach, S. C. Mitchell, J. A. Skidmore, M. A. Emanuel, S. B. Sutton, S. A. Payne, P. V. Avizonis, R. S. Monroe, and D. G. Harris, "High-power dual-rod Yb : YAG laser," *Optics Letters*, vol. 25, pp. 805-807, 2000.

[36] A. Giesen and J. Speiser, "Fifteen years of work on thin-disk lasers: Results and scaling laws," *IEEE Journal of Selected Topics in Quantum Electronics*, vol. 13, pp. 598-609, 2007.

[37] S. A. Payne, R. J. Beach, C. Bibeau, C. A. Ebbers, M. A. Emanuel, E. C. Honea, C. D. Marshall, R. H. Page, K. I. Schaffers, J. A. Skidmore, S. B. Sutton, and W. F. Krupke, "Diode arrays, crystals, and thermal management for solid-state lasers," *IEEE Journal of Selected Topics in Quantum Electronics*, vol. 3, pp. 71-81, 1997.

[38] D. J. Richardson, J. Nilsson, and W. A. Clarkson, "High power fiber lasers: current status and future perspectives [Invited]," *Journal of the Optical Society of America B*, vol. 27, pp. B63-B92, 2010.

[39] A. Giesen, H. Hugel, A. Voss, K. Wittig, U. Brauch, and H. Opower, "Scalable Concept For Diode-Pumped High-Power Solid-State Lasers," *Applied Physics B-Lasers and Optics*, vol. 58, pp. 365-372, 1994.

[40] M. Kuznetsov, F. Hakimi, R. Sprague, and A. Mooradian, "High-power (>0.5-W CW) diode-pumped vertical-external-cavity surface-emitting semiconductor lasers with circular TEM00 beams," *IEEE Photonics Technology Letters*, vol. 9, pp. 1063-1065, 1997.

[41] W. Koechner, *Solid State Laser Engineering*, Fifth ed. Berlin: Springer, 1999.

[42] P. Millar, R. B. Birch, A. J. Kemp, and D. Burns, "Synthetic Diamond for Intracavity Thermal Management in Compact Solid-State Lasers," *IEEE Journal of Quantum Electronics* vol. 44, pp. 709-717, 2008.

[43] S. Weiss, E. Zakel and H. Reichl, "Mounting of high powered laser diodes on diamond heatsinks," *IEEE Transactions on Components, Packaging, and Manufacturing Technology, Part A*, vol. 19, pp. 46-53, 1996.

[44] W. W. Bewley, C. L. Felix, E. H. Aifer, D. W. Stokes, I. Vurgaftman, L. J. Olafson, J. R. Meyer, M. J. Yang, and H. Lee "Thermal Characterisation of Diamond-Pressure-Bond Heat Sinking for Optically Pumped Mid-Infrared Lasers" *IEEE Journal of Quantum Electronics*, vol. 35, pp. 1597-1601, 1999.

[45] Y. Liao, R. J. Dwayne Millar, and M. R. Armstrong "Pressure tuning of thermal lensing for high-power scaling," *Optics Letters*, vol. 24, pp. 1343-1345, 1999.

[46] E. Yablonovitch, D. M. Hwang, T. J. Gmitter, L. T. Florez, and J. P Harbison, "Van der Waals bonding of GaAs epitaxial liftoff films onto arbitrary substrates," *Applied Physics Letters*, vol. 56, pp. 2419-2421, 1990.

[47] Z. L. Liau, "Semiconductor wafer bonding via liquid capillarity," *Applied Physics Letters*, vol. 77, pp. 651-653, 2000.

[48] W. J. Alford, T. D. Raymond, and A. A. Allerman, "High power and good beam quality at 980nm from a vertical external-cavity surface-emitting laser," *Journal of the Optical Society of America B*, vol. 19, pp. 663-666, 2002

[49] J. M. Hopkins, S. A. Smith, C. W. Jeon, H. D. Sun, D. Burns, S. Calvez, M. D. Dawson, T. Jouhti, and M. Pessa, "0.6 W CW GaInNAs vertical external-cavity surface emitting laser operating at 1.32 μm," *Electronics Letters*, vol. 40, pp. 30-31, 2004.

[50] J. E. Hastie, "High Power Surface Emitting Semiconductor Lasers," Ph.D. Thesis, University of Strathclyde, 2004.

[51] P. Millar, A. J. Kemp, and D. Burns, "Power scaling of Nd:YVO_4 and Nd:$GdVO_4$ disk lasers using synthetic diamond as a heat spreader," *Optics Letters*, vol. 34, pp. 782-784, 2009.

[52] A. J. Kemp, G. J. Valentine, J. M. Hopkins, J. E. Hastie, S. A. Smith, S. Calvez, M. D. Dawson, and D. Burns, "Thermal management in vertical-external-cavity surface-emitting lasers:

Finite-element analysis of a heatspreader approach," *IEEE Journal of Quantum Electronics*, vol. 41, pp. 148-155, 2005.

[53] A. J. Kemp, J. E. Hastie, S. A. Smith, J.-M. Hopkins, S. Calvez, G. J. Valentine, M. D. Dawson, and D. Burns, "Heatspreader-based thermal management in VECSELs: thermal lensing in microchip devices," presented at Advanced Solid-State Photonics, Vienna, 2005.

[54] R. Weber, B. Neuenschwander, M. MacDonald, M. B. Roos, and H. P. Weber, "Cooling schemes for longitudinally diode laser-pumped Nd : YAG rods," *IEEE Journal of Quantum Electronics*, vol. 34, pp. 1046-1053, 1998.

[55] I. Friel, S. L. Geoghegan, D. J. Twitchen, and G. A. Scarsbrook, "Development of high quality single crystal diamond for novel laser applications," presented at Optics and Photonics for Counterterrorism and Crime Fighting VI and Optical Materials in Defence Systems Technology VII, Toulouse, France, 2010.

[56] A. J. Kemp , G. J. Valentine , J. M. Hopkins , J. E. Hastie , S. A. Smith , S. Calvez , M. D. Dawson and D. Burns "Thermal management in vertical-external-cavity surface-emitting lasers: Finite-element analysis of a heatspreader approach", *IEEE Journal of Quantum Electronics*, vol. 41, p.148-155 , 2005.

[57] http://www.ioffe.ru/SVA/NSM/Semicond/SiC/mechanic.html#Elastic *accessed 29/09/11.*

[58] P. Ščajev and K. Jarašiunas "Application of a time-resolved four-wave mixing technique for the determination of thermal properties of 4H–SiC crystals", *Journal of Physics D: Applied Physics,* Vol.42**,** 055413, 2009

[59] Z. Li and R. C. Bradt, "Thermal expansion of the hexagonal (4H) polytype of SiC," Journal of Applied Physics, vol. 60, pp. 612–614, 1986.

[60] W. N. Sharpe, O. Jadaan, G. M. Beheim, G. D. Quinn, and N. N. Nemeth, "Fracture strength of silicon carbide microspecimens," *Journal of Microelectromechanical Systems*, vol.14, pp. 903- 913, 2005

[61] F. van Loon, A. J. Kemp, A. J. Maclean, S. Calvez, J.-M. Hopkins, J. E. Hastie, M. D. Dawson, and D. Burns, "Intracavity diamond heatspreaders in lasers: the effects of birefringence," *Optics Express*, vol. 14, pp. 9250-9260, 2006.

[62] A. R. Lang, "Causes of Birefringence in Diamond," *Nature*, vol. 213, pp. 248-251, 1967.

[63] G. Turri, Y. Chen, M. Bass, D. Orchard, J. E. Butler, S. Magana, T. Feygelson, D. Thiel, K. Fourspring, R. V. Dewees, J. M. Bennett, J. Pentony, S. Hawkins, M. Baronowski, A. Guenthner, M. D. Seltzer, D. C. Harris, and C. M. Stickley, "Optical absorption, depolarization, and scatter of epitaxial single-crystal chemical-vapor-deposited diamond at 1.064 µm," *Optical Engineering*, vol. 46, pp. 064002, 2007.

[64] I. Friel, S. L. Clewes, H. K. Dhillon, N. Perkins, D. J. Twitchen, and G. A. Scarsbrook, "Control of surface and bulk crystalline quality in single crystal diamond grown by chemical vapour deposition," *Diamond and Related Materials*, vol. 18, pp. 808-815, 2009.

[65] R. S. Balmer, J. R. Brandon, S. L. Clewes, H. K. Dhillon, J. M. Dodson, I. Friel, P. N. Inglis, T. D. Madgwick, M. L. Markham, T. P. Mollart, N. Perkins, G. A. Scarsbrook, D. J. Twitchen, A. J. Whitehead, J. J. Wilman, and S. M. Woollard, "Chemical vapour deposition synthetic diamond: materials, technology and applications," *Journal of Physics-Condensed Matter*, vol. 21, pp. 364221, 2009.

2. Finite element analysis of heatspreader based thermal management in microchip lasers

2.1 Introduction

The aim of this chapter is to model potential heatspreaders and gain materials in a microchip format in order to assess their thermal performance. As discussed in chapter one, thermal management plays a key role in microchip lasers and by using computer simulations it can be better understood. The advantage of using software over experiment to model the various configurations seen in this chapter is that various scenarios can be investigated with a good degree of flexibility. Whilst the parameters and boundary conditions assumed within this chapter have been selected to mirror the physical conditions as much as possible, there are various inherent uncertainties that limit the accuracy of simulated values compared to values obtained by experiment. However, the modelling in this chapter allows for various trends to be observed and these trends will inform the experimental optimisation of future microchip lasers.

The thermal analysis of complex structures such as semiconductor disk lasers (SDLs) and anisotropic doped-dielectric media cannot typically be done analytically. A more practical method to model these structures is to apply numerical techniques in the form of *finite element analysis* (FEA). The whole structure is split into smaller volumes and an iterative approach is used to examine heat flow between these elements until a steady-state solution is found.

To model the thermal properties of a microchip laser undergoing optical pumping, it is necessary to employ the standard heat equation to simulate the effect of the heat load density Q [1]:

$$\nabla \cdot (k\nabla T) = Q \qquad \textit{Eq2.1.i}$$

where T is the temperature of the volume and k is the thermal conductivity. The FEA approach calculates the absorbed heat and temperature rise in a specified region due to optical pumping and then considers the propagation of the heat energy through the structure by taking into account the temperature differential and thermal conductive properties of the adjoining elements. For the steady state condition the temperature rise within a given element that allows the total heat inflow into the element to equal the total heat outflow is calculated. A number of iterations are performed until the net heat flux out of the structure equals the heat load deposited into it and a steady-state solution is achieved. Computationally, the calculation is typically terminated when the temperature change between elements is smaller than a certain value between iterations.

There are limitations which can affect the accuracy of the final result using this type of iterative numerical analysis. In FEA the total volume is split up into a mesh comprising a number of elements. By increasing the mesh detail, the number of elements examined can be increased allowing for a more accurate end result. Applying a highly detailed mesh across a structure, however, demands greater memory capacity and an increase in the processing time and thus the accuracy is limited by the available computational power.

The FEA software used in this work was Comsol Multiphysics (Comsol AB, Sweden) in which the mesh detail can be varied selectively across the structures examined. This allows for a finer mesh to be used across locations of interest or of rapid change within the structure, and a coarser mesh used across areas where mesh detail is less important, reducing computational requirements but retaining a good degree of accuracy.

Another method of reducing the computational requirements is to simplify a 3-D model into a 2-D axially symmetric format by building the structure in 2-D with an axis of symmetry running through the centre of the incident pump beam. This allows for a pseudo-3-D structure to be examined using less computational resources.

2.2 Axially symmetric vs 3D thermal modelling of Nd:YVO_4 with a diamond heatspreader

In this section an a-cut 0.5mm thick Nd:YVO_4 microchip laser optically contacted to a 0.5mm thick diamond heatspreader is examined. The Nd:YVO_4 sample is a disk of radius 2mm. The sample was sandwiched between two layers of 0.125mm thick indium with a circular hole in the upper layer to allow for pump light to pass through. A cylindrical brass mount was used to hold the sample and was used to provide cooling from the bottom surface as can be seen in figure 2.2.i. This approximates the experimental configuration discussed in chapter three.

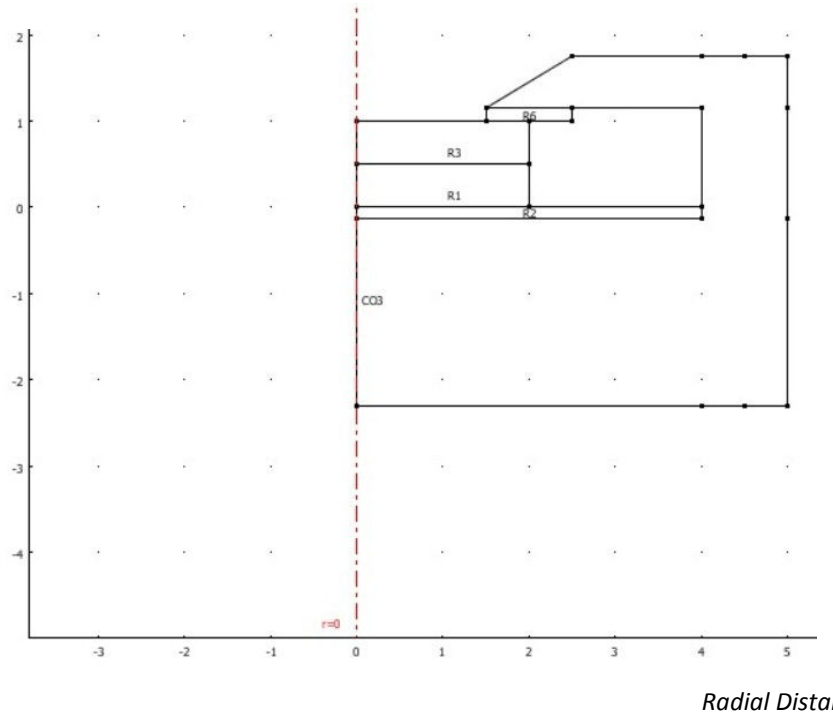

Figure 2.2.i *2-D axially symmetric schematic of the Nd:YVO_4 microchip laser with diamond heatspreader positioned in a cylindrical brass mount. The dashed red line indicates the axis of rotational symmetry, r and z are the radial and axial coordinates respectively. R1 is a 0.5mm thick, a-cut 1 atm. % Nd:YVO_4 crystal, R2 and R5 are layers of indium foil, R3 is a 0.5mm thick diamond heatspreader and CO3 is a brass mount.*

The bottom of the brass mount is assumed to be held at a fixed temperature and the change in temperature of the rest of the structure with respect to this reference

temperature is calculated. This allows for the temperature gradient to be more easily determined. In the 2-D axially symmetric model an axis of symmetry runs through the centre of the device, from the top of the sample to the bottom, as denoted by the striped line.

The Nd:YVO_4 microchip is optically pumped by a randomly polarised laser diode and so due to the uniaxial nature of Nd:YVO_4, there are two absorption coefficients to consider (since a-cut material is assumed). In the case of the 2-D axially symmetric model, the total heat generated per unit volume *Qp* in the Nd:YVO_4 region is:

$$Q_p = Q_{pa} + Q_{pc} \qquad \textit{Eq2.2.i}$$

Where Q_{pa} and Q_{pc} are the heat loading contributions from the fractions of the pump light polarised along the *a* and *c* crystallographic axes respectively. The heat load of Qp_a and Qp_c as functions of the radial and axial coordinates (r,z) can be expressed as:

$$Q_{pa}(r,z) = \left(\frac{\alpha_a \eta\, P_{inc}}{\pi {\omega_p}^2}\right)\left(e^{\frac{-2r^2}{\omega_p^2}}\right)\left(e^{-\alpha_a(t-z)} + e^{-\alpha_a(t+z)}\right) \qquad \textit{Eq2.2.ii}$$

$$Q_{pc}(r,z) = \left(\frac{\alpha_c \eta\, P_{inc}}{\pi {\omega_p}^2}\right)\left(e^{\frac{-2r^2}{\omega_p^2}}\right)\left(e^{-\alpha_c(t-z)} + e^{-\alpha_c(t+z)}\right) \qquad \textit{Eq2.2.iii}$$

Where α_a, α_c are the absorption coefficients of the a and c axes respectively, η is the fraction of absorbed pump power converted to heat in the Nd:YVO_4, P_{inc} is the incident power entering the Nd:YVO_4, ω_p is the $1/e^2$ radius of the pump intensity profile, and *t* is the thickness of the Nd:YVO_4. The second bracketed term assumes that the pump beam possesses a transverse Gaussian profile, which is approximately the profile measured for the fibre-coupled diode lasers used in the experimental sections of this thesis. The third

bracketed term accounts for double pass absorption of pump light in the Nd:YVO_4, reflecting the experimental situation. The pump is incident along the negative *z* direction.

The 3-D geometric model uses the same parameters as used in the 2-D axially symmetric model but is modelled fully in 3-D, using 103165 elements compared to the 7124 elements used in the axially symmetric case. In the case of the fully 3-D model, the total heat load deposited Q_{p3D} in the Nd:YVO_4 region is:

$$Q_{p3D} = Q_{p3Da} + Q_{p3Dc} \qquad \textit{Eq2.2.iv}$$

The heat load of Q_{p3Da} and Q_{p3Dc} as functions of the Cartesian coordinates (x,y,z) can be expressed as:

$$Q_{p3Da}(r,z) = \left(\frac{\alpha_a \eta\, P_{inc}}{\pi {\omega_p}^2}\right)\left(e^{\frac{-2x^2}{\omega_p^2}} + e^{\frac{-2y^2}{\omega_p^2}}\right)\left(e^{-\alpha_a(t-z)} + e^{-\alpha_a(t+z)}\right) \quad \textit{Eq2.2.v}$$

$$Q_{p3Dc}(r,z) = \left(\frac{\alpha_a \eta\, P_{inc}}{\pi {\omega_p}^2}\right)\left(e^{\frac{-2x^2}{\omega_p^2}} + e^{\frac{-2y^2}{\omega_p^2}}\right)\left(e^{-\alpha_c(t-z)} + e^{-\alpha_c(t+z)}\right) \quad \textit{Eq2.2.vi}$$

Where the second bracketed term describes a transverse Gaussian profile and the third bracketed term accounts for double pass absorption of pump light in the Nd:YVO_4. The parameters used in this section for both the axially symmetric and 3-D models are shown in table 2.2.i and the structure can be seen in figure 2.2.ii. Nd:YVO_4 is an anisotropic material and so the thermal conductivity is not constant for all directions in the crystal. The thermal conductivity is different along the single c-axis compared to the two a-axes. The a-cut Nd:YVO_4 used experimentally has both an a-axis and a c-axis in the plane of the microchip.

This means that an average value for thermal conductivity must be assumed in the radial direction for the axially-symmetric model. For the 3-D case, all axes can be assigned the correct thermal conductivity value. In the rest of this section, the extent to which this enforced approximation in the axially symmetric model compromises its accuracy will be assessed.

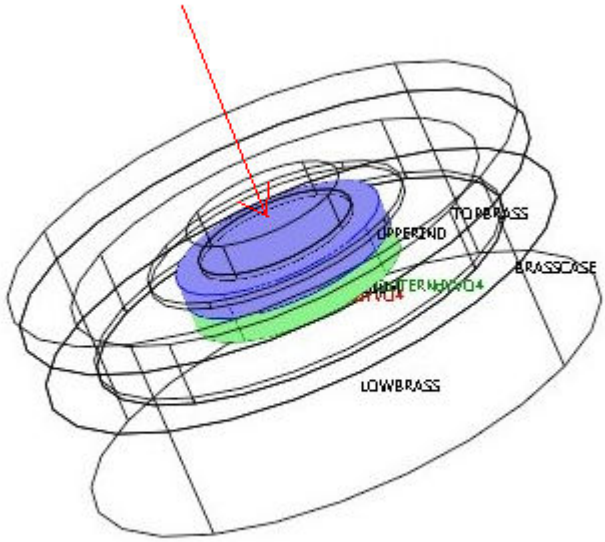

Figure 2.2.ii *3-D schematic of Nd:YVO_4 (coloured green) microchip laser with diamond heatspreader (coloured blue) positioned in a cylindrical brass mount as used in figure 2.2.i. The red arrow indicates the direction of incident pump light.*

Both the axially symmetric and 3-D modelled brass mounts were assumed to be cooled on their underside to a fixed temperature and the temperature rise, ΔT, with respect to this reference was calculated. In the axially symmetric case a symmetry boundary condition was used along the symmetry axis; all other boundaries in both models were assumed to be thermally insulated.

Symbol	Description	Value
P_{inc}	Input pump power	10 W
ω_p	Pump Spot Radius	50 µm
T	Thickness of Nd:YVO_4	0.5 mm
η	Heat loading factor in Nd:YVO_4	0.36 [2]
$k_{Nd:YVO4-a}$	Thermal Conductivity of Nd:YVO_4 along a axis	5.5 W/m.K [3]
$k_{Nd:YVO4-c}$	Thermal Conductivity of Nd:YVO_4 along c axis	6.5 W/m.K [3]
$\alpha_{Nd:YVO4-a}$	Absorption coefficient of 1 atm. % doped Nd:YVO_4 a-axis	1000 m^{-1} [4]
$\alpha_{Nd:YVO4-c}$	Absorption coefficient of 1 atm. % doped Nd:YVO_4 c-axis	3400 m^{-1} [4]
t_{DIA}	Thickness of Diamond	0.5 mm
k_{DIA}	Thermal Conductivity of Diamond	2000 W/m.K [5]
t_{IND}	Thickness of Indium	0.125 mm
k_{IND}	Thermal Conductivity of Indium	81.8 W/m.K
k_{BRA}	Thermal Conductivity of Brass	115 W/m.K

Table 2.2.i *Summary of material properties used in the axially symmetric and 3-D modelling in this section*

The axially symmetric and 3-D cylindrically symmetric models were performed and the maximum temperature rise within the Nd:YVO_4 recorded, the results can be seen in table 2.2.ii. The incident power of the first set of simulations was kept constant at 10W whilst in the second set of simulations the absorbed power was kept constant at 8W which is the power absorbed by the 2-D axially symmetric case for 10W of incident power for this microchip set-up. The number of elements used in each model indicates the complexity of the model which results in increased processing and memory requirements and hence a longer solution time.

	2-D axially symmetric Model ΔT	3-D Model ΔT
Constant incident power (10W)	360 K	332 K
Constant absorbed power (8W)	360 K	340 K
Number of elements in model	7124	103165
Solution time (s)	0.753 s	24.984 s

Table 2.2.ii *Results of comparison between 2-D axially symmetric and 3-D models of a 0.5mm thick, a-cut 1 atm. % doped Nd:YVO_4 microchip laser. The absorbed power of 2.88W is derived from the absorbed power of the 2-D axially symmetric case when 10W of pump is incident upon the gain sample and hence the 3-D ΔT appears normalised to the 2-D axially symmetric case. ΔT is the maximum temperature rise within the sample.*

The axially symmetric model displayed a larger temperature rise than that of the 3-D model. Ensuring that the absorbed power within the Nd:YVO_4 is kept constant for the two cases, there remains a difference in maximum temperature of 20K or 6% of the modelled temperature rise. Whilst it would be expected that the two models should experience the same value of pump absorption, the gridding of the models is not identical which leads to a pump absorption discrepancy. The fact that the 3-D model can account for anisotropy more accurately suggests that the 3-D model is more accurate than the axially symmetric mode but more demanding computationally. Throughout this chapter, however, the primary use of finite element analysis is for comparative purposes and not for rigorous quantitative results for experimental fits and thus the relative simplicity and shorter solution time of the 2-D axial symmetric model offers a more practical approach than the 3-D model to exploring a number of different parameters. The uncertainty introduced by the variation in key parameters as shown in the next section proves to be much larger than the uncertainty between the 2-D axially symmetric and 3-D models (around 6% in the sample simulation above) which reinforces the decision to continue to use the 2-D axially symmetric model throughout the rest of this chapter.

2.3 Comparison of $Nd:YVO_4$ and $Nd:GdVO_4$ parameters as measured by Georges and Taira

There is disagreement in the literature concerning the thermal conductivity of $Nd:YVO_4$ and $Nd:GdVO_4$, as exemplified by the significantly different results presented by the widely respected groups of Patrick Georges (Institut d'Optique, France) and Takunori Taira (Institute for Molecular Science, Japan). Whilst a small discrepancy in any data is understandable, the values recorded by each group differ significantly as shown in table 2.3.i. Sato *et al* (Taira's group) used the flash method to measure thermal conductivity under non-lasing conditions [6] whilst Didierjean *et al* (Georges' group) used thermal mapping to ascertain the thermal conductivity under lasing conditions [3].

	Sato [6]	Didierjean [3]
Thermal Conductivity of $Nd:YVO_4$ a-axis	9 W/m.K	5.5 W/m.K
Thermal Conductivity of $Nd:YVO_4$ c-axis	14 W/m.K	6.6 W/m.K
Thermal Conductivity of $Nd:GdVO_4$ a-axis	8.6 W/m.K	5.6 W/m.K
Thermal Conductivity of $Nd:GdVO_4$ c-axis	10.4 W/m.K	8 W/m.K

Table 2.3.i *Summary of $Nd:YVO_4$ and $Nd:GdVO_4$ parameters as measured by the groups of Georges and Taira*

To determine the effect this discrepancy would have on the FEA modelling in this chapter, the two sets of thermal conductivity values were used in an identical axially symmetric FEA microchip laser model as that used in figure 2.2.i using the same parameters as used table 2.2.i. The results can be seen in the graph and table below.

From table 2.2.ii it can be seen that Georges' data leads to a significantly larger rise in maximum temperature within the $Nd:YVO_4$ gain region than that of Takai's group. Whilst the flash method is an established and commonly used technique, it was not used under lasing conditions unlike the new infrared thermography method Georges' group used. The flash method has a number of inherent caveats, chiefly the experimental uncertainty

associated with the dependence upon thermal diffusivity or specific heat measurements to calculate thermal conductivity. In addition, the results presented by Sato and Taira are significantly out of line with those more generally quoted for YVO_4 (typically around 5 W/m.K) and with the more common conclusion that Nd:$GdVO_4$ has a higher thermal conductivity than Nd:YVO_4.

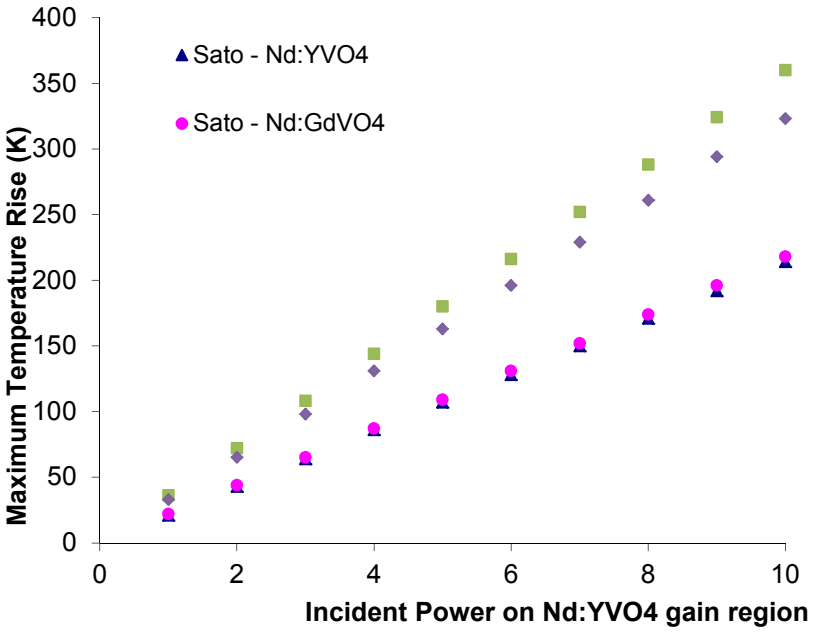

Figure 2.3.i *Plot of maximum temperature versus incident power for Nd:YVO_4 and Nd:$GdVO_4$ microchip lasers for a pump spot radius of 50μm. Each microchip laser is face-cooled by a diamond heatspreader. Thermal conductivity values vary between the measurements made by Sato and Didierjean.*

	Maximum Temperature rise per unit incident pump power	
	Sato [6]	Didierjean [3]
Nd:YVO_4	21 K	36 K
Nd:$GdVO_4$	22 K	32 K

Table 2.3.ii *Summary FEA results using Nd:YVO_4 and Nd:$GdVO_4$ parameters as measured by Sato and Didierjean. The incident power is 10W for each gain material.*

The thermography method provides a direct measurement of thermal conductivity under lasing conditions and the experimental conditions under which the measurements were taken by Georges' group more closely resemble the experimental conditions that are assumed in this chapter. In addition, the results are more closely in line with values more typically taken in the literature. It is for these reasons that George's measurements for the thermal conductivity of Nd:YVO_4 and Nd:$GdVO_4$ will be used throughout this chapter.

2.4 Axially symmetric thermal modelling - model structures

Having established the preferred model and thermal conductivity parameters, the aim was to examine various microchip gain material and heatspreader configurations. A 2-D axially symmetric model with an identical geometry to that in figure 2.2.i was constructed using FEA software. The laser materials used in the following simulations were Nd:YVO_4, Nd:$GdVO_4$, Yb:KYW and a 1060nm semiconductor disk laser (SDL). The heatspreader materials chosen were sapphire, SiC and diamond, all commercially available. The thicknesses of the doped-dielectric microchip media and the heatspreaders used were kept constant at 0.5mm. The semiconductor gain structure examined is discussed later in this section. The material parameters for the heatspreaders and gain media to be examined can be seen in tables 2.4.i-iii; all other material parameters are given in table 2.2.i. 10W of incident pump power was used in the cases where incident pump power is kept constant. The pump spot radius was 50µm unless otherwise noted.

Symbol	Parameter Description	Value
k_{SIC}	Thermal conductivity of SiC	500 W/m.K [7]
k_{SAP}	Thermal conductivity of Sapphire	34 W/m.K [5]
k_{DIA}	Thermal conductivity of Diamond	2000 W/m.K
$k_{Nd:YVO4-a}$	Thermal Conductivity of Nd:YVO_4 along a axis	5.5 W/m.K
$k_{Nd:YVO4-c}$	Thermal Conductivity of Nd:YVO_4 along c axis	6.5 W/m.K
$k_{Nd:GdVO4-a}$	Thermal conductivity of Nd:$GdVO_4$ along a axis	5.6 W/m.K [3]
$k_{Nd:GdVO4-c}$	Thermal conductivity of Nd:$GdVO_4$ along c axis	8.0 W/m.K [3]
$k_{Yb:KYW-Ng}$	Thermal conductivity of Yb:KYW along Ng axis	3 W/m.K [8]
$k_{Yb:KYW-Nm}$	Thermal conductivity of Yb:KYW along Nm axis	3 W/m.K [8]
$k_{Yb:KYW-Np}$	Thermal conductivity of Yb:KYW along Np axis	3 W/m.K [8]

Table 2.4.i *Summary of thermal conductivities of the heatspreaders and doped-dielectric gain material used in this section.*

Symbol	Parameter Description	Value
$\eta_{Nd:YVO4}$	Heat loading factor in Nd:YVO_4	0.36
$\eta_{Nd:GdVO4}$	Heat loading factor in Nd:$GdVO_4$	0.3 [9]
$\eta_{Yb:KYW}$	Heat loading factor in Yb:KYW	0.066
$\alpha_{Nd:YVO4-a}$	Absorption coefficient of 1 atm. % doped Nd:YVO_4 for light polarised along a-axis	1000 m^{-1} [4]
$\alpha_{Nd:YVO4-c}$	Absorption coefficient of 1 atm. % doped Nd:YVO_4 c axis for light polarised along c-axis	3400 m^{-1} [4]
$\alpha_{Nd:GdVO4-a}$	Absorption coefficient of 1 atm. % doped Nd:$GdVO_4$ for light polarised along a-axis	1060 m^{-1} [10]
$\alpha_{Nd:GdVO4-c}$	Absorption coefficient of 1 atm. % doped Nd:$GdVO_4$ c axis for light polarised along c-axis	7400 m^{-1} [10]
$\alpha_{Yb:KYW-Ng}$	Absorption coefficient of 5 atm. % doped Yb:KYW for light polarised along Ng-axis	4000 m^{-1} [11]
$\alpha_{Yb:KYW-Nm}$	Absorption coefficient of 5 atm. % doped Yb:KYW for light polarised along Nm-axis	4000 m^{-1} [11]
$\alpha_{Yb:KYW-Np}$	Absorption coefficient of 5 atm. % doped Yb:KYW for light polarised along Np-axis	4000 m^{-1} [11]

Table 2.4.ii *Summary of heat loading and absorption coefficients of Nd:YVO_4, Nd:$GdVO_4$ and Yb:KYW used in this section.*

Symbol	Parameter Description	Value
$t_{SDL-cap/confine}$	Thickness of composite cap +confinement layer 1060nm SDL	0.169µm
$k_{SDL-cap/confine}$	Thermal conductivity of composite cap +confinement layer	13 W/m.K
$t_{SDL-Gain}$	Thickness of Gain	1.58µm
$k_{SDL-Gain}$	Thermal conductivity of 1060nm SDL gain region	33 W/m.K
$\eta_{SDL-Gain}$	Heat loading factor in Gain	0.237
$\alpha_{SDL-Gain}$	Absorption coefficient of gain 1060nm SDL	1E-6 m^{-1}
$t_{SDL-DBR}$	Thickness of DBR 1060nm SDL	5.1µm
$k_{SDL-DBR}$	Thermal conductivity of DBR 1060nm SDL	61 W/m.K
$t_{SDL-Subs}$	Thickness of Substrate 1060nm SDL	500µm
$k_{SDL-Subs}$	Thermal conductivity of Substrate 1060nm SDL	44 W/m.K
$\eta_{SDL-Subs}$	Heat loading factor in 1060nm substrate	1
$\alpha_{SDL-Subs}$	Absorption coefficient of Substrate 1060nm SDL	1E6 m^{-1}

Table 2.4.iii *Summary of SDL material properties used in this section [12]*

There has been relatively extensive research into the spectroscopic and thermal properties of Nd:YVO_4 and Nd:$GdVO_4$ unlike in the case of Yb:KYW. It is for this reason that the thermal conductivity and absorption coefficient parameters have been necessarily defined as being isotropic rather than anisotropic due to the uncertainty of these values in the literature and to simplify the calculations. Similarly, due to the lack of available information, the heat loading factor $\eta_{Yb:KYW}$ is defined as the quantum defect:

$$\eta_{Yb:KYW} = 1 - \left(\frac{\lambda_{pump}}{\lambda_{laser}}\right) \qquad \text{Eq.2.4.i}$$

This does not take into account non-radiative losses and so the actual value for $\eta_{Yb:KYW}$ is likely to be larger. Nevertheless equation 2.4.i, although not optimal, is a reasonable starting point until the properties of Yb:KYW are investigated in greater detail in the future.

It was assumed that the incident pump was absorbed solely within the Nd:YVO_4, Nd:$GdVO_4$ and Yb:KYW crystals respectively leading to a heat load corresponding to equation 2.2.ii where the total heat load is the summation of the heat load contributions in the crystallographic axes. Each heat load contribution $Q_X(r,z)$ is given by:

$$Q_X(r,z) = \left(\frac{\alpha_X \eta_X P_{inc}}{\pi {\omega_p}^2}\right)\left(e^{\frac{-2r^2}{\omega_p^2}}\right)\left(e^{-\alpha_X(t-z)} + e^{-\alpha_X(t+z)}\right) \qquad \text{Eq.2.4.ii}$$

Where the relevant axes of Nd:YVO_4, Nd:$GdVO_4$ or Yb:KYW are substituted for X. In the SDL case, pump absorption is assumed to take place in the gain region as described by equation 2.4.iii and in the substrate. In the substrate, all pump power absorbed is assumed to be dissipated as heat as described in equation 2.4.iv. There is no pump absorption in the DBR for the SDL structure chosen.

$$Q_{Gain}(r,z) = \left(2\frac{\alpha_{Gain} \eta_{Gain} P_{inc}}{\pi {\omega_p}^2}\right)\left(e^{\frac{-2r^2}{\omega_p^2}}\right)\left(e^{-\alpha_{Gain}(t-z)} + e^{-\alpha_{Gain}(t+z)}\right)$$

Eq.2.4.iii

$$Q_{Subs}(r,z) = \left(2\frac{\alpha_{Subs} \eta_{Subs} P_{inc}}{\pi {\omega_p}^2}\right)\left(e^{\frac{-2r^2}{\omega_p^2}}\right)\left(e^{-\alpha_{Subs}(t-z)} + e^{-\alpha_{Subs}(t+z)}\right)$$

Eq.2.4.iv

A number of simplifications have to be made when modelling an SDL structure as seen in figure 2.4i using FEA due to the large number of layers and the layer thickness which is measured in terms of nanometres rather than millimetres (Kemp, Valentine et al. 2005; Lindberg, Strassner et al. 2005). An increase in the number of layers present within a structure requires a finer degree of meshing in the FEA software which leads to an increase in computational requirements. To reduce the complexity of the model whilst minimising the reduction in accuracy a reduced layer model can be adopted. Layers of similar thermal

properties and function were combined, reducing the layer scheme into a structure containing four layers including the substrate at the bottom of the device. The top layer consisted of a combination of the capping and confinement layers, the gain layer consisted of the quantum well and barrier regions whilst the DBR layer consisted of the mirror pairs. In addition to adopting the reduced layer structure, the radius of the top three layers, was limited to 300µm in order to further reduce the degree of meshing required. The thicknesses of the reduced layers equal the sum of the respective component layers. The reduced layer structure results in regions where the thermal conductivity is averaged across regions of differing thermal conductivities therefore the thermal conductivity throughout much of the structure is anisotropic and so the axial and radial components have to be considered independently. In practice the addition of radial and axial values for the thermal conductivity to a FEA model does not achieve a significantly different result when compared to treating each section as isotropic in nature (Kemp, Valentine et al. 2005). The semiconductor material was assumed to be optically contacted to the heatspreader and sandwiched between indium and mounted in a brass mount using the same arrangements as for the Nd:YVO_4, Nd:$GdVO_4$ and Yb:KYW lasers.

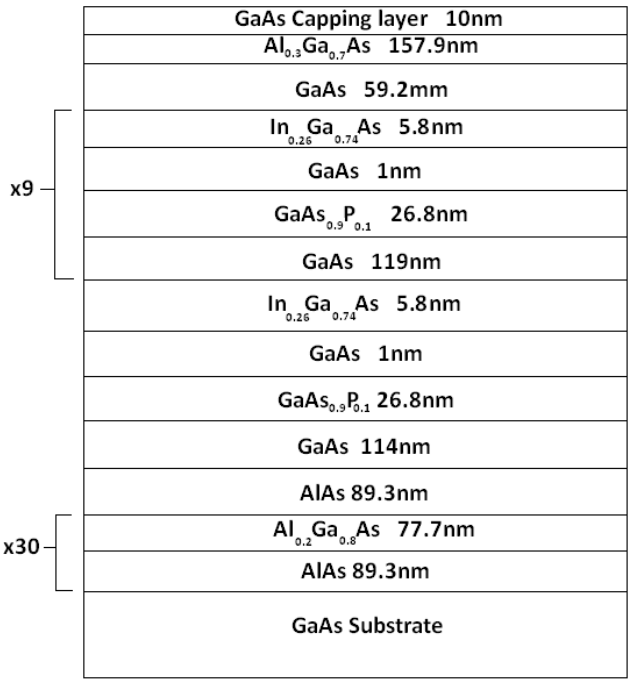

Figure 2.4.i *Layer schematic of 1060nm SDL based on experimental structure [12]*

2.5 Axially symmetric thermal modelling of Nd:YVO_4, SDL, Nd:$GdVO_4$, Yb:KYW with a diamond heatspreader (HS)– results and discussion

To compare the temperature rises within each of the microchip laser materials examined, the maximum temperature rise of each microchip model was calculated for a range of absorbed powers up to 8W for a pump spot radius of 50µm. Each structure was assumed to be bonded to a diamond heatspreader, the parameters of which can be seen in table 2.4.i. The results can be seen in figure 2.5.i. It is apparent that for each microchip there is a linear increase in maximum temperature with respect to absorbed power as would be expected for the model used since the equations are linear in with respect to heat load and hence pump power. This linearity was used to scale some of the data in later sections to bypass the need to calculate for each pump power if all other parameters were kept constant. The Yb:KYW model calculated the smallest temperature rise out of the doped dielectrics which is due to the heat loading factor of Yb:KYW being the lowest examined. Indeed the highest temperature rises were experienced by the Nd:YVO_4 being less thermally conductive and having a larger heat loading fraction compared to the next highest gain material, Nd:$GdVO_4$. Finally the SDL experienced the lowest temperature rise due to the thinness of its heat-loading layers.

The pump spot radius was then varied from 10µm up to 500µm and the pump power kept constant at 10W incident. Due to the reduced structure of the SDL, the maximum pump spot radius that could be modelled was 150µm. For larger values of pump spot radius, the wings of the pump distribution extend appreciably beyond the region within which the layer structure is modelled. The maximum temperature rise was recorded for each gain structure and the results can be seen in figure 2.5.ii. The Yb:KYW microchip laser experienced the smallest temperature rises out of the doped-dielectric structures examined whilst the 1060nm SDL laser experienced the smallest out of all the structures due to the higher thermal conductivities and thinner dimensions of the constituent layers.

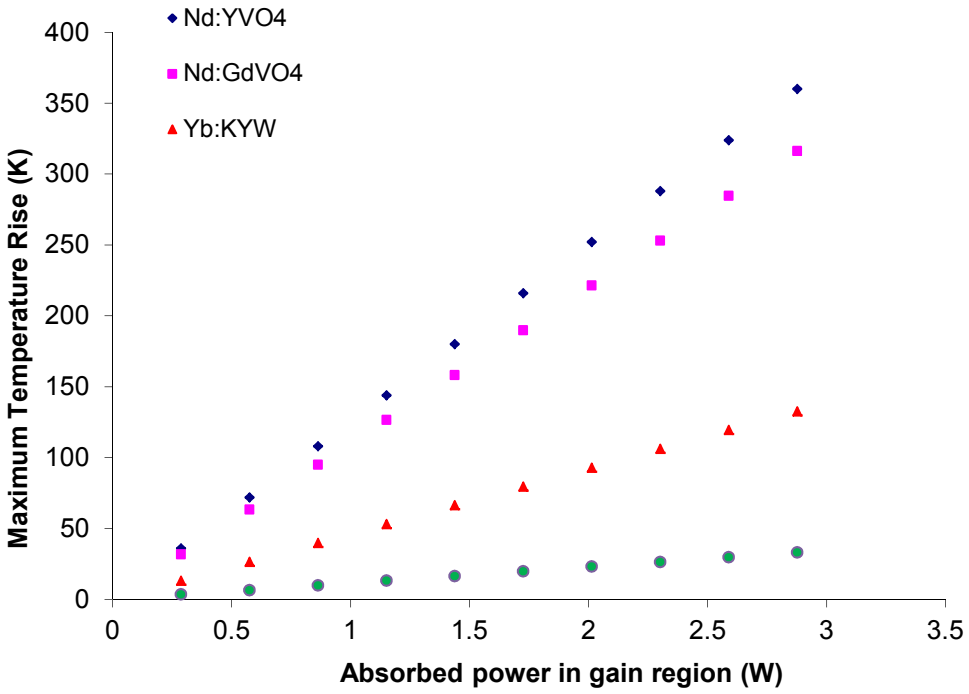

Figure 2.5.i *Plot of maximum temperature versus absorbed power for Nd:YVO$_4$, Nd:GdVO$_4$, Yb:KYW and 1060nm SDL microchip lasers for a pump spot radius of 50µm. Each microchip laser is face-cooled by a diamond heatspreader.*

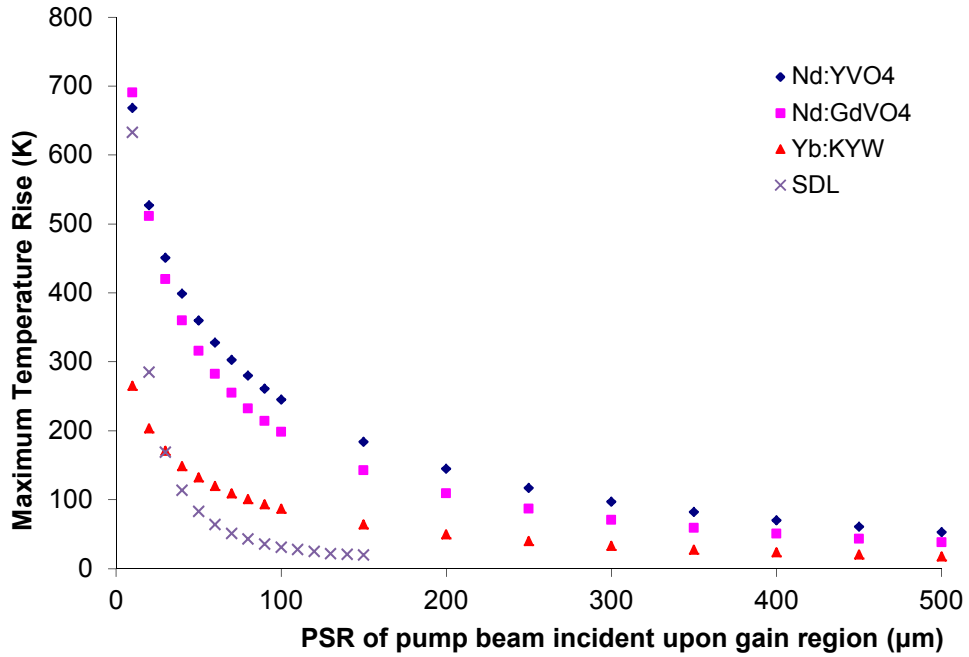

Figure 2.5.ii *Plot of maximum temperature rise versus pump spot radius (PSR) for Nd:YVO$_4$, Nd:GdVO$_4$, Yb:KYW and 1060nm SDL microchip lasers for an absorbed pump power of 8W. Each microchip laser is face-cooled by a diamond heatspreader. The PSR of the SDL was limited to 150µm due to computational requirements.*

2.6 Axially symmetric thermal modelling of $Nd:YVO_4$, SDL, $Nd:GdVO_4$, Yb:KYW with various heatspreaders (HS)– results and discussion

As mentioned in section 2.1, a potentially effective method to thermally manage microchip lasers is to use a heatspreader bonded to the gain region. This section will compare sapphire, silicon carbide (SiC) and diamond heatspreader thermal performance in $Nd:YVO_4$, $Nd:GdVO_4$, Yb:KYW and 1060nm SDL microchip lasers. Comparisons will be made with the same lasers using no heatspreader for thermal management. The 2-D axially symmetric model displayed in figure 2.2.i was used to model the $Nd:YVO_4$, $Nd:GdVO_4$ and Yb:KYW microchip lasers whilst the SDL geometry was identical to that used in the previous sections of this chapter. The model of the gain material without a heatspreader is still face-cooled, not by a heatspreader but from the rear by the brass mount, unlike the more common edge-cooled microchip lasers. The maximum temperature rise in each of the gain regions in each of the lasers was modelled and is displayed in figure 2.6.i.

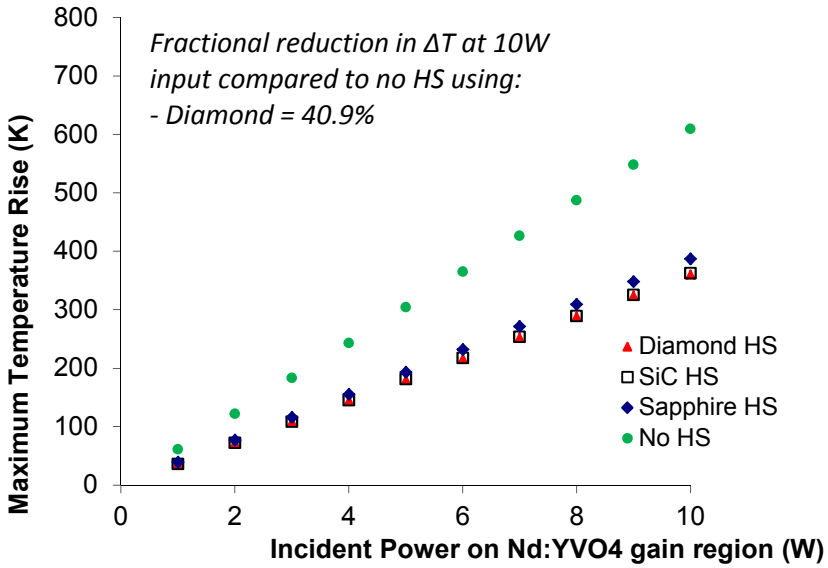

Figure 2.6.i graph a) *Plot of maximum temperature versus incident pump power for a $Nd:YVO_4$ microchip laser incorporating different heatspreaders for a pump spot radius of 50µm. HS stands for heatspreader. The fractional reduction is with respect to the case where the gain material is not bonded to a heatspreader.*

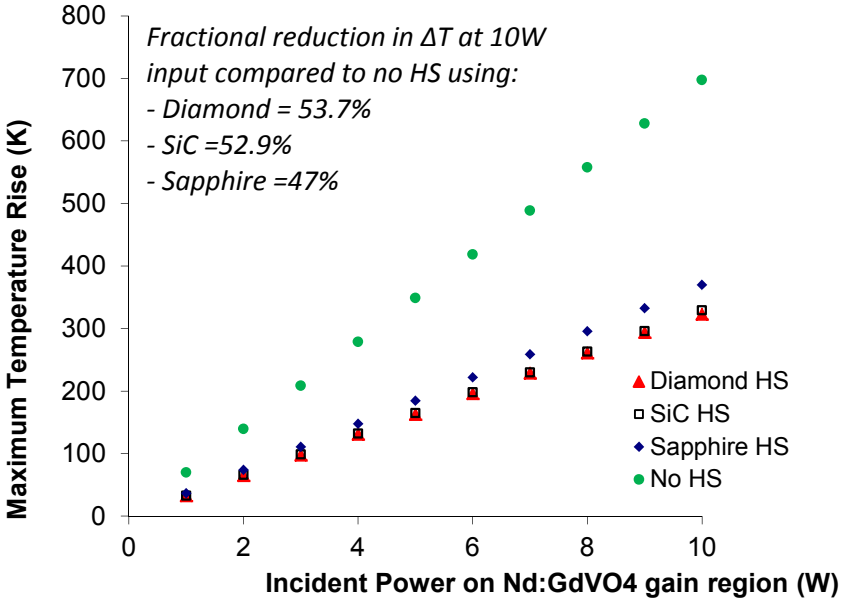

Figure 2.6.i graph b) *Plot of maximum temperature versus incident pump power for a Nd:$GdVO_4$ microchip laser incorporating different heatspreaders for a pump spot radius of 50µm. HS stands for heatspreader. The fractional reduction is with respect to the case where the gain material is not bonded to a heatspreader.*

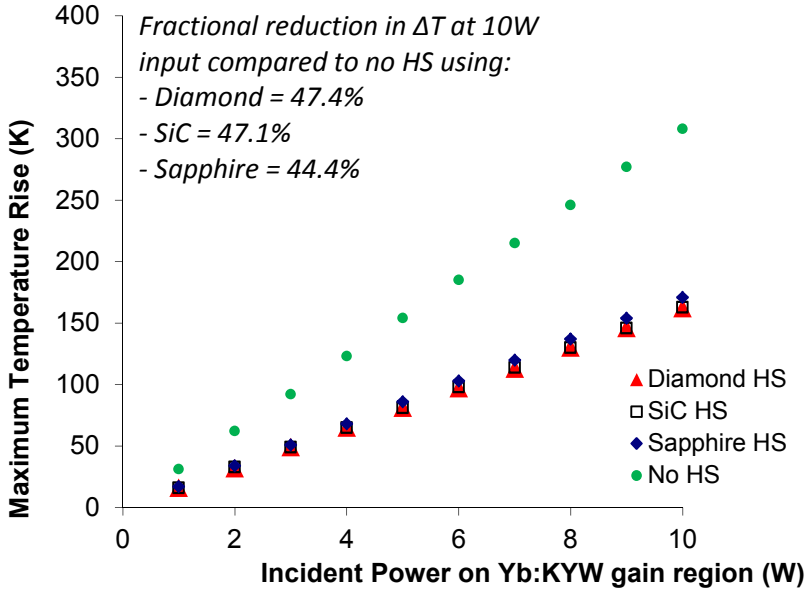

Figure 2.6.i graph c *Plot of maximum temperature versus incident pump power for a Yb:KYW microchip laser incorporating different heatspreaders for a pump spot radius of 50µm. HS stands for heatspreader. The fractional reduction is with respect to the case where the gain material is not bonded to a heatspreader.*

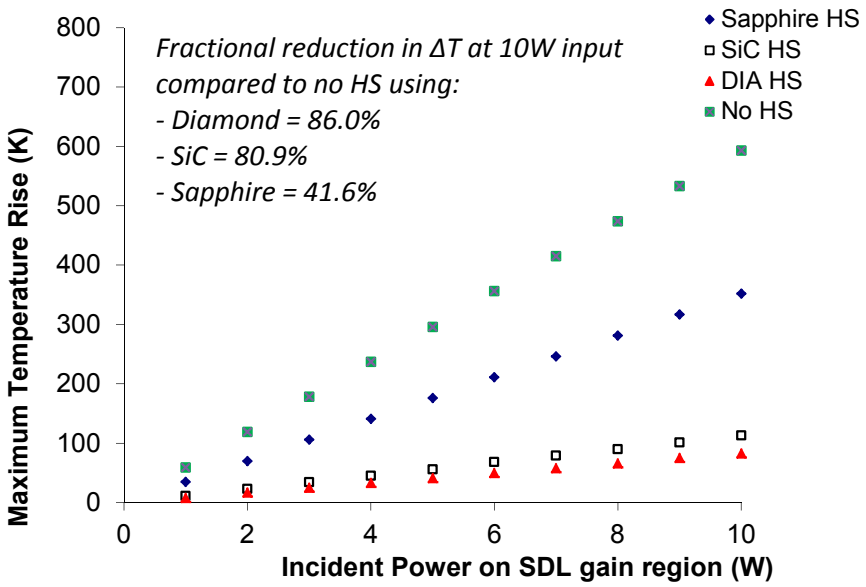

d)

Figure 2.6.i graph d) *Plot of maximum temperature versus incident pump power for a 1060nm SDL microchip lasers incorporating different heatspreaders for a pump spot radius of 50µm. HS stands for heatspreader. The fractional reduction is with respect to the case where the gain material is not bonded to a heatspreader.*

In the SDL case, the diamond heatspreader offers superior thermal management than the SiC heatspreader; moving from using a SiC heatspreader to a diamond heatspreader results in a fractional temperature reduction of 5% when compared to the temperature rise of the same structure incorporating no heatspreader. Overall, the diamond heatspreader offers an 86% reduction in temperature when compared to an SDL that incorporates no heatspreader. This is due in the main to the small thickness of the pump-absorbing gain region (around 1 µm) – this minimises the thermal resistance between the pumped region and the heatspreader allowing high thermal conductivity heatspreaders to be used to greater advantage. In the case of the doped-dielectric media, however, although diamond offers more effective thermal management than the SiC, the benefit is much smaller than in the SDL case. Compared to the SDL case where the temperature decrease moving from SiC to diamond is 24%, the superior performance that diamond displays over SiC is marginal where the fractional temperature drop using diamond with respect to SiC is about 0.6%, 1.8% and 0.6% for Nd:YVO_4, Nd:$GdVO_4$, and Yb:KYW.

In each laser the results demonstrate the advantages of using a heatspreader to reduce the maximum temperature rise within the gain region. Using a diamond heatspreader leads to the lowest maximum temperature rises followed by SiC and sapphire in order of decreasing thermal conductivity. Improvements in lowering the maximum temperature rise scale with the inverse of the thermal conductivity. To examine the effectiveness of heatspreaders based on thermal conductivity alone, a plot of maximum temperature rise versus heatspreader conductivity was plotted for each microchip laser as seen in figure 2.6.ii for an absorbed power of 8W.

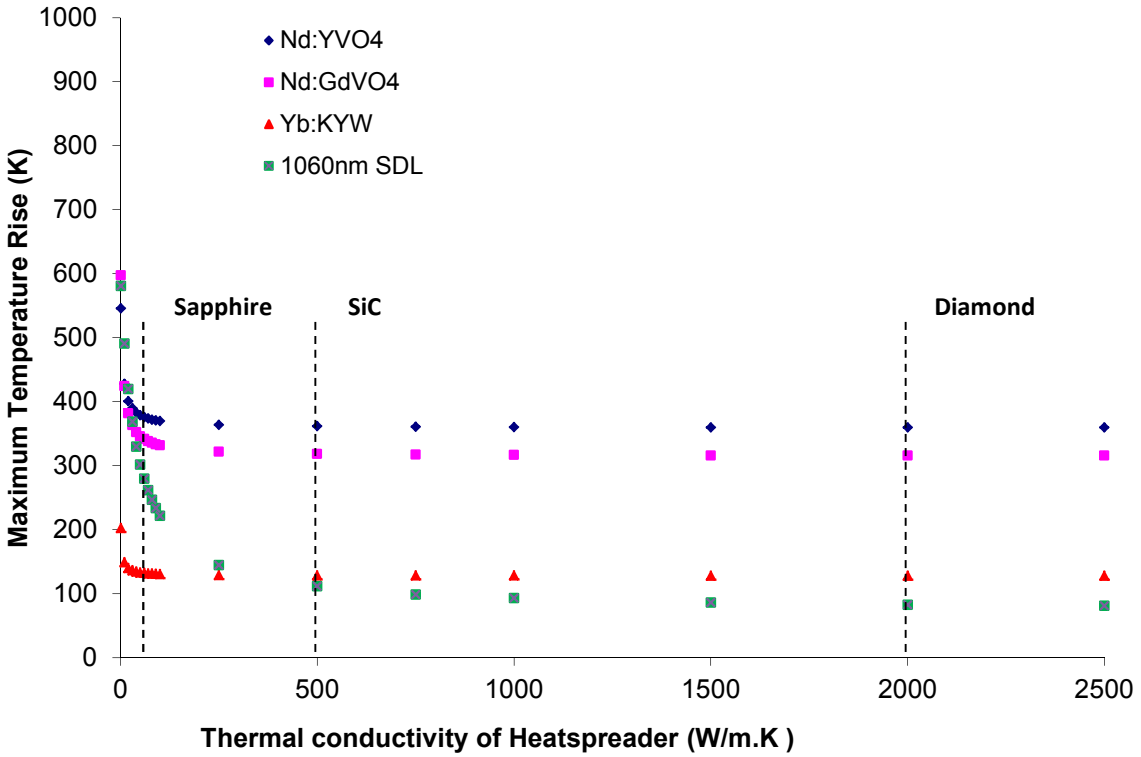

Figure 2.6.ii *Plot of maximum temperature versus incident thermal conductivity of heatspreader at a constant absorbed power of 8W for 0.5mm thick doped-dielectric gain region, pump spot radius of 50µm.The SDL has been included for reference.*

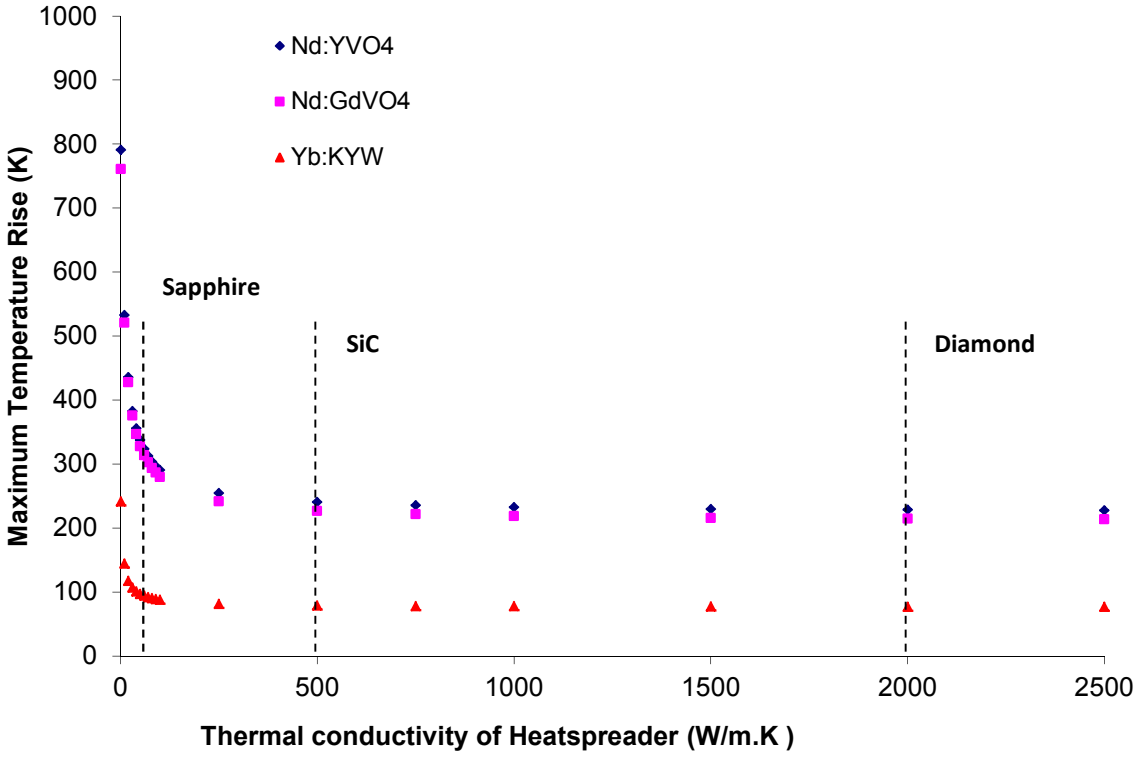

Figure 2.6.iii *Plot of maximum temperature versus incident thermal conductivity of heatspreader at a constant absorbed power of 8W for* ***a)*** *0.5mm thick doped-dielectric gain region,* ***b)*** *12.5µm thick doped-dielectric gain region, pump spot radius of 50µm.The SDL has not been included for reference in as the dimensions of the SDL are identical to the values listed in table 2.4c and so the gain region is not 0.5mm thick.*

The fact that the pump spot radius is 10 times less than that of the gain material thickness, however, means that the microchip laser is not operating under thin disk conditions whereby the radius of the pump spot is equal to or greater than the thickness of the gain material. A small pump spot size in comparison to the gain material thickness means that radial heat flow will dominate over axial heat flow and the thermal resistance will be larger leading because the superior thermal conductivity of the heatspreader is less well exploited. This in turn leads to higher maximum temperatures. To investigate the doped dielectric materials in a thin disk format using FEA the gain media were scaled down to thicknesses of 12.5µm whilst keeping the pump spot radius at 50µm and the calculations repeated and

shown in figure 2.6.iii. The fractional temperature drop using diamond with respect to SiC is about 5%, 5.3% and 3% for Nd:YVO_4, Nd:$GdVO_4$ and Yb:KYW. Thus for decreasing thicknesses of doped-dielectric gain material, diamond is the optimal heatspreader choice; however, polishing crystals to thicknesses of tens of microns is a very challenging task to accomplish with respectable yields. The alternative would be to keep the thickness larger and increase the pump spot radius. When choosing a heatspreader material for thicker doped-dielectric microchip lasers however, the lower cost of SiC might well make it a more optimal choice over diamond in certain applications but in high power applications where heatspreader rigidity might become an issue, diamond displays superior properties over SiC.

2.7 Axially symmetric thermal modelling of different thicknesses of Nd:YVO_4, Nd:$GdVO_4$ and Yb:KYW with various heatspreaders (HS)– results and discussion

In this section the effect of gain material thickness upon maximum temperature rise within the gain regions was examined. The geometric model seen in section 2.1 was adopted once more and the gain material thickness adjusted, using Nd:YVO_4, Nd:$GdVO_4$ and Yb:KYW as the gain media. The absorbed pump power was kept constant at 8W. The simulations were made for three different pump spot radii of 50µm, 200µm and 500µm. The results can be seen in figure 2.7.i.

For the Nd:YVO_4, Nd:$GdVO_4$ and Yb:KYW gain media at a pump spot radius of 50µm, the maximum temperature peaks at approximately at a thickness of approximately 100µm, roughly twice the pump spot radius, and drops off with increasing thickness. At thicknesses larger than approximately 500µm, the maximum rise in temperature plateaus in the Yb:KYW case whilst for the Nd:YVO_4 and Nd:$GdVO_4$ cases the rise in temperature plateaus at thicknesses approximately above 1mm.

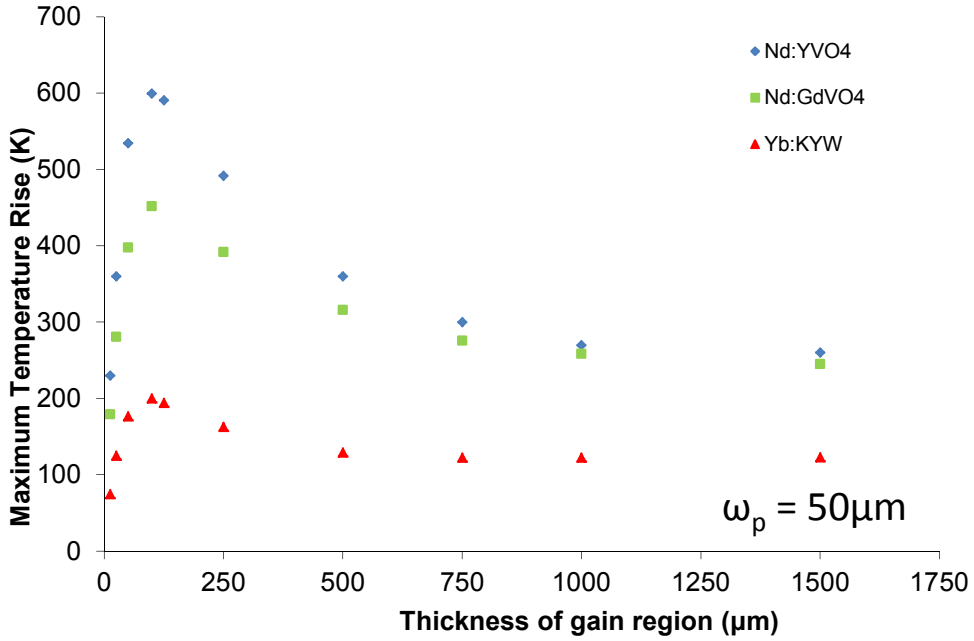

Figure 2.7.i graph a) *Plot of maximum temperature versus thickness of gain region for a 50µm pump spot radius, at a constant absorbed power of 8W.*

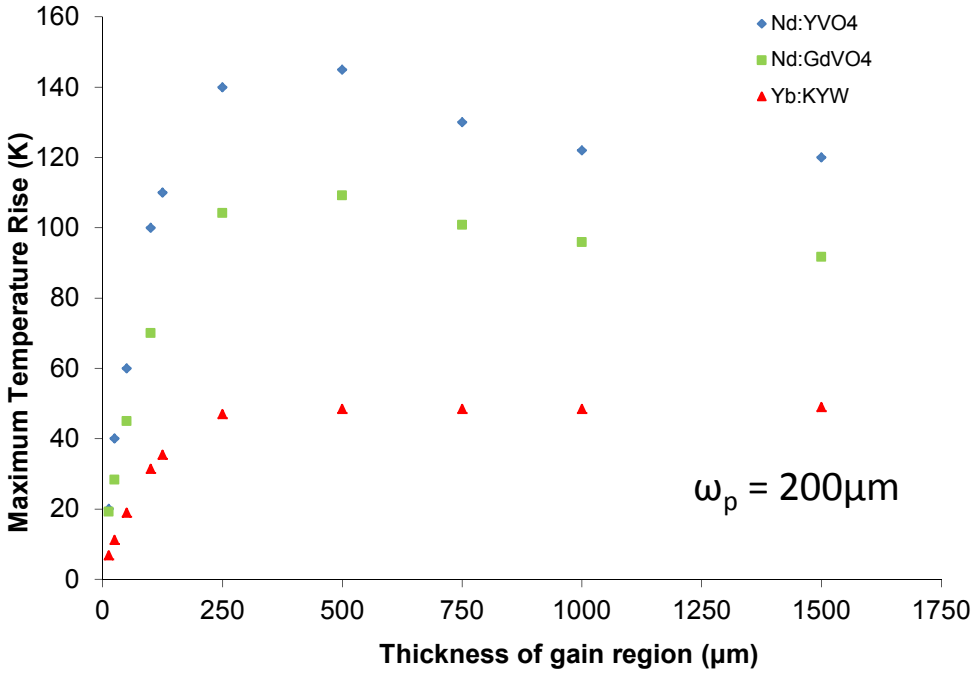

Figure 2.7.i graph b) *Plot of maximum temperature versus thickness of gain region for a 200µm pump spot radius, at a constant absorbed power of 8W.*

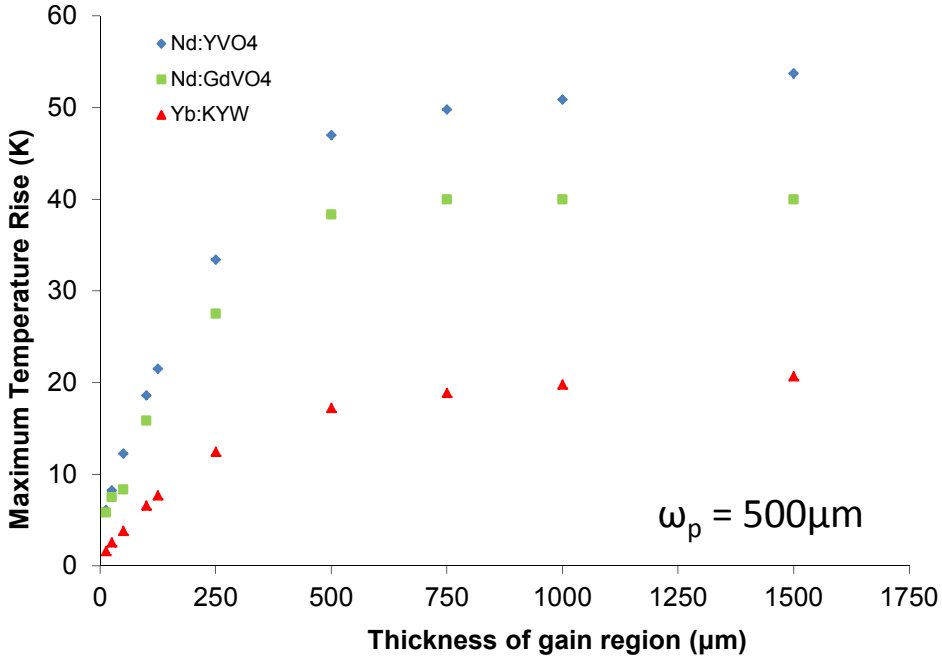

Figure 2.7.i graph c) *Plot of maximum temperature versus thickness of gain region for a 500µm pump spot radius, at a constant absorbed power of 8W.*

For the case of a 200µm pump spot radius in graph b) there is a peak in the temperature rise for a gain material thickness of roughly twice the pump spot radius for each of the gain materials. To minimise heating it is necessary to operate at thicknesses under approximately 250µm for the Nd:YVO_4, Nd:$GdVO_4$ and Yb:KYW microchip lasers respectively. For thicknesses above these values, the temperature drops off and then plateaus at ~1000µm for the Nd:YVO_4 and Nd:$GdVO_4$ cases whereas in the Yb:KYW case, the maximum temperature plateaus between 250µm and 500µm.

The Nd:YVO_4 and Nd:$GdVO_4$ microchip lasers show a steady increase in maximum temperature in b) up to approximately twice the pump spot radius of 500µm where the temperature levels off. The Yb:KYW does not show a plateau at this pump spot radius within the range of data points but whilst the maximum temperature increases as the thickness of the Yb:KYW increases, the rise in maximum temperature becomes less steep.

The shape of the graphs in figure 2.7.i is likely to depend upon the ratio of pump radius to the thickness of the gain material. At gain thicknesses less than the pump spot radius the laser can be assumed to be operating in the thin-disk regime [13] where axial heat flow is predominant and the thermal resistance is lowered in the gain region as the thickness decreases, leading to a reduced temperature rise. The heat flow paths for the Nd:YVO_4 can be seen in figure 2.7.ii where it can be seen that axial heat flow is indeed in evidence. At gain thicknesses larger than the pump spot radius, the laser behaves in a similar manner to that of a rod laser and predominantly radial heat flow can be observed in figures 2.7.iii to 2.7.v. This can be seen in the maximum temperature rises in a) and b) where a peak is evident at roughly twice the pump spot radius. Below the thicknesses equivalent to two times the pump spot radius, the thermal resistance drops and so the maximum temperature rise drops as well.

At largest thicknesses modelled, there is a reduction in the maximum temperature rise as the thickness is increased which is analogous to a rod-laser where the increase in rod length spreads the heat load over a larger volume. However, when the thickness of the gain material increases beyond its absorption depth then the heat is no longer spread throughout the sample but inside a number of absorption lengths which means that for the vanadates, the maximum temperature rise will saturate at a thickness of around 1mm for pump polarisation around the a-axis. For Yb:KYW with a stronger absorption coefficient, we can expect this saturation to occur earlier.

In graph c) the disk-like behaviour is effectively overlapping the rod behaviour zone and so the maximum temperature rise peak seen in graphs a) and c) is reduced and cannot be seen.

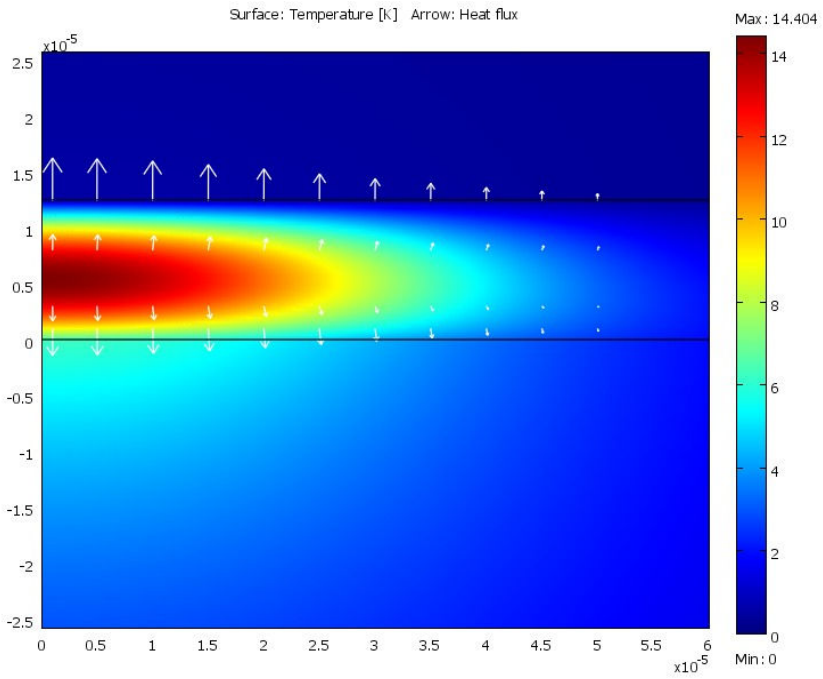

Figure 2.7.ii *Heat flux plot of a 12.5µm thick Nd:YVO_4 microchip laser with a diamond heatspreader for a constant absorbed power of 8W and a pump spot radius of 50µm. The heat rise occurs in the gain region which is sandwiched between the heatspreader above and the indium below. Arrow size indicates the magnitude of heat flow.*

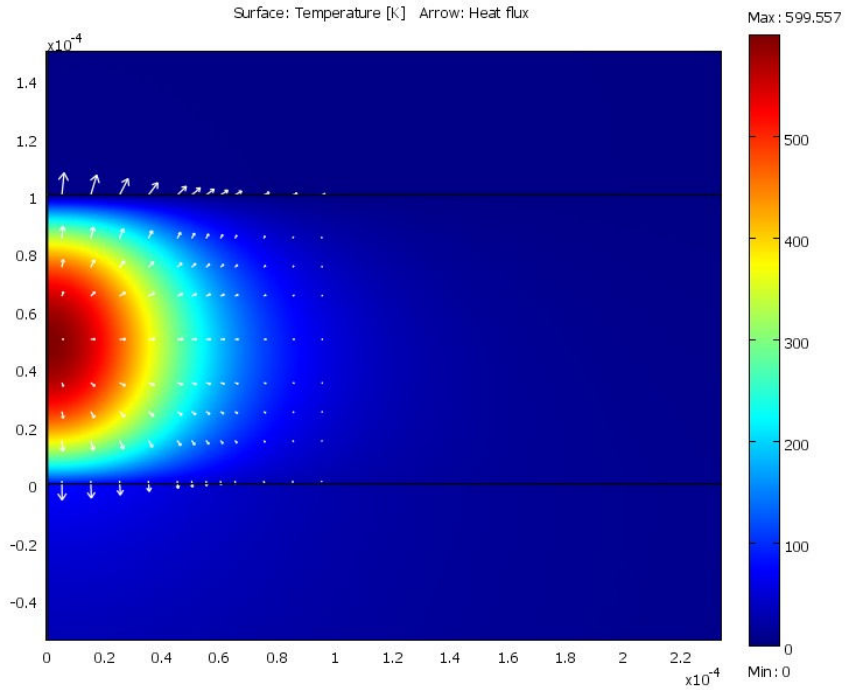

Figure 2.7.iii *Heat flux plot of a 12.5µm thick Nd:YVO_4 microchip laser with a diamond heatspreader for a constant absorbed power of 8W and a pump spot radius of 50µm. The heat rise occurs in the gain region which is sandwiched between the heatspreader above and the indium below. Arrow size indicates the magnitude of heat flow.*

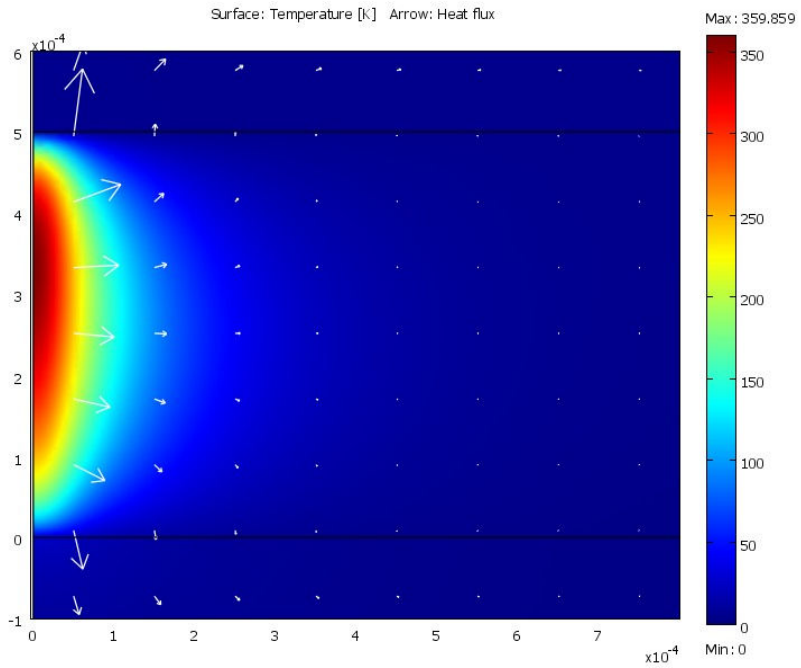

Figure 2.7.iv *Heat flux plot of a 100µm thick Nd:YVO_4 microchip laser with a diamond heatspreader for a constant absorbed power of 8W and a pump spot radius of 50µm. The heat rise occurs in the gain region which is sandwiched between the heatspreader above and the indium below. Arrow size indicates the magnitude of heat flow.*

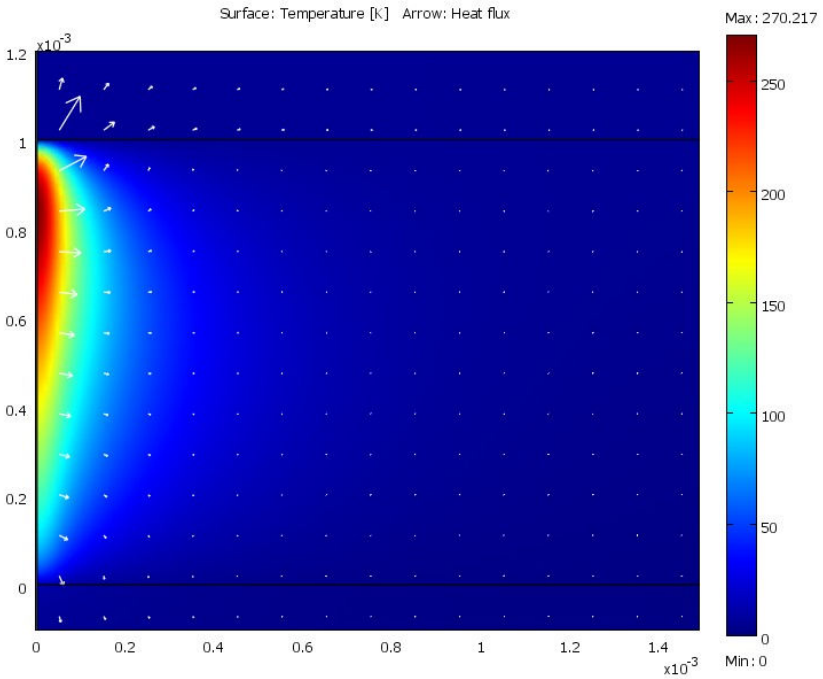

Figure 2.7.v *Heat flux plot of a 1000µm thick Nd:YVO_4 microchip laser with a diamond heatspreader for a constant absorbed power of 8W and a pump spot radius of 50µm. The heat rise occurs in the gain region which is sandwiched between the heatspreader above and the indium below. Arrow size indicates the magnitude of heat flow.*

2.8 Thermal lens investigation of a Nd:YVO_4 microchip laser incorporating a diamond and SiC heatspreader

As discussed in chapter one of this thesis, a thermal lens arises in a solid-state microchip laser when it is optically pumped. This thermal lens is derived from the thermo-optic coefficient, *dn/dT*. As heat is deposited in the gain medium via optical pumping, it will diffuse away from the pumped region to the edges of the gain material leading to a radially varying temperature distribution. This results in a thermally-induced refractive index variation across the pumped region. A second contributing factor to the thermal lens stems from the differential thermal expansion. The thermal lens analysis in this section only takes into account the thermal lens contribution from *dn/dT* and not the contribution from mechanical deformation and thus it is a simplified model. However, the presence of a heatspreader will to some extent constrain any mechanical deformation reducing the contribution to the overall thermal lens.

The thermal lens of the Nd:YVO_4 microchip laser used in section 2.1 was investigated for an absorbed pump power of 8W, pump spot radius of 50µm. The thickness of the Nd:YVO_4 sample was varied and two heatspreaders, diamond and SiC, were modelled. A radial cross section of the maximum temperature rise in the gain medium and heatspreader was extracted from the FEA models and then averaged over the thickness of the material.

The change in optical lengths Δl_{gain} and $\Delta l_{heatspreader}$ from the contributions of the gain and heatspreader could be calculated using the following formulae:

$$\Delta \mathrm{l}_{\mathrm{gain}} = \mathrm{t}_{\mathrm{gain}} \left[\mathrm{n}_{\mathrm{gain}} + \frac{\mathrm{dn}}{\mathrm{dT}_{\mathrm{gain}}} \, \mathrm{dT}_{\mathrm{gain}} \right] \qquad \text{Eq.2.8i}$$

$$\Delta l_{HS} = t_{HS} \left[n_{HS} + \frac{dn}{dT_{HS}} \, dT_{HS} \right] \qquad \text{Eq.2.8ii}$$

Where *t* is the thickness of the material, *dT* is the temperature change averaged parallel to the cavity axis, *n* is the refractive index and *dn/dT* is the thermo-optic coefficient. By

calculating the change in optical length, the thermal lens could be found and expressed in terms of a radius of curvature of the equivalent mirror, assuming that the thermal lens resembles a spherical lens. For each gain material thickness, the change in axially averaged refractive index with respect to the radial position for the 50µm pump spot radius case was plotted by using data extracted from the FEA simulations for the diamond heatspreader case. A spherical lens profile was then fitted as seen in figure 2.8.i so that a qualitative comparison could be made between the two profiles to ascertain the accuracy of the spherical lens assumption.

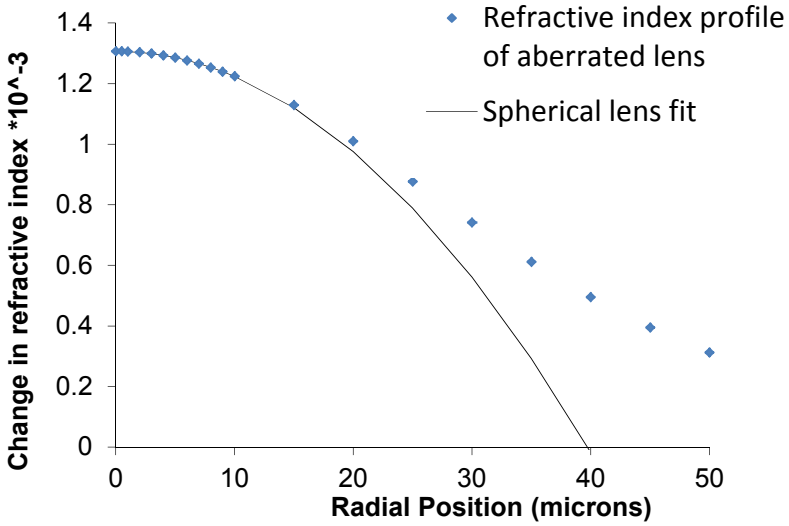

a)

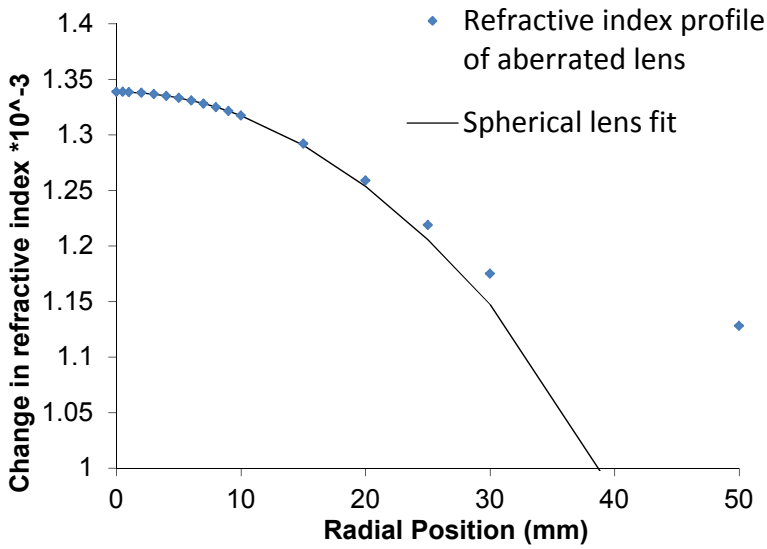

b)

Figure 2.8.i *A plot of the change in refractive index of the gain region versus radial position for a) a 12.5µm thick gain region and b) a 1mm thick gain region.*

It can be seen that for a radial position equal to half that of the pump spot radius, the refractive index difference between the two profiles is approximately 10% for the 12.5µm thickness and 1% for the 1mm thickness indicating that the spherical assumption is more accurate for the thicker gain regions examined.

Using equation 2.8.iii, the fundamental cavity mode radius ω_0 could be calculated for each model, where R_{total} is the total radius of curvature calculated from the contributions of the thermal lens within the gain and the heatspreader.

$$\omega_0 = \sqrt{\left(\frac{\lambda}{\pi\, n_{gain}}\right)\sqrt{\left(t_{gain} + t_{HS}\right)\left(R_{total} - \left(t_{gain} + t_{HS}\right)\right)}} \qquad \text{Eq.2.8.iii}$$

A plot of the thermal lens vs. gain thickness can be seen in figure 2.8.iia. It can be seen that the thermal lens is very similar in the SiC heatspreader case to the diamond case at gain thicknesses of above 100µm. Below 100µm the thermal lens of the SiC model becomes noticeably stronger than the diamond model. For both models, the radius of curvature of the equivalent mirror of the thermal lens drops rapidly below 100µm due to decreasing thermal resistance and axial heat flow becoming predominant over radial flow. At a thickness of 12.5µm, the use of a diamond heatspreader led to a predicted radius of curvature drop of 55%. The higher thermal conductivity of diamond ensures that the Nd:YVO_4 sees a smaller thermal lens over the entire range of thicknesses modelled compared to SiC, below 50µm diamond shows much better performance in reduction of the thermal lens.

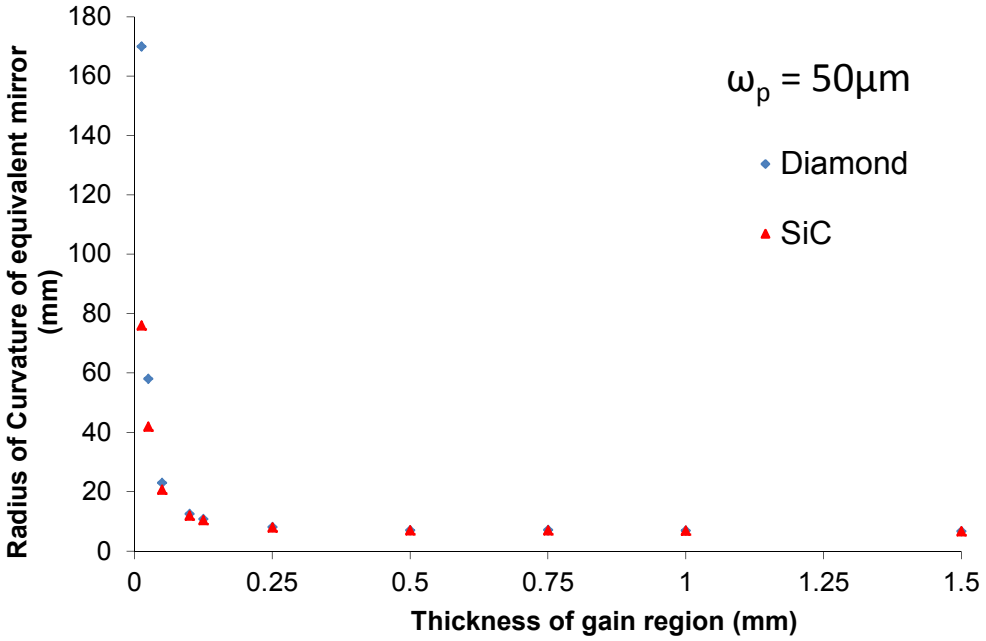

a)

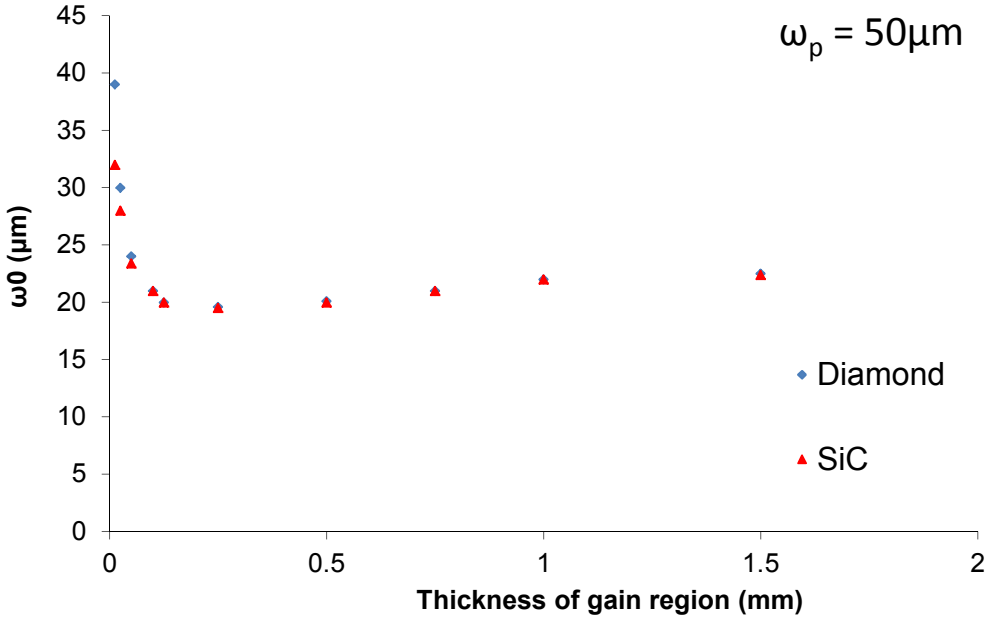

b)

Figure 2.8.ii *A plot of thermal lens versus thickness of gain region can be seen in* ***a)*** *for SiC and diamond heatspreaders. In* ***b)*** *a plot of minimum cavity mode radius versus thickness of gain region can be seen for the respective heatspreaders.*

In figure 2.8.iib) a plot of the calculated cavity mode radius vs. gain thickness can be seen. It is assumed for this calculation that the M^2 of this laser is 1 for convenience. There is a minimum in cavity mode radius for gain material thicknesses between 125µm and 500µm, the thickness predominately used in the experimental sections of this thesis. This must to some extent explain the poor beam quality observed since, as explained above, increasing the fundamental cavity mode radius to better match that of the pump is likely to be an essential part of improving the beam quality. Below 125µm, the cavity mode increases rapidly. Again diamond shows superior performance compared to the SiC at thicknesses less than or equal to about 12.5µm where the fundamental cavity mode radius is predicted to increase by 18% when moving from using SiC to diamond.

Larger pump spot radii of 200µm and 500µm were examined for the diamond heat spreader case, the results of which can be seen in figure 2.8.iii. It can be seen that at a constant absorbed power of 8W, the larger pump spot radii lead to longer thermal lens focal lengths and larger cavity mode radii than the 50µm pump spot radius case. For the 200µm pump spot radius case, a minimum in cavity mode radius occurs for gain material thicknesses between the 500µm and 750µm from the centre; for the 500µm pump spot radius, the minimum occurs between 500µm and 1000µm.

To ensure weaker thermal lensing and larger cavity modes in Nd:YVO_4 microchip lasers, it is predicted that the gain thickness needs to be kept small compared to the pump spot radius so that axial heat flow is attained. However, practicalities of sample fabrication and the need to ensure efficient pump absorption may limit the extent to which such thin samples of Nd:YVO_4 can be exploited. The finite element analysis also predicts that it is unlikely that the cavity and pump mode radii can be matched at absorbed powers of 8W or greater; however experimental data would be needed to confirm this. In addition the modelling suggests that at an absorbed power of 8W, the smaller pump spot radius of 50µm enables a larger cavity to pump spot radius ratio (cavity mode/pump mode) at all gain thicknesses compared to the 200µm and 500µm pump spot cases. In future, the effect of the thermal-mechanically induced thermal lens should also be taken into account in future models. Whilst diamond has showed superior performance in the simplified models above, if the

models are adapted to take into account thermally induced stress, diamond can be expected to outperform SiC further due to the superior mechanical properties of diamond.

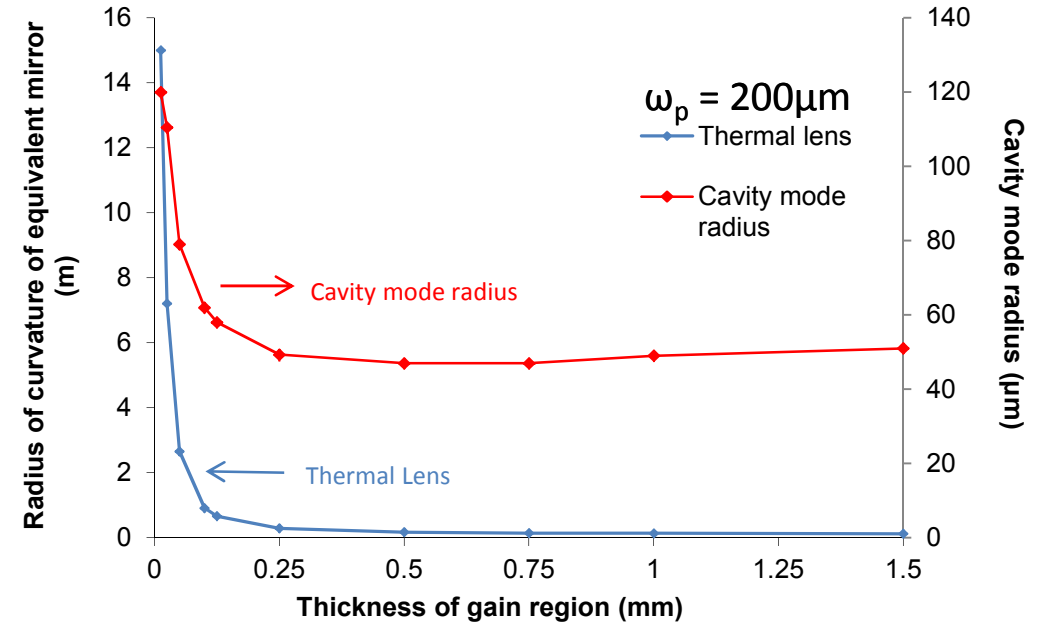

a)

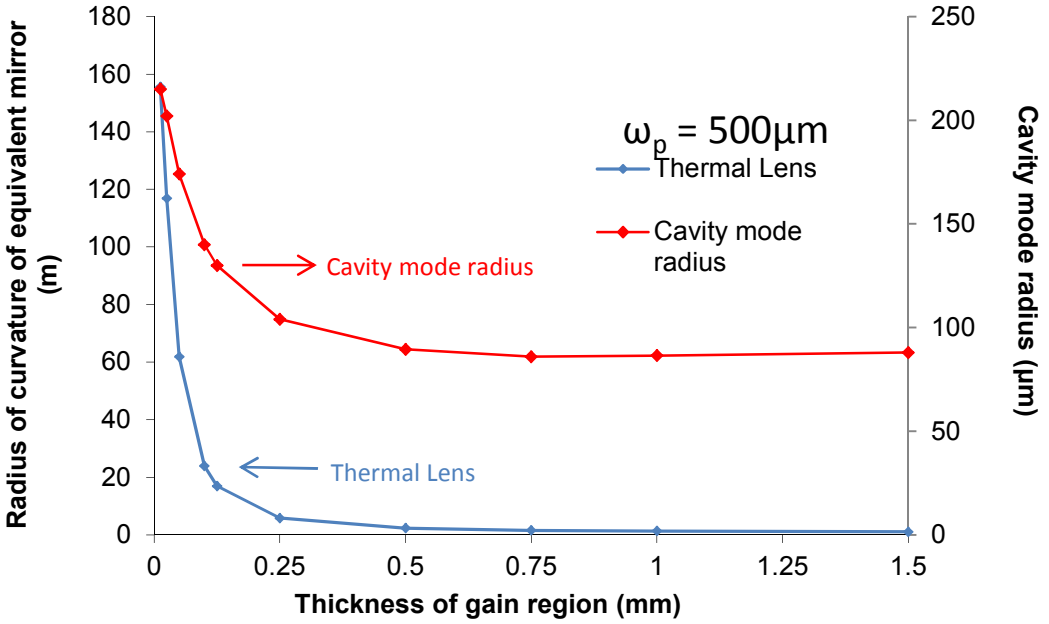

b)

Figure 2.8.iii *A plot of the radius of curvature of an equivalent mirror (measured in metres rather than millimetres) versus thickness of gain region can be seen for a pump spot radius of* ***a)*** *200µm and a pump spot radius of* ***b)*** *500µm. Aline has been plotted for each set of data points in order to make the two sets more distinct rather than to suggest a theoretical fit.*

2.9 Conclusion

A number of different microchip configurations have been investigated in this chapter using finite element thermal analysis. The 3-D model can simulate the anisotropy of the doped-dielectric crystals more accurately by virtue of modelling all 3 principal axes for each crystal, producing a more accurate result compared to the 2-D axially symmetric case. However, it has been shown that using a 2-D axially symmetric model in place of a 3-D model results in an error in the final calculated temperature rise of only around 5%. Accepting that there will be a small degree of inaccuracy in using the axially symmetric format, benefits are gained in the form of reduced demands on computational resources which results in a reduced computational time. For the purposes of investigating trends in performance, the 2-D axially symmetric approach was adopted for the rest of the simulations.

A greater deal of uncertainty in the final result arises from the choice of material parameters when dealing with disagreement in the scientific community for the case of the vanadates; Nd:YVO_4 and Nd:$GdVO_4$. The groups of Patrick Georges and Takunori Taira have measured the thermal conductivity of Nd:YVO_4 and Nd:$GdVO_4$ using different experimental techniques and have reported a wide difference in values as shown in table 2.3i. This results in a maximum temperature rise difference of 59% in the Nd:YVO_4 model when going from using Taira's group's values to using Georges' group's values. Similarly, there is a difference of 47% in the Nd:$GdVO_4$ case. On inspection of each group's experimental method it was decided to use the values provided by George's group due to the fact that the experimental conditions used in their method mirror more closely the conditions that the microchip lasers modelled in this chapter would expect to operate under.

When comparing the models of Nd:YVO_4, Nd:$GdVO_4$, Yb:KYW and a 1060nm SDL bonded to a diamond heatspreader at constant absorbed power using FEA, it was found that Yb:KYW suffered the lowest temperature rise out of the doped-dielectric gain media examined. Nd:YVO_4 experienced a larger temperature rise compared to Nd:$GdVO_4$ which has a smaller thermal conductivity. The SDL sample experienced the lowest rise out of all the materials examined. This was due to the higher thermal conductivity of the semiconductor layers but

more importantly to the layers being on the order of a few microns in thickness resulting in a much lower thermal resistance.

Different heatspreader materials were modelled for each of the different gain materials in order to assess the optimal heatspreader for use in a microchip system. In the case of the SDL, diamond proved to be the obvious choice showing a 24% fractional improvement going from diamond to SiC. Indeed, the overall fractional improvement in temperature from using no heatspreader to using a diamond heatspreader was found to be 86% demonstrating that diamond is indeed the heatspreader of choice for SDL systems. For the doped dielectrics, however, the improvement in using a diamond heatspreader for a gain thickness of 0.5mm, pump spot radius of 50µm, was not as dramatic compared to the SDL case but impressive nonetheless, resulting in an improvement of 41% in reduction in maximum temperature rise. When comparing different heatspreader types for use in the doped dielectrics it was discovered at gain thicknesses of 0.5mm, the thermal improvement from using a SiC heatspreader to using a diamond heatspreader is again not as pronounced as in the SDL case with a reduction in temperature of only 0.6% in the Nd:YVO_4 case. This is due to the difference in thickness of the absorbing layers in the SDL and doped-dielectric cases; when the thickness of the doped-dielectrics is reduced to 12.5µm whilst the pump spot ratio is held at 50µm, going from using a SiC heatspreader to using a diamond heatspreader results in a reduction in temperature of 5% in the Nd:YVO_4 case. Diamond is the best performing heatspreader for the doped-dielectrics compared to SiC and sapphire and the performance gap between diamond and SiC increases as the thickness of the gain material in the microchip decreases. For some applications, however, SiC might be the preferred heatspreader when high performance is not as important as cost etc. On the other hand, the superior mechanical properties of diamond will give it the edge in high power applications.

The final section of this chapter investigated the relationship between gain thickness and a range of pump spot radii for a constant absorbed power across Nd:YVO_4, Nd:$GdVO_4$ and Yb:KYW. It was found that at gain material thicknesses around twice the pump spot radius, a peak in the maximum temperature rise is likely to occur and so when designing future

microchip lasers it is best to choose a ratio of pump spot radius and gain thickness that avoids this region by either reducing the gain thickness or increasing the pump spot radius to operate in the thin-disk regime. Out of the three doped-dielectric gain materials examined in this chapter, the ability to highly dope Yb:KYW makes it the best candidate for working in the thin-disk regime. In addition, thermal lensing was modelled in a Nd:YVO_4 microchip laser bonded to SiC and diamond heatspreaders, and it was predicted that the thermal lensing experienced in the microchip laser decreases by operating in the thin-disk regime. The diamond heatspreader provided increasingly superior performance than SiC as the gain thickness was decreased, potentially allowing for easier cavity/pump spot mode overlap to be achieved at higher powers and highlighting diamond as the heatspreader of choice in doped-dielectric microchip lasers operating in the thin disk regime.

It was also predicted that for the Nd:YVO_4 microchip laser bonded to a diamond heatspreader, it will be very difficult to match the cavity and pump mode radii at absorbed powers of 8W or greater. At these absorbed powers, a lower pump spot radius might achieve a closer pump spot/cavity mode radius match but it must be noted that crystal fracture is more likely to occur at lower pump spot radii at higher powers and the contribution from stress effects will become greater. The lower maximum temperature rises of Yb:KYW compared to Nd:YVO_4 and Nd:$GdVO_4$ as seen in figure 2.7.i likely indicate that a weaker thermal lens is present and so it can be assumed that a larger cavity mode can be supported. Depending on the size of this cavity mode, mode matching is more likely to be attainable at higher input powers for Yb:KYW than for Nd:YVO_4. Decreasing the pump mode radius might improve the cavity/pump mode overlap for Nd:YVO_4 due to the inherent small size of the cavity mode at these input powers; however, in the Yb:KYW case it may prove possible to achieve god mode overlap for larger pump spot radii. Future modelling should be carried out to examine thermal lensing within Yb:KYW at similar input powers and pump spot radii in order that the magnitude of the cavity mode may be estimated. If a cavity mode can be supported by the Yb:KYW that is similar in radius to the pump spot then high power, high brightness operation may be possible. The low quantum defect of the Yb:KYW will serve to provide a larger cavity mode than supported by the Nd:YVO_4, whilst the ability to dope Yb:KYW to higher levels coupled with the use of diamond means that efficient

operation in the thin disk regime should be easier to achieve and allow for the magnitude of the cavity mode radius to be increased further.

2.10 References

[1] R. Weber, B. Neuenschwander, M. MacDonald, M. B. Roos, and H. P. Weber, "Cooling schemes for longitudinally diode laser-pumped Nd : YAG rods," *IEEE Journal of Quantum Electronics*, vol. 34, pp. 1046-1053, 1998.

[2] J. L. Blows, T. Omatsu, J. Dawes, H. Pask, and M. Tateda, "Heat generation in Nd:YVO_4 with and without laser action," *IEEE Photonics Technology Letters,* vol. 10,pp. 1727–1729, 1998.

[3] J. Didierjean, E. Herault, F. Balembois, and P. Georges, "Thermal conductivity measurements of laser crystals by infrared thermography. Application to Nd:doped crystals," *Optics Express*, vol. 16, pp. 8995-9010, 2008.

[4] T. Jensen, V. G. Ostroumov, J.-P. Meyn, G. Huber, A. I. Zagumennyi, and I. A. Scherbakov, "Spectroscopic characterization and laser performance of diode-laser-pumped Nd:$GdVO_4$," *Applied Physics B*, vol. 58, pp. 373–379, 1994

[5] I. Friel, S. L. Geoghegan, D. J. Twitchen, and G. A. Scarsbrook, "Development of high quality single crystal diamond for novel laser applications," presented at Optics and Photonics for Counterterrorism and Crime Fighting VI and Optical Materials in Defence Systems Technology VII, Toulouse, France, 2010.

[6] Y. Sato and T. Taira, "The studies of thermal conductivity in $GdVO_4$, YVO_4, and $Y_3Al_5O_{12}$ measured by quasi-one-dimensional flash method," *Optics Express*, vol. 14, pp. 10528-10536, 2006.

[7] A. J. Kemp , G. J. Valentine , J. M. Hopkins , J. E. Hastie , S. A. Smith , S. Calvez , M. D. Dawson and D. Burns "Thermal management in vertical-external-cavity surface-emitting lasers: Finite-element analysis of a heatspreader approach", *IEEE Journal of Quantum Electronics*, vol. 41, p.148-155 , 2005.

[8] A. A. Kaminskii, K. Ueda, H. J. Eichler, J. Findeisen, S. N. Bagaev, F. A. Kuznetsov, A. A. Pavlyuk, G. Boulon, and F. Bourgeois, "Monoclinic tungstates KDy(WO4)2 and KLu(WO4)2: new χ(3)-active crystals for laser Raman shifters," *Japanese Journal of Applied Physics*, vol. 37, pp. 929–932, 1998

[9] P. K. Mukhopadhyay, A. Nautiyal, P. K. Gupta, K. Ranganathan, J. George, S. K. Sharma, and T. P. S. Nathan, "Experimental determination of the thermo-optic coefficient (dn/dT) and the effective stimulated emission cross-section (σe) of an a-axis cut 1.-at. % doped Nd:GdVO4 crystal at 1.06 μm wavelength," *Applied Physics. B*, vol. 77, pp. 81–87, 2003

[10] A. I. Zagumennyi, V. A. Mikhailov, V. I. Vlasov, A. A. Sirotkin, V. I. Podreshetnikov, Yu. L. Kalachev, Yu. D. Zavartsev, S. A. Kutovoi, and I. A. Shcherbakov, "Diode-pumped lasers based on GdVO4 crystal," *Laser Physics*, vol. 13, pp. 311-318, 2003.

[11] N. V. Kuleshov, A. A. Lagatsky, A. V. Podlipensky, V. P. Mikhailov, and G. Huber, "Pulsed laser operation of Y b-dope d $KY(WO_4)_2$ and $KGd(WO_4)_2$," Optics Letters, vol. 22, pp. 1317-1319, 1997

[12] A. J. Maclean, "Power Scaling and Wavelength Control of Semiconductor Disk Lasers," Ph.D. Thesis: University of Strathclyde, 2008.

[13] A. Giesen, H. Hugel, A. Voss, K. Wittig, U. Brauch, and H. Opower, "Scalable Concept For Diode-Pumped High-Power Solid-State Lasers," *Applied Physics B-Lasers and Optics*, vol. 58, pp. 365-372, 1994.

3. Experimental analysis of heatspreaders in three-mirror and quasi-microchip cavity arrangements

3.1 Introduction

The modelling presented in chapter 2 indicated the potential of face cooling, via a heatspreader, to improve thermal management in microchip lasers; in this chapter, that potential will be examined experimentally. To maximise the output power and brightness of a microchip laser, it is necessary to identify the most effective material for the heatspreading role. Sapphire, SiC and diamond heatspreaders were modelled in a Nd:YVO_4 microchip system and it was shown that whilst the diamond case delivered the lowest temperature gradients within the gain material, the predicted performance of the SiC heatspreader was also encouraging. The heatspreader properties of diamond, SiC and sapphire can be seen in table 3.1.i. which has been reproduced from table 1.4.i in chapter 1. When choosing a heatspreader material the considerations of expense and sample size need to be taken into account especially if there are industrial and commercial interests to be considered.

Material	Thermal Conductivity (W/(m.K))	Young's Modulus (GPa)	Thermal Expansion Coefficient ($x10^{-6}$ K^{-1})	Thermo-optical Coefficient ($x10^{-6}$ K^{-1})	Tensile Strength (MPa)	Approximate cost of heatspreader (£)
Diamond	2000 [1]	1100 [1]	1.0 [1]	9.6 [1]	2860 [1]	1000
SiC	490 [2]	393 [3]	4.5 [4]	36 [5]	~1000 [6]	160*
Sapphire	34 [1]	344 [1]	5.3 [1]	12 [1]	400 [1]	30
YAG	12.9 [7]	282 [7]	8 [7]	7.3 [7]	200 [8]	-

Table 3.1.i *A comparison of the properties of candidate heatspreader materials with Nd:YAG – an archetypal solid-state laser material. The costing of the diamond, SiC, and sapphire heatspreaders are sourced form Element 6, TankeBlue, and Optosigma respectively.*This is the approximate price for a 2 inch wafer.*

In this chapter the suitability of sapphire, SiC and diamond heatspreaders are examined experimentally for use in future power and brightness-scaled microchip lasers. The heatspreaders will be bonded to 0.5mm thick samples of 1 and 3 atm. %

doped Nd:YVO_4 and mounted in two cavity configurations: a three mirror cavity and a quasi-microchip cavity. In the terminology used in this thesis a microchip laser consists of a monolithic or quasi-monolithic device with no air-gaps present and the mirror coatings are deposited on the outer element(s) so that the cavity is of fixed length. A quasi-microchip laser is defined, for the purposes of this thesis, as a microchip laser which has a discrete output-coupling mirror separated from the gain material by an air gap; quite frequently this is simply an ordinary output coupler that completes the cavity. Essentially the quasi-microchip is a conventional 2-mirror laser configuration that allows for certain parameters to be optimised for future use in microchip lasers. The recent development of low-loss synthetic diamond is discussed, as is the method used experimentally to bond heatspreaders to the gain material.

3.2 Performance of heatspreaders in a conventional laser resonator configuration

A conventional three mirror cavity configuration was used in this section and can be seen in figure 3.2.i**.** A 10W fibre-coupled laser diode (100µm core-diameter, 0.2NA) operating at a wavelength of 808nm was used as a pump laser. It was focussed to a pump spot radius (PSR) of 114µm using a 14mm focal length collimating lens and a 32mm focal length focussing lens. The cavity was designed to give a fundamental cavity mode radius of 113µm at the gain medium in order to ensure reasonable mode-matching.

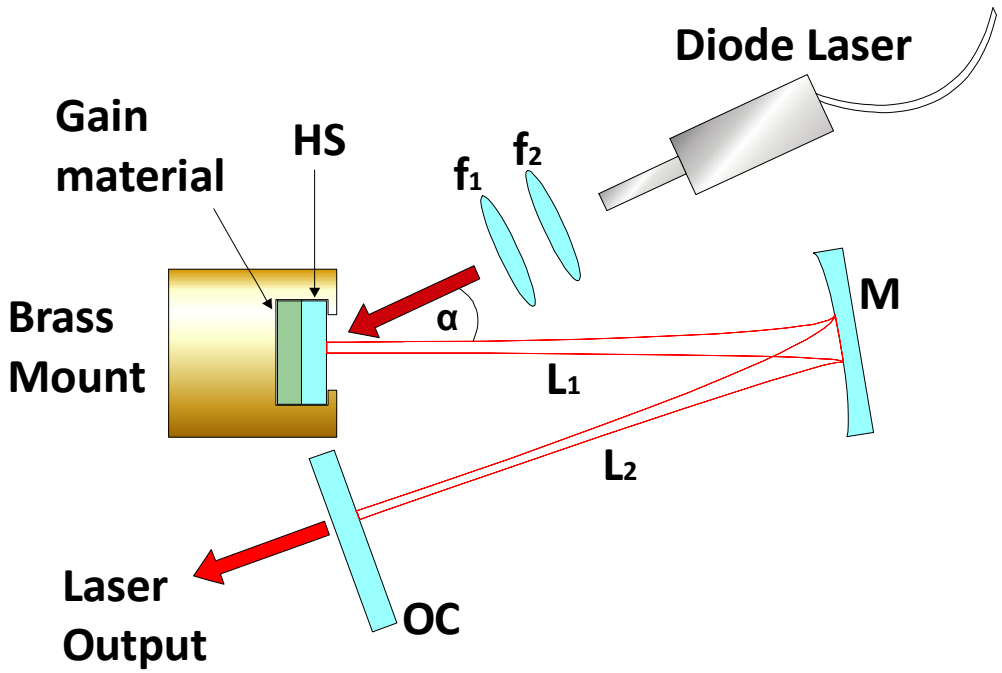

Figure 3.2.i *Diagram of three-mirror cavity used in this section. The distance between the chip and the folding mirror* ***M*** *is labelled* ***L1*** *and the distance between the folding mirror and the plane output coupler* ***OC*** *is labelled* ***L2****. A 10W diode laser was used to pump the gain material at an angle* ***α*** *to the normal of the heatspreader where* ***α*** *= 22 degrees; the input pump power was collimated through a lens* ***f2*** *and focussed through an additional lens* ***f1*** *to produce the desired pump spot size. A diamond heatspreader* ***HS*** *was bonded to different types of gain materials and a set of output couplers of varying fractions of transmission was used. The rear surface of the gain material is coated for high reflection at laser and pump wavelengths.*

Adjustment of the heatsink temperature of the diode-laser pump was required in the case for the Nd:YVO_4 laser material due to the shift in diode-laser operating wavelength with increasing input current. It was therefore necessary to tune the temperature of the laser diode to ensure that the wavelength of maximum absorption was attained throughout the input current range.

The a-cut Nd:YVO_4 sample in each case was bonded to the relevant heatspreader and sandwiched between two layers of 0.125mm thick indium foil (one of which had a circular aperture for the incident and emitted light) and inserted into position in a brass, water cooled mount as seen in figure 3.2.ii. There was no anti-reflection

coating present on the heatspreader. The rear surface of the Nd:$YdVO_4$ sample was coated for high reflection at the pump and laser wavelengths of 808nm and 1064nm respectively. An a-cut orientation of the gain material was chosen to give access to the higher emission and absorption cross-sections for light polarised parallel to the c-axis. Water cooled to a temperature of 9.5°C was pumped through the brass mount in order to provide cooling for the sample.

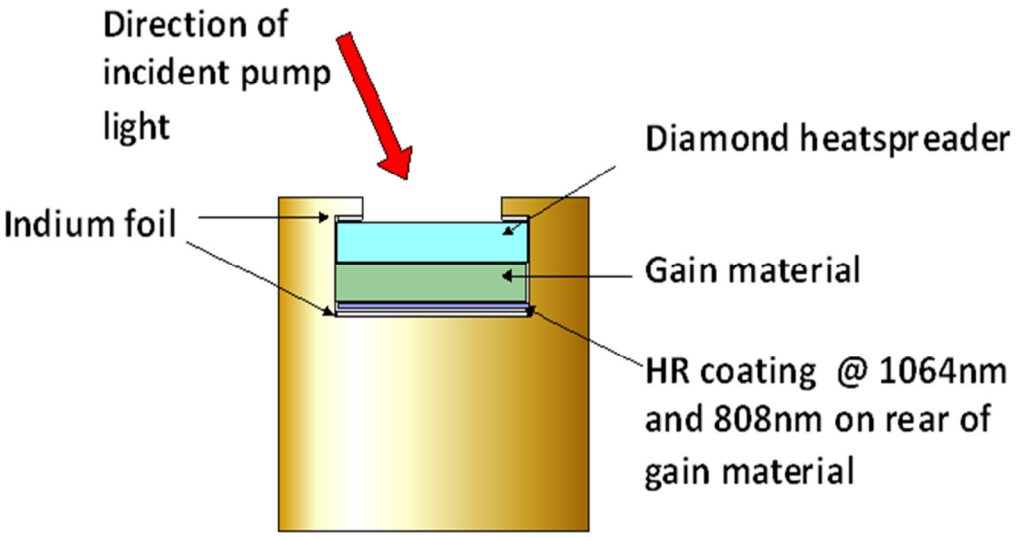

Figure 3.2.ii *Arrangement of Nd:YVO_4 gain material and diamond heatspreader within water-cooled brass mount*

3.2a Nd:YVO_4 – Sapphire characterisation

A 2mm thick piece of sapphire of radius 5mm and unspecified cut was bonded to a 3x3mm, 0.5mm thick sample of 3 atm. % doped Nd:YVO_4 and mounted in the three mirror cavity to form one end mirror. A series of output couplers of increasing transmission were used in turn to optimise this parameter. The maximum output power achieved was 3W at an incident pump power of 10.3W. Efforts to further scale the output power resulted in fracture of the initial Nd:YVO_4 sample and cessation of laser operation. On inspection of the Nd:YVO_4-sapphire sample shown in figure 3.2.a.i, it was found that the two materials still retained their bond. This indicated that the cause of fracture was not a result of failure of the bond.

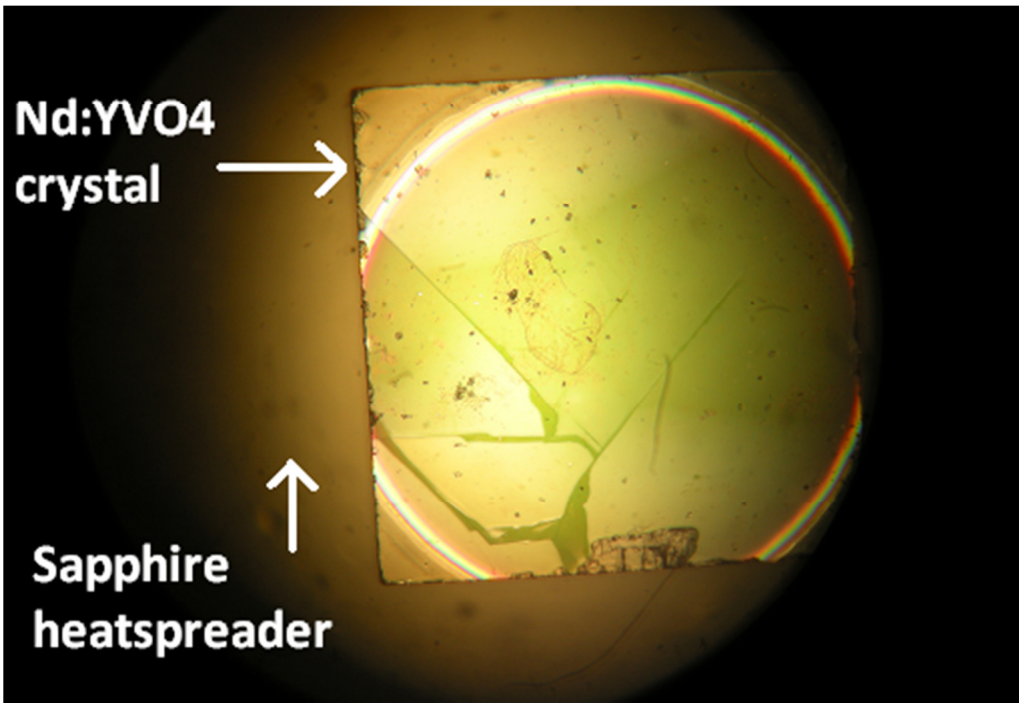

Figure 3.2.a.i *Nd:YVO_4 crystal fracture resulting from excessive incident pump power viewed under a microscope. The bond between the Nd:YVO_4 and sapphire heatspreader is still intact.*

The sapphire was re-bonded to an identical sample of Nd:YVO_4 and the experiment was repeated using a lower incident pump power to ensure that crystal fracture did not occur. The results of these experiments can be seen in figure 3.2.a.ii**.** The maximum CW output power achieved was 2.6W for a 7% output coupling and an incident pump power of 8.1W. The slope efficiency and threshold, both with respect to incident pump power were 39% and 0.3W respectively. The rollover in output power at higher incident pump powers results from strong thermal lensing in the Nd:YVO_4 sample.

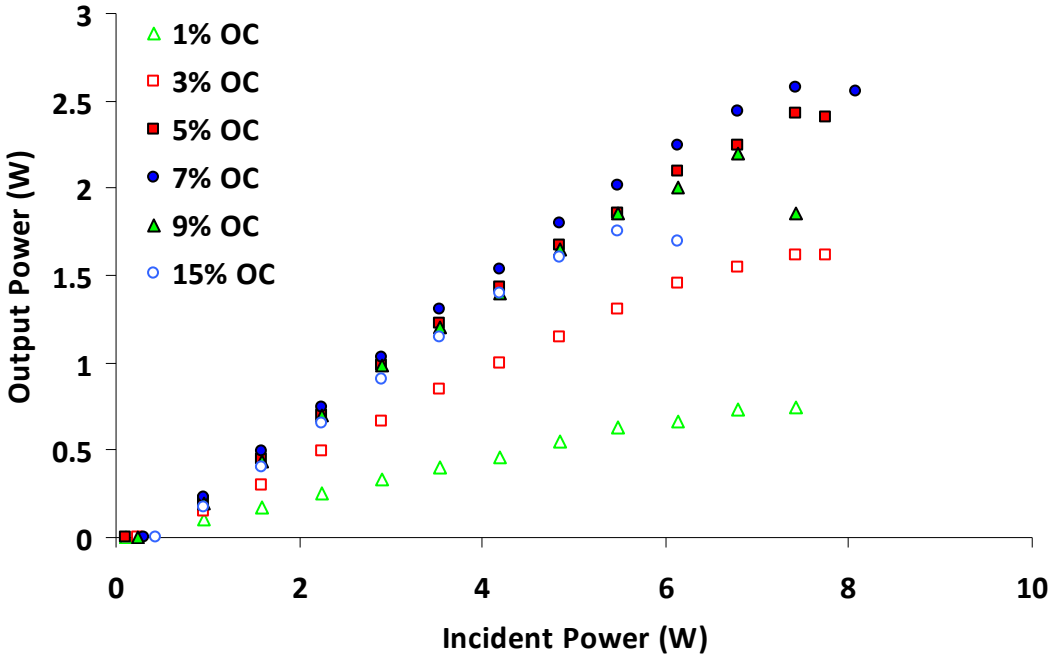

Figure 3.2.a.ii *Output power of 3 atm.% Nd:YVO_4 – Sapphire laser in three mirror-cavity configuration using a set of output couplers of varying fractions of transmission. OC stands for output coupler.*

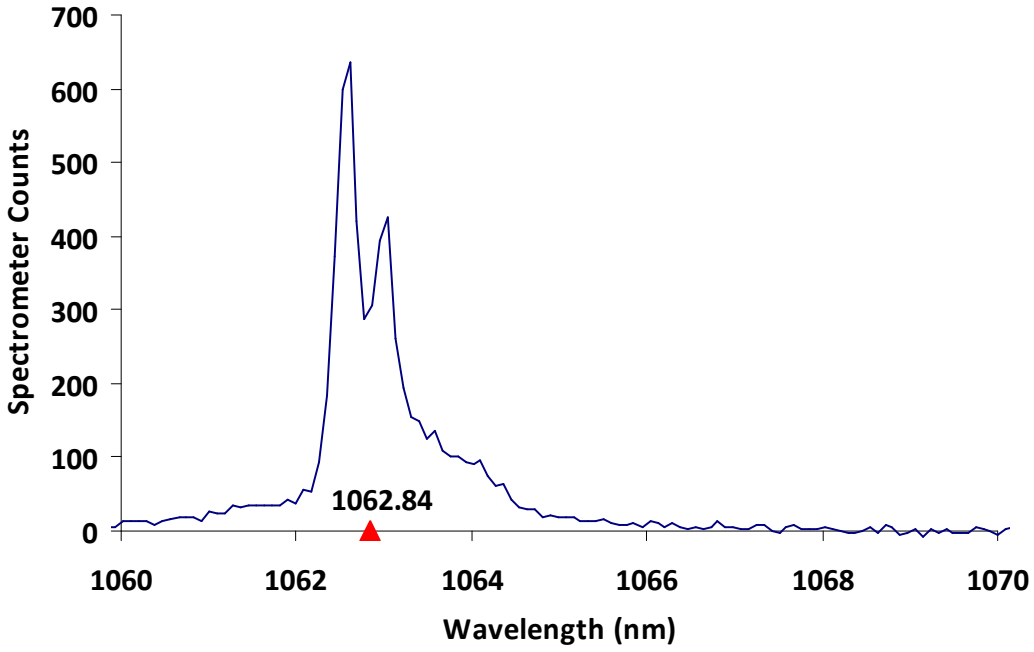

Figure 3.2.a.iii *Spectrum of 3 atm. % Nd:YVO_4 – Sapphire laser in three mirror-cavity configuration using a 7% output coupler. The triangular point indicates the centroid wavelength. An Ocean Optics S2000 grating spectrometer with a resolution of 0.5nm was used.*

The spectrum of the laser can be seen in figure 3.2.a.iii**.** The centroid of the laser emission was calculated to be 1062.8nm. The offset of the centroid wavelength position with respect to the wavelength giving the maximum emission cross-section in Nd:YVO_4 (1064.2nm) is possibly due to a Vernier effect produced by the different etalons within the cavity but further analysis would be needed to confirm this.

3.2.b Nd:YVO_4 – SiC characterisation

A 4x4 mm, 0.3mm thick piece of 4H high purity semi-insulating (HPSI) SiC was bonded to a 3x3mm, 0.5mm thick sample of 3 atm.% doped Nd:YVO_4 and mounted in the three mirror cavity configuration. Identical pump-mode/cavity-mode radii to those used in section 3.2 were chosen for comparative purposes. The results of the output coupler optimisation can be seen in figure 3.2.b.i. The maximum CW output power achieved was 1W for a 7% output coupling and an incident pump power of 10.3W. The slope efficiency and threshold, both with respect to incident pump power were 10% and 0.74W respectively. The spectrum of the laser can be seen in figure 3.2.b.i**.** The centroid of the laser emission was calculated to be 1064.7nm.

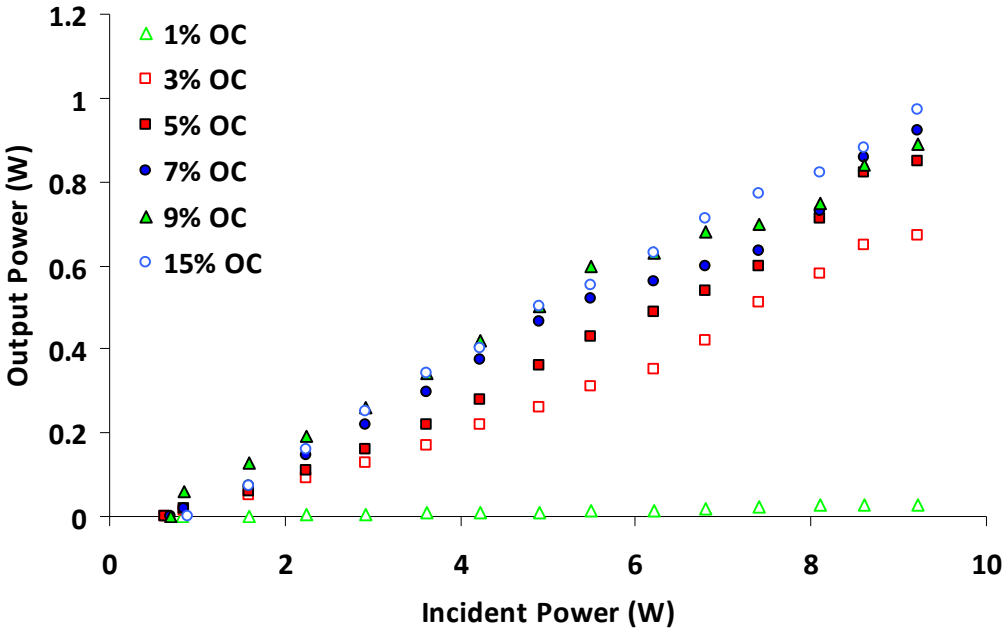

Figure 3.2.b.i *Output power of 3 atm. % Nd:YVO_4 – SiC laser in three mirror-cavity configuration using a set of output couplers of varying transmission. OC stands for output coupler. The SiC heatspreader used here is labelled sample a.*

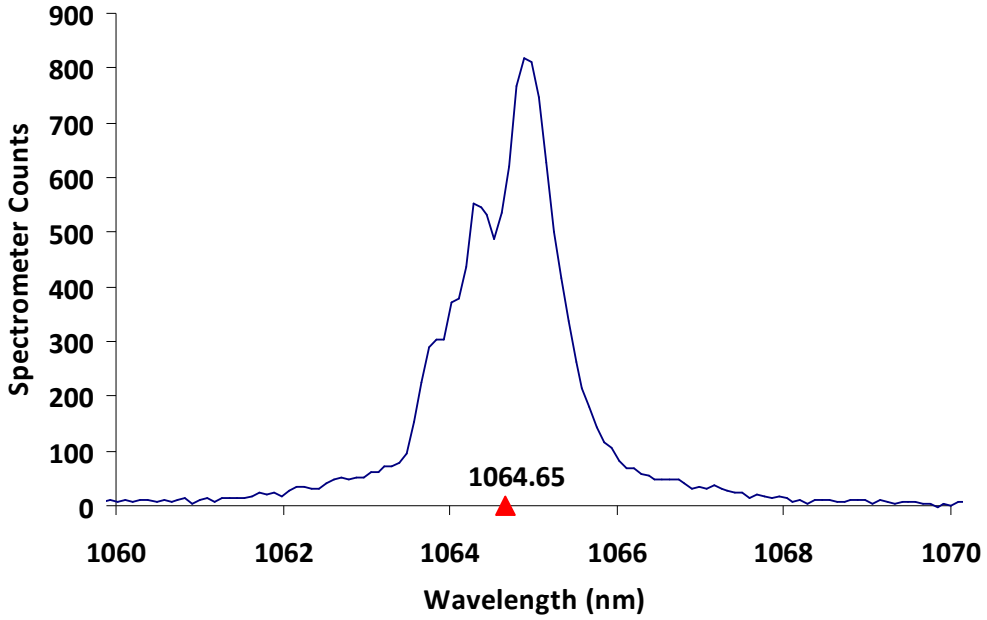

Figure 3.2.b.ii *Spectrum of 3 atm. % Nd:YVO_4 – SiC laser in three mirror-cavity configuration using a 7% output coupler. The SiC heatspreader used here is labelled sample a. The triangular point indicates the centroid wavelength. An Ocean Optics S2000 grating spectrometer with a resolution of 0.5nm was used.*

The low output powers achieved suggest that the SiC heatspreader is the cause of this lower performance. Thermal management was unlikely to be the root of this reduction in power due to the higher thermal conductivity of SiC compared to that of sapphire and there was no issue apparent with the bonding process that might cause lower efficiencies. To assess whether this reduction in output power might be due to the SiC heatspreader introducing higher than expected losses, a series of transmission and absorption measurements were taken.

Three heatspreader samples were examined:

- The sample of SiC used in the experiments above, labelled “SiC sample a”
- A different sample of SiC of the same polytype bought at a later date from the identical supplier that supplied the original SiC, labelled “SiC sample b”.
- A 4.6mm diameter type IIa single crystal synthetic diamond heatspreader

These samples were chosen in order to provide comparative figures for reflective and absorption loss and would indicate if the SiC sample used was introducing additional losses within the laser cavity. In table 3.2bi the reflection and absorption losses of the SiC and diamond samples can be seen: the SiC sample a) used in the power transfer experiments above introduces absorption losses that are almost 7 times greater than SiC sample b), equating to a round trip loss of approximately 14%. The diamond heatspreader sample exhibits the lowest absorption losses of all three heatspreaders. To achieve increased accuracy when measuring heatspreader loss with regards to the error associated with the absorbed power of the diamond sample, laser calorimetry would be a more effective technique to adopt in future [9].

Heatspreader Material	Power reflected as % of incident pump power	Power absorbed as % of incident pump power
SiC a)	29.1 ± 1.46	6.94 ± 0.19
SiC b)	30.4 ± 1.52	1.02 ± 0.11
Diamond	29.4 ± 1.47	0.14 ± 0.16

Table 3.2.b.i *Table of reflection and absorption losses within SiC and diamond heatspreader samples at 1064nm. The errors are based upon random error and do not include the power meter calibration uncertainty which is ±5%.*

The second sample of SiC, which exhibited lower losses than the original sample, was bonded to a piece of 4x4mm, 0.5mm thick 1 atm. % doped Nd:YVO_4 and the experiments above were repeated. 1% rather than 3 atm. % doped Nd:YVO_4 was used due to the unavailability of additional 3 atm. % material. The maximum CW output power achieved was 3.5W for a 21% output coupling and an incident pump power of 10.3W. The slope efficiency and threshold, both with respect to incident pump power were 36% and 0.55W respectively; with respect to absorbed power, a slope efficiency of 54% and threshold of 0.37W was achieved at an absorbed power of 6.8W. The output coupling optimisation can be seen in figure 3.2.b.iii**;** the spectrum of the laser can be seen in figure 3.2.b.iv**.** The centroid of the laser emission was calculated to be 1064.7nm.

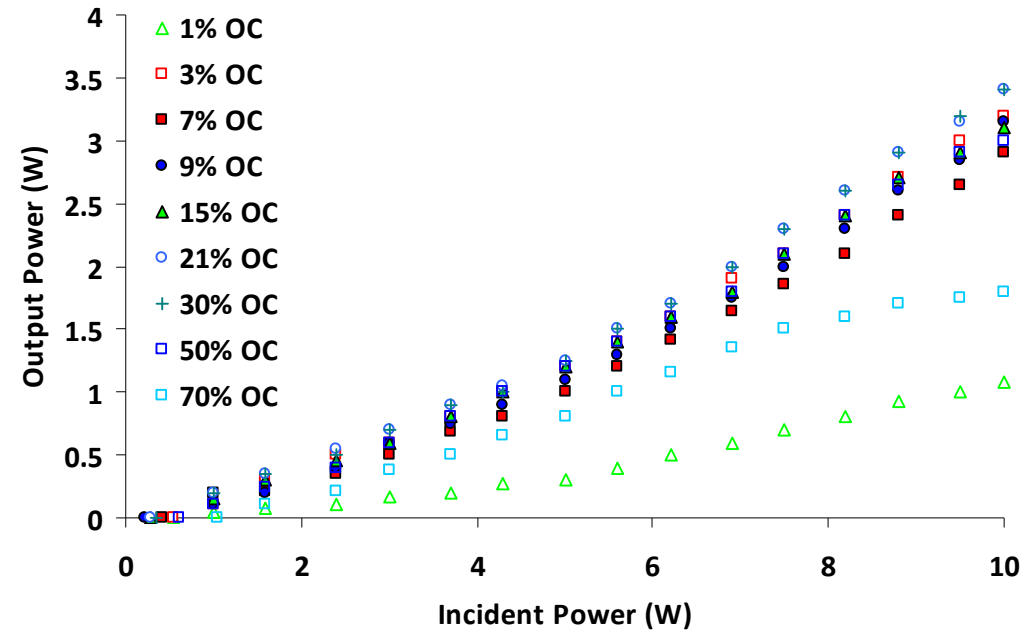

a)

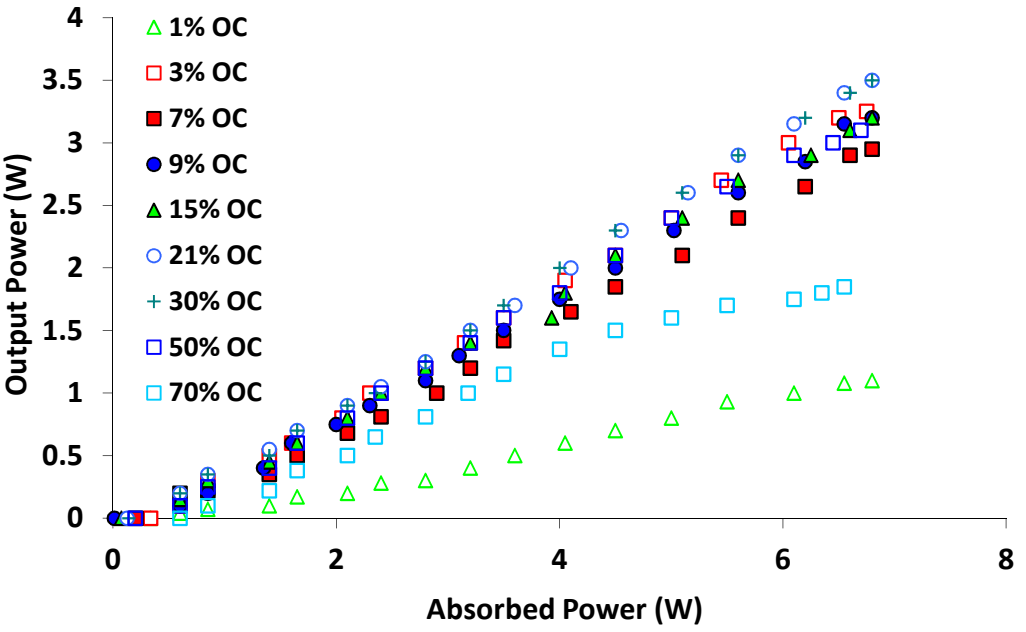

b)

Figure 3.2.b.iii *Output power of 1 atm. % Nd:YVO_4 – SiC laser in three mirror-cavity configuration using a set of output couplers of varying transmission against a) incident power and b) absorbed power . The SiC heatspreader used here is labelled sample b. OC stands for output coupler.*

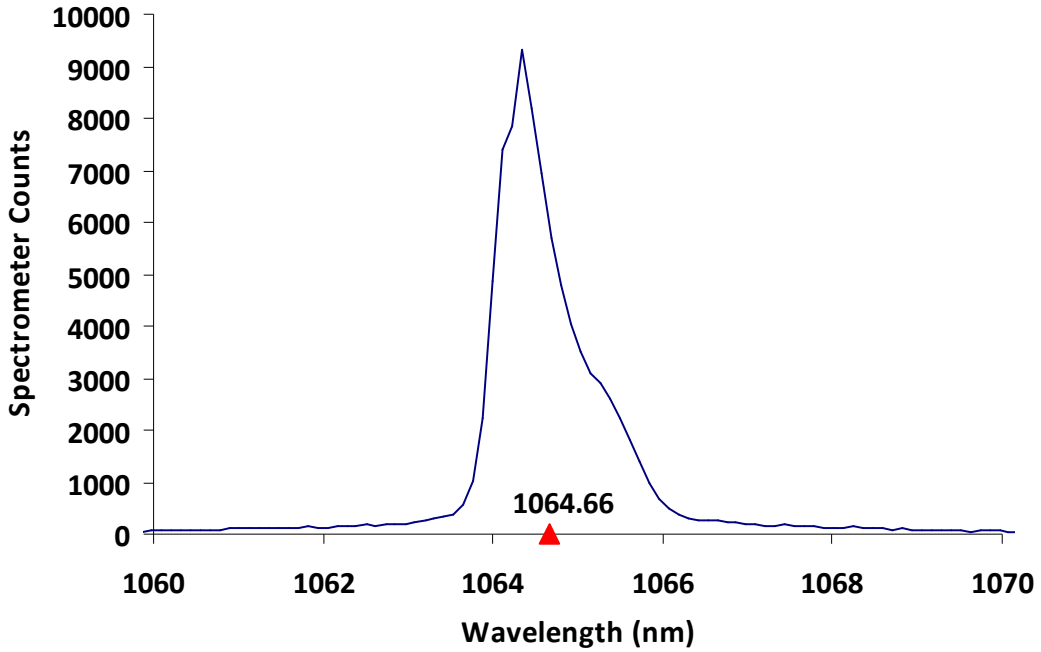

Figure 3.2.b.iv *Spectrum of 1 atm. % Nd:YVO_4 – SiC laser in three mirror-cavity configuration using a 15% output coupler. The SiC heatspreader used here is labelled sample b. The triangular point indicates the centroid wavelength. An Ocean Optics S2000 grating spectrometer with a resolution of 0.5nm was used.*

The higher output coupling used in this laser compared to the previous set-ups is attributable to optical sub-cavity effects that arose using this sample of Nd:YVO_4 . The sub-cavity effects are likely to be attributable to a combination of the high parallelism of the Nd:YVO_4 sample and the Fresnel reflectivity arising from the SiC heatspreader. This is likely to lead to a reduction in the effective output coupling (from the perspective of the gain medium) due to recycling of the light in the cavity set-up between the back mirror on the gain material and the diamond-air interface. The same sub-cavity effects arise for this piece of Nd:YVO_4 when bonded to a diamond heatspreader as shall be seen in the next section of this chapter.

3.2.c Nd:YVO_4 – Diamond characterisation

In this section a 0.5mm thick, type IIa single crystal synthetic CVD diamond heatspreader of radius 2mm was bonded to a 3x3mm, 0.5mm thick sample of 3 atm. % doped Nd:YVO_4. An identical cavity to that used in sections 3.2.a and 3.2.b was constructed to characterise and compare the performance of the diamond heatspreader with that of the SiC and sapphire samples. In figure 3.2.ci the results of the output coupling optimisation can be seen. The maximum CW output power achieved was 3.2W for a 7% output coupling and an incident pump power of 10.3W. The slope efficiency and threshold, both with respect to incident pump power were 35.3% and 0.52W respectively. The spectrum is displayed in figure 3.2cii.

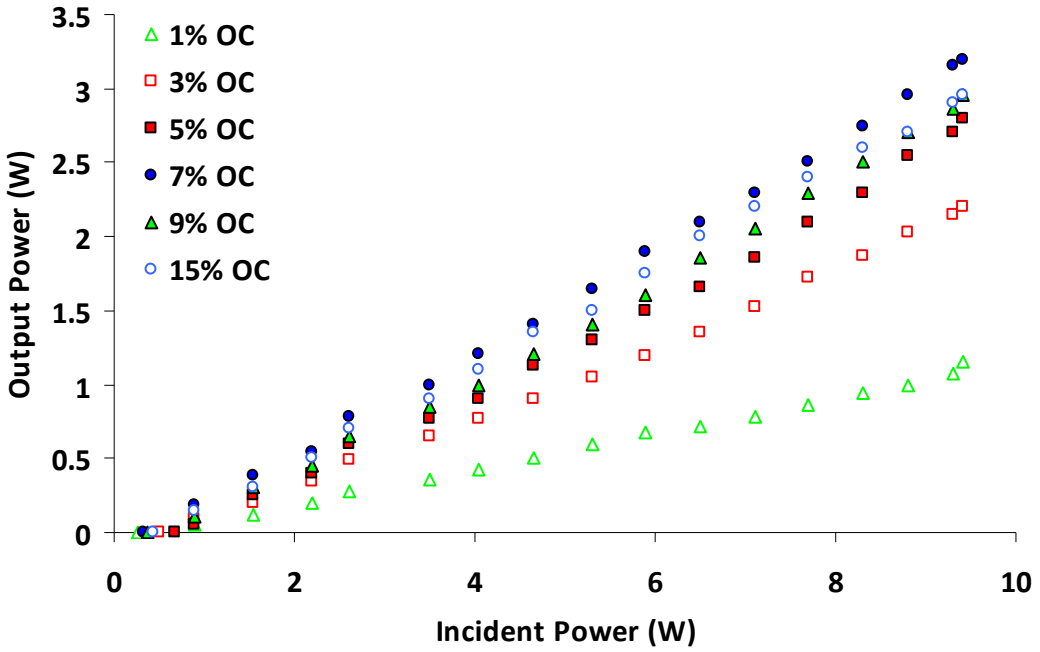

Figure 3.2.ci *Output power of 3 atm. % Nd:YVO_4 – Diamond laser in three mirror-cavity configuration using a set of output couplers of varying transmission. OC stands for output coupler.*

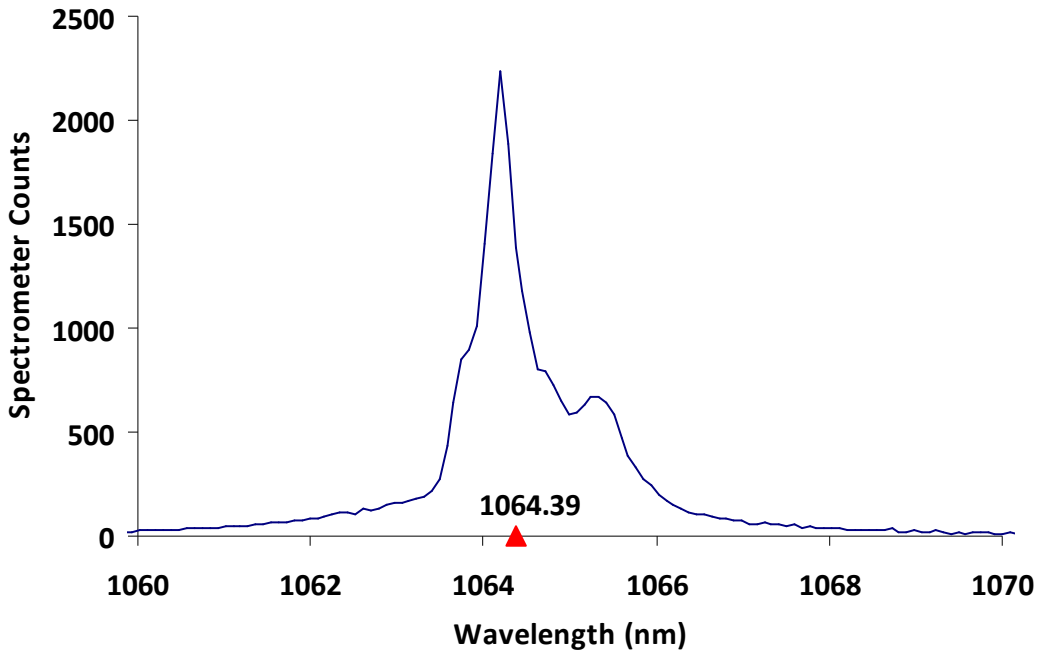

Figure 3.2.cii *Spectrum of 3 atm. % Nd:YVO_4 – Diamond laser in three mirror-cavity configuration using a 7% output coupler. The triangle point indicates the centroid wavelength. An Ocean Optics S2000 grating spectrometer with a resolution of 0.5nm was used.*

To compare the performance of the SiC heatspreader sample b with that of the diamond heatspreader, a 4x4mm x 0.5mm thick 1 atm. % doped Nd:YVO_4 (3% atm. % doped material being unavailable at this time) was bonded to the diamond and the characterisation repeated. At an incident pump power of 10.3W, a maximum output power of 3.9W was achieved using a 9% output coupler. The slope efficiency and threshold, both with respect to incident pump power were 41% and 0.49W respectively; with respect to measured absorbed power, a slope efficiency of 58% and threshold of 0.34W was achieved. The power transfers for each output coupler configuration can be seen in figure 3.2.ciii; the large range of output coupling suggests that substantial sub-cavity effects are present. The spectrum of the laser can be seen in figure 3.2.civ**.**

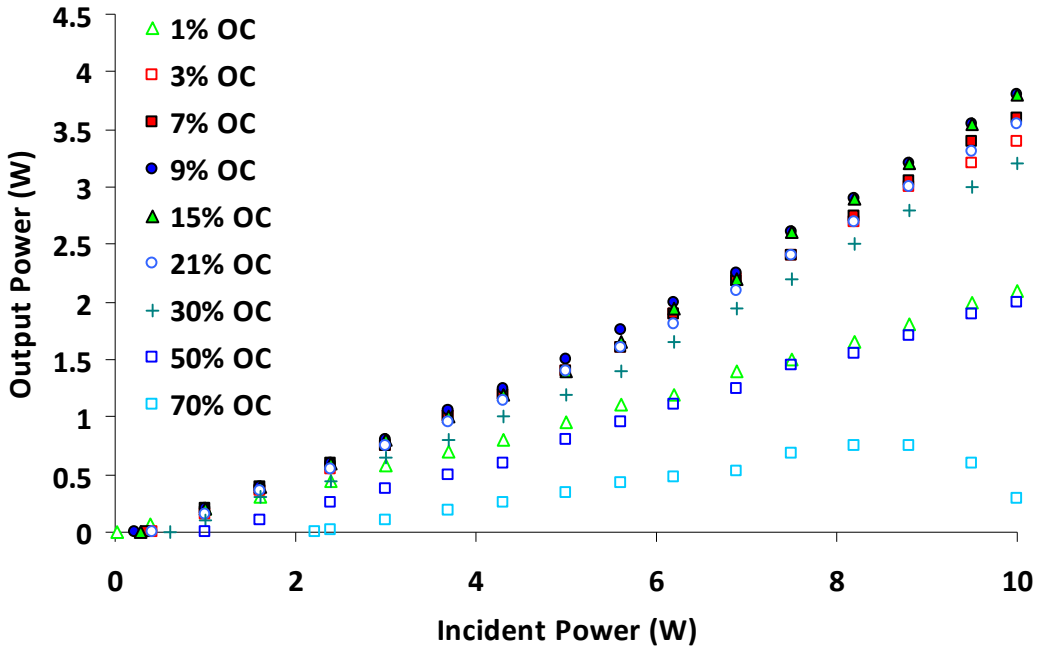

Figure 3.2.ciii graph a) *Output power of 1 atm. % Nd:YVO_4 – Diamond laser in three mirror-cavity configuration using a set of output couplers of varying transmission against incident power. OC stands for output coupler.*

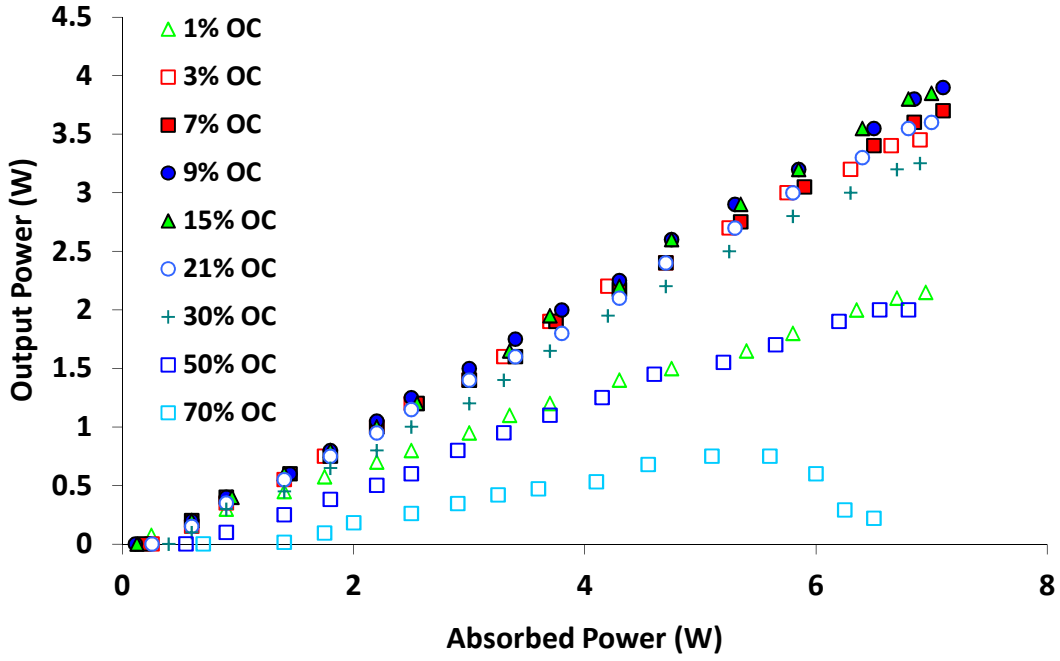

Figure 3.2.ciii graph b) *Output power of 1 atm. % Nd:YVO_4 – Diamond laser in three mirror-cavity configuration using a set of output couplers of varying transmission against measured absorbed power. OC stands for output coupler.*

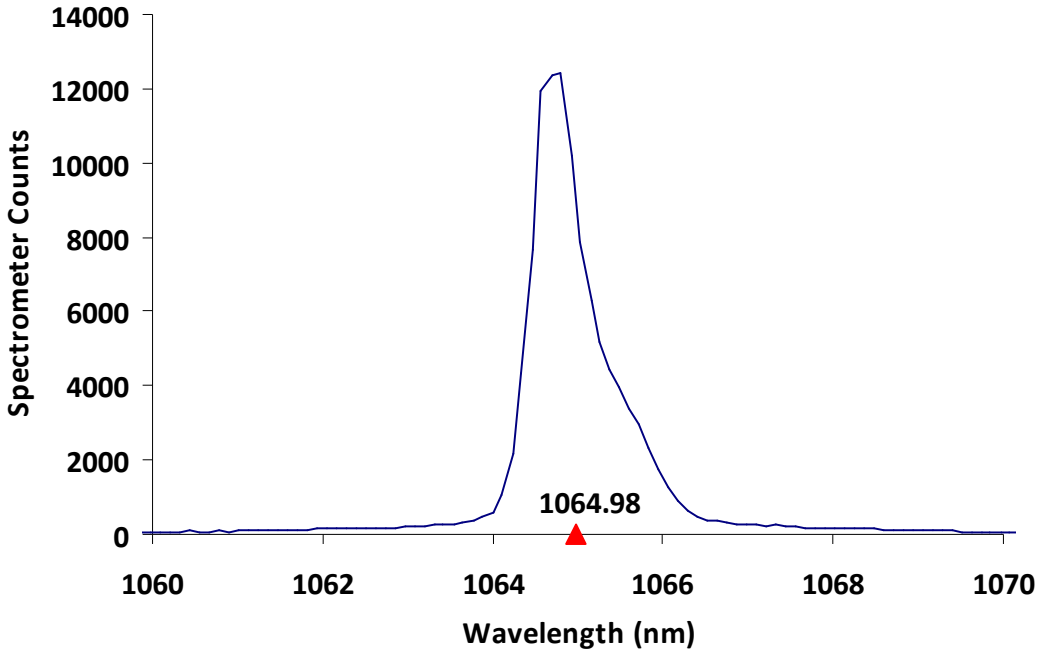

Figure 3.2.civ *Spectrum of 1 atm. % Nd:YVO_4 – Diamond laser in three mirror-cavity configuration using a 7% output coupler. The triangular point indicates the centroid wavelength. An Ocean Optics S2000 grating spectrometer with a resolution of 0.5nm was used.*

3.2.d Summary of heatspreader performance in three-mirror configuration

From figure 3.2.di and table 3.2.di it is clear that, compared to the sapphire and SiC heatspreaders, the use of a diamond heatspreader allows for superior CW laser performance, giving an output power of 3.9W for an absorbed pump power of 7.1W, pump spot radius of 114µm. In the case of the sapphire heatspreader it was found that no more than 3W of output power could be obtained before catastrophic fracture of the crystal occurred; using lower incident pump powers it was found that incident slope efficiencies up to 38.5% could be obtained with an output power of 2.6W. Crystal fracture did not occur at the pump limited incident power of 10W and pump spot radius of 114µm when using either diamond or SiC in the heatspreading role due to the higher thermal conductivity of these materials compared to that of sapphire. Using SiC as a heatspreader allowed for higher output powers of 3.5W to be achieved in the case of the 1 atm. % Nd:YVO_4. Due to its lower cost than diamond, SiC is an attractive candidate for use as a heatspreader in a power scaling set-up at

the incident pump powers used in these experiments; in these experiments; however, the unexpectedly poor performance obtained with the first sample highlights the importance of determining the appropriate specifications for this material.

In the 1% doped Nd:YVO_4 – SIC and the Nd:YVO_4 – diamond heatspreader cases, the laser operated at larger than expected output couplings. This is thought to arise from the sub-cavity set up between the mirror on the rear of the Nd:YVO_4 and the heatspreader / air interface. As described in [7], this effectively reduces the output coupling as experienced by the gain medium by increasing the field in the sub-cavity. This effect was presumably stronger for the SiC heatspreader case, presumably due to superior sample parallelism; however further investigation would be required to confirm this.

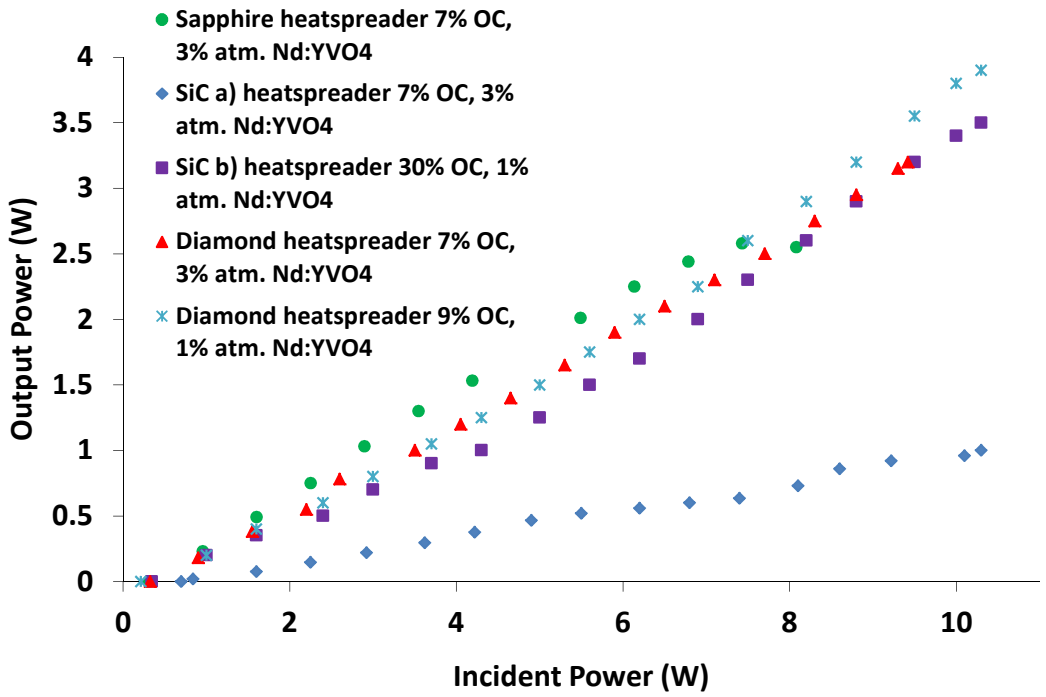

Figure 3.2.di *Power transfers of each heatspreader configuration at optimal output coupling used in this section. OC stands for output coupler.*

Heatspreader Material	Nd:YVO_4 Doping	Optimal OC	Maximum P_{out}	Slope Efficiency with respect to Incident/ Absorbed pump power	Threshold with respect to Incident/Absorbed pump power
Sapphire	3 atm. %	7%	2.58W	39% / -	0.28W/ -
SiC a)	3 atm. %	7%	1W	10.40% / -	0.74W/ -
SiC b)	1 atm. %	30%	3.5W	35.9% / 53.9%	0.55W/ 0.37W
Diamond	3 atm. %	7%	3.2W	35% / -	0.52W/ -
Diamond	1 atm. %	9%	3.9W	41% / 58%	0.49W/ 0.34W

Table 3.2.di *Summary table of laser characterisation of three-mirror Nd:YVO_4 – heatspreader configuration. SiC a) indicates the higher loss SiC sample; SiC b) indicates the low loss SiC sample. OC stands for output coupler; the optimal output coupler refers to the output coupling transmissions examined in this chapter.*

It is apparent from the above results that diamond is the most effective heatspreader choice in a microchip laser in terms of maximum output power and slope efficiency at incident pump powers up to 10W. The lower absorption losses and the more effective thermal management of diamond sample make it a more attractive heatspreader than SiC. The results from the three-mirror cavity form a useful conventional laser baseline for comparison with the microchip-style cavities that will be examined in the next section.

3.3 Comparison of heatspreaders in a quasi-microchip configuration

To assess the impact of heatspreader choice on microchip power scaling and beam brightness optimisation it is necessary to investigate these parameters using a cavity configuration similar to that of a microchip set-up. Ideally, a conventional microchip cavity would be used in these investigations; however, the quasi-monolithic nature of this type of cavity limits the flexibility of cavity design using the resources available – the output coupling, for example, cannot readily be changed. In this chapter a fully monolithic microchip laser is defined as a laser that incorporates only a single piece of material within the cavity, where dielectric coatings are applied to the crystal facets aligned along the lasing axis to form the cavity. A quasi-monolithic device is defined in this chapter as a device where more than one solid material is

used (e.g. a piece of gain material and a heatspreader) but where the materials are bonded together such that there are no air-gaps.

To investigate optimal output coupling and heatspreader selection in quasi-monolithic microchip lasers, a large number of different optical coatings would need to be applied to large numbers of samples of gain and heatspreader material: the cost would be prohibitive. By contrast, however, a conventional air-spaced resonator allows a range of output couplers to be swapped in and out of the cavity quickly and easily leading to allow for optimisation of the design. To investigate heatspreaders in microchip lasers, the set-up illustrated in figure 3.3.i was used throughout this section. This provides some of the flexibility of a conventional cavity in terms of systematically changing components but it also more accurately reflects the situation in a true microchip laser. For the purposes of this thesis, this will be described as a quasi-microchip (QMC) configuration.

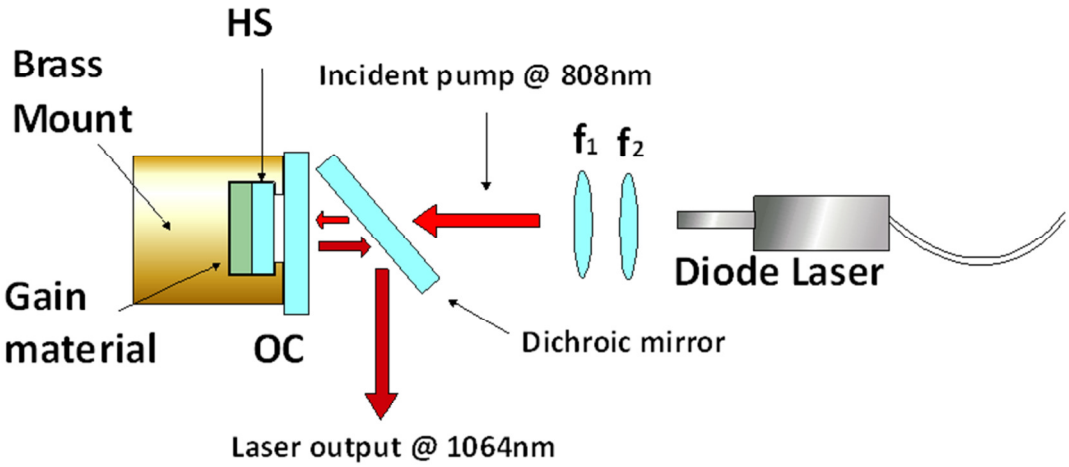

Figure 3.3i *Diagram of quasi-microchip cavity used in this section. A 10W diode laser was used to pump the gain material; the input pump power was collimated through a lens* ***f2*** *and focussed through an additional lens* ***f1*** *to produce the desired pump spot size on the gain material. The incident beam is transmitted through a dichroic mirror which reflects light at 1064nm. A diamond heatspreader* ***HS*** *was bonded to different types of gain materials and a set of output couplers of varying fractions of transmission was used. The rear surface of the gain material is coated for high reflection at laser and pump wavelengths.*

A quasi-microchip configuration allows for data to be measured using a range of different output couplers and intracavity heatspreaders, which can then be used to design and implement a quasi-monolithic microchip configuration. An identical diode laser to that in section 3.4 was used in the QMC arrangement to optically pump the gain material. The output wavelength of the diode-laser was temperature tuned to the absorption peak of Nd:YVO_4. The pump optics were chosen to produce a pump spot radius of 255µm on the heatspreader-gain sample. This sample was sandwiched between two layers of indium (one of which had a circular aperture for the incident and emitted light) and mounted in a water-cooled brass mount. A dichroic mirror was used to separate the 1064nm laser output from the 808nm pump incident pump power and an 850nm long-pass reflective filter used to ensure only the laser output was recorded by the power meter. The output coupler was mounted on a translation stage to vary the cavity length.

3.3.a Nd:YVO_4 – Sapphire characterisation

The same sample of sapphire used in section 3.2.a was bonded to the same 3x3mm, 0.5mm thick, 3 atm. % doped sample of Nd:YVO_4 sample used in that section and mounted in the QMC arrangement. A number of output couplers were used to assess output coupler optimization, the results of which can be seen in figure 3.3.ai**.** A maximum output power of 2.6W at a slope efficiency of 38% and threshold of 0.54W (both with respect to incident pump power) was achieved using a 7% output coupler; with respect to estimated absorbed power, a slope efficiency of 55% and threshold of 0.38W was achieved. The spectrum of the laser can be seen in figure 3.3.aii**,** the centroid of which is offset by approximately a nanometre from the gain peak of Nd:YVO_4.

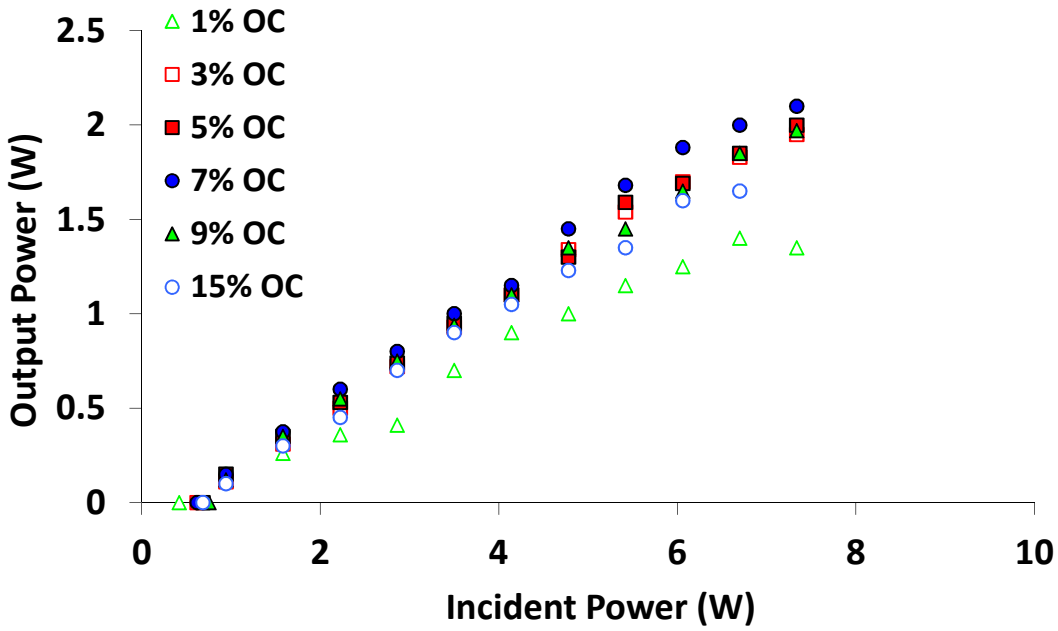

Figure 3.3.ai graph a) *Output power of 3 atm. % Nd:YVO_4 – Sapphire laser in QMC-cavity configuration plotted against incident power using a set of output couplers of varying transmission. OC stands for output coupler.*

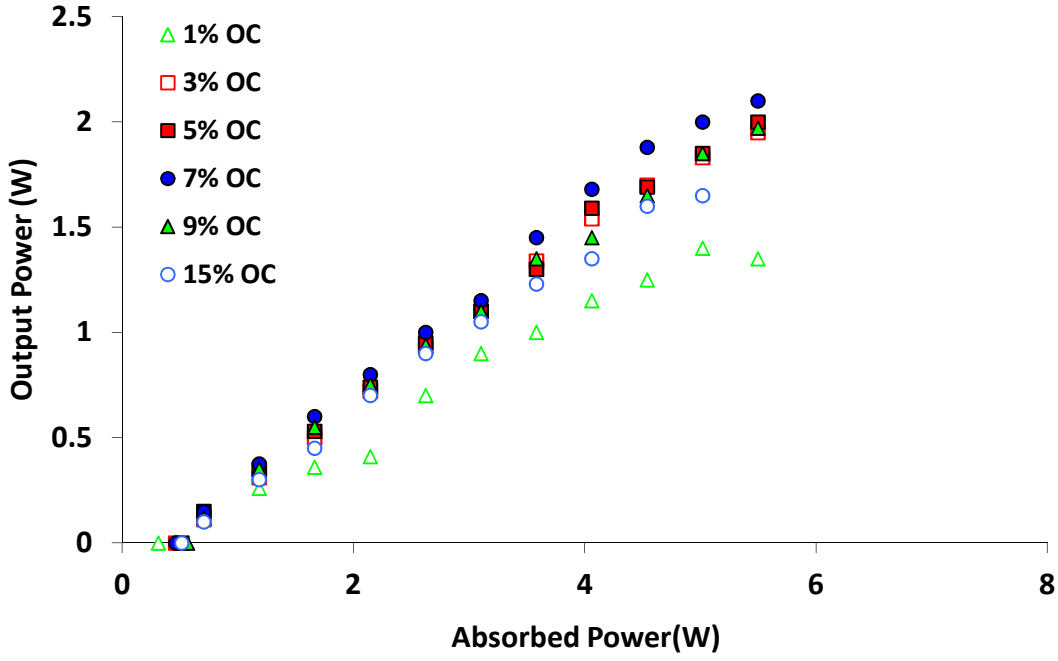

Figure 3.3.ai graph b) *Output power of 3 atm. % Nd:YVO_4 – Sapphire laser in QMC-cavity configuration plotted against absorbed power, using a set of output couplers of varying transmission. OC stands for output coupler.*

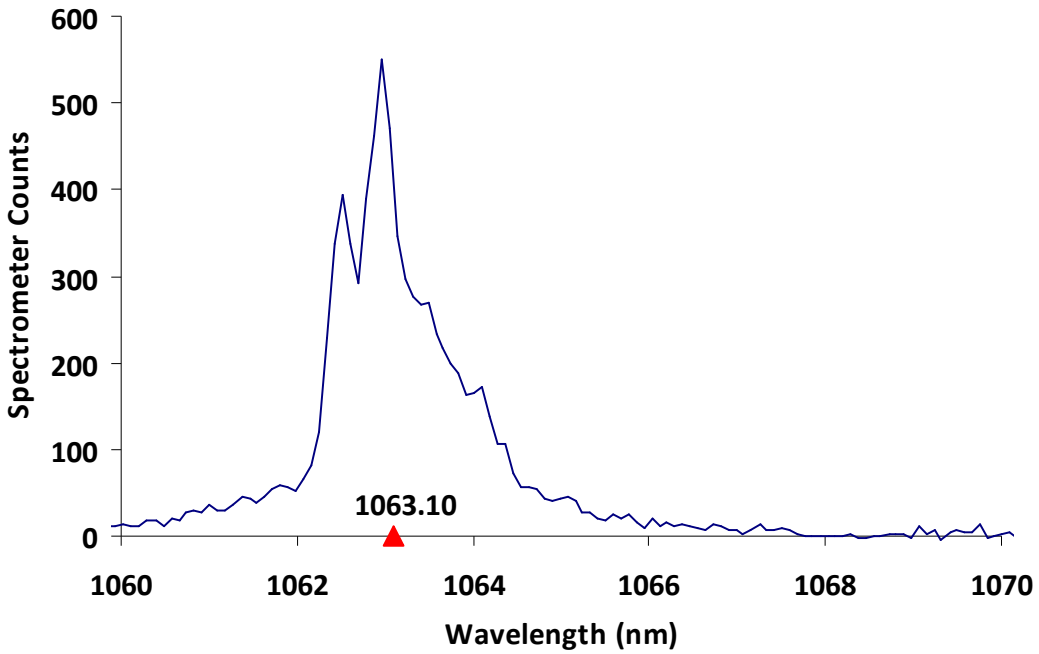

Figure 3.3.aii *Spectrum of 3 atm. % Nd:YVO_4 – Sapphire laser in QMC-cavity configuration using a 15% output coupler. The triangular point indicates the centroid wavelength. An Ocean Optics S2000 grating spectrometer with a resolution of 0.5nm was used.*

Using a Dataray Inc Beamscope-P7 (automated scanning slit beam profiler), the M^2 parameters of the output laser beam were measured at the maximum output power and found to be 3.7 in the x-axis and 4.9 in the y-axis indicating a multi-transverse-mode, elliptical output. This was for an estimated cavity length of 3mm which was the shortest cavity length achievable with the set-up used. The dependence of beam quality on fundamental cavity mode to pump mode ratio (i.e. the fundamental cavity mode radius / pump spot radius) in terms of the M^2 of the laser output was measured by extending the length of the cavity of the laser and recording the change in M^2. In figure 3.3.a.iii the results are plotted for the cavity length and the M^2 can be seen to decrease as the cavity length is increased which was possibly the result of an increase in fundamental cavity mode to pump mode ratio towards unity. The M^2 values vary quite significantly in the Y-axis compared to those measured in the x-axis; this might be due to a slight misalignment in the Y-axis of the Beamscope as a higher alignment tolerance of the Beamscope is preferable. Nevertheless, it can be seen that there is a trend of decreasing M^2 with respect to cavity length.

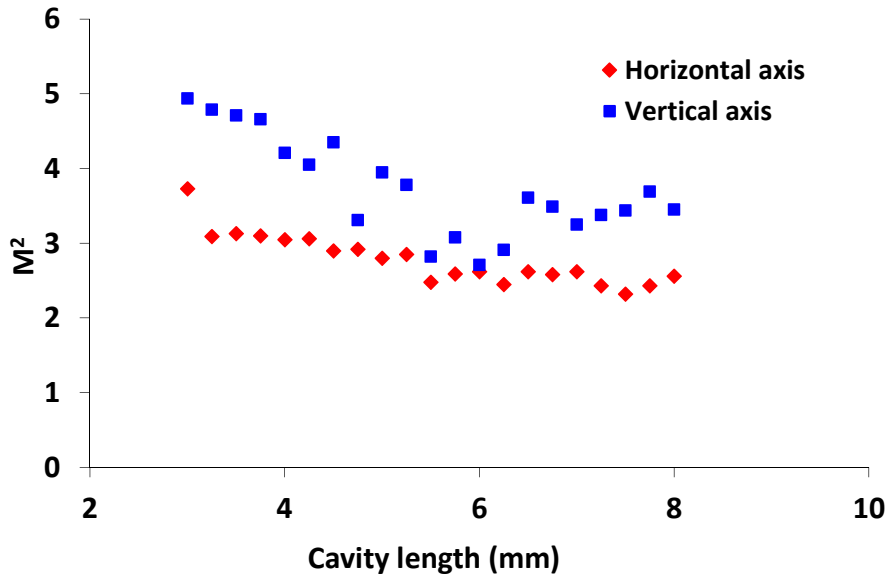

a)

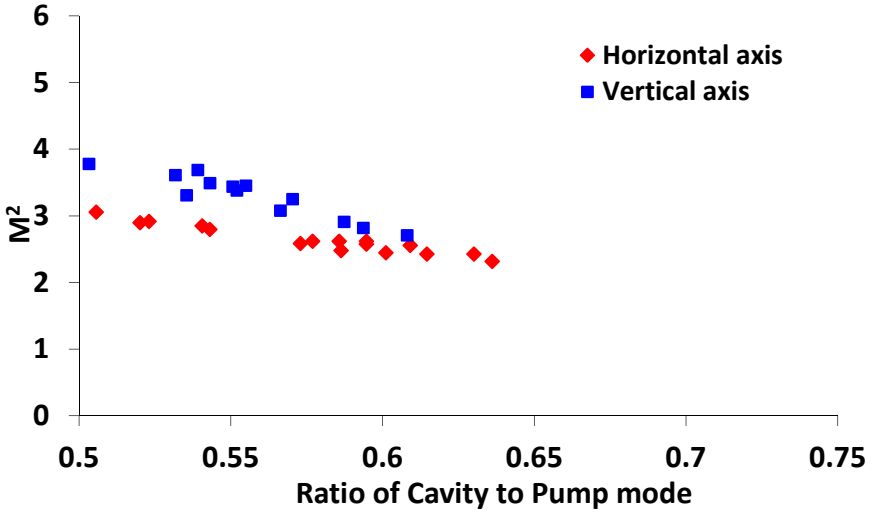

b)

Figure 3.3.a.iii *Plot of M^2 vs. a) cavity length and b) fundamental cavity to pump mode ratio (i.e. the fundamental cavity mode radius / pump spot radius) of a 3 atm. % Nd:YVO_4 – Sapphire laser in QMC-cavity configuration at maximum output power. A 7% output coupler was used.*

The M^2 was then plotted against the fundamental cavity mode radius / pump spot radius so that the dependence of beam quality on fundamental cavity mode to pump mode ratio could be observed. This showed that the M^2 improved as the

fundamental cavity mode to pump mode ratio increased. The cavity mode calculations were inferred by measuring the M^2 and beam diameter of the output beam at a known distance and then calculating the cavity mode radius that would be required to produce the beam diameter at the set distance.

Without taking thermal lensing-derived aberrations into account at this point, to improve the quality of the beam output it would be necessary to design the pump optics to ensure a cavity/pump mode ratio of ≥1 at the shortest possible cavity length for QMC operation. The pump spot radius in the case of the estimated shortest cavity length of 3mm was found to be 266µm using knife edge measurements. The fundamental cavity mode radius was calculated to be 112.4µm in the x-axis and 110µm in the y-axis at a cavity length of 3mm so to obtain a better beam output it would be necessary to increase the cavity mode radius to match and exceed the pump spot radius or to reduce the thermal lens within the Nd:YVO_4 sample.

The thermal lens was measured by using a two-mirror set-up shown in figure 3.3.a.iv. An incident pump power of 3.7W, and a pump spot radius of 179µm were used to pump the 3% Nd:YVO_4 – Sapphire sample. A 0.5% output coupler was used. The length of the cavity was increased until the cavity became unstable and laser oscillation ceased, indicating the lower limit on the focal length of the thermal lens present within the Nd:YVO_4 sample. The thermal lens expressed in terms of a radius of curvature of the equivalent mirror was found to be >56mm.

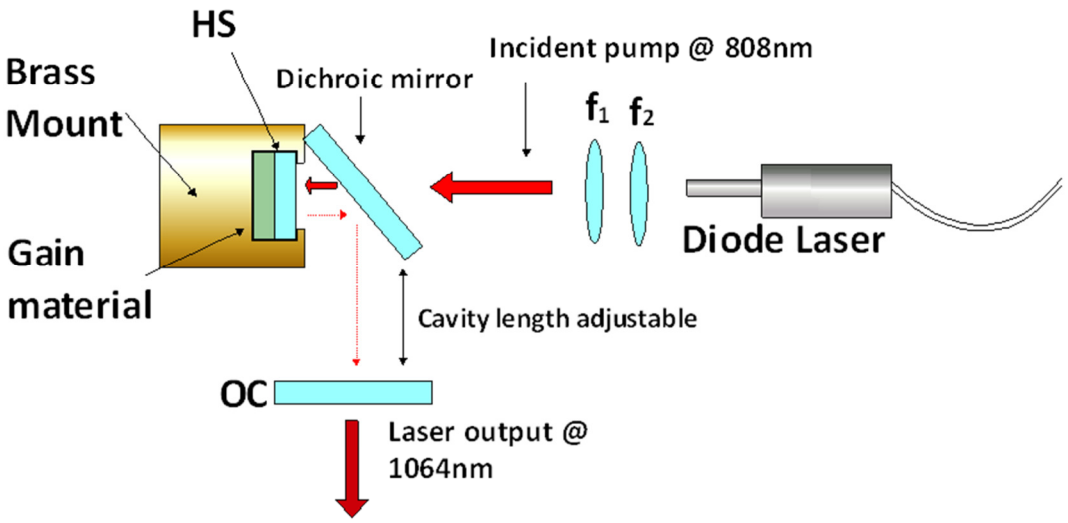

Figure 3.3.a.iv *Thermal Lens measurement set-up. A 10W diode laser was used to pump the gain material; the input pump power was collimated through a lens* ***f2*** *and focussed through an additional lens* ***f1*** *to produce the desired pump spot size on the gain material. The incident beam is transmitted through a dichroic mirror which reflects light at 1064nm. A diamond heatspreader* ***HS*** *was bonded to different types of gain materials and a set of output couplers of varying fractions of transmission was used. The rear surface of the gain material is coated for high reflection at laser and pump wavelengths. The cavity is extended in length by adjusting the position of the output coupler* ***OC****. The cavity becomes unstable when length of the cavity approximately equals the thermal lens focal length in the gain material.*

3.3.b Nd:YVO_4 – SiC characterisation

A sample of 4H high purity semi-insulating (HPSI) SiC (sample b from the previous section) was bonded to a 4x4x0.5mm thick piece of 1 atm. % Nd:YVO_4 and mounted in the QMC set-up. 1% rather than 3 atm. % doped Nd:YVO_4 was used due to the unavailability of additional 3 atm. % material. Using identical pump optics to those used in section 3.3.b, a series of power transfers was taken to optimize the output coupling. A maximum output of 3.1W was achieved at an incident pump power of 10.5W using a 3% output coupler; the slope efficiency and threshold with respect to the incident pump power were 31% and 0.63W respectively; with respect to estimated absorbed power, a slope efficiency of 47% and threshold of 0.41W was achieved as shown in figure 3.3.b.i. The spectrum of the laser output can be seen in figure 3.3.b.ii.

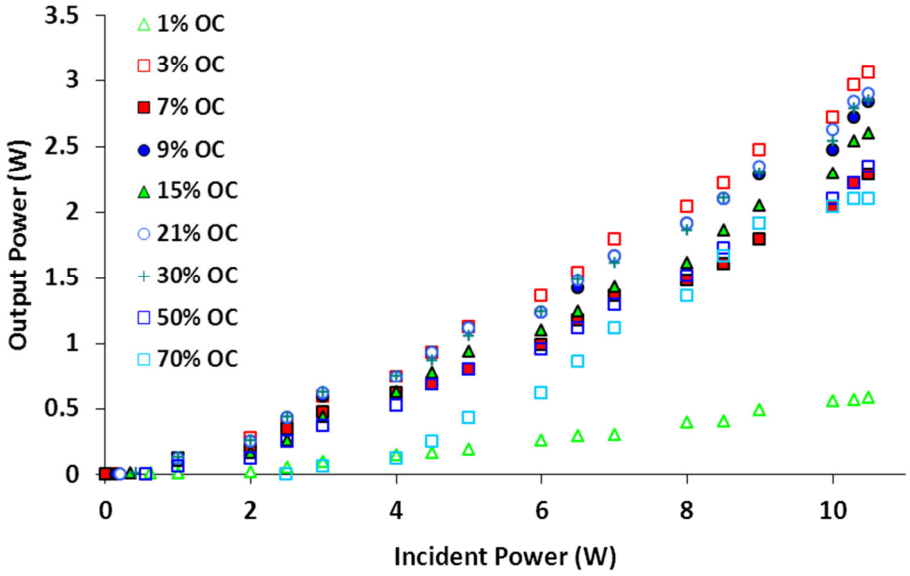

Figure 3.3.b.i graph a) *Output power of 1 atm. % Nd:YVO_4 – SiC laser in QMC-cavity configuration plotted against incident power, using a set of output couplers of varying transmission. OC stands for output coupler.*

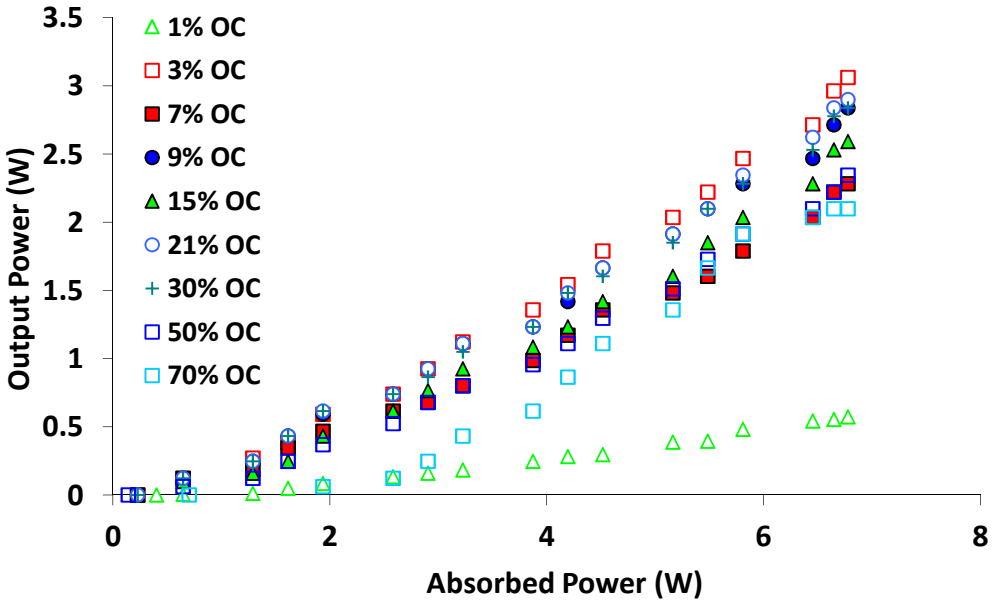

Figure 3.3.b.i graph b) *Output power of 1 atm. % Nd:YVO_4 – SiC laser in QMC-cavity configuration plotted against absorbed power, using a set of output couplers of varying transmission. OC stands for output coupler.*

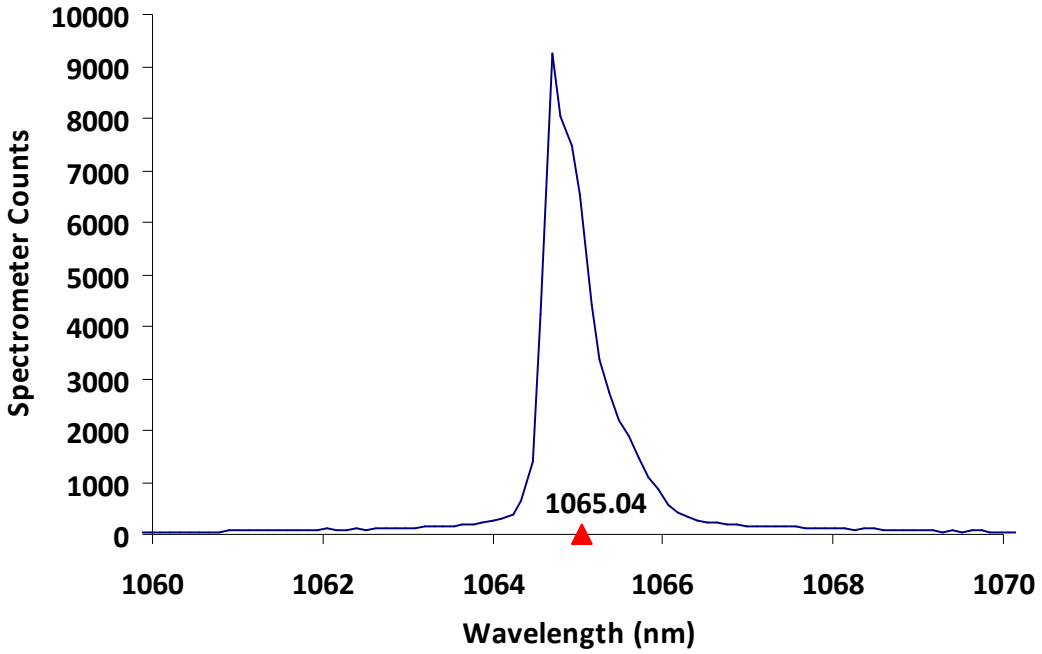

Figure 3.3.b.ii *Spectrum of 1 atm. % Nd:YVO_4 – SiC laser in QMC-cavity configuration using a 15% output coupler. The triangular point indicates the centroid wavelength. An Ocean Optics S2000 grating spectrometer with a resolution of 0.5nm was used.*

3.3.c Nd:YVO_4 – Diamond characterisation

A 0.5mm thick type-IIa single crystal synthetic CVD diamond heatspreader of radius 2mm was bonded to a sample of 3x3mm, 0.5mm thick 3 atm. % doped Nd:YVO_4 and mounted in a water cooled brass mount. The set-up, pump and cavity mode configurations used in figure 3.3.a were adopted and a series of power transfers were taken to ascertain the optimal output coupling. Using a 9% output coupler, a maximum output power of 3.7W was achieved at an incident optical power of 8.6W. The slope efficiency, threshold (both with respect to incident pump power) and centroid of the output spectrum (figure 3.3.c.i and figure 3.3.c.ii) were found to be 37%, 0.56W and 1064.2nm respectively; with respect to estimated absorbed power, a slope efficiency of 51% and threshold of 0.32W was achieved.

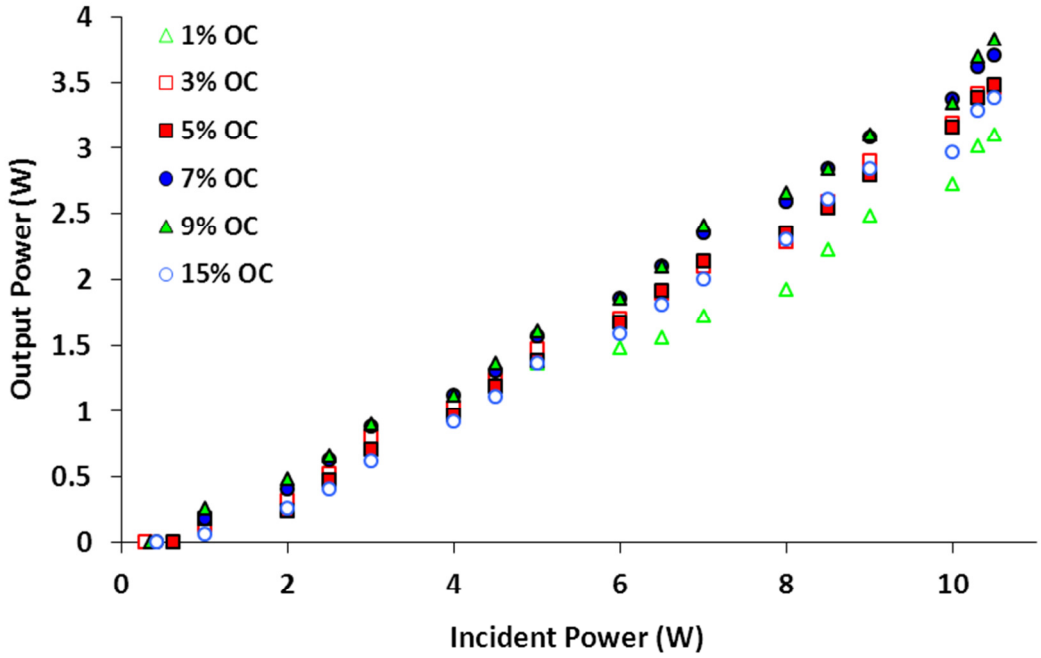

Figure 3.3.c.i graph a) *Output power of 3 atm. % Nd:YVO_4 – Diamond laser in QMC-cavity configuration plotted against incident power, using a set of output couplers of varying transmission. OC stands for output coupler.*

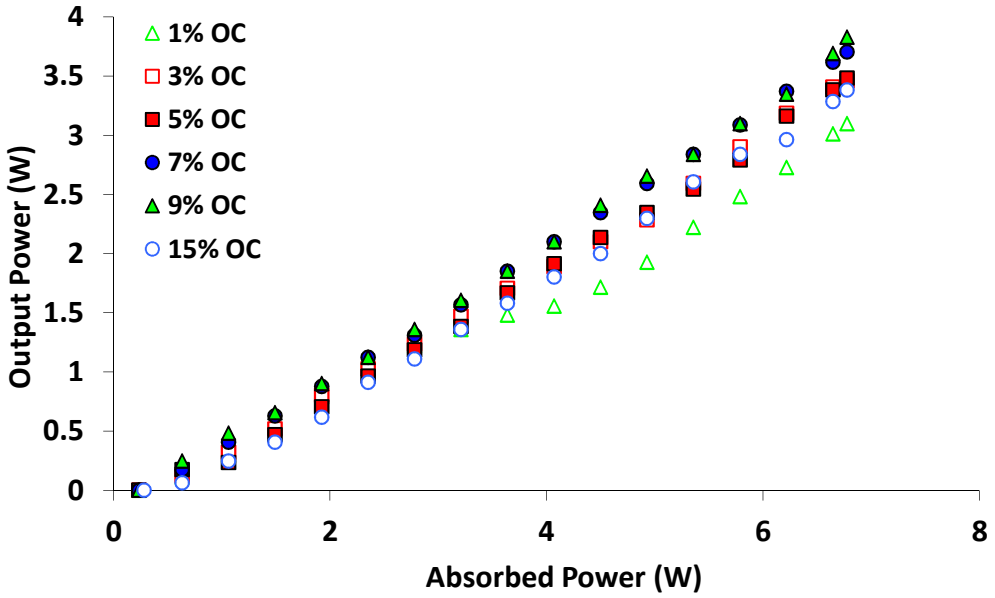

Figure 3.3.c.i graph b) *Output power of 3 atm. % Nd:YVO_4 – Diamond laser in QMC-cavity configuration plotted against absorbed power, using a set of output couplers of varying transmission. OC stands for output coupler.*

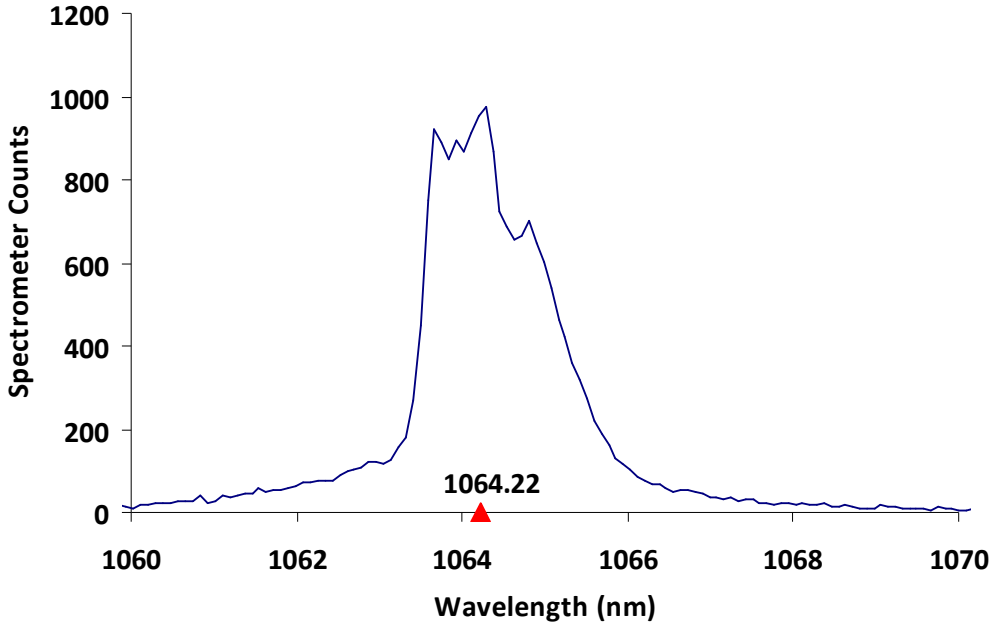

Figure 3.3.c.ii *Spectrum of 3 atm. % Nd:YVO_4 – Diamond laser in QMC-cavity configuration using a 15% output coupler. The triangular point indicates the centroid wavelength. An Ocean Optics S2000 grating spectrometer with a resolution of 0.5nm was used.*

The M^2 parameter of the beam at maximum output power was found to be 4.6 in the horizontal axis and 4.5 in the vertical axis. The dependence of beam quality on fundamental cavity mode to pump mode ratio (i.e. the fundamental cavity mode radius / pump spot radius) in terms of the M^2 of the laser output was measured by extending the length of the cavity of the laser and recording the change in M^2. In figure 3.3.c.iii the results are plotted for the cavity length and the M^2 can be seen to decrease as the cavity length is increased which was possibly the result of an increase in fundamental cavity mode to pump mode ratio towards unity. The M^2 was then plotted against the fundamental cavity mode radius / pump spot radius so that the dependence of beam quality on fundamental cavity mode to pump mode ratio could be observed. This showed that the M^2 improved as the fundamental cavity mode to pump mode ratio increased. The cavity mode calculations were inferred by measuring the M^2 and beam diameter of the output beam at a known distance and then calculating the cavity mode radius that would be required to produce the beam diameter at the set distance.

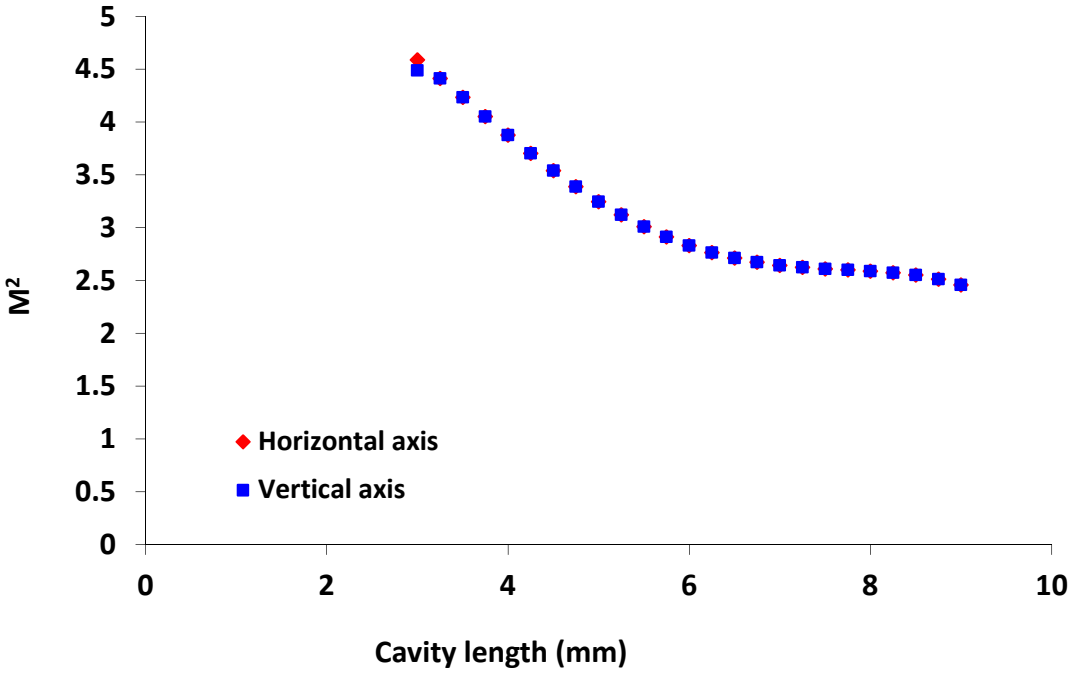

Figure 3.3.c.iii graph a) *Plot of M^2 vs. a) cavity length of a 3 atm. % Nd:YVO_4 – Diamond laser in QMC-cavity configuration at maximum output power. A 7% output coupler was used.*

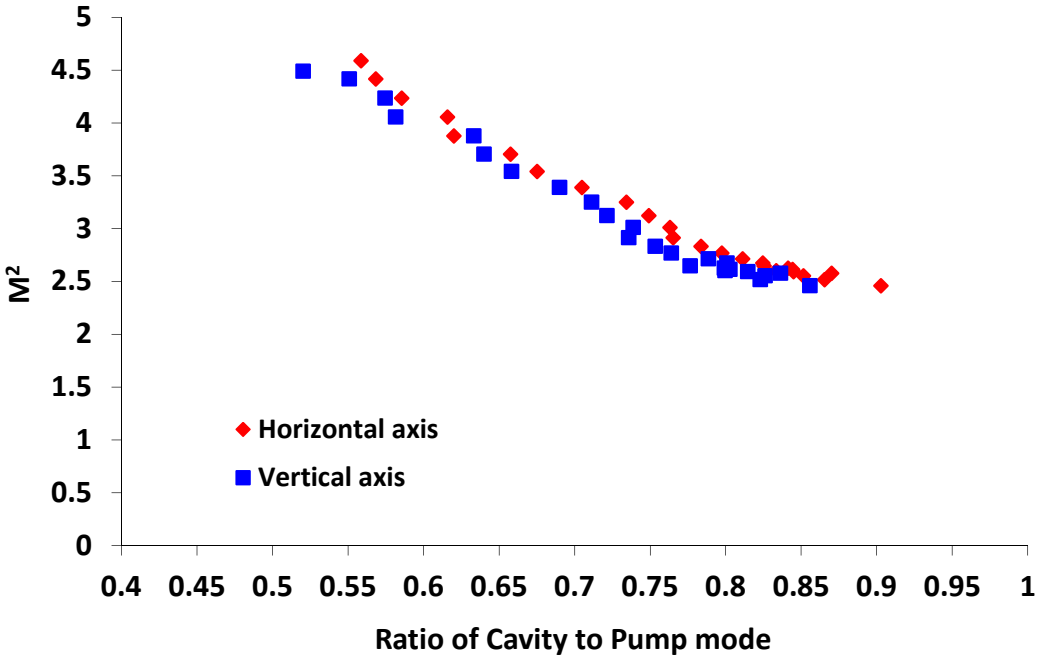

b)

Figure 3.3.c.iii graph b) *Plot of M^2 vs. fundamental cavity to pump mode ratio (i.e. the fundamental cavity mode radius / pump spot radius) of a 3 atm. % Nd:YVO_4 – Diamond laser in QMC-cavity configuration at maximum output power. A 7% output coupler was used.*

The thermal lens within the Nd:YVO_4 was examined by adopting the same experimental approached described in section 3.2.a. Using identical pump optics to those used in the Nd:YVO_4 – sapphire heatspreader thermal lens analysis in section 3.51 and at the same incident pump power of 10W, the thermal lens expressed in terms of a radius of curvature of the equivalent mirror was found to be 221mm indicating that use of a diamond heatspreader leads to a weaker thermal lens when compare to a sapphire heatspreader which is to be expected from the superior thermal conductivity of diamond.

To compare the performance of the SiC heatspreader sample b with that of the diamond heatspreader, a 1 atm. % doped, 4x4x0.5mm thick sample of Nd:YVO_4 was bonded to an identical diamond heatspreader as that used in section 3.2c and mounted in a water-cooled brass mount (3% atm. % doped material being unavailable at this time). Using the same experimental conditions used throughout the QMC sections of this chapter, a series of power transfers were taken to obtain the optimal output coupling as seen in figure 3.3.c.iv**.** Similarly to section 3.3b it was apparent from the fact that laser oscillation is possible even at large output couplings that a substantial sub-cavity resonance was present. It was found that a maximum output power of 3.7W was measured using a 9% output coupler at an incident optical power of 10.5W. A slope efficiency and threshold with respect to incident pump power of 36% and 0.5W were achieved respectively; with respect to estimated absorbed power, a slope efficiency of 50% and threshold of 0.35W was achieved. A spectrum of the output beam was recorded as seen in figure 3.3.c.v, the centroid of which was 1064.8nm.

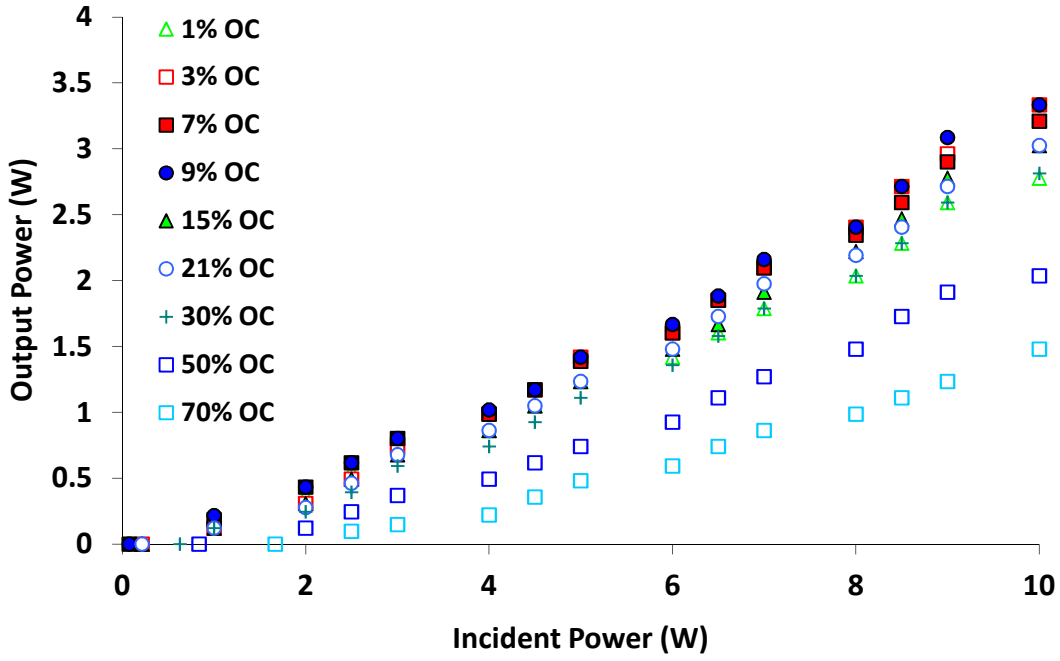

Figure 3.3.c.iv graph a) *Output power of 1 atm. % Nd:YVO_4 – Diamond laser in QMC-cavity configuration plotted against incident power, using a set of output couplers of varying transmission. OC stands for output coupler.*

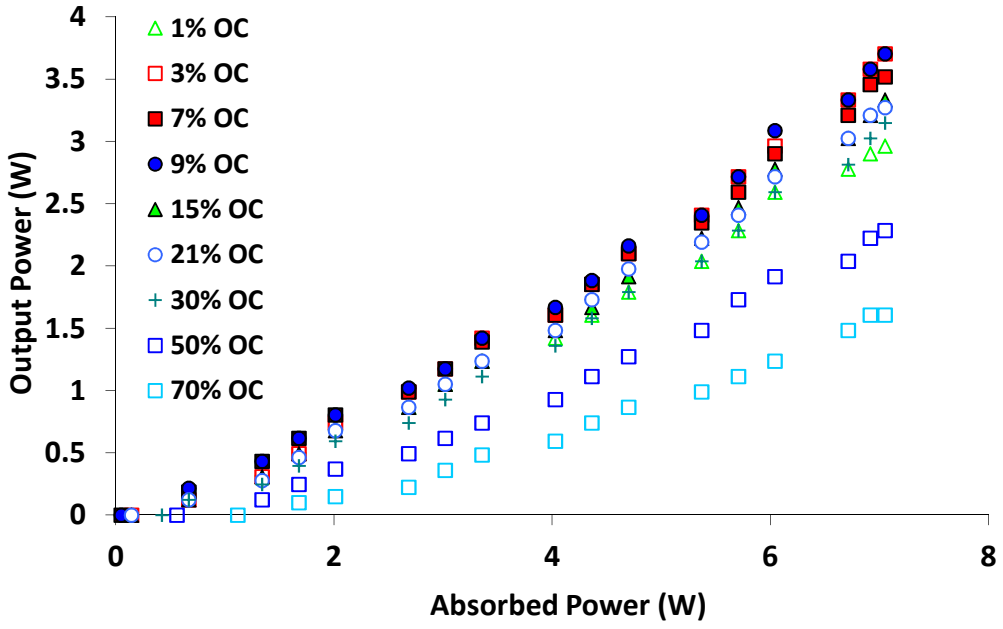

b)

Figure 3.3.civ graph b) *Output power of 1 atm. % Nd:YVO_4 – Diamond laser in QMC-cavity configuration plotted against absorbed power, using a set of output couplers of varying transmission. OC stands for output coupler.*

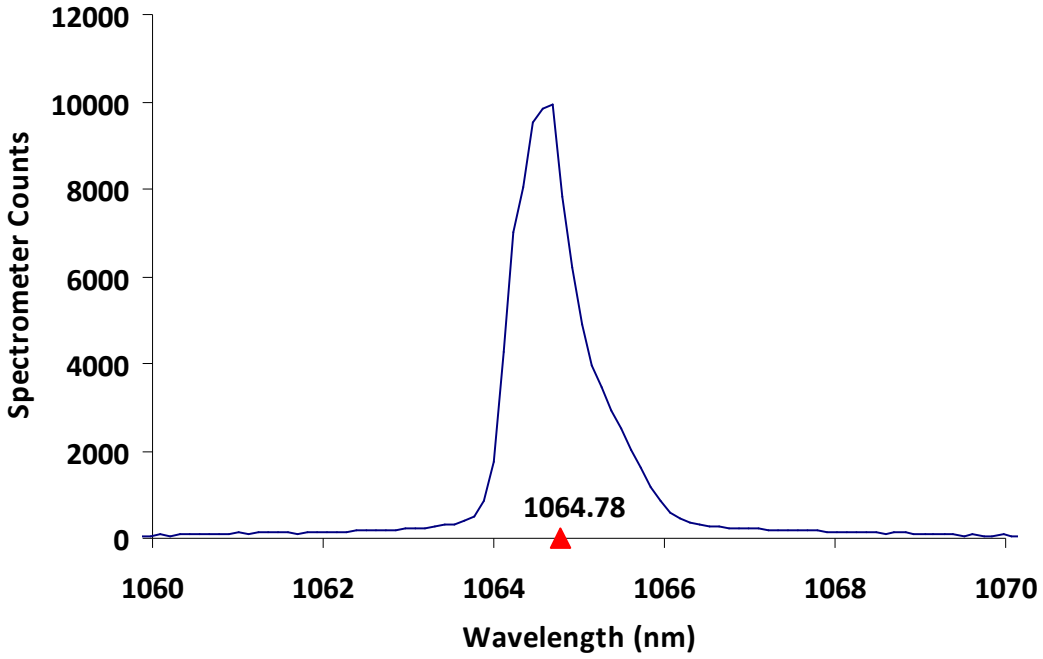

Figure 3.3.c.v *Spectrum of 1 atm. % Nd:YVO_4 – Diamond laser in QMC-cavity configuration using a 15% output coupler. The triangular point indicates the centroid wavelength. An Ocean Optics S2000 grating spectrometer with a resolution of 0.5nm was used*

3.3.d Summary of heatspreader performance in the quasi-microchip configuration

As seen in figure 3.3.d.i and table 3.3.d.i, the diamond heatspreader allows for higher output powers to be obtained in CW operation compared to the sapphire or SiC samples used in these experiments. The crystal fracture of the Nd:YVO_4 chip in the sapphire heatspreader set-up at an incident pump power of 10W shows that diamond and SiC based systems can tolerate larger pump densities than sapphire-based systems. The optimal output coupling varied across the three different heatspreader types; the SiC 3% optimal coupling is anomalous but may be due to a combination of the presence of sub-cavity effects and higher losses introduced by the SiC however further investigation would be necessary to firmly establish an explanation. In section 3.2.c it was apparent that the 1 atm. % doped Nd:YVO_4 was superior in performance in terms of maximum output power to that of the 3 atm. % doped Nd:YVO_4 in the three mirror case; however, in the QMC case it appears that both provide similar output powers, efficiencies and thresholds.

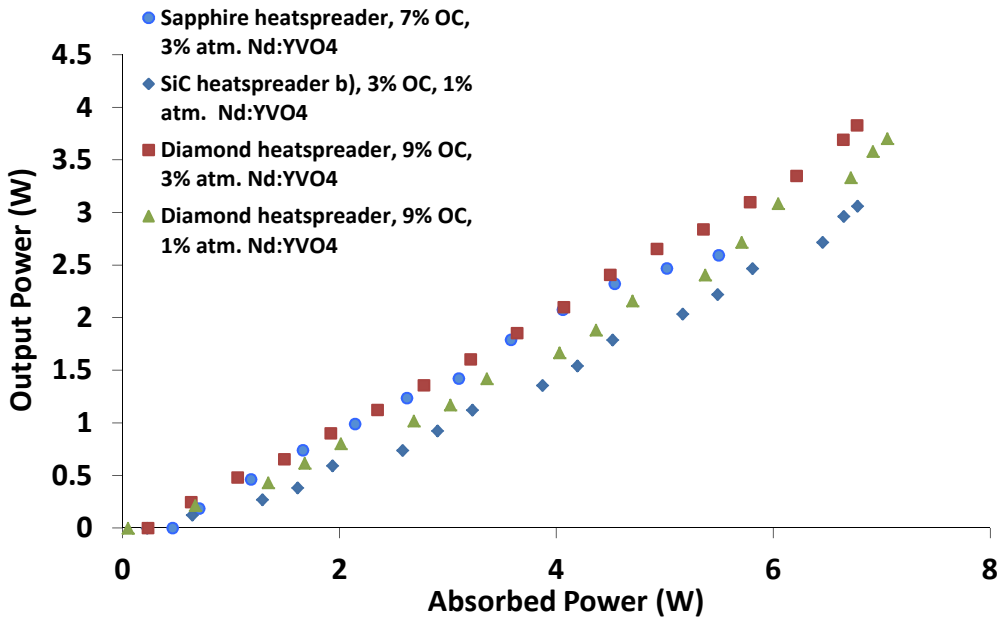

Figure 3.3.d.i *Power transfers, with respect to absorbed pump power, for each heatspreader configuration at optimal output coupling used in this section. OC stands for output coupler.*

Heat-spreader material	Nd:YVO_4 Doping	Optimal OC	Max. Pout	Slope Efficiency with respect to Incident/Absorbed pump power	Threshold with respect to Incident/Absorbed pump power	M^2	Thermal lens focal length
Sapphire	3%	7%	2.6W	38% / 55%	0.54W /0.38W	4.3	56mm
SiC sample b	1%	3%	3.1W	31% / 47%	0.63W / 0.41W	-	-
Diamond	3%	9%	3.8W	37% / 51%	0.5W /0.32W	4.5	221mm
Diamond	1%	9%	3.7W	36% / 50%	0.5W /0.35W	-	-

Table 3.3.d.i *Summary table of laser characterisation of QMC Nd:YVO_4 – heatspreader configuration. The optimal output coupling refers to the output couplers available to the author at the time of the experiment. The maximum output powers are presented with respect to the maximum available pump power except in the case of the sapphire heatspreader where the pump power was reduced to prevent crystal fracture. The M^2 data is for the case of the shortest cavity length of 3mm. The M^2 values have been calculated using the geometric mean of the horizontal and vertical values.*

In terms of beam quality, the measured M^2 of the sapphire case was roughly equal to that of the diamond case; however, the incident pump power in the latter case was larger than the sapphire case indicating that the diamond heatspreader would give rise to a beam with higher brightness if the incident pump power was kept equal for both heatspreaders. It must be noted that the sapphire heatspreader was 2mm thick whilst the diamond heatspreader was 0.5mm thick therefore the longer cavity length provided by the sapphire heatspreader equates to a lower M^2 for a given thermal lens focal length. The geometrical average of the fundamental cavity mode radius in the diamond case was 136µm, in the sapphire case it was 111µm indicating that it would be easier to achieve mode matching using the diamond heatspreader. The cavity mode calculations were inferred by measuring the M^2 and beam diameter of the output beam at a known distance and then calculating the cavity mode radius that would be required to produce the beam diameter at the set distance.

Using equation 3.5.5 [10] to calculate the beam brightness of the sapphire and diamond heatspreader cases it is found that a beam brightness of 0.51W/µm^2/sr was achieved in the sapphire case and 0.63W/µm^2/sr was achieved in the pump power limited diamond case.

$$B = \frac{4P}{\lambda^2 M_x^2 M_y^2}$$

Eq. 3.3.di

The data presented here shows that diamond is a more attractive heatspreader for use in a quasi-monolithic microchip laser at higher pump powers: for the set-up described here this means pump powers above about 5W. In terms of maximum output power achievable, the diamond heatspreader outperformed both the sapphire and SiC heatspreaders; in terms of beam brightness, the diamond maintained a higher brightness of the output beam when compared to the sapphire. Further data would be required to compare diamond and SiC heatspreaders in terms of brightness.

3.4 Summary and conclusions

This chapter has focussed on examining the suitability and effectiveness of three different types of heatspreader for use in power and brightness scaling in microchip lasers, namely sapphire, SiC and diamond. A quasi-microchip (QMC) approach was used in order to obtain sufficient data to allow optimization of a quasi-monolithic microchip laser in Chapter 5. A conventional three mirror extended cavity provided a baseline for a comparison to the QMC cavity arrangement. This comparison indicated that there were no significant decreases in the maximum output power in moving from a conventional extended cavity to quasi-microchip arrangement.

The spread in slope efficiency as a function of output coupling was notably smaller in the quasi-microchip case when compared to the extended cavity. Such a change would be expected were there a sufficient reduction in the round trip loss in moving from an extended cavity to a quasi-microchip configuration. The reduction in component count in making this change would indeed tend to lead to a corresponding reduction in losses. However, a Caird analysis [11] aimed at investigating this hypothesis was inconclusive, largely due to the poor quality of the poor fit of the data in the quasi-microchip case. This is not unexpected since a Caird analysis assumes that the mode overlap contribution to the slope efficiency is constant in order to extract the loss. However in the case of a microchip or quasi-microchip lasers, the cavity mode radius changes markedly with thermal lens focal length. It may be that this greater adaptation of the cavity mode in the quasi-microchip laser case, alongside cavity losses that are likely to be lower, plays a role in reducing the change of slope efficiency with output coupling. However, such a conclusion would require further experimental evidence.

In terms of maximum output power and slope efficiency diamond proved to be superior to SiC and sapphire as a heatspreader role in a QMC configuration, as can be seen in table 3.4.i. Although the SiC gave reasonably good performance, diamond should be used if available for more efficient, higher power microchip lasers. Both the diamond and SiC heatspreaders were able to operate under greater pump

densities than sapphire as evidenced by crystal fracture at an incident pump of 10W in the sapphire heatspreader three-mirror configuration.

Heat-spreader material	Nd:YVO_4 Doping	Optimal OC	Max. Pout	Slope Efficiency with respect to Incident/Absorbed pump power	Threshold with respect to Incident/Absorbed pump power	M^2	Thermal lens*
Sapphire	3 atm. %	7% *7%*	2.6W *2.58W*	38% / 55% *39% / -*	0.54W /0.38W *0.28W/ -*	4.3	56mm
SiC sample b	1 atm. %	3% *30%*	3.1W *3.5W*	30.3% / 47% *36% / 54%*	0.63W / 0.41W *0.55W/ 0.37W*	-	-
Diamond	3 atm. %	9% *7%*	3.8W *3.2W*	37% / 51% *35% / -*	0.5W /0.32W *0.52W/ -*	4.5	221mm
Diamond	1 atm. %	9% *9%*	3.7W *3.9W*	36% / 50% *41% / 58%*	0.5W /0.35W *0.49W/ 0.34W*	-	-

Table 3.4.i *Summary table of laser characterisation of Nd:YVO_4 – heatspreader configuration in quasi-microchip and three mirror cavities. The data for the three mirror cavity configurations is in italics. The percentage of Nd doping varied due to the availability of material. The maximum output powers are presented with respect to the maximum available pump power except in the case of the sapphire heatspreader where the pump power was reduced to prevent crystal fracture. The M^2 data is for the case of the shortest cavity length.*
** The thermal lens expressed in terms of a radius of curvature of the equivalent mirror.*

The brightness of the sapphire and diamond systems was investigated in more detail. Both systems were operated at maximum output power and the length of the cavity increased. M^2 and beam radius measurements were taken at each cavity length. At a cavity length of 3mm, the fundamental cavity mode radii of the diamond and sapphire cases were estimated to be 136µm and 111µm respectively for pump mode radii of 255µm and 266µm respectively. This indicates that in a microchip system it would be easier for mode matching to be achieved using diamond. This approach could take the form of either an increase in cavity length of the microchip laser or a reduction in the thermal lens due to the temperature rise generated within the gain medium caused by the optical pumping. Moving to smaller pump spot radii might at first glance lead to better mode overlap, however at higher input powers a smaller pump spot radius will ultimately lead to an increased chance of crystal fracture. Moving to longer cavity lengths would be a better way to achieve mode-matching

however for microchip lasers it would be detrimental in keeping the overall size of the microchip system to a minimum and would make it more difficult to achieve a short pulsed Q-switched system.

A separate experiment established thermal lens values for diamond and sapphire heatspreaders which showed that sapphire possesses a four-fold stronger thermal lens than diamond for the same incident pump power; this would serve to reduce the size of the fundamental cavity mode and make the task of mode matching more difficult.

In chapter two of this thesis, finite element analysis (FEA) indicated that the thermal lens is stronger when a SiC heatspreader is used compared to using diamond, more so at thinner gain thicknesses. Although it has not been examined experimentally in this thesis, it is believed that the larger thermal lensing resulting from the use of a SiC heatspreader will make it less favourable for use in microchip lasers in terms of brightness scaling. It has been shown that the lower loss displayed by diamond results in an increase in output power, slope efficiency and reduction in threshold compared to SiC. Taking into account the higher thermal lensing shown within SiC heatspreader systems using FEA, diamond would be the heatspreader of choice for power and brightness scaling within microchip lasers. Future work would be required to experimentally validate this statement however.

Improving the beam quality in microchip lasers will require an improved understanding of the complex interplay between the pump parameters, the cavity length, the heatspreader properties, and the cooling geometry in determining the overlap between the pump and fundamental laser modes. The next chapter will discuss gain material choice and will characterise a selection of different gain media to assess their suitability on future microchip configurations.

3.5 References

[1] I. Friel, S. L. Geoghegan, D. J. Twitchen, and G. A. Scarsbrook, "Development of high quality single crystal diamond for novel laser applications," presented at Optics and Photonics for Counterterrorism and Crime Fighting VI and Optical Materials in Defence Systems Technology VII, Toulouse, France, 2010.

[2] A. J. Kemp , G. J. Valentine , J. M. Hopkins , J. E. Hastie , S. A. Smith , S. Calvez , M. D. Dawson and D. Burns "Thermal management in vertical-external-cavity surface-emitting lasers: Finite-element analysis of a heatspreader approach", *IEEE Journal of Quantum Electronics*, vol. 41, p.148-155 , 2005.

[3] http://www.ioffe.ru/SVA/NSM/Semicond/SiC/mechanic.html#Elastic *accessed 29/09/11.*

[4] P. Ščajev and K. Jarašiunas "Application of a time-resolved four-wave mixing technique for the determination of thermal properties of 4H–SiC crystals", *Journal of Physics D: Applied Physics,* Vol.42**,** 055413, 2009

[5] Z. Li and R. C. Bradt, "Thermal expansion of the hexagonal (4H) polytype of SiC," Journal of Applied Physics, vol. 60, pp. 612–614, 1986.

[6] W. N. Sharpe, O. Jadaan, G. M. Beheim, G. D. Quinn, and N. N. Nemeth, "Fracture strength of silicon carbide microspecimens," *Journal of Microelectromechanical Systems*, vol.14, pp. 903- 913, 2005

[7] P. Millar, R. B. Birch, A. J. Kemp, and D. Burns, "Synthetic Diamond for Intracavity Thermal Management in Compact Solid-State Lasers," *IEEE Journal of Quantum Electronics* vol. 44, pp. 709-717, 2008.

[8] W. Koechner, *Solid State Laser Engineering*, Fifth ed. Berlin: Springer, 1999.

[9] ISO 11551: test method for absorptance of optical laser components," (International Organization for Standardization, Geneva, Switzerland, 1997)

[10] A. J. Kemp, G. J. Valentine, and D. Burns, "Progress towards high-power, high-brightness neodymium-based thin-disk lasers," *Progress in Quantum Electronics*, vol. 28, pp. 305-344, 2004.

[11] J. A. Caird, S. A. Payne, P. R. Staver, A. J. Ramponi, L. L. Case, and W. F. Krupke, "Quantum electronic properties of the $Na_3Ga_2Li_3F_{12}:Cr^{3+}$ laser" *IEEE Journal of Quantum Electronics*, vol. 24, pp. 1077-1099, 1988

4. Experimental comparison of gain materials for use in a future microchip laser

4.1 Introduction

In chapter three Nd:YVO_4 was used as the gain material in a variety of different configurations in order to assess suitable parameters for future use in a microchip system. This chapter will examine a number of different gain materials in a three mirror cavity configuration to assess which is likely to perform best in the microchip format. The materials examined in this chapter are Nd:YVO_4, Nd:$GdVO_4$ and two types of 1060nm InGaAs/GaAs semiconductor material. Yb:KYW is examined briefly as a potential gain material for use in future work.

The material parameters of Nd:YVO_4, Nd:$GdVO_4$, and Yb:KYW are displayed in table 4.1.i. Nd:YAG is included for comparison. Nd:YAG and the vanadates, Nd:YVO_4 and Nd:$GdVO_4$, are four-level systems that operate most commonly at an output wavelength of 1064nm. Nd:YAG has been used extensively in the past for high powered applications and has good thermal conductivity when compared to the vanadates. In addition to these properties, the upper state lifetime of Nd:YAG lends itself to Q-switching applications where a long lifetime is desirable for high pulse energies.

Nd:YVO_4 possesses a larger effective emission cross section compared to both Nd:YAG and Nd:$GdVO_4$, which combined with a pump absorption full width half maximum width of 4nm, makes it attractive for efficient diode-laser pumped operation. Nd:YVO_4 has a shorter upper state lifetime than that of Nd:YAG which makes it more suited for Q-switching applications that require higher repetition rates. Due to natural crystal birefringence in Nd:YVO_4, high power operation is not affected by depolarization losses unlike Nd:YAG; however, in terms of thermal conductivity, Nd:YAG is superior to Nd:YVO_4.

The second vanadate that shall be examined in this chapter, Nd:$GdVO_4$ lies in between Nd:YAG and Nd:YVO_4 in terms of laser emission cross section, thermal conductivity and

pump absorption width, but stands out as having the largest pump absorption coefficient of all three materials. For this reason, it has been seen as a potential thin disk material whereby the large absorption coefficient provides a route to using thinner crystals to achieve axial heat flow and hence power scalability [1,2].

Gain material	**Nd:YAG**	**Nd:YVO_4**	**Nd:$GdVO_4$**	**Yb:KYW**
Doping range (atm.%) [3-5]	0.2-1.4 [3]	0.1-3.0, 2-8.5 [4, 5]	0.27 – 3.0 [4]	0.5-100 [6]
Doping for parameters below (atm.%)	1%	1%	1%	5%
Wavelength (nm)	1064 [1]	1064.2 [1]	1063 [1]	1025-1058 [7]
Peak Effective emission cross section σ ($x10^{-23}$ m^2)	2.8 [1]	11.5/14.1 [8,9]	7.6/10.3 [10,9]	0.3 (λ_{lasing} = 1025nm)
Peak Absorption cross section (Pump) ($x10^{-23}$ m^2)	0.7 [9]	5.1/3.9 [8,9]	5.2/2.6 [10,9]	1.33 [11]
Upper-state lifetime τ (μs)	230 [1]	100 [1]	90 [1]	232 [7]
Laser figure of merit σ. τ ($x10^{-21}$ m^2μs)	6.44	11.5/14.1	6.8/9.3	0.7
Peak Pump absorption coefficient (m^{-1})	910 [1]	3400 [10]	7400 [10]	4000 [12]
Pump absorption width FWHM (nm)	2.5 [1]	4 [1]	3.2 [1]	3.5 [11]
Quantum defect	0.24	0.24	0.24	0.04 (λ_{lasing} = 1025nm)
Refractive index	1.82 [13]	2.06* [14]	2.08* [14]	2.09* [15]
Thermal conductivity* (W K^{-1} m^{-1})	14 ([13]	6.1/11.5* [14,16]	6.8/9.5* [14,16]	3* [15]
dn/dT* ($x10^{-6}$ K^{-1})	7.3 [13]	5.8* [14]	5.8* [14]	-12* [17]

Table 4.1.i *Summary table of laser characterisation of material parameters for Nd:YVO_4, Nd:$GdVO_4$ Nd:YAG Yb:KYW, [3-6]. An asterisk indicates that the value is averaged over the optical axes of the crystal. Two values are given in the case of disagreement in literature.*

A different type of material that has the potential for use in a microchip laser is known as the *semiconductor disk laser* (SDL) or vertical-external-cavity-surface-emitting-laser (VECSEL) (e.g. [18, 19]). SDLs can offer a range of properties that doped-dielectric disk lasers cannot, and can be engineered to offer a wide range of output wavelengths [20-23]. Multi-watt microchip lasers based on SDL technology have been demonstrated [18] and combined with

their wavelength versatility; SDLs present a potentially attractive choice for high power, high brightness microchip lasers.

As mentioned before, this chapter aims to examine different gain materials to assess which would be optimal for use in a compact multi-watt microchip laser using available pump sources and gain materials. Nd:YVO_4 which was examined in the previous chapter offers high laser efficiencies which make it an attractive candidate for use in a microchip laser; however, the superior pump absorption characteristics of Nd:$GdVO_4$ provide the potential to use thinner samples and hence to better exploit power scaling strategies akin to those used in thin disk lasers. Two strengths that the SDL format offers are the ability to tailor the output wavelength of SDL's and the tunability of these devices; however, the dependence of the effective gain upon temperature limits the output power and thus thermal management is of paramount importance if SDLs are to be used in a high power microchip laser [24].

4.2 Comparison of optically pumped Nd:YVO_4, Nd:$GdVO_4$ and SDL material in a three-mirror cavity

A three mirror cavity configuration was used in this section to allow for parameters such as optimal output coupling and mode radii to be investigated with greater flexibility then would be achieved by varying these parameters in a microchip format. The three mirror cavity can be seen in figure 4.2.i**.** A 10W fibre-coupled diode laser (100μm core-diameter, 0.2NA) operating at a wavelength of 808nm was used as a pump laser (unless otherwise noted).

The heatsink temperature of the diode-laser pump was adjusted when using the Nd:YVO_4 and Nd:$GdVO_4$ laser material to account for the shift in the diode-laser operating wavelength with increasing input current. It was therefore necessary to tune the temperature of the diode laser to ensure that optimum absorption was maintained throughout the input current range. This was not the case for semiconductor disk lasers (SDLs) due to the very large absorption cross section (where light with a photon energy greater than the bandgap energy is absorbed) and the spectrally broad absorption inherent in the semiconductor design compared to the narrow absorption features of the doped-dielectrics (4nm and

3.2nm full width half maximum pump absorption width for Nd:YVO_4 and Nd:$GdVO_4$ respectively).

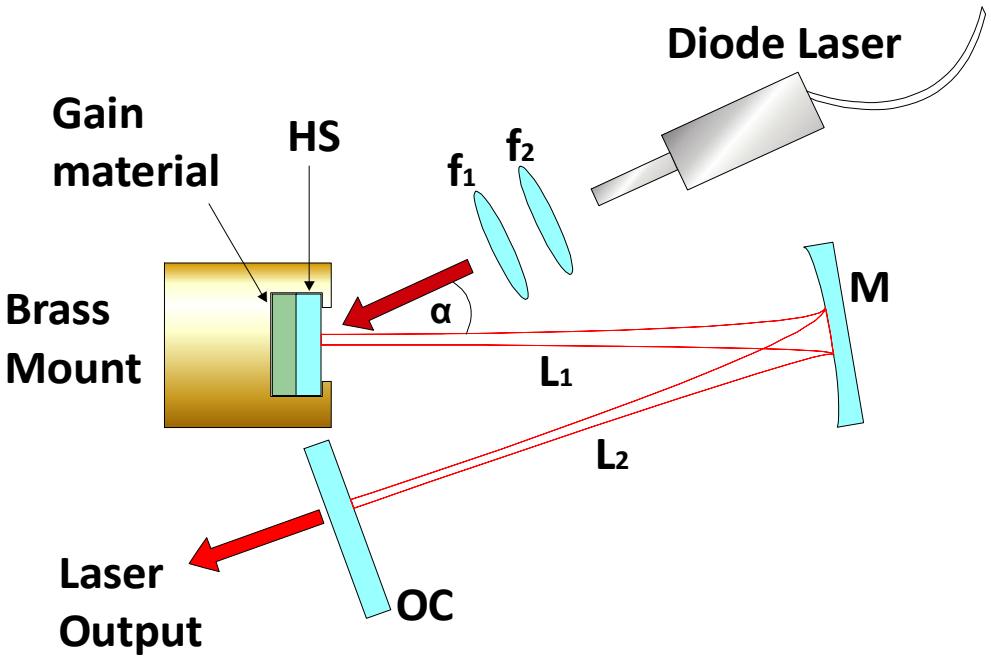

Figure 4.2.i *Diagram of three-mirror cavity used in this section. The distance between the chip and the folding mirror* ***M*** *is labelled* ***L1*** *and the distance between the folding mirror and the plane output coupler* ***OC*** *is labelled* ***L2****. A 10W diode laser was used to pump the gain material at an angle* ***α*** *to the normal of the heatspreader where* ***α*** *= 22 degrees; the input pump power was collimated through a lens* ***f2*** *and focussed through an additional lens* ***f1*** *to produce the desired pump spot size. A diamond heatspreader* ***HS*** *was bonded to different types of gain materials and a set of output couplers of varying fractions of transmission was used. The rear surface of the gain material is coated for high reflection at laser and pump wavelengths except in the case of the distributed Bragg reflector (DBR) of the SDL.*

A 0.5mm thick, type IIa single-crystal chemical-vapour deposition (CVD) grown diamond heatspreader of radius 2mm was bonded to the gain material to be examined; the composite structure was then sandwiched between two layers of 0.125mm thick indium foil (one of which had a circular aperture for the incident and emitted light) and inserted in to position in a brass, water cooled mount. Water cooled to a temperature of 9.5°C was pumped through the brass mount in order to provide cooling for the sample.

4.2.a 1 atm. % doped Nd:$GdVO_4$ – diamond characterisation

In this section a 0.5mm thick sample of 1 atm. % doped Nd:$GdVO_4$ was used as the gain material in the laser, bonded to the diamond heatspreader described in section 4.2. The rear surface of the Nd:$GdVO_4$ sample was coated for high reflection at the pump and laser wavelengths of 808nm and 1064nm respectively. An a-cut orientation of the gain material was used in order to maximise absorption at the pump wavelength and emission cross-section at the laser wavelength of 1064nm – similar to the Nd:YVO_4 material used in the previous chapter. An identical cavity to that used in figure 4.2.i was constructed to characterise the performance of the laser. Collimating and focussing lenses of 14mm and 32mm focal length respectively were used to produce a pump spot radius of approximately 114µm on the Nd:YVO_4 crystal facet nearest the pump source. Lengths L1 and L2 (see fig 4.3a) were 74mm and 80mm respectively, producing a calculated fundamental cavity mode radius of 113µm at the crystal facet nearest the pump source.

In figure 4.2.a.i the results of the output coupling optimisation can be seen. The maximum CW output power achieved was 3.4W for a 9% output coupling and an incident pump power of 10.3W. The slope efficiency and threshold, both with respect to incident pump power, were 36% and 0.34W respectively. The power absorbed within the crystal was estimated by measuring the reflected pump power off the crystal and subtracting it from the total pump power incident upon the crystal. The slope efficiency and threshold with respect to absorbed power were estimated to be 52% and 0.21W respectively.

To allow the reader to compare the Nd:$GdVO_4$ set-up with a Nd:YVO_4 set-up of identical pump and fundamental cavity mode radius, the Nd:YVO_4 results from chapter 3 are reprised in figure 4.2.a.ii. At an input power of 10.3W, a maximum output power of 3.9W was achieved using a 9% output coupler for the Nd:YVO_4 case. The slope efficiency and threshold, both with respect to incident pump power were 39.6% and 0.31W respectively; with respect to absorbed power, a slope efficiency of 57.3% and threshold of 0.15W were achieved.

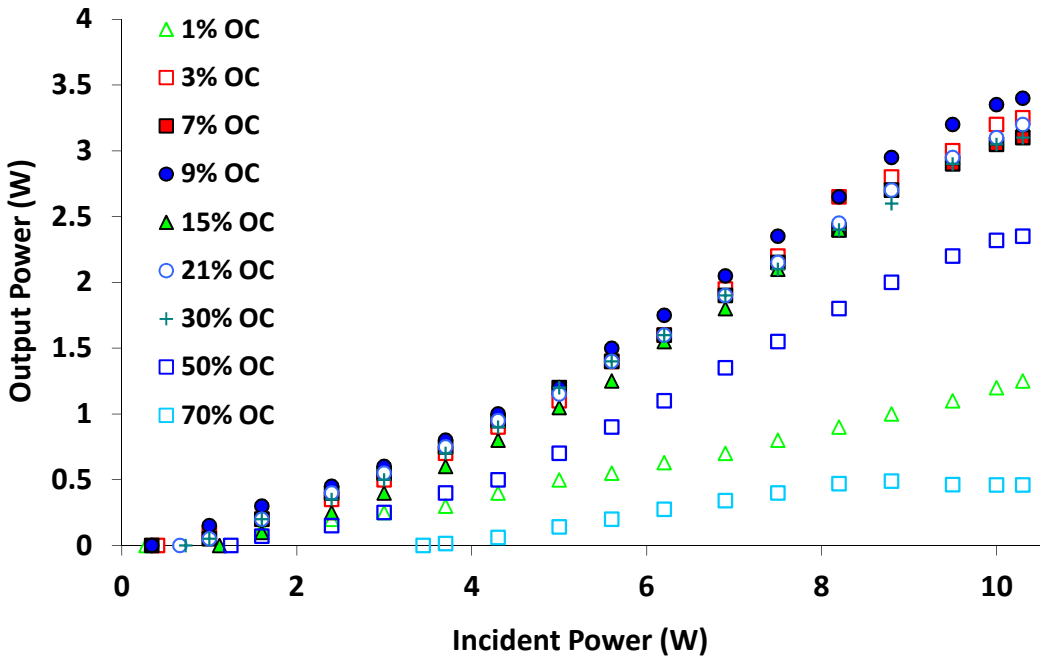

a)

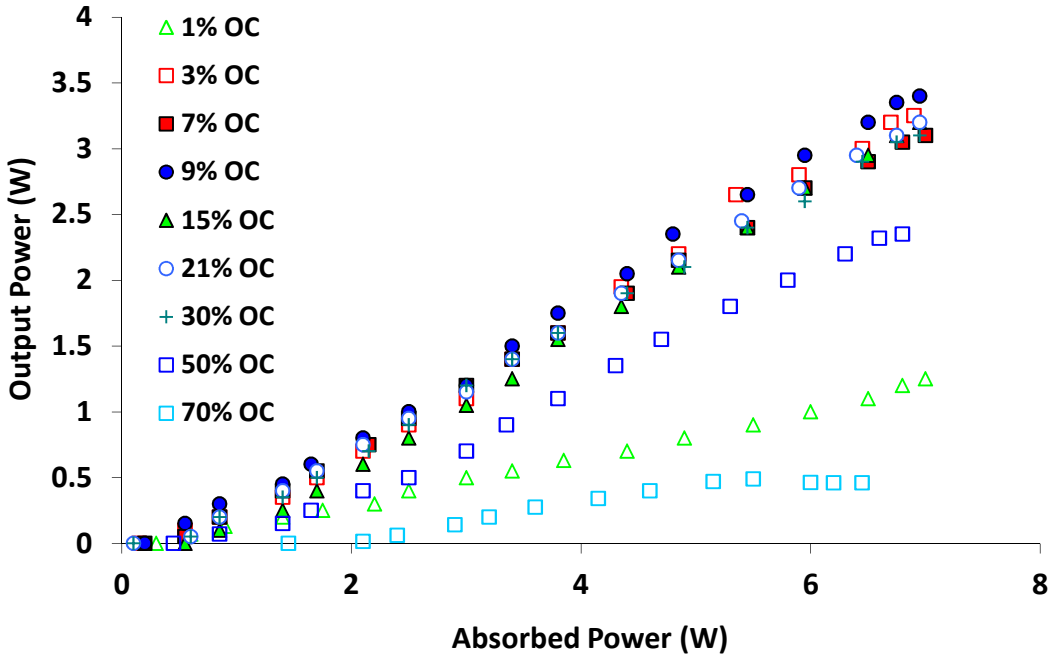

b)

Figure 4.2.a.i *Output power of 1 atm. % Nd:$GdVO_4$ laser plotted against a) incident power and b) absorbed power. OC stands for output coupler.*

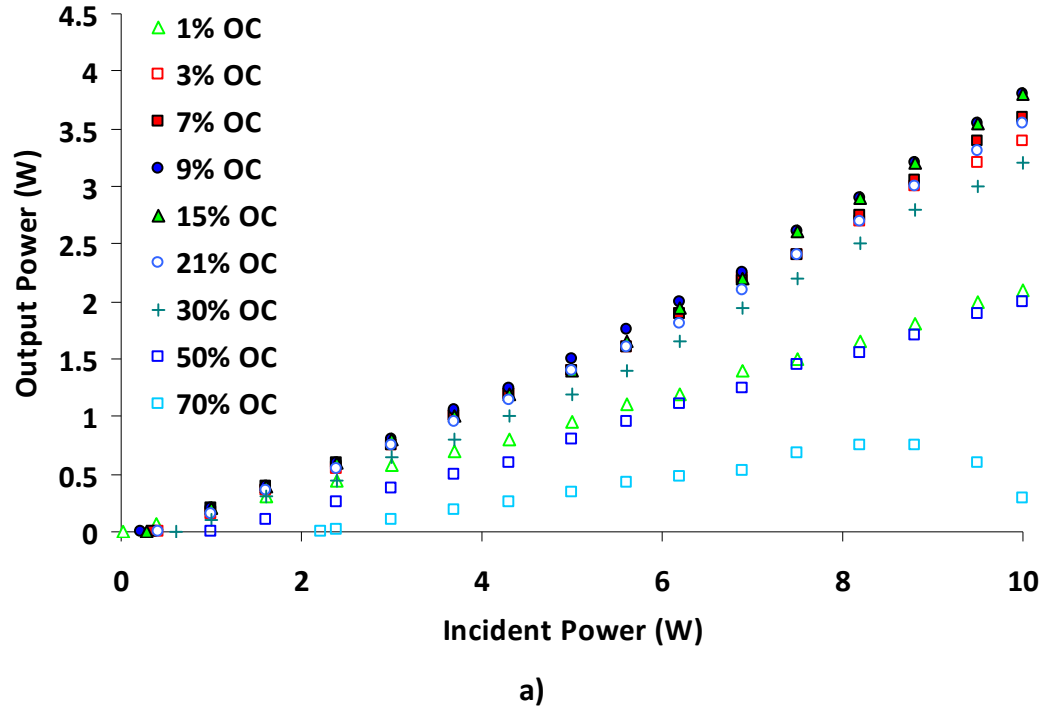

a)

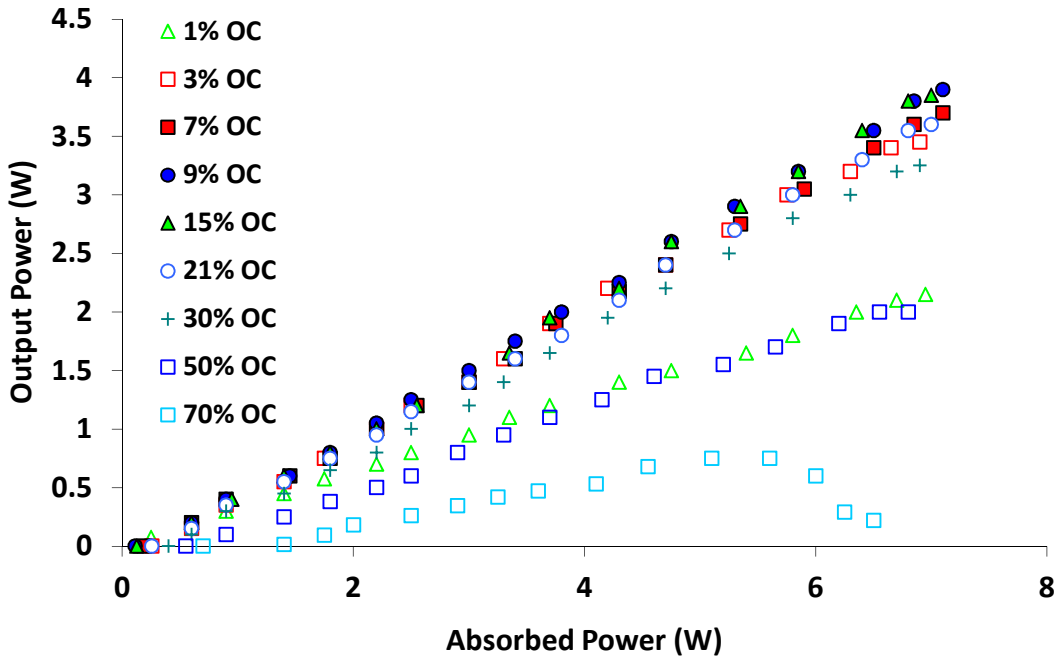

b)

Figure 4.2.a.ii *Output power of 1 atm. % Nd:YVO_4 laser plotted against a) incident power and b) absorbed power taken from chapter 3 of this thesis for comparison. OC stands for output coupler.*

4.2.b 15 quantum well 1060nm InGaAs/GaAs SDL characterisation

In this section a InGaAs/GaAs semiconductor gain structure is examined. It was grown and provided by the Samsung Advanced Institute of Technology [25, 26]. The semiconductor structure was used as the gain material in the laser, bonded to the diamond heatspreader described in section 4.2**.** A 30-pair distributed Bragg reflector (DBR) of λ/4 layers of $Al_{0.3}Ga_{0.7}As$ and AlAs was grown on top of a GaAs substrate; gain was then provided by 15 layers of 7nm thick $In_{0.28}Ga_{0.72}As$ quantum wells spaced at λ/2 by GaAs barriers. $GaAs_{0.9}P_{0.1}$ strain compensating layers were placed next to the quantum wells. A window layer of $Al_{0.3}Ga_{0.7}As$ and a capping layer of GaAs completed the structure.

An identical cavity to that used in figure 4.2.i was constructed to characterise the performance of the laser. Collimating and focussing lenses of 14mm and 11mm focal length respectively were used to produce a pump spot radius of 40μm. Lengths L1 and L2 were 55mm and 300mm respectively, producing a calculated fundamental cavity mode radius of 40μm at the gain chip.

In figure 4.2.b.i the power transfer characteristics of the SDL can be seen at two different positions on the semiconductor chip. The maximum CW output power achieved for the first position was 2.9W for a 9% output coupling and an incident pump power of 10.3W. This output coupling was chosen as it was found to give the optimal output powers as seen in [27]. The slope efficiency and threshold, both with respect to incident pump power were 30% and 0.59W respectively.

The maximum CW output power achieved for the second position was 2.5W for under the same pumping conditions and output coupling. The slope efficiency and threshold, both with respect to incident pump power were 30% and 0.59W respectively. The spectrum of the output can be seen in figure 4.2.b.ii. The characteristic structure results from the sub-cavity set-up between the distributed Bragg reflector and the diamond-air interface [28].

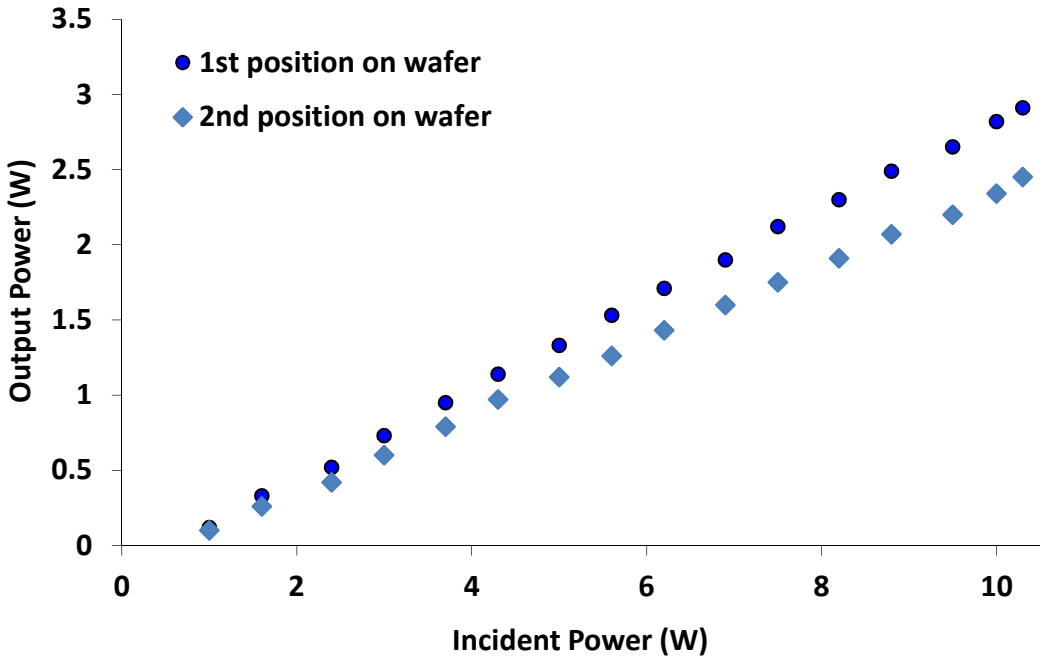

Figure 4.2.b.i *Output power of 15 quantum well 1060nm InGaAs/GaAs SDL plotted against incident power for two positions on the semiconductor surface*

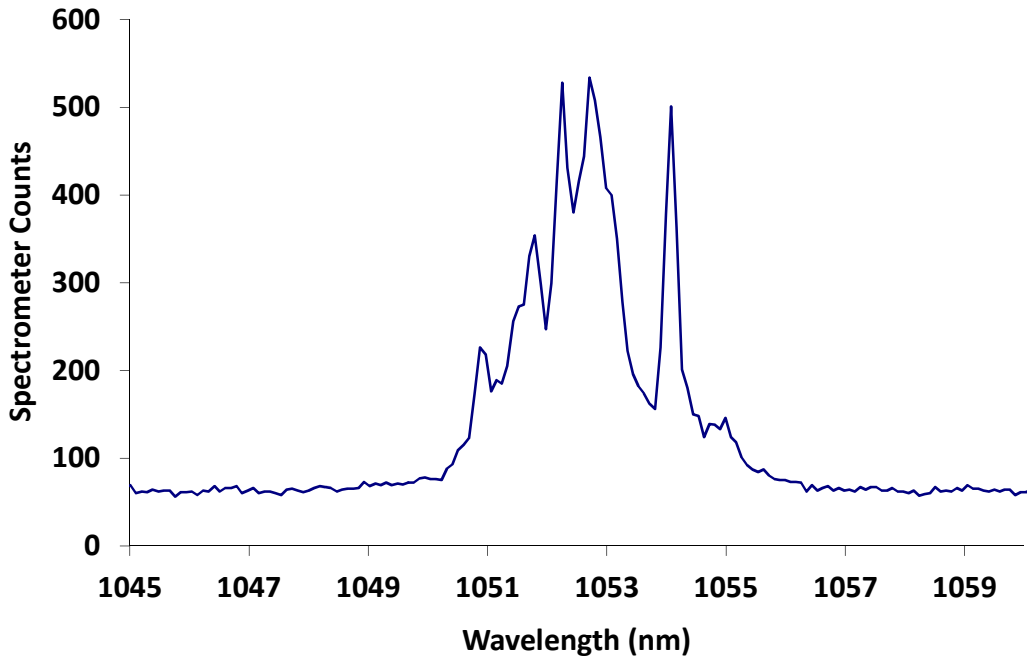

Figure 4.2.b.ii *Spectrum of 15 quantum well 1060nm InGaAs/GaAs SDL output. An Ocean Optics S2000 grating spectrometer with a resolution of 0.5nm was used to monitor the spectral output*

4.2.c 10 quantum well 1060nm InGaAs/GaAs SDL characterisation

In this section an similar semiconductor gain structure to that described in section 4.2.b was used as the gain material in the laser, bonded to the diamond heatspreader described in section 4.2**.** Damage to the sample used in the previous section and lack of availability of more 15 quantum well material forced the use of a similar SDL structure from the same grower. The alternative semiconductor structure used in this section differed only in the number of quantum wells present: 10 7nm thick $In_{0.28}Ga_{0.72}As$ quantum wells as opposed to the 15 in the previous section.

An identical cavity to that used in figure 4.2 was constructed to characterise the performance of the laser. Collimating and focussing lenses of 14mm and 11mm focal length respectively were used to produce a pump spot radius of 74µm, taking into account propagation through the diamond heatspreader. Lengths L1 and L2 were 55mm and 300mm respectively, producing a fundamental cavity mode radius of 40µm. A number of output couplers of varying transmissions were examined to assess the optimal output coupling of the laser. In figure 4.2.c.i the power transfer characteristics of the SDL can be seen. The maximum CW output power achieved for the first position was 2.5W for a 9% output coupling and an incident pump power of 10.3W. The slope efficiency and threshold, both with respect to incident pump power were 23% and 0.55W respectively. The lower slope efficiency and higher threshold result – at least in part – from the thinner quantum well and barrier section in the 10 quantum well structure compared to the 15 quantum well structure this device (70nm compared to 105nm). This resulted in a smaller fraction of the incident pump power being absorbed in this section and hence fewer excited carriers are available to provide gain.

To assess the power scaling potential of this SDL material, the available incident input power was increased by switching the pump source from a 10W laser diode to a 90W fibre-coupled laser diode with a core-diameter of 200µm (0.22NA). The collimating and focussing lenses were switched to 14mm and 8mm focal length respectively and positioned to attain a pump spot radius of 68µm. Lengths L1 and L2 were chosen to be 59mm and 160mm respectively,

resulting in a fundamental cavity mode radius of 61µm at the gain material. The maximum CW output power achieved using this SDL was 6.5W for a 5% output coupling and an incident pump power of 34.2W as seen in figure 4.2.c.ii. The slope efficiency and threshold, both with respect to incident pump power were 22% and 2.4W respectively. In the case of SDLs, output power is limited because the spectral peak of the gain from the quantum wells moves to longer wavelengths at a different rate to the resonance in the sub-cavity located in the active region, eventually leading to a spectral misalignment leading to reduced gain and eventually to the laser oscillation ceasing. The point at which the maximum output power occurs is termed the roll over point, beyond which roll over occurs whereby there is a rapid decrease in output power. For the SDL used in this section, roll over occurred at an input power between 34.2W and 35.5W for a pump spot radius of 68µm.

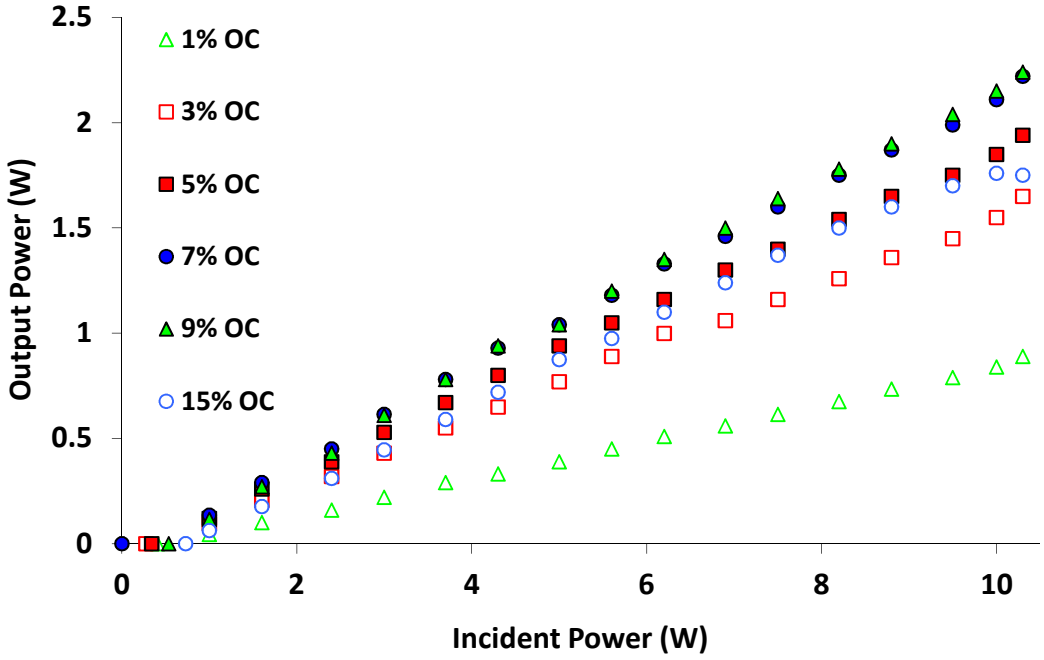

Figure 4.2.c.i *Output power of 10 quantum well 1060nm InGaAs/GaAs SDL plotted against incident power for a pump limited incident power of 10.3W. OC stands for output coupler.*

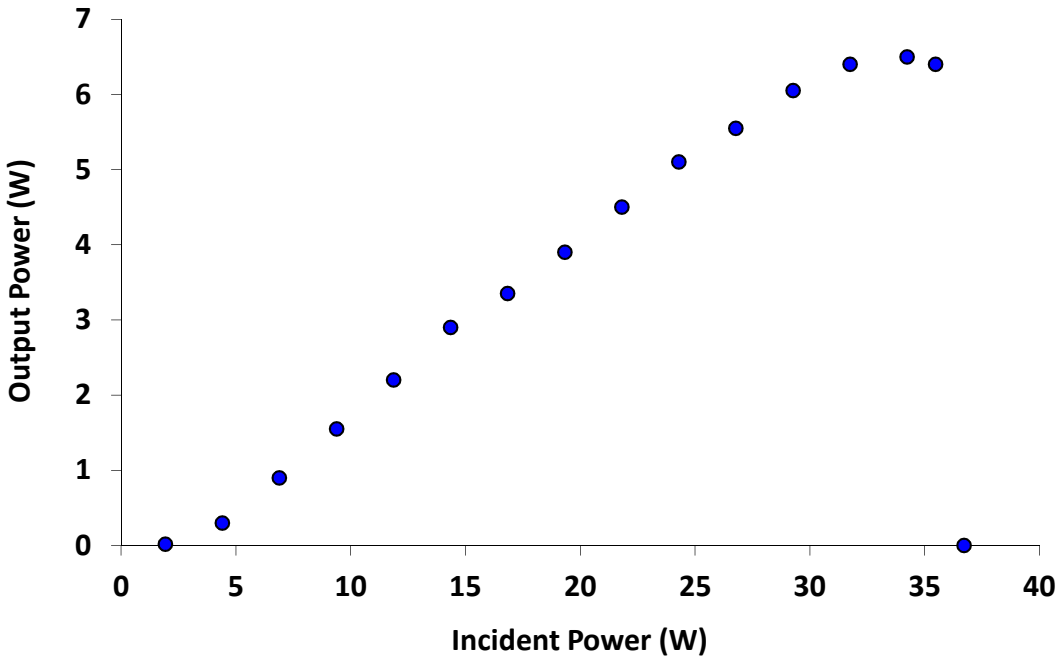

Figure 4.2.c.ii *Power scaling of 15 quantum well 1060nm InGaAs/GaAs SDL beyond 10W of incident power for a 5% output coupler.*

4.3. Discussion of Nd:YVO_4, Nd:$GdVO_4$ and SDL material

A number of different gain materials have been investigated under lasing conditions in this chapter to assess which available material would be best for use in a high power microchip laser. As can be seen in figure 4.3.i and table 4.3.i in terms of maximum output power, incident slope efficiency and threshold, Nd:YVO_4 proves to be the optimal choice of gain material. In terms of absorbed power, both Nd:YVO_4 and Nd:$GdVO_4$ absorb approximately 7W when pumped by the 10W diode laser; the Nd:YVO_4 material achieved a larger slope efficiency with respect to absorbed pump power of 58% compared to that of Nd:$GdVO_4$ which achieved 52%. This may possibly be as a result of the Nd:YVO_4 being of higher quality due to the the relative maturity of Nd:YVO_4 growth compared to Nd:$GdVO_4$. The threshold of the Nd:$GdVO_4$ set-up was lower than that of the Nd:YVO_4 set-up; the experimental values were 0.21W and 0.34W respectively with respect to absorbed pump power. Although Nd:$GdVO_4$ possesses superior pump absorption characteristics and a higher thermal conductivity than Nd:YVO_4 (according to Didierjean [14], see chapter two for a more detailed discussion) which are advantageous for thermal management in the geometry shown in figure 4.2, to date higher output powers have been achieved with Nd:YVO_4 [29];

however, it is believed that the Nd:$GdVO_4$ growth processes have not reached the same stage of maturity as those associated with Nd:YVO_4 leading to a reduction in crystal quality and hence laser performance.

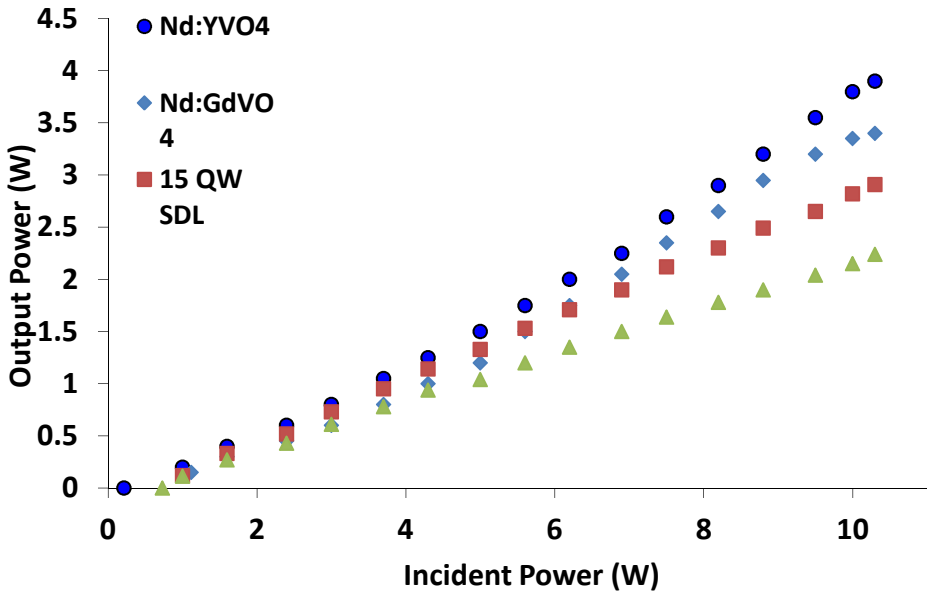

Figure 4.3.i *Power transfers of each gain material examined in this chapter at optimal output coupling used in this section. Data from the previous chapter concerning Nd:YVO_4 has been included for comparative purposes. OC stands for output coupler and QW stands for quantum well.*

Gain material	Max. P_{out}	Max. Slope efficiency w.r.t. incident/ absorbed pump power	Lasing efficiency w.r.t. incident pump power	Threshold w.r.t. incident/ absorbed pump power	Pump spot radius	Fundamental cavity mode radius
1% Nd:YVO_4	3.9W	41% / 58%	38%	0.49W / 0.34W	114µm	113µm
1% Nd:$GdVO_4$	3.4W	36% / 52%	33%	0.36W / 0.21W	114µm	113µm
15 QW SDL	2.9W	37% / -	29%	0.59W / -	78µm	40µm
10 QW SDL	2.2W	30% / -	22%	0.55W / -	78µm	40µm

Table 4.3.i *Summary table of laser characterisation of various gain media in a three-mirror cavity configuration. The maximum output powers are presented with respect to the maximum available pump power of 10.3W. Data from the previous chapter concerning Nd:YVO_4 has been included for comparative purposes. The optimal output coupling in each case was 9%. QW stands for quantum well, PSR stands for pump spot radius and FCMR stands for fundamental cavity mode radius at the gain material.*

The SDL material consisting of the 15 QW and 10 QW structures do not provide as much output power as either of the vanadates using the available 10W of input power provided by the 808nm diode laser. As noted previously, although the 15 QW SDL material outperformed the 10 QW material, availability issues ruled out the further use of the former. Power scaling of the 10 QW SDL material to the roll-over point demonstrated an output power of 6.5W at an input power of 34.2W. Although a reasonable power scaling result for an SDL, if one wanted to obtain a larger power output in a microchip format it would be more sensible to choose the vanadate route which can provide higher output powers [29]. The advantage of using a semiconductor approach, however, would be the larger wavelength range and the tunability that SDL's can offer over most doped-dielectric materials.

It has been shown that the vanadates examined in this chapter offer greater output powers than the SDL structures used; however, there are some drawbacks associated with four level doped dielectric material such as Nd:YVO_4 and Nd:$GdVO_4$. As seen in chapter three of this thesis, the move to higher doping levels in Nd:YVO_4 results in lower output powers and efficiencies which conflicts with the aim of decreasing the thickness of the gain material in a microchip laser to improve the thermal management whilst increasing the doping level to compensate for pump absorption over a smaller length. This reduction in thickness in a microchip laser allows one to move closer to the thin-disk regime where increased axial heat flow, and consequently reduced radial heat flow can reduce the focal length of the thermal lens and associated aberrations. Given the poor performance of Nd:YVO_4 and Nd:$GdVO_4$ at higher doping levels (>1%) alternative material were considered that would allow for the use of thinner pieces of gain material whilst retaining good pump absorption and laser efficiency. The sparse energy level structure of ytterbium doped materials such as Yb:KYW means they do not suffer significant quenching effects at higher dopant concentrations compared to the neodymium doped materials and so are a promising gain material to use in microchip laser formats. The quantum defect of Nd:YVO_4 and Nd:$GdVO_4$ is approximately 0.24 for pumping and lasing wavelengths of 808nm and 1064nm, compared to that of Yb:KYW which is 0.06 for pumping and lasing wavelengths of 981nm and 1040nm which means that significantly less heat loading is experienced for Yb:KYW as modelled in chapter 2 of this thesis which is a big advantage in terms of improving thermal management.

Furthermore Yb:KYW does not suffer from a reduction in gain due to processes such as cross-relaxation and upconversion unlike Nd:YVO_4. With this mind the next section will report on the initial characterisation of Yb:KYW in a three-mirror cavity format using intracavity diamond in the heatspreading role and its potential, in the future, as an alternative to Nd:YVO_4 in microchip lasers.

4.4 Yb:KYW – Diamond characterisation

4.4.a Characterisation of 0.5mm thick 25 atm. % doped Yb:KYW

In this section a 0.5mm thick sample of c-cut uncoated 25 atm. % doped Yb:KYW was used as the gain material in the laser, bonded to the diamond heatspreader described in section 4.2. Due to the lack of an optical coating on the rear surface of the Yb:KYW, another diamond heatspreader with a mirror coating on it was bonded to this rear surface as shown in figure 4.4.a.i. The rear surface of the second diamond heatspreader was coated for high reflection at 1064nm for lasing operation and 808nm optical pumping – these coatings were designed for use with neodymium doped materials; however, at the pump (981nm) and laser (~1050nm) wavelengths for Yb:KYW the coating transmissions were calculated to be 0.3% and 0.01% respectively (from the manufacturer's data).

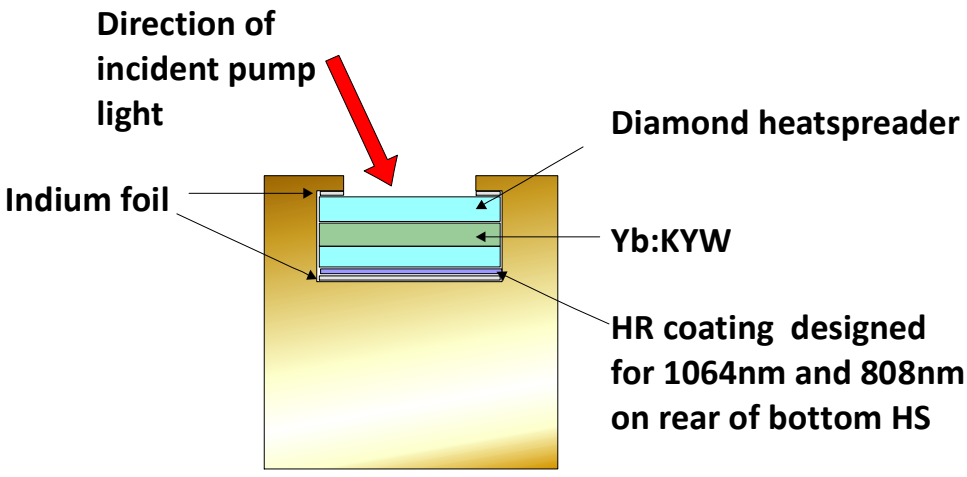

Figure 4.4.a.i *Diagram of diamond-Yb:KYW-diamond composite structure. HS stands for heatspreader.*

The unpolarized output of a 30W fibre-coupled laser diode with a core-diameter of 200µm (0.22NA) was used to pump the Yb:KYW at a wavelength of 981nm at an angle of 23 degrees

to the normal. By monitoring the pump power reflected off the sample as the temperature and hence wavelength of the pump diode laser were varied, the absorption in the Yb:KYW could be optimized. An incident power of 14W was used and an Ocean Optics S2000 grating spectrometer with a resolution of 0.5nm was used to monitor the spectrum of the pump laser. The results can be seen in figure 4.4.a.ii.

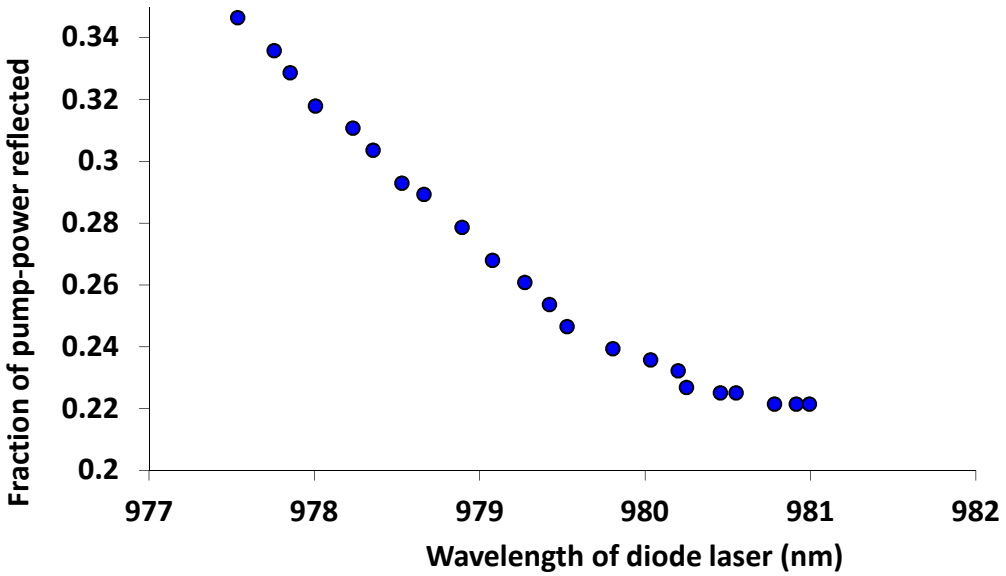

Figure 4.4.a.ii *Absorbed incident power in Yb:KYW plotted against wavelength.*

An identical cavity to that used in figure 4.2 was constructed to characterise the performance of the laser. Collimating and focussing lenses of 25mm and 80mm focal length respectively were used to produce a pump spot radius of 320µm on the Yb:KYW crystal facet nearest the pump source. Lengths L1 and L2 were 100mm and 70mm respectively, producing a fundamental cavity mode radius of 182µm on the Yb:KYW crystal facet nearest the pump source. A 50-50 beam splitter was introduced between the focussing and collimating lenses so that the pump laser could be operated at a lower heatsink temperature but still produce an output wavelength of 981nm at the desired incident pump power. It was found, however, that lasing action was not achievable under continuous wave and pulsed operation of the incident pump. The likely explanation is excess reabsorption loss due to the high doping level and the thickness of the sample. This may have resulted in

insufficient excitation at the rear of the sample to reach transparency in this quasi three-level material [30].

4.4.b Characterisation of 0.25mm thick 10 atm. % doped Yb:KYW

To reduce issues with reabsorption loss, the 25 atm. % doped 0.5 mm thick Yb:KYW crystal was replaced with a 0.25mm thick , Ng-cut 10 atm. % doped Yb:KYW crystal which was bonded to identical diamond heatspreaders using the configuration as shown previously in figure 4.4.a.i. A photograph of the structure can be seen in figure 4.4.b.i.

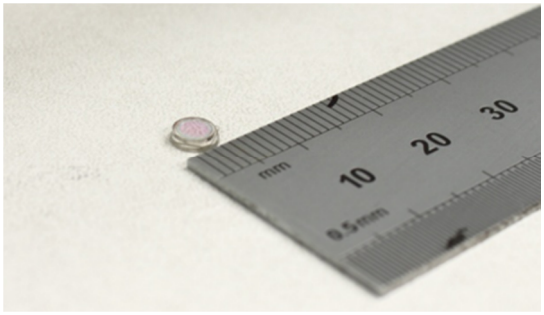

Figure 4.4.b.i *Photograph of diamond-Yb:KYW-diamond composite bonded successfully.*

A three mirror cavity configuration, similar to that used in the previous section, was used to characterise the laser. A smaller pump spot size was desirable to pump the Yb:KYW, however the 200µm core diameter of the pump diode laser precluded the use of similar pump optics to those used in the previous sections and so collimating and focussing lenses of 50mm and 50mm focal length were used to produce a pump spot radius of 100µm. A mirror with a ROC of -100mm was used and lengths L1 and L2 were 90mm and 85mm respectively, producing a fundamental cavity mode radius of 109µm on the Yb:KYW crystal facet nearest the pump source.

The results of the output coupling optimisation can be seen in figure 4.4.b.ii. The maximum CW output power achieved was 1.9W for a 2% output coupling and an incident pump power of 10W. The slope efficiency and threshold, both with respect to incident pump power, were 29% and 3W respectively. The slope efficiency and threshold, both with respect to calculated absorbed pump power, were estimated to be 66% and 1.38W respectively.

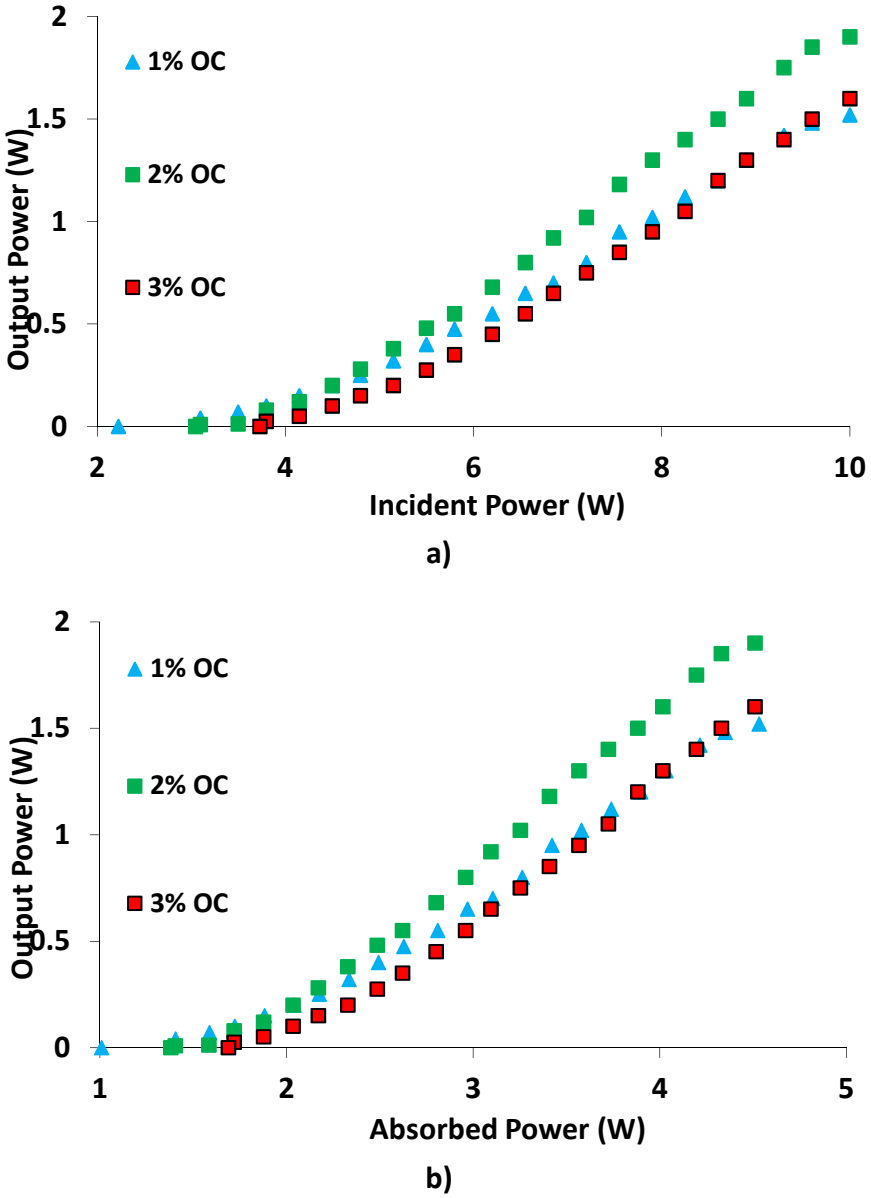

Figure 4.4.b.ii *Output power of 0.25mm thick, 10 atm. % doped diamond heatspreader sandwich Yb:KYW laser plotted against a) incident power and b) calculated absorbed power. OC stands for output coupler.*

The spectra of the laser output of the 1%, 2% and 3% output coupler cases are shown in figure 4.4.b.iii. As can be seen there is a shift to shorter output wavelengths with respect to an increase in the output coupler transmission value [31]. The spectral separation of modes correlates with the internal etalon of the 0.25mm thick Yb:KYW crystal.

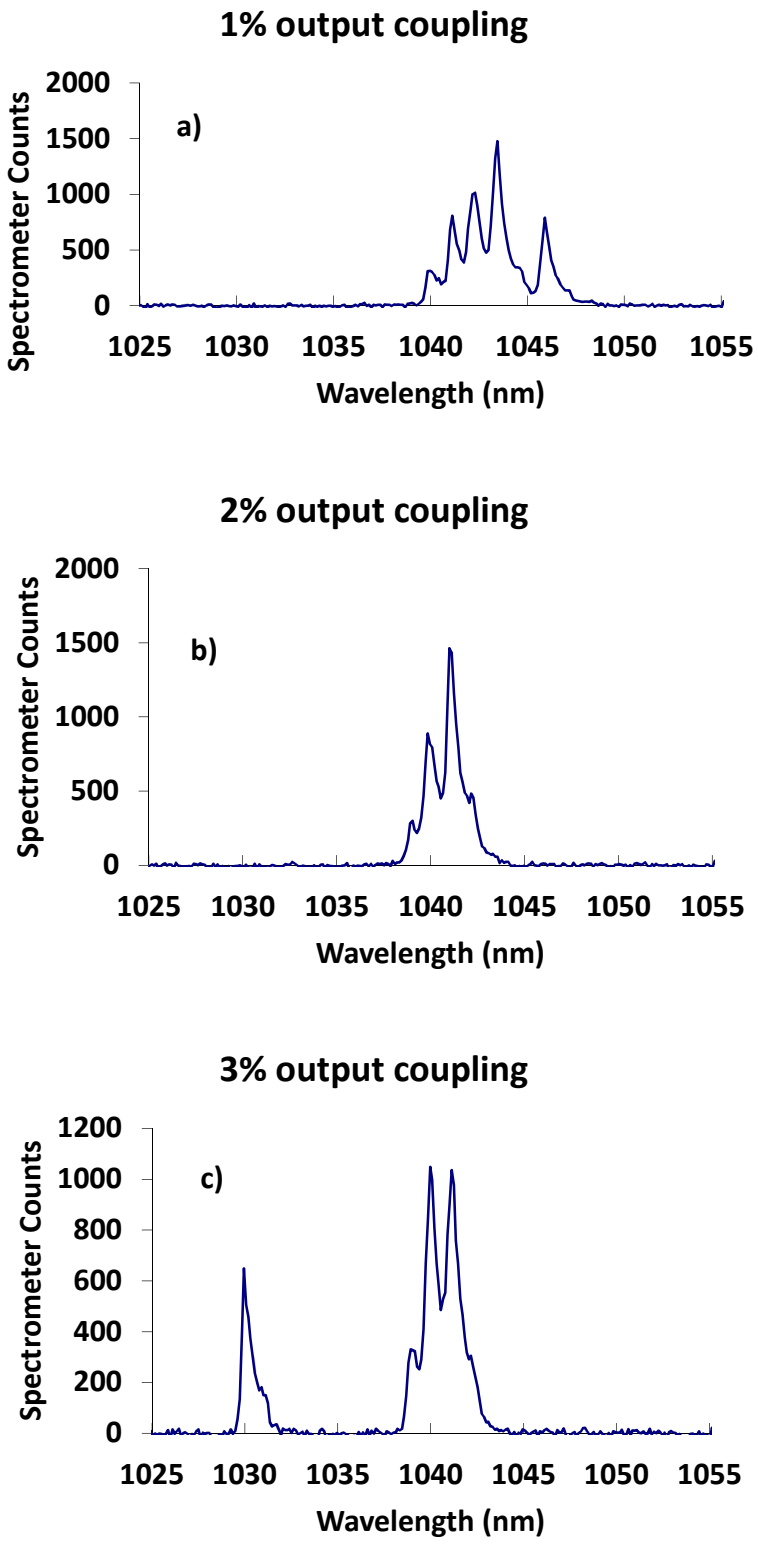

Figure 4.4.b.iii *Spectra of 0.25mm thick, 10 atm. % doped diamond heatspreader sandwich Yb:KYW laser. The spectral output for a) the 1% OC case, b) the 2% OC case and c) the 3% case can be seen. OC stands for output coupler. An Ocean Optics S2000 grating spectrometer with a resolution of 0.5nm was used to monitor the spectral output.*

4.4.c Discussion of Yb:KYW compared to Nd:YVO_4 and Nd:$GdVO_4$

It was found that liquid capillarity could be used to bond diamond heatspreaders to the 0.25mm thick Yb:KYW without causing damage to the gain material whilst the optimal output coupling can be said to be between 1% and 3% transmittance. The output power of the Yb:KYW material was the lowest measured out of all the gain materials examined, similarly the threshold was measured to be the highest out of the materials with respect to incident power. As a quasi-three-level material, Yb:KYW requires a higher pump intensity to obtain threshold when compared to four-level systems such as the vanadates. In this system the pump laser field reabsorption and thermalisation of the upper manifold are two of the primary causes behind the higher thresholds with quasi-three-level materials [2]**.**The estimated absorbed efficiency on the other hand was the highest measured out of the gain materials in this chapter but future work must be taken to verify the pump absorption experimentally to be more certain. If further experimental tests suggest that the estimates of pump absorption used here are reliable, then the high slope efficiencies with respect to absorbed pump power achieved with this make-shift set up suggest that Yb:KYW is a promising material for high power microchip lasers. There are a number of points to consider that rule out a direct comparison between the experimental results obtained for Yb:KYW and the vanadates in this thesis. The Yb:KYW experiments presented in the previous section form a preliminary study into the future use of Yb:KYW as a potential gain material for use in microchip lasers hence the detailed optimisation of parameters such as gain thickness, pump spot radius and material doping could not be carried out in the available time.

In some ways, thermal management is of greater importance to quasi-three-level ytterbium doped materials than four level materials due to the lower laser level forming part of the ground-state manifold and hence being subject to thermalisation of ground state population between the levels of the manifold, However, this is typically more than mitigated by the lower quantum defect and hence lower pump induced heating in ytterbium doped materials. In addition, ytterbium doped materials suffer less from a number of detrimental processes that limit the efficiency of the laser such as upconversion and cross relaxation [1, 2]. Taking this into account along with the potential for further optimisation with regards to

the thickness of the gain material, the dopant concentration and the optimal pump spot radius, it would be worthwhile to assess the power scaling suitability of Yb:KYW in the future for use in thin disk microchip lasers.

4.5. Summary

This chapter has examined a number of different laser gain materials, ultimately for use in a microchip format. To this end, a conventional three mirror air-spaced cavity has been used in order to assess the output powers that these materials offer. The conventional cavity allows for the use of materials that have not been coated for microchip use and so offer a more flexible and cheaper option than having the whole range of materials coated for microchip work.

Two four-level laser crystals, one quasi-three-level laser crystal and two different SDLs were investigated. These were Nd:YVO_4, Nd:$GdVO_4$, Yb:KYW, VG-100 and VG-73. All materials in this section were bonded to a 0.5mm thick type IIa synthetic CVD diamond heatspreader, with the exception of the Yb:KYW material which had a diamond heatspreader bonded to front and rear surfaces.

Drawing from the experimental results in the preceding sections, it was found that Nd:YVO_4 performed better than Nd:$GdVO_4$ and the two SDL structures for use microchip lasers in terms of maximum obtainable output power; however, it was noted that there are limitations to using Nd:YVO_4 that would be apparent when moving towards thin disk laser style thermal management at higher powers. It is therefore recognised that further investigation into materials that permit efficient operation at higher doping levels (e.g. Yb:KYW) will be necessary in order to exploit the power scaling potential that diamond and thin-disk like approaches to thermal management offer when thin pieces of gain material are used.

The next chapter will examine different microchip configurations incorporating diamond heatspreaders. As discussed in this chapter, there are limitations to using the vanadates however Nd:YVO_4 is used as the gain material due to the unavailability of suitable Yb:KYW material at the time.

4.6. References

[1] A. J. Kemp, G. J. Valentine, and D. Burns, "Progress towards high-power, high-brightness neodymium-based thin-disk lasers," *Progress in Quantum Electronics*, vol. 28, pp. 305-344, 2004.

[2] A. Giesen and J. Speiser, "Fifteen years of work on thin-disk lasers: Results and scaling laws," *IEEE Journal of Selected Topics in Quantum Electronics*, vol. 13, pp. 598-609, 2007.

[3] VLOC, "YAG Yttrium Aluminium Garnet Laser Materials", http://www.vloc.com /PDFs/YAGBrochure.pdf, accessed 26/09/2011.

[4] AOTK, "Neodymium-doped Yttrium Vanadate Material", http://www.aotk.com /products-list.asp?id=53, accessed 26/09/2011.

[5] T. Shonai, M. Huguchi, and K. Kodaira, "High-speed float zone growth of heavily Nd-doped YVO_4 single crystals", *Journal of Crystal Growth*, vol. 233, pp. 477-482, 2001.

[6] EKSMA Optics, "Yb:KGW and Yb:KYW crystals", http://www.eksmaoptics.com/ en/p/yb-kgw-and-yb-kyw-crystals-498 , accessed 26/09/2011.

[7] K. Petermann, D. Fagundes-Peters, J. Johannsen, M. Mond, V. Peters, J. J. Romero, S. Kutovoi, J. Speiser, and A. Giesen, " Highly Yb-doped oxides for thin-disc lasers", *Journal of Crystal Growth*, vol. 275, pp.135-140, 2005

[8] Giorgio Turri, Hans P. Jenssen, Francesco Cornacchia, Mauro Tonelli, and Michael Bass, "Temperature-dependent stimulated emission cross section in Nd^{3+}:YVO_4 crystals," *Journal of the Optical Society of America* B, vol 26, pp. 2084-2088, 2009

[9] Y. Sato and T. Taira, "Comparative study on the spectroscopic properties of Nd:GdVO4 and Nd:YVO4 with hybrid process," *IEEE. Journal of Selected Topics in Quantum Electronics,* vol. 11, pp. 613-620, 2005

[10] T. Jensen, V. G. Ostroumov, J.-P. Meyn, G. Huber, A. I. Zagumennyi, and I. A. Scherbakov, "Spectroscopic characterization and laser performance of diode-laser-pumped Nd:$GdVO_4$," *Applied Physics B*, vol. 58, pp. 373–379, 1994

[10] A. I. Zagumennyi, V. A. Mikhailov, V. I. Vlasov, A. A. Sirotkin, V. I. Podreshetnikov, Yu. L. Kalachev, Yu. D. Zavartsev, S. A. Kutovoi, and I. A. Shcherbakov, "Diode-pumped lasers based on GdVO4 crystal," *Laser Physics*, vol. 13, pp. 311-318, 2003

[11] F. Bain, "Yb:Tungstate Waveguide Lasers," Ph.D. Thesis, University of St. Andrews, 2010.

[12] N. V. Kuleshov, A. A. Lagatsky, A. V. Podlipensky, V. P. Mikhailov, and G. Huber, "Pulsed laser operation of Yb-doped $KY(WO_4)_2$ and $KGd(WO_4)_2$," Optics Letters, vol. 22, pp. 1317-1319, 1997

[13] W. Koechner, *Solid State Laser Engineering*, Fifth ed. Berlin: Springer, 1999.

[14] J. Didierjean, E. Herault, F. Balembois, and P. Georges, "Thermal conductivity measurements of laser crystals by infrared thermography. Application to Nd:doped crystals," *Optics Express*, vol. 16, pp. 8995-9010, 2008.

[15] A. A. Kaminskii, K. Ueda, H. J. Eichler, J. Findeisen, S. N. Bagaev, F. A. Kuznetsov, A. A. Pavlyuk, G. Boulon, and F. Bourgeois, "Monoclinic tungstates KDy(WO4)2 and KLu(WO4)2: new χ(3)-active crystals for laser Raman shifters," *Japanese Journal of Applied Physics*, vol. 37, pp. 929–932, 1998

[16] Y. Sato and T. Taira, "The studies of thermal conductivity in $GdVO_4$, YVO_4, and $Y_3Al_5O_{12}$ measured by quasi-one-dimensional flash method," *Optics Express*, vol. 14, pp. 10528-10536, 2006.

[17] P. A. Loiko, K. V. Yumashev, N.V. Kuleshov, G.E. Rachkovskaya, and A.A. Pavlyuk "Thermo-optic dispersion formulas for monoclinic double tungstates K*Re*$(WO_4)_2$ where *Re* = Gd, Y, Lu, Yb," *Optical Materials*, vol. 14, pp. 1688-1694, 2011.

[18] J. E. Hastie, J. M. Hopkins, C. W. Jeon, S. Calvez, D. Burns, M. D. Dawson, R. Abram, E. Riis, A. I. Ferguson, W. J. Alford, T. D. Raymond, and A. A. Allerman, "Microchip vertical external cavity surface emitting lasers," *Electronics Letters*, vol. 39, pp. 1324-1326, 2003.

[19] S. A. Smith, J. M. Hopkins, J. E. Hastie, D. Burns, S. Calvez, M. D. Dawson, T. Jouhti, J. Kontinnen, and M. Pessa, "Diamond-microchip GaInNAs vertical external-cavity surface-emitting laser operating CW at 1315 nm," *Electronics Letters*, vol. 40, pp. 935-937, 2004.

[20] A. J. Maclean, R. B. Birch, P. W. Roth, A. J. Kemp, and D. Burns, "Limits on efficiency and power scaling in semiconductor disk lasers with diamond heatspreaders," *Journal of the Optical Society of America B-Optical Physics*, vol. 26, pp. 2228-2236, 2009.

[21] M. Kuznetsov, F. Hakimi, R. Sprague, and A. Mooradian, "Design and characteristics of high-power (> 0.5-W CW) diode- pumped vertical-external-cavity surface-emitting semiconductor lasers with circular TEMoo beams," *IEEE Journal of Selected Topics in Quantum Electronics*, vol. 5, pp. 561-573, 1999.

[22] S. Calvez, J. E. Hastie, M. Guina, O. G. Okhotnikov, and M. D. Dawson, "Semiconductor disk lasers for the generation of visible and ultraviolet radiation," *Laser & Photonics Review*, 2009.

[23] N. Schulz, J. M. Hopkins, M. Rattunde, D. Burns, and J. Wagner, "High-brightness long-wavelength semiconductor disk lasers," *Laser & Photonics Review*, vol. 2, pp. 160-181, 2008.

[24] A. J. Kemp, A. J. Maclean, J. E. Hastie, S. A. Smith, J. M. Hopkins, S. Calvez, G. J. Valentine, M. D. Dawson, and D. Burns, "Thermal lensing, thermal management and transverse mode control in microchip VECSELs," *Applied Physics B-Lasers and Optics*, vol. 83, pp. 189-194, 2006.

[25] J. Y. Kim, S. Cho, J. Lee, G. B. Kim, S. I. Lim, J. Yoo, K. S. Kim, S. M. Lee, J. Shim, T. Kim, and Y. Park, "A measurement of modal gain profile and its effect on the lasing performance in vertical-external-cavity surface-emitting lasers," IEEE Photon. Technol. Lett. 18, 2496–2498 (2006).

[26] J. Y. Kim, S. Cho, S. M. Lee, G. B. Kim, J. Lee, J. Yoo, K. S. Kim, T. Kim, and Y. Park, “Highly efficient green VECSEL with intra-cavity diamond heat spreader,” Electron. Lett. 43, 105–106 (2007).

[27] A. J. Maclean, "Power Scaling and Wavelength Control of Semiconductor Disk Lasers," Ph.D. Thesis: University of Strathclyde, 2008.

[28] S. Giet, A. J. Kemp, D. Burns, S. Calvez, M. D. Dawson, S. Suomalainen, A. Harkonen, M. Guina, O. Okhotnikov, and M. Pessa, "Comparison of thermal management techniques for semiconductor disk lasers," *Proceedings of SPIE*, vol. 6871, pp. 687115, 2008.

[29] P. Millar, A. J. Kemp, and D. Burns, "Power scaling of Nd:YVO_4 and Nd:$GdVO_4$ disk lasers using synthetic diamond as a heat spreader," *Optics Letters*, vol. 34, pp. 782-784, 2009.

[30] W. P. Risk, "Modeling of longitudinally pumped solid-state lasers exhibiting reabsorption losses," *Journal of the Optical Society of America*., vol. 5, pp. 1412-1423, 1988

[31] A. A. Lagatsky, N. Kuleshov, andV. P. Mikhailov, "Diode-pumped CW lasing of Yb:KYW and Yb:KGW," *Optics Communications*, vol. 165, pp. 71-75, 1988

5. Multi-watt Nd:YVO_4 microchip lasers incorporating diamond heatspreaders

5.1 Introduction

A variety of microchip configurations have been investigated and their potential for power and brightness scaling discussed in this chapter. The microchip configurations investigated within this chapter have been chosen with high power, high brightness applications in mind. It is advantageous to keep the cavity length as short as possible if such lasers are to be used for single frequency and short pulse Q-switched applications in the future. At the same time, other considerations such as ruggedness, compactness, ease of manufacture and overall cost must be taken into consideration. Whilst the previous chapter highlighted the potential of Yb:KYW as a gain material for use in microchip lasers, the work done in this chapter was completed before suitable Yb:KYW material became available and thus Nd:YVO_4 was used in most of the microchip configurations examined in this chapter. This chapter will examine four different microchip geometries; a Nd:$GdVO_4$ "millichip" laser configuration, a Nd:YVO_4 microchip laser incorporating an extra-cavity diamond heatspreader, a Nd:YVO_4 microchip laser incorporating an intra-cavity heatspreader and finally a Nd:YVO_4 microchip "diamond sandwich" configuration.

For the case of a Nd:YVO_4 microchip laser incorporating no heatspreader, work carried out by a colleague[1] indicates that for the case of a 3x3x0.5mm long 3 atm. % doped, a-cut Nd:YVO_4 microchip laser operating at a wavelength of 1064nm, the maximum output power achievable is measured in hundreds of milliwatts. A 25W fibre-coupled diode laser (100µm core-diameter, 0.22NA) operating at a wavelength of 808nm was used to pump the Nd:YVO_4 crystal. The crystal facet (3x3mm) nearest the pump was coated for 10% transmission output at the lasing wavelength of 1064nm and for >90% reflection at 808nm; the opposite crystal facet (3x3mm) was coated for high reflection and high transmission at wavelengths of 1064nm and 808nm respectively. The crystal was mounted in a water-cooled brass block whereby the water was cooled to 9.5 °C. The gain material was sandwiched between Indium

[1] The experimental work described in section 5.1 was carried out by Dr Patricia Millar and not by the author. It is included here for as a baseline comparison for work subsequently carried out by the author and described later in this chapter.

foil of 0.125mm thickness to ensure more effective thermal contact with the brass mount similar to that shown in figure 3.2.ii in chapter 3. An aperture in the indium allowed for incident and output light to pass through. Adjustment of the heatsink temperature of the diode-laser pump was required due to the shift in operating wavelength with increasing input current to maintain a spectral match with the absorption feature in Nd:YVO_4. A pump spot of 220µm was used to pump the microchip at an angle of 22 degrees to the normal and the power transfer can be seen in figure 5.1.i.

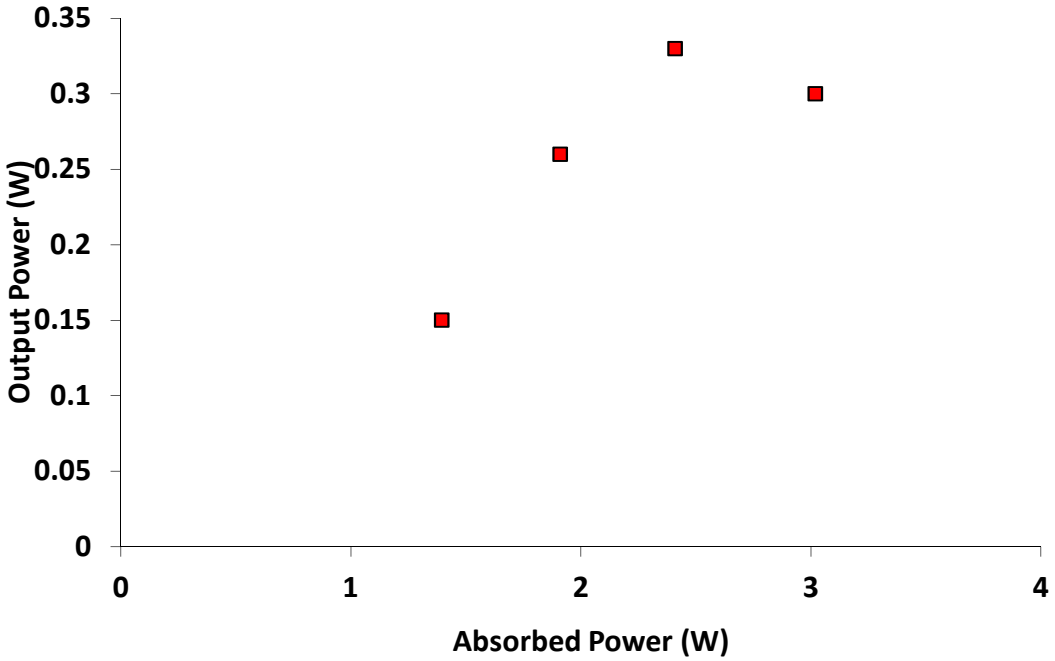

Figure 5.1.i *Output power of 1 atm. % Nd:YVO_4 microchip laser plotted against absorbed power. This data was taken by Dr Patricia Millar.*

As can be seen, the maximum output power achieved was 0.33W before thermal fracture occurred and it can be seen that the power decreases before laser oscillation ceases. It is clear that better thermal management is required to obtain higher output powers from Nd:YVO_4 and so a heatspreader approach will be adopted in this chapter.

As the output power of a microchip laser is increased, maintenance of good beam quality typically becomes an issue due to aberrations of the thermal lens at higher pump power. Hence this chapter will also discuss how best to improve output powers and beam

brightness. The microchip laser configuration examined in the next section, however, does not employ a heatspreader for thermal management unlike the rest of the lasers in subsequent sections. This serves as a comparison to the heatspreader approach adopted throughout this thesis.

5.2 Millimetre cavity length monolithic laser: the "Millichip" format

5.2.a Background

In 2008 Liao *et al* achieved an output power of 10.2W at an incident input power of 23.9W using an end-pumped Nd:$GdVO_4$ microchip laser in continuous wave operation operating at a pump spot radius of 260μm [1]. The slope efficiency and threshold with respect to incident pump power were 42.6% and 0.21W respectively.

The gain medium was a 0.5% atm. doped, 3x3x1.5mm long a-cut Nd:$GdVO_4$ crystal. The crystal facet nearest the pump was coated for high reflectivity at 1064nm and for high transmission at 808nm. The opposite crystal facet was coated for 1% transmission output coupling at the lasing wavelength of 1064nm. The crystal was mounted in a water-cooled copper block using indium foil at the interfaces. The cooling water temperature was 12°C. By analogy to the term 'microchip', this millimetre cavity length format will be referred to henceforth in this thesis as the "millichip" format for the purposes of convenience and brevity.

Although, arguably not a microchip laser in the strictest sense in that the length of the crystal along the crystal axis exceeds 1000μm, 10.2W of CW output power is one of the highest output powers achieved by a microchip laser. The size of the device as a whole (including the pump laser) is comparable to other microchip set-ups and the absence of a heatspreader on the pump-end facet ensures a higher degree of ruggedness and a lower degree of complexity in device fabrication compared to a thinner microchip incorporating a heatspreader. It is more expensive compared to a normal microchip laser of sub-millimetre length incorporating no heatspreader however. In addition, the millimetre cavity length

format is exclusively edge cooled and hence it cannot expect to benefit from the advantages of face-cooling associated with the heatspreader approach adopted in this thesis.

With regards to beam quality, whilst the authors noted that higher order transverse modes were present in the output beam, no quantitative assessment – such as a measurement of the M^2 parameter – was reported. To assess whether or not the "millichip" approach offers superior performance in terms of beam brightness than the face-cooled microchip approach described in chapter 2 of this thesis, it is necessary to repeat the same experiment using similar experimental parameters.

5.2.b Characterisation of the "Millichip"

A 25W fibre-coupled diode laser (100µm fibre core-diameter, 0.22NA) operating at a wavelength of 808nm was used to pump the 3x3x1.5mm long 0.5 atm. % doped, a-cut Nd:$GdVO_4$ crystal. The crystal facet nearest the pump was coated for high reflectivity at the lasing wavelength of 1063nm and high transmission at the pump wavelength of 808nm. The opposite crystal facet was coated for 1% transmission output coupling at the lasing wavelength of 1064nm. Indium foil of 0.125mm thickness was placed around the four 3x1.5mm facets of the crystal. The crystal was mounted in a water-cooled brass block and the water was cooled to 9.5 °C. Adjustment of the heatsink temperature of the diode-laser pump was required to counteract the shift in operating wavelength with increasing input current. The pump optics were chosen to provide calculated pump spot radii ($1/e^2$) of 69µm, 114µm, 150µm and 200µm, enabling optimisation of the pump spot radius. The crystal was end-pumped as shown in figure 5.2b.i to a maximum incident power of 9W.

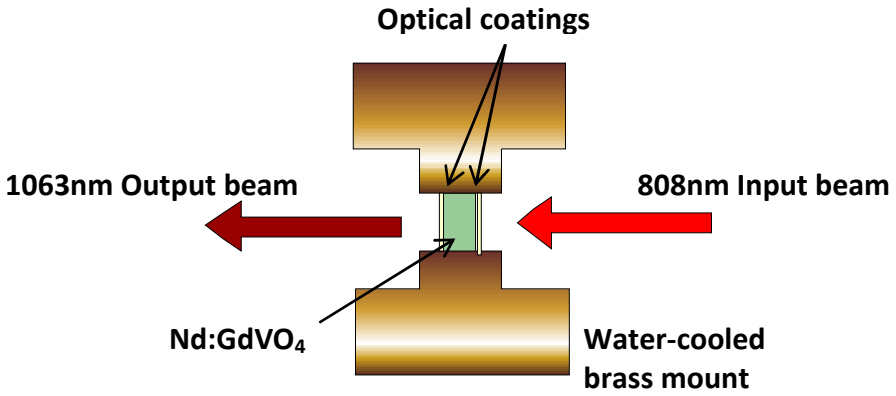

Figure 5.2.b.i *Diagram of "Millichip" experimental arrangement used in this section.*

The output power of the laser was measured for each pump spot radius and the results can be seen in figure 5.2bii. The maximum CW output power achieved was 3.7W at an incident pump power of 9W using a pump spot radius of 114µm. The slope efficiency and threshold, both with respect to incident pump power, were 43% and 0.41W respectively. The slope efficiency and threshold with respect to absorbed pump power were estimated to be 51% and 0.31W respectively.

Using a Dataray Inc Beamscope-P7 (automated scanning slit beam profiler), the M^2 parameter of the output beam was measured at various output powers for each pump spot radius and the results can be seen in figures 5.2b.iii to 5.2b.iv. Using a pump spot radius of 69µm and at input power of 9W, an M^2 of 5.16 and 4.33 was achieved in the horizontal and vertical axes respectively, the lowest M^2 achieved compared to the rest of the pump spot radii. For the pump spot radius of 114µm which gave the highest output power, an M^2 of 8 and 6.5 was measured in the horizontal and vertical axes.

The geometric means of the fundamental cavity mode radius and actual mode radius of the "millichip" at maximum output power were calculated to be 45µm and 106µm for the 69µm pump waist radius case respectively. The cavity mode calculations were inferred by measuring the M^2 and beam diameter of the output beam at a known distance and then calculating the cavity mode radius that would be required to produce the beam diameter at

the set distance. The fundamental cavity mode radius was then calculated by dividing the actual cavity mode radius by the M^2 parameter of the beam [2].

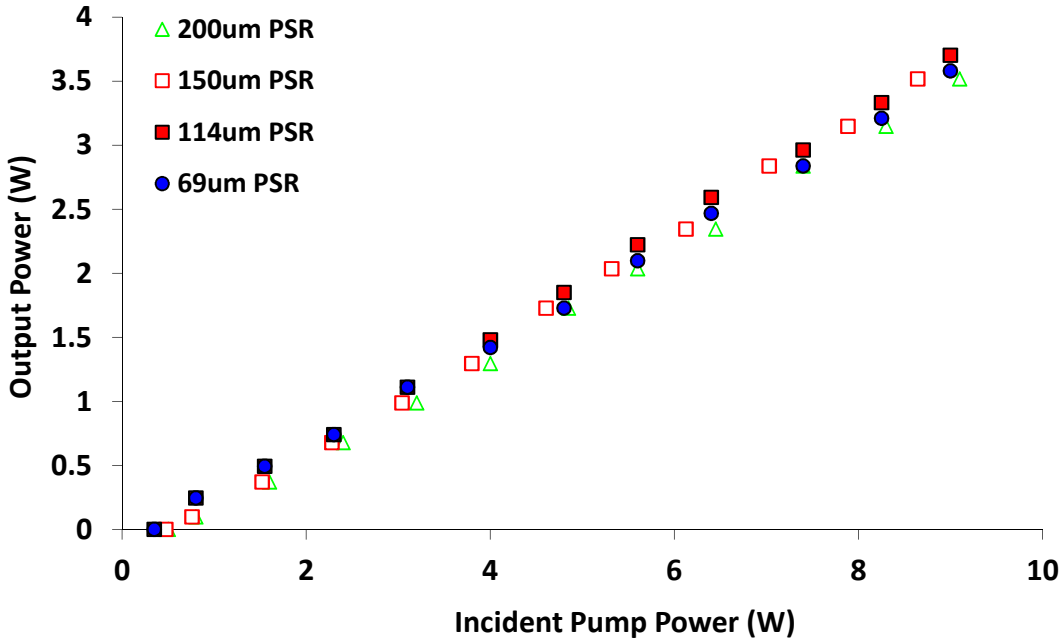

a)

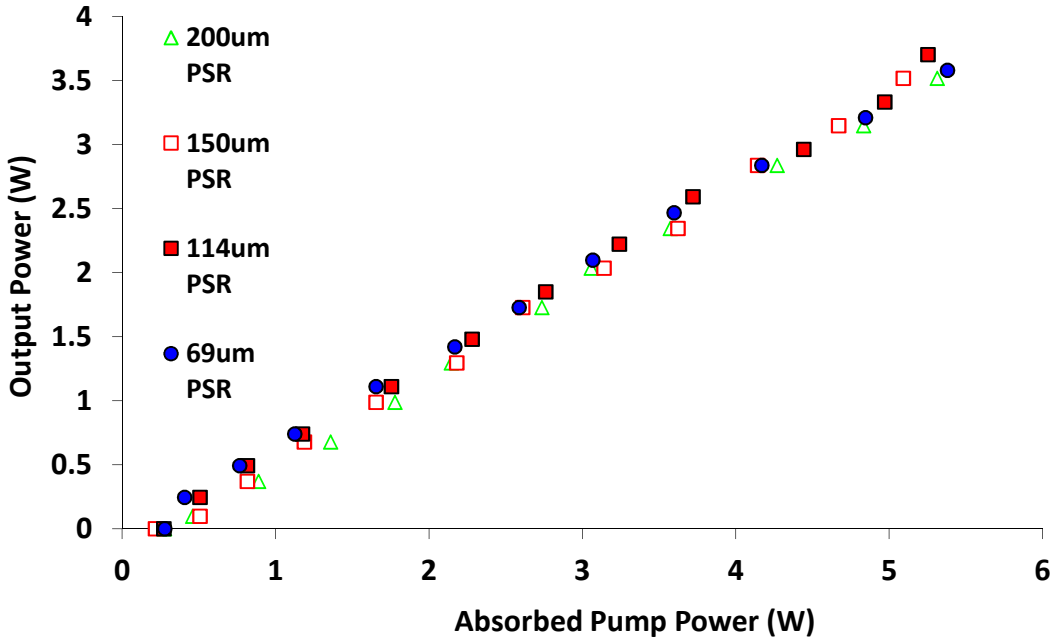

b)

Figure 5.2.b.ii *Output power of 0.5 atm. % Nd:$GdVO_4$ laser plotted against a) incident power and b) absorbed power. PSR stands for pump spot radius.*

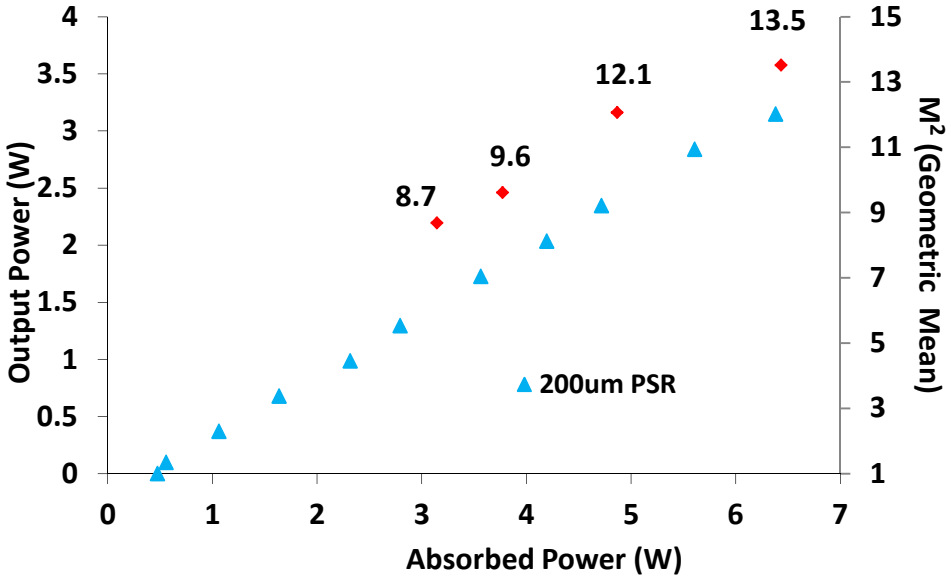

Figure 5.2.b.iii *M^2 data (geometrical mean of the values in the horizontal and vertical planes) of a 0.5 atm. % Nd:$GdVO_4$ laser vs. incident power for a 200µm pump spot radii. The output power has been overlaid for reference. PSR stands for pump spot radius.*

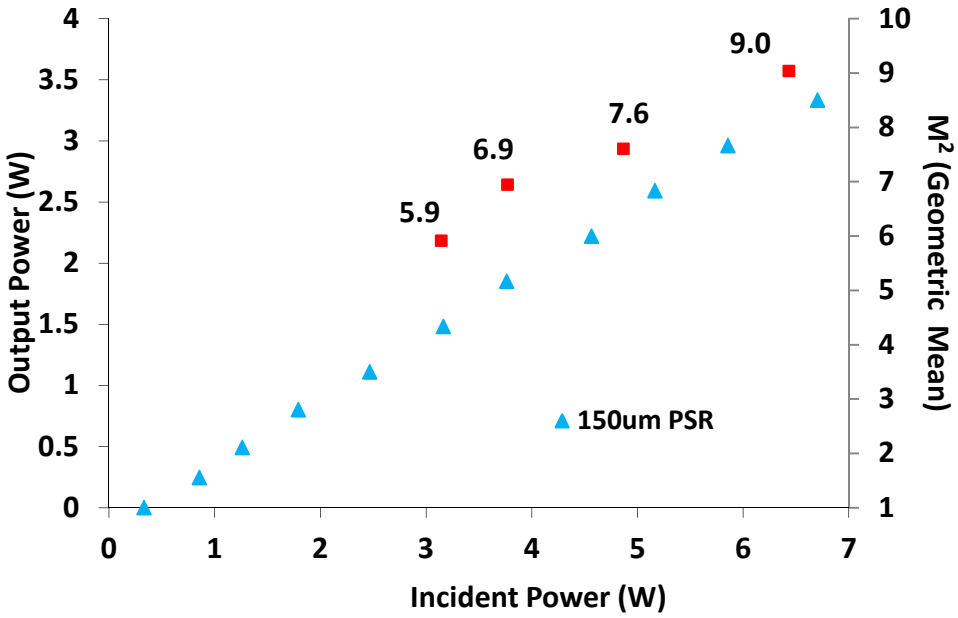

Figure 5.2.b.iv *M^2 data (geometrical mean of the values in the horizontal and vertical planes) of a 0.5 atm. % Nd:$GdVO_4$ laser vs. incident power for a 150µm pump spot radii. The output power has been overlaid for reference. PSR stands for pump spot radius.*

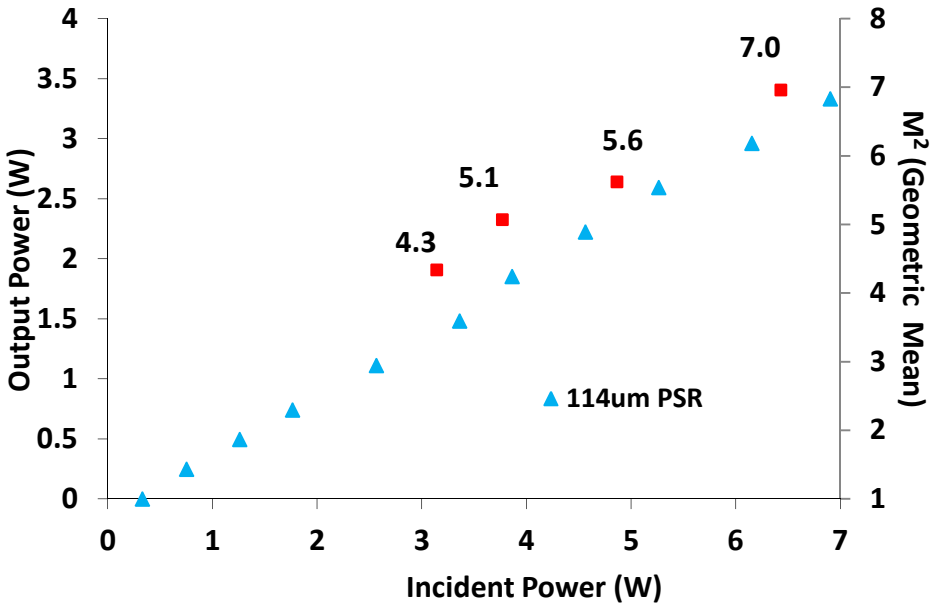

Figure 5.2.b.v *M^2 data (geometrical mean of the values in the horizontal and vertical planes) of a 0.5 atm. % Nd:$GdVO_4$ laser vs. incident power for a 114µm pump spot radii. The output power has been overlaid for reference. PSR stands for pump spot radius.*

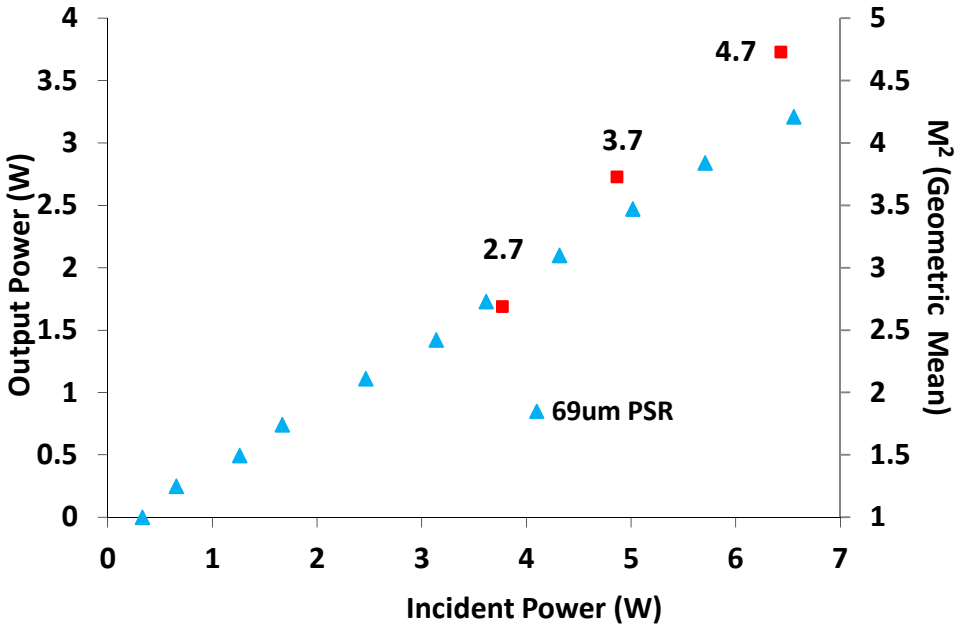

Figure 5.2.b.vi *M^2 data (geometrical mean of the values in the horizontal and vertical planes) of a 0.5 atm. % Nd:$GdVO_4$ laser vs. incident power for a 69µm pump spot radii. The output power has been overlaid for reference. PSR stands for pump spot radius.*

The fundamental cavity mode radius is smaller than the pump waist radius and poor beam quality is hence to be expected. However, the actual cavity mode radius is estimated to be significantly larger than the pump spot radius which is unexpected. One might expect higher order transverse mode to oscillate at higher pump powers and fill the pump region, but not necessarily to significantly overfill it. One possible reason for this is that the absorption length of the 0.5 atm. % doped Nd:$GdVO_4$ crystal (0.8mm where the pump is polarised along the c-axis) exceeds the Rayleigh range of the pump source (0.5mm) and thus the pump spot radius averaged across the absorption length will be greater than the waist radius. This means that the difference between the pump and fundamental mode radii is larger than expected from the pump waist and so poorer beam quality is to be expected.

In terms of the ellipticity of the output beam for the 69µm pump waist radius, an M^2 of 5.2 and 4.3 was measured in the horizontal and vertical axes. The actual mode radii taking the M^2 parameter of each axis into account were estimated to be 107µm and 97µm for the vertical and horizontal axes; the fundamental cavity mode radius of the "millichip" at maximum output power was then inferred to be 45µm for the vertical and horizontal axes. The M^2 of the output beam was measured with respect to output power at a fixed pump spot radius of 69µm and for each input power the diameter of the output beam was measured at a known distance from the crystal. From this data the ratio of pump mode to fundamental cavity mode was inferred. The results can be seen in figure 5.2b.vii and suggest that the M^2 is increasing with pump power possibly due to an decreasing thermal lens focal length which acts to degrade the overlap between the fundamental cavity and pump modes.

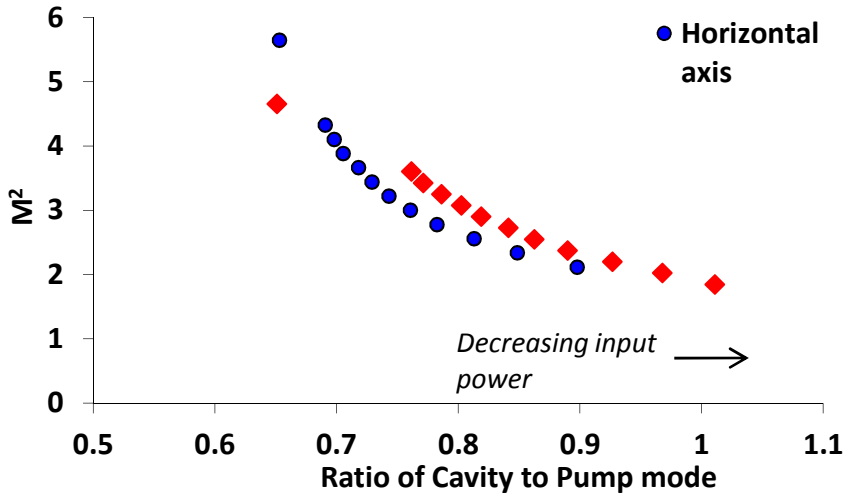

Figure 5.2.b.vii *Plot of M^2 vs. fundamental cavity to pump mode ratio (i.e. the fundamental cavity mode radius / pump spot radius) of a 0.5 atm. % Nd:$GdVO_4$ microchip laser as the input power is decreased.*

5.2.c Summary

Although all pump spot radii investigated gave similar output powers as shown in table 5.2.c.i, the pump spot radius optimisation experiments indicate that in terms of maximum output power attainable, a pump spot radius between 69µm and 150µm is desirable. In this case the 114µm pump spot radius was marginally the best. To achieve greater output powers a face-cooled heatspreader approach would provide improved thermal management; however, the improvement would not be as pronounced as the effectiveness of face-cooling drops as the crystal gets thicker due to the greater distance that the heat must be extracted over through the cooled surfaces.

Pump Spot Radius	Maximum P_{out}	Maximum Incident/Absorbed Slope Efficiency	Incident/ Absorbed Threshold	M^2 at 6.4W absorbed (Geometric mean)	Brightness at max. output power
69µm	3.58W	41% / 52%	0.36W /0.28W	4.7	0.61W/µm^2/sr
114µm	3.7W	43% / 51%	0.39W / 0.31W	7.2	0.28W/µm^2/sr
150µm	3.58W	44% / 53%	0.44W /0.32W	9.0	0.17W/µm^2/sr
200µm	3.52W	41% / 53%	0.5W /0.37W	13.5	0.07W/µm^2/sr

Table 5.2.c.i *Summary table of laser characterisation of a 0.5 atm. % Nd:$GdVO_4$ microchip laser*

The highest brightness of 0.61W/µm^2/sr is achieved at the smallest pump spot radius tested: 69µm. Indeed the brightness achieved dropped monotonically with increasing pump

waist radius. This is because, whilst the output power achieved is a relatively weak function of pump spot radius, the beam quality drops rapidly as the pump waist radius is increased.

By lengthening the Nd:$GdVO_4$ microchip, the cavity mode could be increased to provide better cavity mode/pump mode overlap, potentially increasing the brightness of the output. This approach, however, has the drawback of increasing the size and cost of the microchip and causes the cavity to become unstable at the point at which the cavity length exceeds twice the focal length of the thermal lens. Increasing the cavity length is also detrimental for achieving single frequency operation and short pulses from a Q-switched set-up. In addition, with increasing crystal length, a greater degree of parallelism is required between the mirror-coated surfaces [3], increasing the cost and complexity of manufacture from the crystal manufacturers. Whereas parallel processing could be envisaged for a thin wafer, prepared and coated and then diced into multiple microchips, each millichip would need to be polished and coated individually.

An alternative would be to try to decrease the pump spot radius to match the cavity mode but again there are drawbacks as the pump spot radius is decreased, the intensity of the incident pump is increased, ultimately leading towards the crystal fracture limit, reducing the effectiveness of this approach. It thus seems likely that there will be limitations to how far the brightness of microchip lasers can be scaled using the millichip approach.

An alternative approach to increasing the cavity mode radius is to decrease the thermal lensing within the microchip; face-cooling via a heatspreader and using thinner samples of gain material are means to do this and this approach will be examined in the next section.

5.3 Microchip laser with an extra-cavity heatspreader

5.3.a Introduction

A 25W fibre-coupled diode laser (100µm core-diameter, 0.22NA) operating at a wavelength of 808nm was used to pump a 3x3x0.5mm thick 3 atm. % doped, a-cut Nd:YVO_4 crystal (fig. 5.3.1). A 3 atm. % doped crystal was used to due to the unavailability of a suitable 1 atm. % doped sample. The crystal facet (3x3mm) nearest the pump was coated for 10% transmission output at the lasing wavelength of 1064nm and for >90% transmission at 808nm; the opposite crystal facet (3x3mm) was coated for high reflection and high reflection at wavelengths of 1064nm and 808nm respectively. A 0.5mm thick, type IIa single crystal synthetic CVD diamond heatspreader of radius 2mm was bonded to the crystal facet nearest the pump and mounted in a water-cooled brass block whereby the water was cooled to 9.5 °C. The gain material and heatspreader composite was sandwiched between indium foil of 0.125mm thickness to ensure more effective thermal contact with the brass mount. An aperture in the indium allowed for incident and output light to pass through. Adjustment of the heatsink temperature of the diode-laser pump was required with increasing input current to keep the operating wavelength constant. The pump optics were chosen to provide pump spot radii of 69µm, 114µm, 150µm and 200µm to enable optimisation of the pump spot radius. The crystal was end-pumped as shown in figure 5.3.a.i to a maximum incident power of 9W.

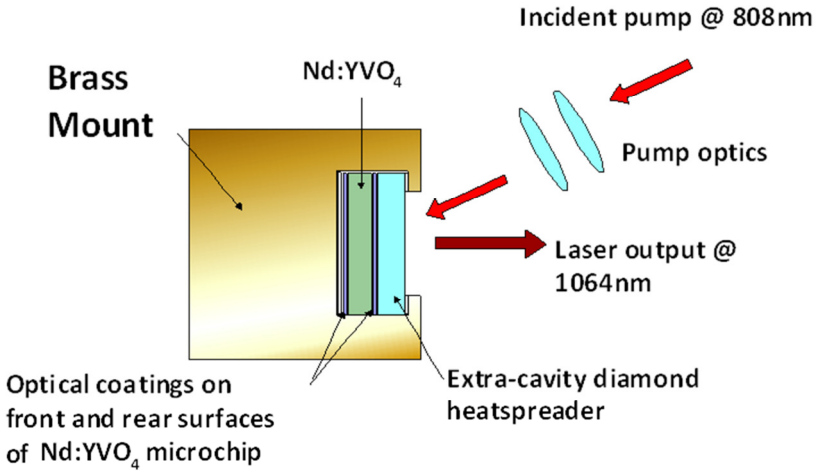

Figure 5.3.a.i *Diagram of experimental arrangement of extracavity diamond Nd:YVO_4 microchip laser used in this section.*

5.3.b Characterisation of microchip laser with an extracavity diamond heatspreader

The output power of the laser was measured for each pump spot radius and the results can be seen in figure 5.3.b.i. The maximum CW output power achieved was 3.1W at an incident pump power of 8.9W using a pump spot radius of 69µm. The slope efficiency and threshold, both with respect to incident pump power were 44.4% and 0.24W respectively. The slope efficiency and threshold, with respect to absorbed pump power was 63% and 0.14W respectively. The spectrum of the laser can be seen in figure 5.3.b.ii.

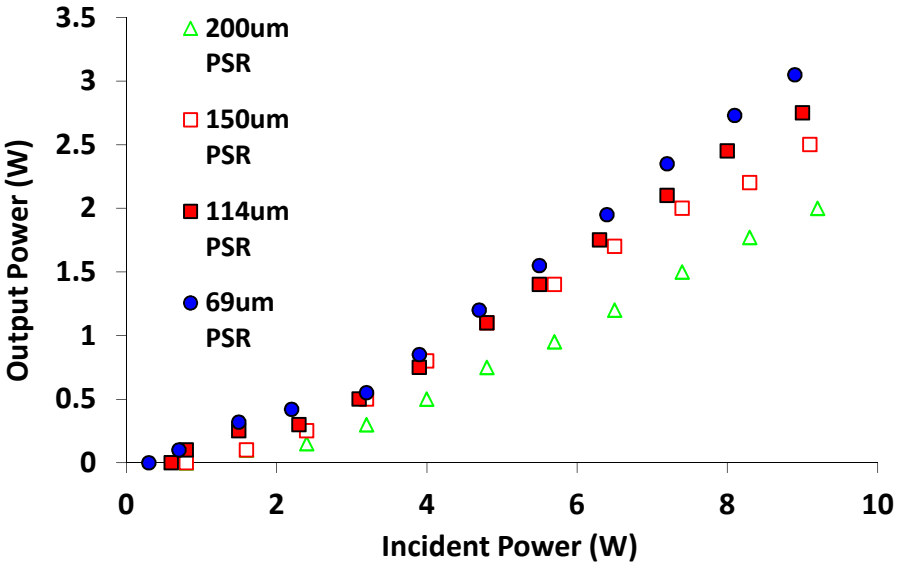

a)

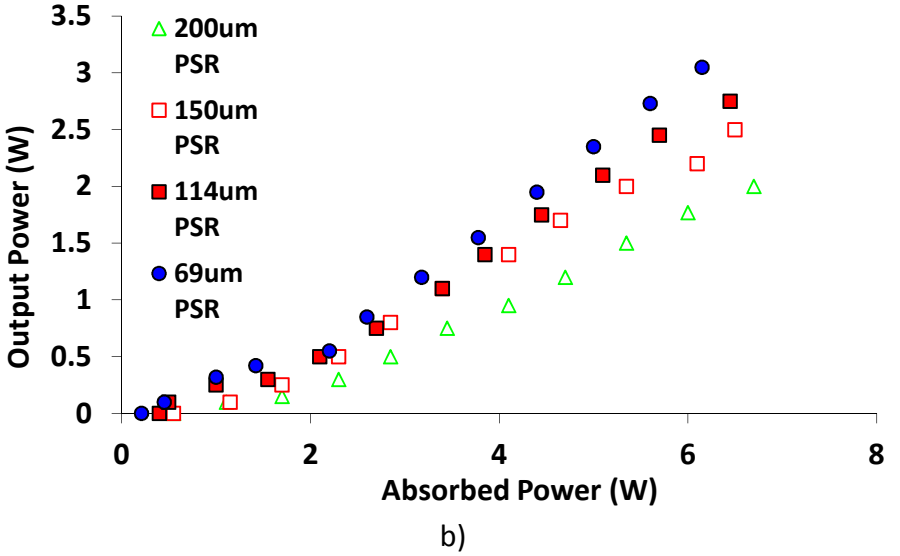

b)

Figure 5.3.b.i *Output power of 1 atm. % Nd:YVO_4 microchip laser incorporating an extracavity diamond heatspreader, plotted against a) incident power and b) absorbed power. PSR stands for pump spot radius.*

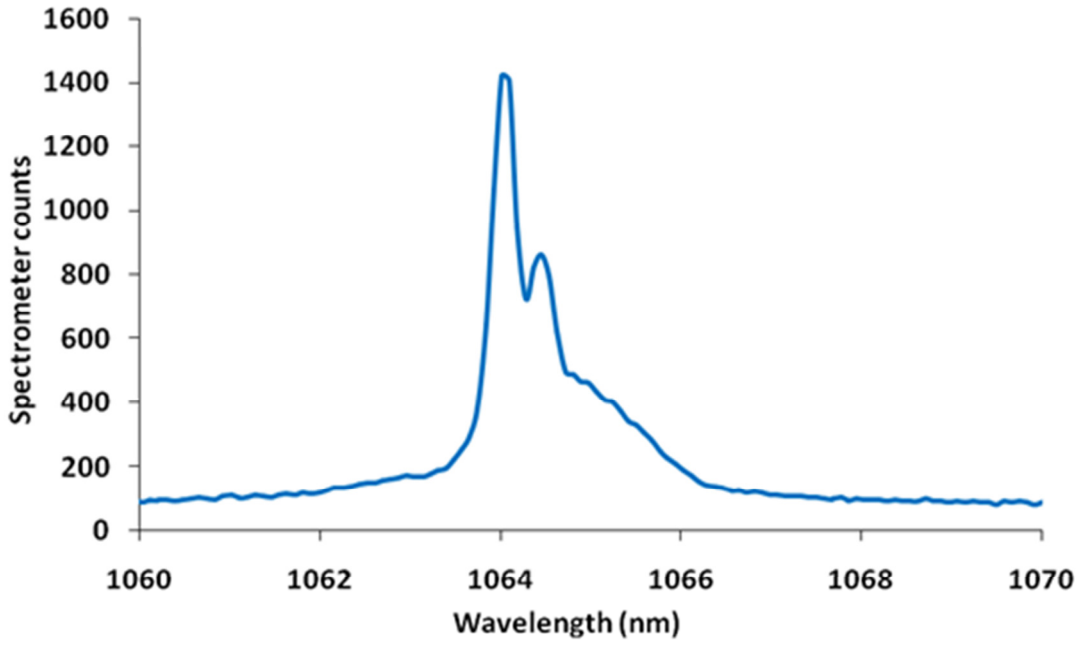

Figure 5.3.b.ii *Spectrum of a 1 atm. % Nd:YVO_4 – microchip laser incorporating an extracavity diamond heatspreader. An Ocean Optics S2000 grating spectrometer with a resolution of 0.5nm was used.*

A Dataray Inc Beamscope-P7 (automated scanning slit beam profiler) was used to measure the M^2 of the laser output at various output powers for each pump spot radius; the results are displayed in figure 5.3.b.iii. At a fixed output power of 1.9W, achievable across the range of pump spot radii used, 69µm proved to be the best radius in terms of lowest M^2, achieving a geometrically averaged M^2 of 6.4. Using a pump spot radius of 69µm and a maximum input power of 9W, the output power was 3.1W and an M^2 of 11.85 and 7.16 was achieved in the horizontal and vertical axes respectively, the lowest M^2 achieved compared to the rest of the pump spot radii (fig 5.3.b.iii). Whilst the M^2 generally reduced with reducing pump spot radius, the horizontal M^2 is essentially unchanged between 114µm and 69µm at both input power settings. This might be the result of anisotropy of the thermal lens within the Nd:YVO_4 crystal due to the different values of thermal conductivity along the *a* and *c* axes of the crystal.

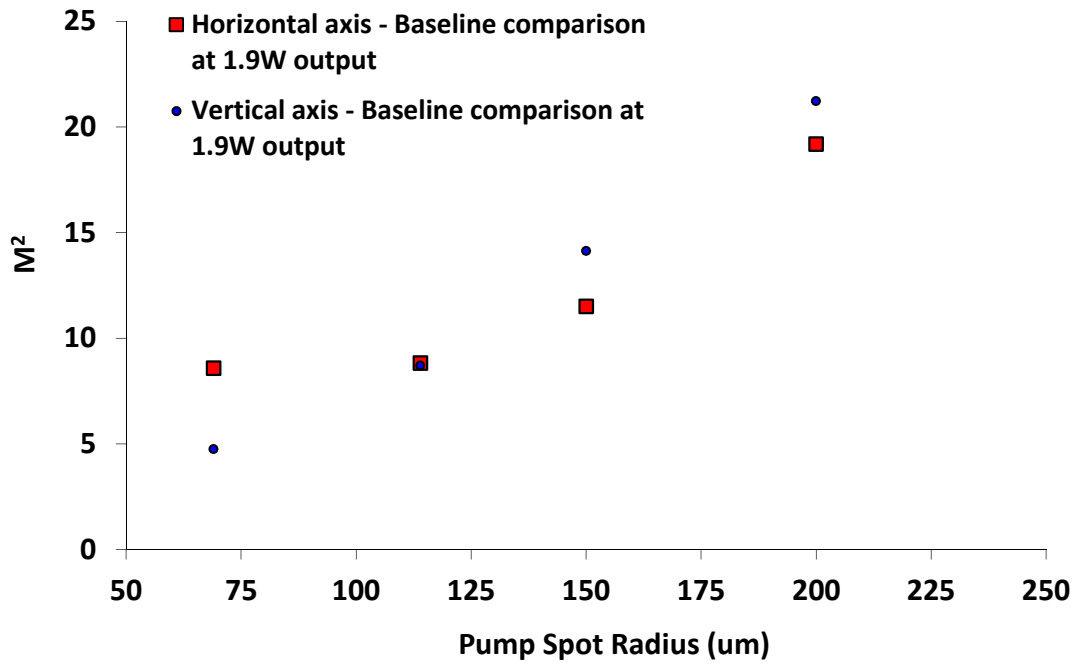

a)

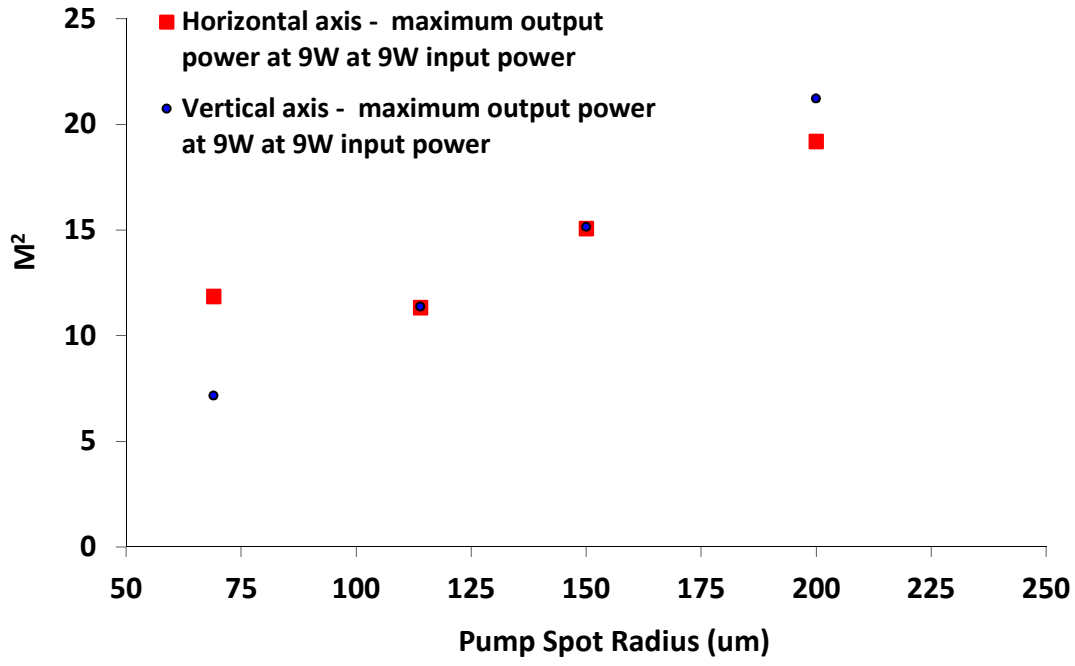

b)

Figure 5.3.b.iii *Plot of M^2 vs. pump spot radius of a 1 atm. % Nd:YVO_4 microchip laser incorporating an extracavity diamond heatspreader at a) a fixed output power of 1.9W and b)at the maximum output power achieved for the case of each pump spot radius.*

5.3.c Summary

Pump Spot Radius	Maximum P_{out}	Maximum Incident/Absorbed Slope Efficiency	Incident/ Absorbed Threshold	M^2 at maximum output power (Geometric mean)	Brightness
69µm	3.1W	36% / 52%	0.3W /0.21W	9.2	0.13W/µm^2/sr
114µm	2.7W	33% / 46%	0.6W / 0.4W	11.3	0.07W/µm^2/sr
150µm	2.5W	32% / 44%	0.8 /0.55W	15.1	0.04W/µm^2/sr
200µm	2.0W	25% / 34%	0.84W /0.57W	20.1	0.02W/µm^2/sr

Table 5.3.c.i *Summary table of laser characterisation of a 1 atm. % Nd:YVO_4 microchip laser incorporating an extracavity diamond heatspreader.*

The results of the pump spot optimization can be seen table 5.3c.i. It is apparent that the pump spot radius of 69µm achieves the highest output power compared to the other radii investigated. In terms of incident and absorbed slope efficiency, the 69µm pump spot radius remains the optimal choice. To improve the efficiency, the uncoated diamond heatspreader could be anti-reflection coated at the pump wavelength of 808nm to reduce Fresnel losses caused by the high refractive index of diamond.

At an input power of 9W, the M^2 parameters for each output beam at each pump spot radius were determined and showed that the 69µm pump spot radius achieved the lowest geometrically averaged M^2 of 9.2. The 69µm pump spot radius achieved a brightness of 0.13W/µm^2/sr. By contrast the next best pump spot size 114µm achieved a brightness of 0.07W/µm^2/sr.

The fundamental cavity mode radius was not measured in the 69µm pump spot radius case unfortunately but was inferred for the 200µm pump spot radius case and was found to be 40µm. It can be assumed that the fundamental cavity mode radius for the 69µm pump spot radius case is <40µm due to the increase in pump intensity as the pump spot radius is reduced. To improve the pump/cavity mode overlap, the thermal lens could be reduced by improving the thermal management of the laser. One method of improving the thermal management of the laser would be to move towards thinner gain crystals so that the gain thickness is smaller than that of the pump spot radius. Another route to improve the pump/cavity mode overlap is to increase the length of the cavity to increase the

fundamental cavity mode radius for a given thermal lens strength. To do so, an intracavity heatspreader approach can be adopted as will be explained in the next section.

5.4 Microchip laser with an intra-cavity diamond heat spreader

5.4.a Introduction

A 25W fibre-coupled laser diode (100µm core-diameter, 0.22NA) operating at a wavelength of 808nm was used to pump a 0.5mm thick 1 atm. % doped, a-cut Nd:YVO_4 crystal. The rear facet of the crystal was coated for high reflection at the wavelengths of 1064nm and 808nm respectively. The crystal was bonded to a 0.5mm thick, type IIa single crystal synthetic CVD diamond heatspreader of radius 2.3mm and mounted in a water-cooled brass block whereby the water was cooled to 9.5 °C. The diamond facet closest to the pump source was coated for 10% transmission at the laser wavelength of 1064nm and for >90% transmission at 808nm. The gain material and heatspreader composite was sandwiched between Indium foil of 0.125mm thickness to ensure more effective thermal contact with the brass mount. An aperture in the indium allowed for incident and output light to pass through. Adjustment of the heatsink temperature of the diode-laser pump was required due to keep the output wavelength constant for increasing input current. As in the case of the microchip laser with an extracavity diamond heatspreader, the pump optics were chosen to provide pump spot radii of 69µm, 114µm, 150µm and 200µm to enable pump spot radius optimisation. The crystal was end-pumped as shown in figure 5.4a.i to a maximum incident power of 9W.

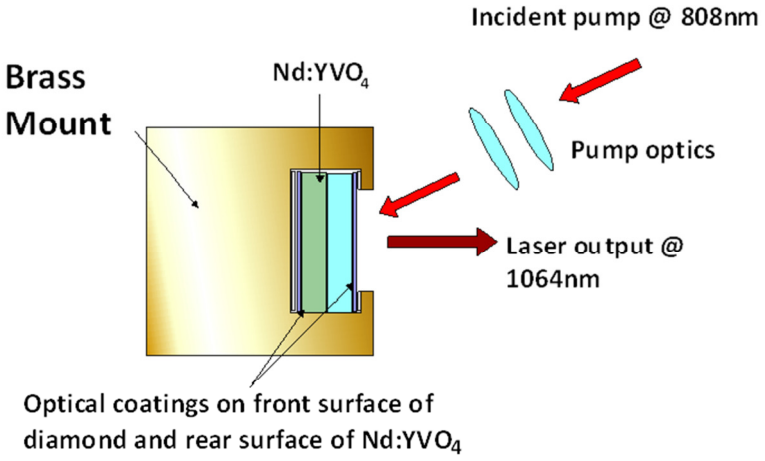

Figure 5.4.a.i *Diagram of experimental arrangement of a 1 atm. % Nd:YVO_4 microchip laser incorporating an intracavity diamond heatspreader laser used in this section.*

5.4.b Characterisation of microchip laser with an intra-cavity diamond heatspreader

The output power of the laser was measured for each pump spot radius and the results can be seen in figure 5.4.b.i. The maximum CW output power achieved was 3.0W at an incident pump power of 8.5W using a pump spot radii of 69µm and 114µm. For the 69µm pump spot radius, the slope efficiency and threshold, both with respect to incident pump power were 37% and 0.36W respectively. The slope efficiency and threshold with respect to absorbed pump power were 55% and 0.24W respectively.

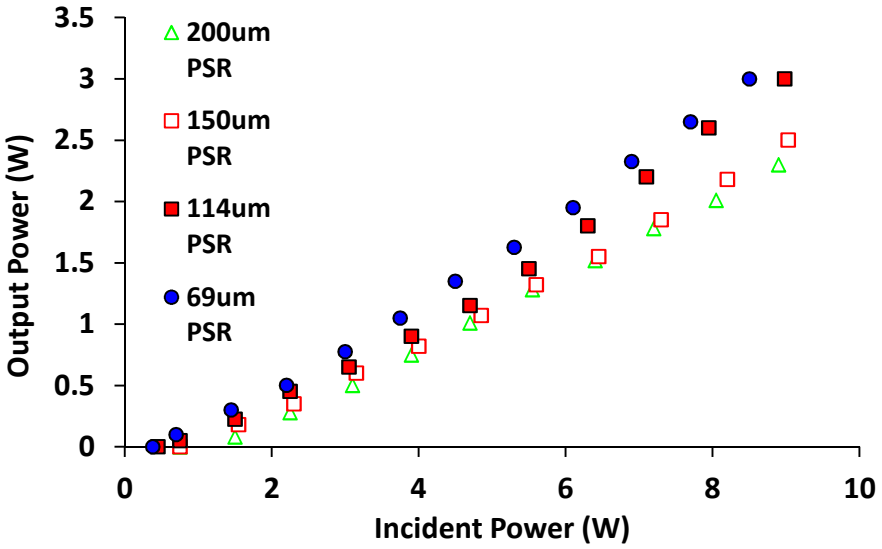

a)

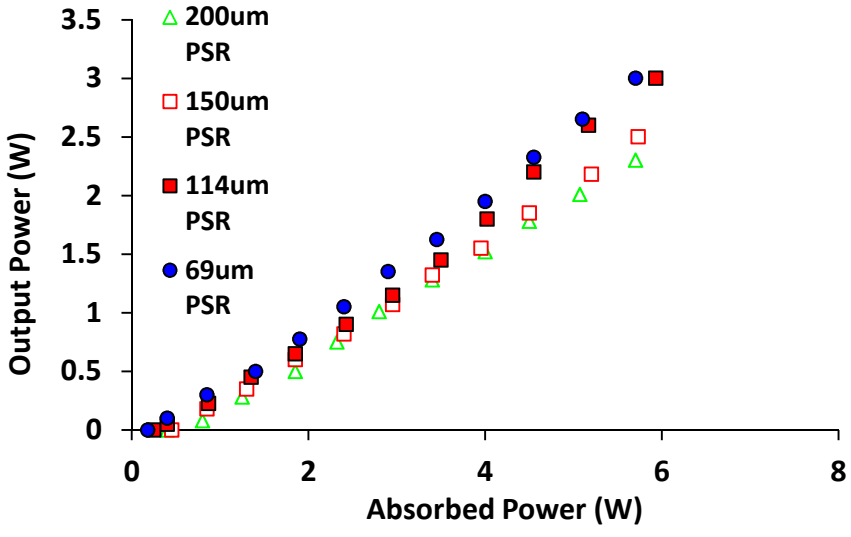

b)

Figure 5.4.b.i *Output power of 1atm. % Nd:YVO_4 microchip laser incorporating an intracavity diamond heatspreader, plotted against a) incident power and b) absorbed power. PSR stands for pump spot radius.*

5.4.c Beam Quality

The output of the beam possessed a comet-tail appearance which evolved as the pump power was increased. This was indicative of a possible lack of parallelism within the cavity, formed by the coated rear surface of the Nd:YVO_4 crystal and the coated facet of the diamond heatspreader [3]. A complementary metal–oxide–semiconductor (CMOS) camera was used to record the transverse profile of the output beam. For each pump spot radius, the output profiles were recorded as the pump power was increased as can be seen in figure 5.4.c.i. and figure 5.4.c.ii.

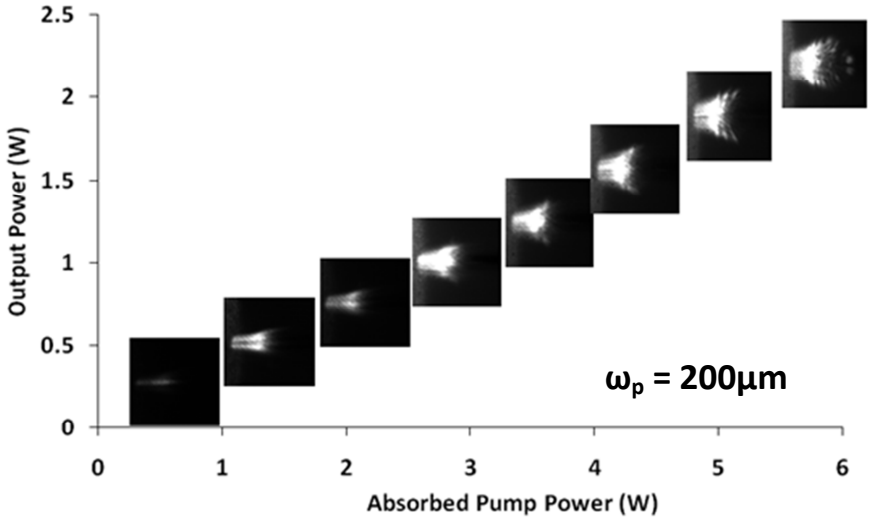

a)

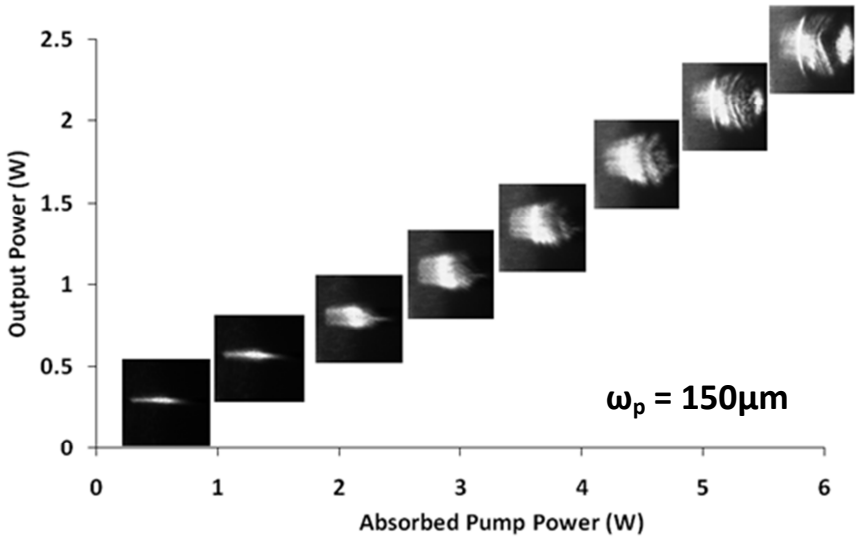

b)

Figure 5.4.c.i *Transverse beam profile output of 1 atm. % Nd:YVO_4 microchip laser incorporating an intracavity diamond heatspreader, for pump spot radii of a) 200µm and b) 150µm.*

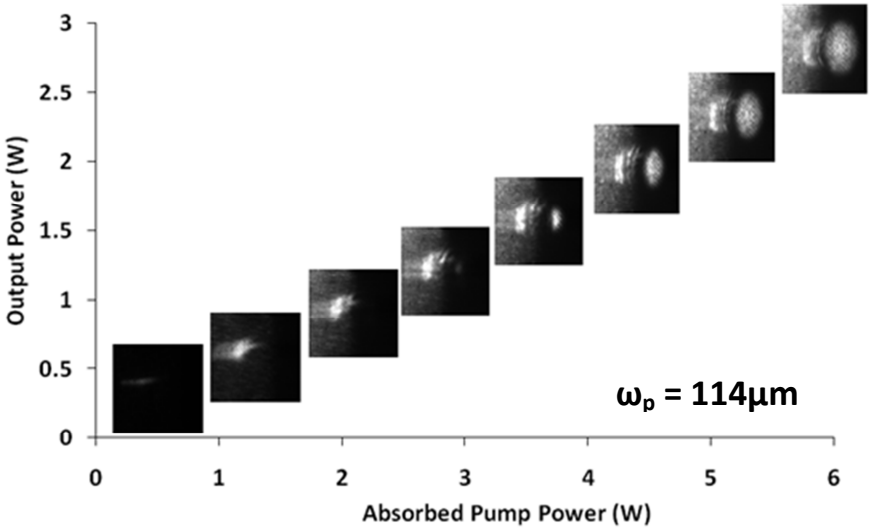

a)

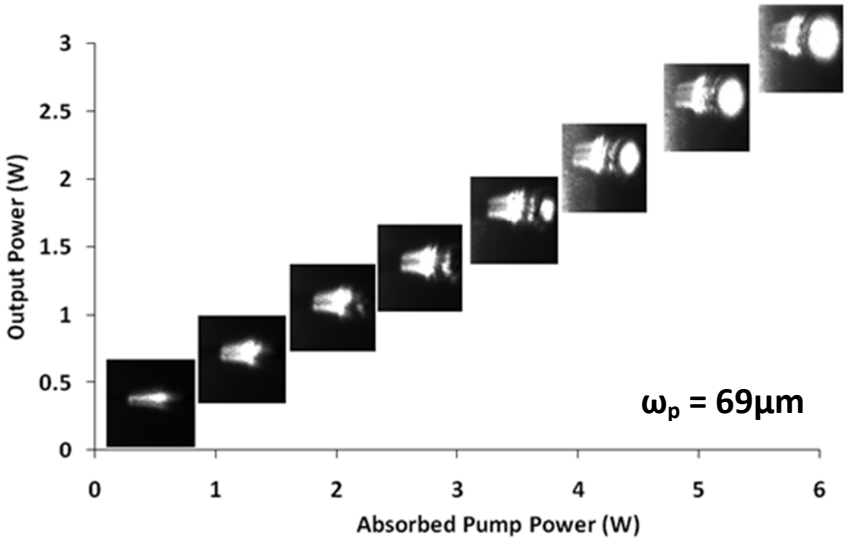

b)

Figure 5.4.c.ii *Transverse beam profile output of 1 atm. % Nd:YVO_4 microchip laser incorporating an intracavity diamond heatspreader, for pump spot radii of a) 114µm and b) 69µm.*

In order to ascertain whether the lack of parallelism was the cause of the degraded output beam profile, the parallelism of the diamond and Nd:YVO_4 was measured. A Fizeau interferometer set-up was used to measure the parallelism quantitatively as shown in figure 5.4.c.iii. The expanded beam from a HeNe laser was used to illuminate a sample, producing a fringe pattern in the reflected light. The fringe pattern is caused by the reflections from the front and rear surface of the sample interfering with one another. A beam splitter was

used to direct the reflected light onto a screen where the fringe pattern could be examined. The wedge angle α is given by [4]:

$$\alpha = \frac{\lambda\,(m+\frac{1}{2})}{2xn} \qquad \text{Eqn. 5.4.c.i}$$

where λ is the wavelength of the reflected light, m is equal to the number of fringes observed, x is the length of sample that the angle is measured over and n is the refractive index of the sample. A number of diamond samples were examined, labelled 1-6, the details of which can be seen in table 5.4.i.c. Photographs of the interference pattern recorded for diamond sample 5 and the 1 atm. % Nd:YVO_4 crystal used in the intracavity work are shown in figure 5.4.c.iv.

The results of the parallelism experiments are shown in table 5.4.c.i. From these results it is apparent that the diamond heatspreaders display poor parallelism compared to that of the Nd:YVO_4 sample examined where no fringes could be observed indicating a high degree of parallelism in the Nd:YVO_4 sample. Therefore the parallelism issue is likely to arise from the diamond heatspreaders rather than the Nd:YVO_4 used in these experiments. Diamonds 4-6 were examined in the microchip format where it was found that the output beam profile remained poor. Using [3], it was possible to estimate the maximum deviation from parallel that can be tolerated between the two mirrors in the microchip laser cavity in terms of an angle Ψ. The cavity cannot support a guided mode when the cavity mirrors possess a wedge angle greater than the value given by:

$$\psi = 0.5\left(\frac{d(nl)}{dr}\right)_{max} \qquad \text{Eqn. 5.4.c.ii}$$

where n is the refractive index of the material within the cavity, l is the length of the cavity and r is the radial distance.

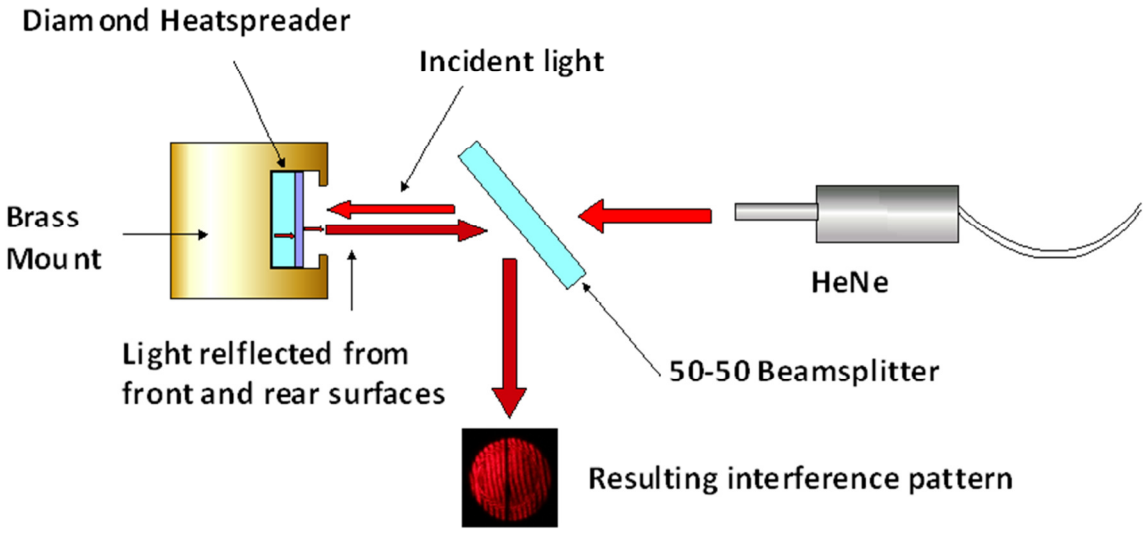

Figure 5.4.c.iii *Diagram of interferometric arrangement used to measure the parallelism of a range of diamond heatspreaders and a 1 atm. % Nd:YVO_4 crystal .*

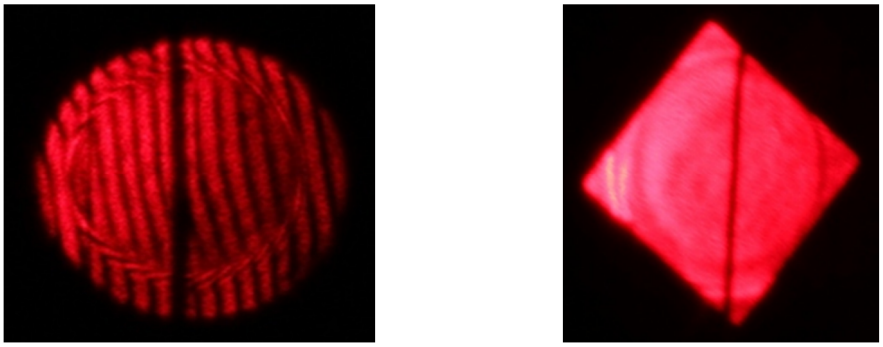

a) b)

Figure 5.4.c.iv *Photographs of interferograms used to measure parallelism of a) diamond heatspreader sample 'E' and b) a 1 atm. % Nd:YVO_4 crystal used in the intracavity microchip experiments in this section. A wire 180µm wide is positioned on the surface of the sample to provide a suitable scale.*

Sample	Coating	Parallelism Quoted by supplier (arcsecs)	Experimentally Measured Parallelism (arcsecs)	Experimentally Measured Parallelism (degrees)
Diamond sample 1	Coating X	< 68	105	0.029
Diamond sample 2		< 68	246	0.068
Diamond sample 3		< 68	73.3	0.020
Diamond sample 4	Coating Y	< 68	97	0.027
Diamond sample 5		< 68	98	0.027
Diamond sample 6		< 68	125	0.035
Nd:YVO_4	Coating X	< 30	-	-

Table 5.4.c.i *Summary of parallelism measurements of diamond samples 1-6 and a 1 atm. % Nd:YVO_4 crystal used in the intracavity microchip experiments in this section. Coating X describes a coating deposited on diamond samples 1-3, which has a reflection of greater than 95% at a wavelength of 808nm and 1064nm for an angle of incidence (AOI) of 0°- 30°, deposited on one side of the crystal. Coating Y describes a single coating deposited on diamond samples 4-6, which is highly transmitting at 808nm for an AOI of 0°- 30° and has a reflection of greater than 93% at a wavelength of 1064nm for an AOI of 0. No fringes were observed for the Nd:YVO_4 so the experimentally measured parallelism is not quoted.*

Finite element analysis (as used in chapter 2 of this thesis) was used to calculate $[d(nl)/dr]_{max}$ by modelling the average temperature rise as a function of *r* for a 0.5mm thick Nd:YVO_4 sample bonded to a 0.5mm thick diamond heatspreader at an incident pump power of 10W, pump spot radius of 100µm, similar to the microchip models discussed in chapter 2. The differential of the axially averaged temperature with respect to radial position was calculated from this modelled data and then converted to the differential of refractive index with respect to the radial position by multiplying by the thermo-optic coefficient. This was done for both the Nd:YVO_4 and diamond components of the microchip laser but it must be noted that the contribution to thermal lensing derived from crystal deformation under heating was not included in the calculation; however, the presence of a diamond heatspreader will reduce the crystal deformation. Nevertheless, it can be expected that the overall thermal lensing is likely to be stronger which suggests that for the microchip laser examined, a lower degree of parallelism may be required for mode guiding than calculated above.

The maximum wedge angle in arc-seconds that a Nd:YVO_4 microchip laser with intracavity diamond heatspreader could support under these conditions was estimated to be in the order of ~100 arcseconds. Regarding the parallelism measurements of each of the diamonds, only diamond sample number 3 appeared to have a parallelism higher than this figure. However, when this diamond was examined in the same microchip format as before, a comet tail profile was observed indicating that the total parallelism of the microchip

5.4.d Summary

It is apparent from table 5.4.c.i that the best output power and slope efficiency was achieved for a pump spot radius of 69µm. In terms of output power and slope, neither pump radius significantly outperforms the other; in terms of threshold, however, the threshold of the 69µm pump spot radius is lower than that of the 114µm case as would be expected.

Pump Spot Radius	Maximum P_{out}	Maximum Incident/Absorbed Slope Efficiency	Incident/ Absorbed Threshold
69µm	3.0W	37% / 55%	0.38 /0.28W
114µm	3.0W	35% / 53%	0.48W / 0.29W
150µm	2.5W	30% / 47%	0.75W /0.47W
200µm	2.3W	29% / 45%	0.85W /0.54W

Table 5.4.d.i *Summary table of laser characterisation of a 1 atm. % Nd:YVO_4 microchip laser incorporating an intracavity diamond heatspreader.*

Due to the parallelism issue introduced by the wedged diamond, the quality of the output beam was severely degraded leading to the comet-tail effect. Ideally diamond with an improved parallelism specification approaching that of the Nd:YVO_4 should be obtained in future to allow for accurate characterisation of the intracavity heatspreader approach. However there are difficulties processing diamond due to its material properties that mean that currently the best available parallelism specification for synthetic, low birefringence diamond is <0.33µm/mm . It must be noted that the parallelism of the diamond used for the experiments in this chapter was worse than <0.33µm/mm. Once diamond with sufficient

parallelism is obtained then sufficient beam quality data based on M^2 and cavity mode measurements would be obtainable and beam brightness analysis could be undertaken to compare it to the other configurations.

5.5 Nd:YVO_4 microchip laser with intracavity diamond heatspreaders bonded on both sides

5.5.a Introduction

A Nd:YVO_4 microchip laser bonded to diamond heatspreaders on the pump-side crystal facet and rear facet potentially offers excellent prospects for power scaling. This configuration will be termed the "diamond heatspreader sandwich" configuration in this chapter for the purposes of convenience and brevity. This approach has the advantage of shifting the locus of thermally-induced stress within the crystal to the diamond which is better suited to dealing with higher stresses and so it should be more resistant to catastrophic crystal fracture than the intra or extracavity diamond microchip configurations [5]. The issue of the lack of parallelism in the available diamond heatspreaders used in the previous section, however, prevented a full characterisation of the microchip laser incorporating an intracavity diamond heatspreader.

The parallelism tolerance for this microchip configuration was also investigated. The incident pump power and pump spot radius were assumed to be 10W and 100µm respectively. The maximum wedge angle was estimated to be 60 arcseconds using equation 5.4ci. This indicates that for such a configuration, the available diamonds would most likely be not parallel enough to ensure a guided mode. It also indicates, as would be expected, that increasing the cavity length requires a greater parallelism.

One method to compensate for the wedge effect in diamond would be to cancel out the overall wedge of the cavity by using this diamond heatspreaders with similar wedges. The idea was to bond these two samples of 0.5mm thick type IIa single crystal synthetic CVD diamond to an uncoated, 0.5mm thick 1 atm. % doped, a-cut Nd:YVO_4 crystal as shown in figure 5.5a.i such that the wedge on one diamond sample cancelled out the wedge on the other as seen in figure 5.5a.ii. Diamond samples 1 and 5 were chosen as their wedge angles, 105 arcseconds and 98 arcseconds, provided the closest match out of the samples available.

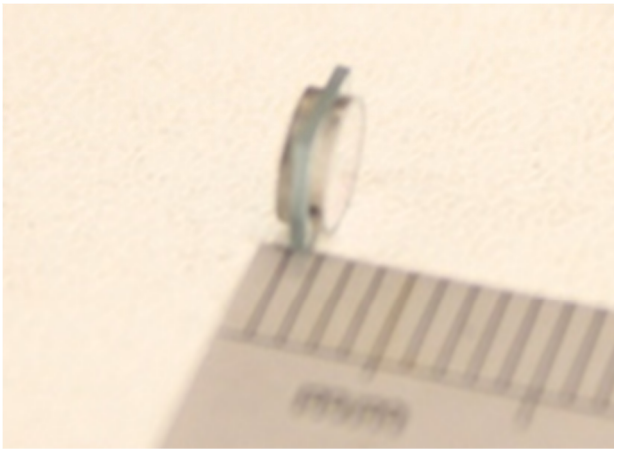

Figure 5.5.a.i *Photograph of two 0.5mm thick diamond heatspreaders successfully bonded to a 0.5mm thick 1 atm. % Nd:YVO_4 crystal forming a microchip laser cavity.*

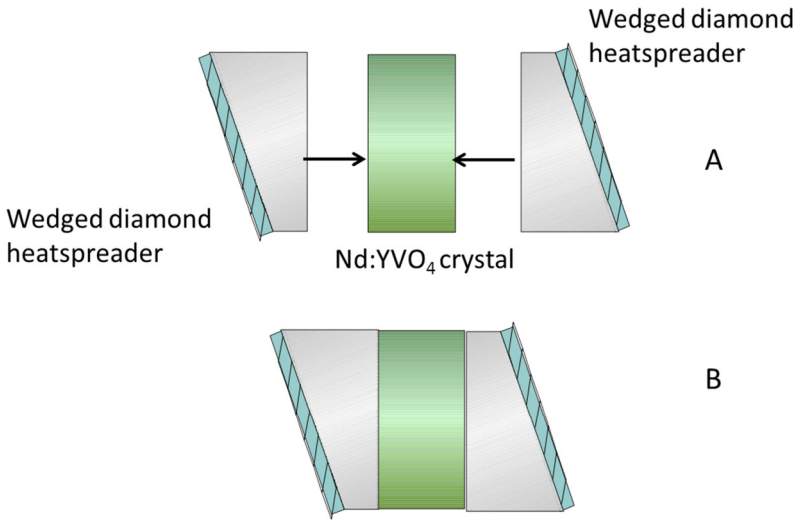

Figure 5.5.a.ii *Method used to compensate for lack of parallelism in diamond heatspreaders. In section A, two diamond heatspreaders of similar wedge angle are prepared alongside a sample of Nd:YVO_4 in the middle. One diamond heatspreader is inverted with respect to the other. In section B the two heatspreaders are bonded to the Nd:YVO_4 sample, creating a cavity with parallel ends at an angle.*

The arrangement of the diamonds with regards to their coatings and their positioning in the overall experimental set-up can be seen in figure 5.5a.ii. A 25W fibre-coupled laser diode (100µm core-diameter, 0.22NA) operating at a wavelength of 808nm was used to pump the

1 atm. % doped, a-cut Nd:YVO_4 crystal. The gain material and heatspreader bonded composite was sandwiched between indium foil of 0.125mm thickness to ensure more effective thermal contact with the brass mount. An aperture in the indium allowed for incident and output light to pass through. The crystal was mounted in a water-cooled brass block, and the water cooled to 9.5 °C. Adjustment of the heatsink temperature of the diode-laser pump was required to maintain a constant output wavelength with increasing input current. A pump spot radius of 114µm was used. The crystal was pumped to a maximum incident power of 9W.

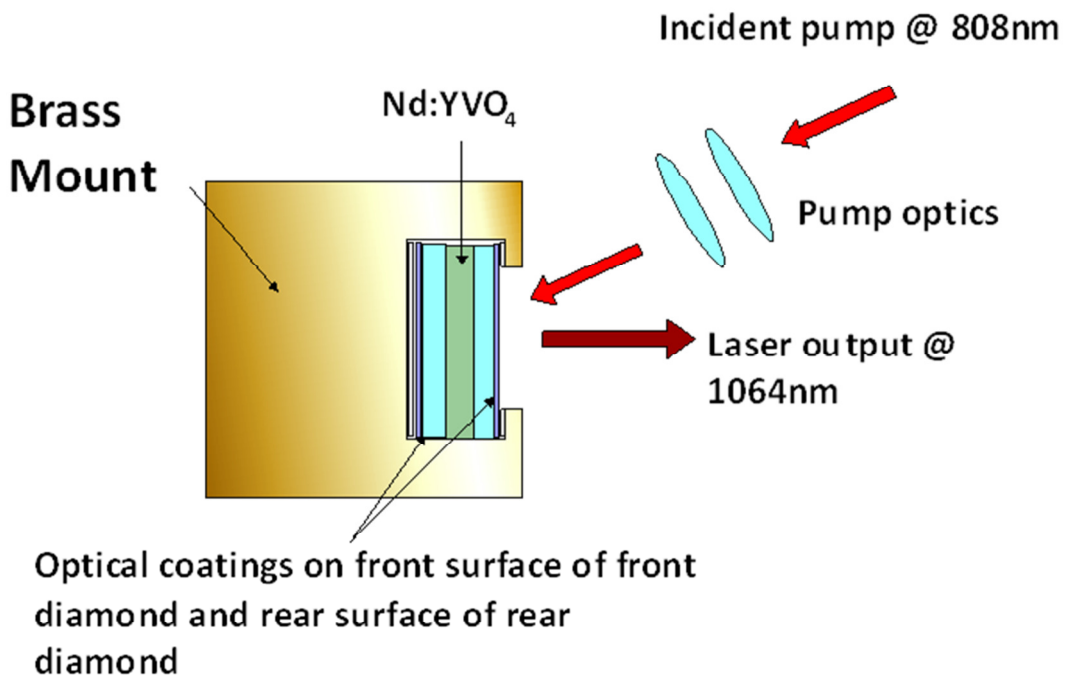

Figure 5.5.a.ii *Diagram of experimental arrangement of intracavity diamond Nd:YVO_4 sandwich microchip laser used in this section. OC stands for output coupler.*

5.5.b Characterisation of "diamond sandwich" microchip laser

The output power of the laser was measured and the results can be seen in figure 5.5b.i. The maximum CW output power achieved was 3.0W at an incident pump power of 9W using a pump spot radius of 114µm. This pump spot radius was chosen on the basis of available pump optics and only one pump spot radius was examined due to time constraints. The slope efficiency and threshold, both with respect to incident pump power were 35% and 0.47W respectively. The slope efficiency and threshold, with respect to absorbed pump power were 55% and 0.29W respectively.

The output beam had a comet-tail effect that indicated that sufficient parallelism had not been achieved as can be seen in figure 5.5b.ii. With regards to achieving the correct orientation of the diamonds so as to cancel out the wedge effect and achieve parallelism of the cavity, difficulties emerged in the bonding process that made it difficult to align the samples with sufficient accuracy. These difficulties arose through from the fact that although the parallelism experiment outlined in the previous section allowed the wedge direction to be measured, it could not indicate which end of the wedge was the thin or thick side. Furthermore, marking the diamonds on their circumference to ensure that the correct orientation of the wedge was known was made difficult by the thinness of the sample, the mark being robust enough to survive the cleaning process and the requirement that it not impede the bonding process. Ensuring that the diamonds remained aligned through the bonding process was done by hand and by eye and so precision was impaired. In the timescale of the project and after multiple attempts, these difficulties were not overcome. The power transfer shown above was taken from a sample whereby wedge alignment had been attempted.

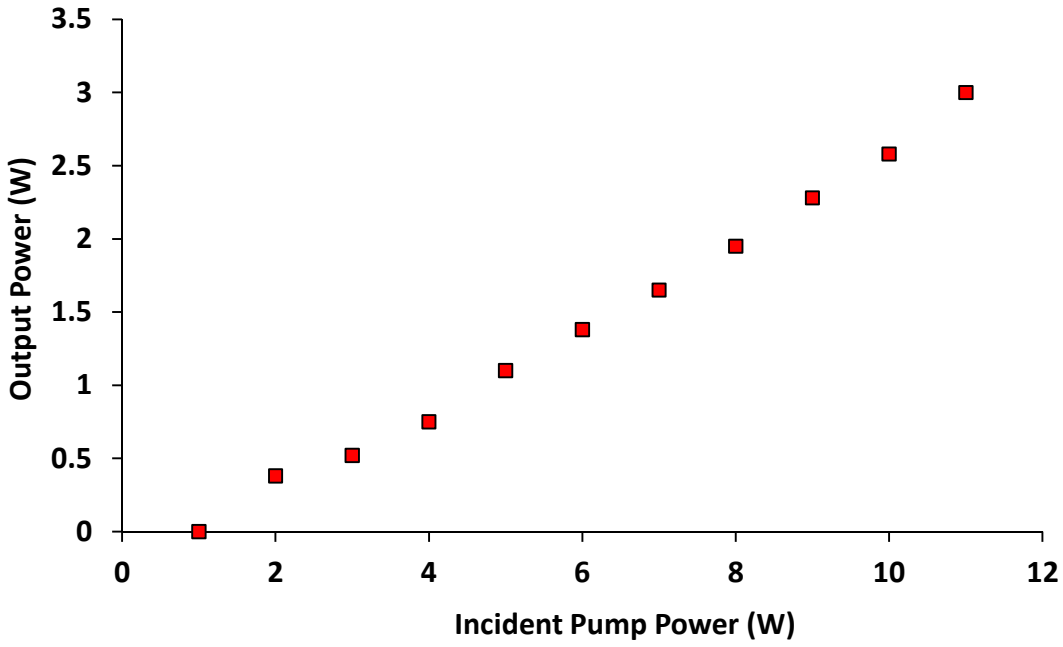

a)

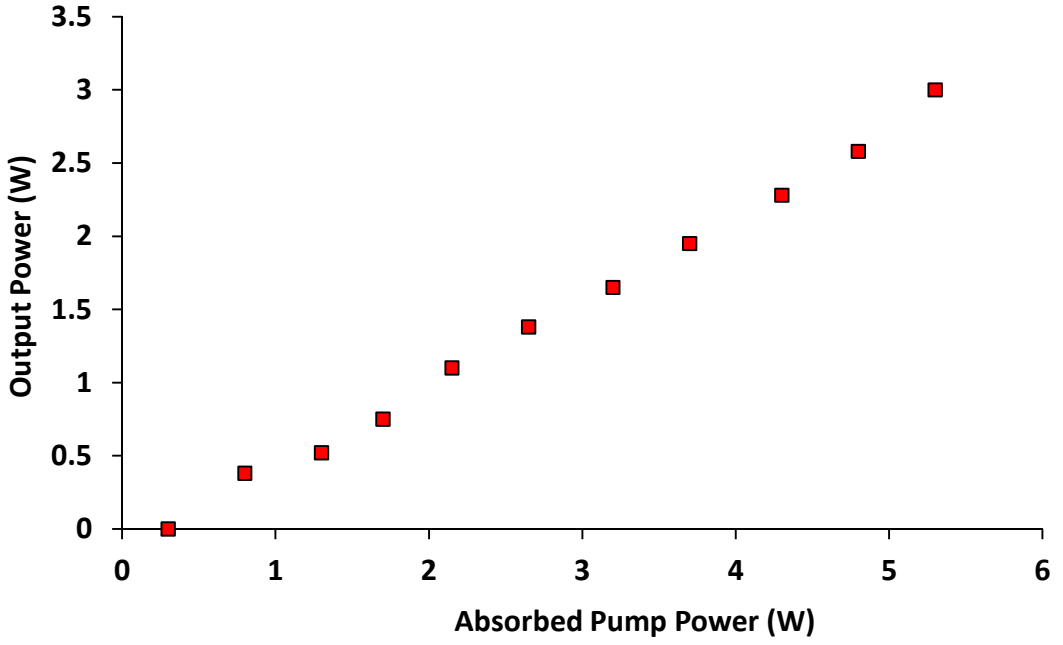

b)

Figure 5.5.b.i *Output power of a 1 atm. % Nd:YVO_4 microchip laser, sandwiched between two intracavity diamond heatspreaders, plotted against a) incident power and b) absorbed power.*

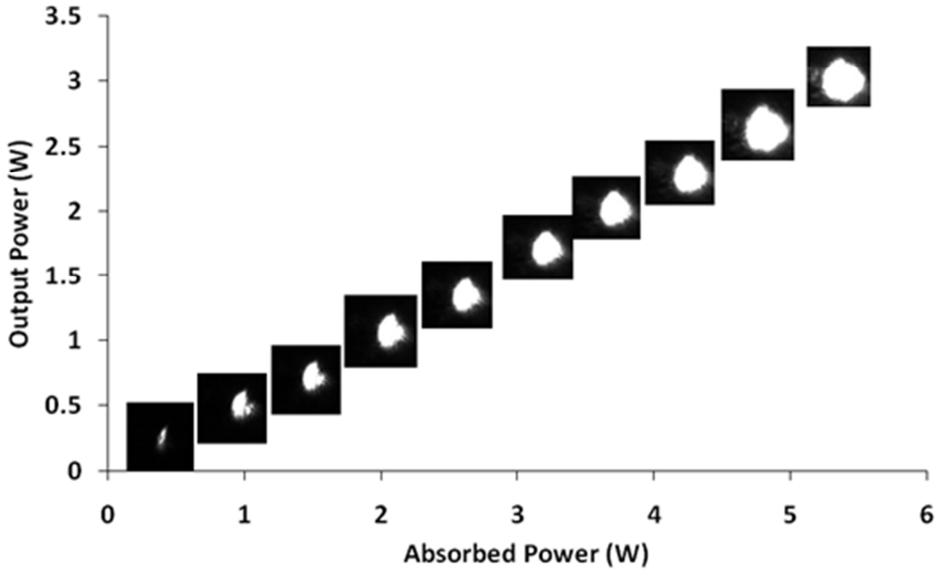

Figure 5.5.b.ii *Transverse beam profile output of 1 atm. % Nd:YVO_4 microchip laser incorporating an intracavity diamond heatspreader, for pump spot radii of 114µm.*

5.5.c Summary

Two coated diamond heatspreaders were successfully bonded either side to an uncoated, 1 atm. % doped, a-cut Nd:YVO_4 crystal. This observation was validated by the maximum output power achieved in power transfers taken being similar to that of the intracavity diamond heatspreader case. An output of 3W was achieved using a pump spot size of 114µm.

Whilst the bonding of the structure was a success, achieving the correct orientation of the intracavity components was not and thus a comet-tail appearance was observed in the transverse output profile of the microchip laser. Achieving the correct orientation is a technical challenge but in the absence of diamond heatspreaders with sufficient parallelism it is a possible solution to the beam quality issue, albeit a time consuming solution.

In the absence of parallelism issues with the diamond, pump spot optimisation and beam brightness analysis are the obvious next steps for future work on this configuration. The brightness is likely to be better than the intra and extra-cavity diamond configurations due to the increased cavity length, allowing for larger fundamental cavity modes and better mode matching at higher powers. In addition, power-scaling of this configuration would likely be achievable up to higher powers before thermal fracture.

5.6 Chapter summary and conclusions

In this chapter, four different microchip laser configurations have been investigated. The first configurations did not utilize a heatspreader to provide face-cooling unlike the other configurations examined. Having been demonstrated in 2008 by Liao *et al* to provide significant output powers without quantitative measurement of the beam quality, it served as a good comparison for the other configurations. The main differences between this configuration and the others was the dopant concentration, length and type of the crystal: a 0.5% atm. doped 1.5mm long piece of Nd:$GdVO_4$ was used.

The diamond heatspreader approach used previously in this thesis was implemented in several ways such as bonding diamond to Nd:YVO_4 in extracavity and intracavity configurations. A diamond heatspreader sandwich configuration, which offers good prospects for power scaling at higher powers, was examined to assess the feasibility of bonding this type of configuration and to investigate its power transfer characteristics compared to the previous configurations. This configuration also had the potential to overcome cavity parallelism issues.

Microchip Configuration	Max. P_{out}	Max. Incident/ Absorbed Slope Efficiency	Incident/ Absorbed Threshold	M^2 (Geometric mean)	Brightness
Millichip	3.7W	40% / 52%	0.38W /0.25W	7.2	0.28W/μm^2/sr
Extracavity	3.1W	36% / 52%	0.25W /0.17W	9.2	0.13W/μm^2/sr
Intracavity	3.0W	37% / 55%	0.36W / 0.24W	-	-
Sandwich	3.0W	35% / 53%	0.36W /0.25W	-	-

Table 5.6.i *Summary table of laser characterisation of microchip laser configurations used in this chapter. "Millichip" describes the 0.5% atm. doped, 3x3x1.5mm long Nd:$GdVO_4$ microchip laser used in section 5.2. "Extracavity" describes the 3% atm. doped, 3x3x0.5mm long Nd:YVO_4 microchip laser with extracavity diamond heatspreader used in section 5.3. "Intracavity" describes the 1% atm. doped, 3x3x0.5mm long Nd:YVO_4 microchip laser with an intracavity diamond heatspreader as used in section 5.4. "Sandwich" describes the 1% atm. doped, 3x3x0.5mm long Nd:YVO_4 microchip laser with both facets bonded to diamond heatspreaders as used in section 5.5. The M^2 of the Millichip was taken at an absorbed power of 6.4W whilst the M^2 of the extracavity heatspreader case was taken at an absorbed power of 6.2W.*

As can be seen in table 5.6.i and figure 5.6.i, in terms of maximum output power available, the millichip configuration achieved an output power of 3.7W at an absorbed power estimated to be 7.6W. However, at an absorbed power of 6W, the output powers of all the configurations achieve roughly 3W, although the heatspreader sandwich and intracavity configurations are estimated to achieve a few hundred milli-watts more. The intracavity heatspreader configuration gave the highest slope efficiency but it also displayed a higher threshold alongside the diamond "sandwich" configuration than the extracavity heatspreader configuration which might be due to the misalignment of the coated diamonds.

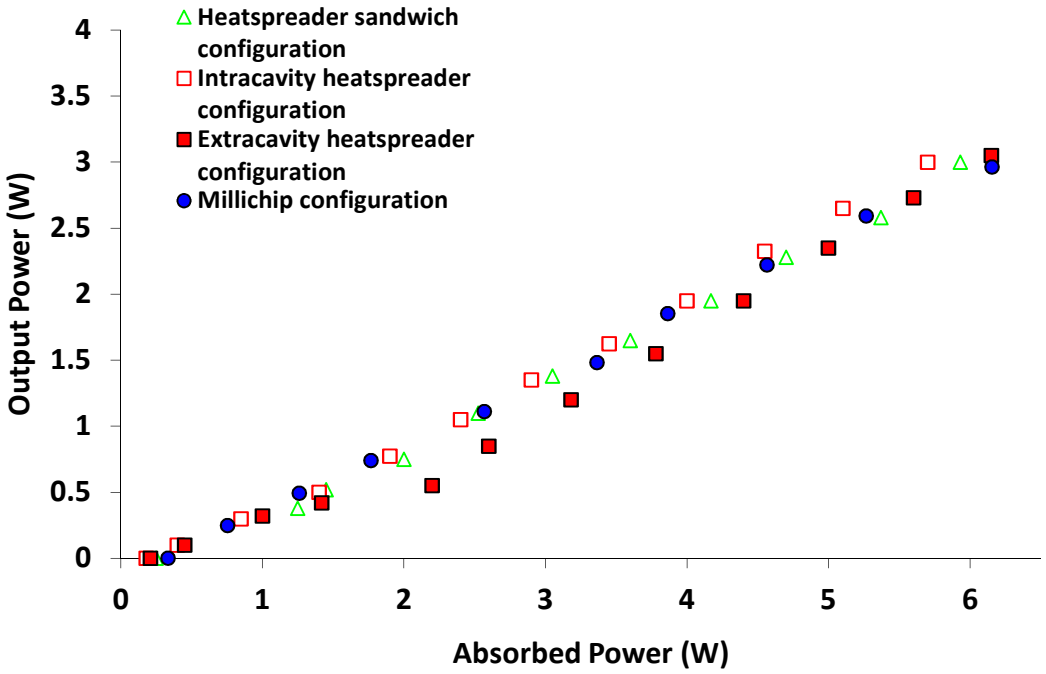

Figure 5.6.i *Output power of the microchip configurations used in this chapter, optimised where possible, absorbed pump power is limited to 6W. The pump spot radii for the "heatspreader sandwich", intracavity heatspreader, extracavity heatspreader and "millichip" configurations were 114µm, 69µm, 69µm and 114µm respectively.*

The output beam of the millichip configuration at an absorbed power of 6.4W was measured to have a geometrically averaged M^2 of 7.2, lower than the M^2 of 9.2 of the extracavity heatspreader configuration at an absorbed power of 6.2W. This could be

attributable to the longer cavity length of the millichip compared to the other microchip set-ups examined, allowing for a more optimal pump/fundamental cavity mode overlap to be achieved.

The extracavity heatspreader configuration was modified by using an intracavity heatspreader approach. This would allow for an increase in cavity length and so allow for an increase in the fundamental cavity mode which would in theory improve the beam quality and lower the M^2. Due to issues with lower than expected parallelism present in the diamond heatspreaders it was not possible to achieve good beam quality as shown by the comet-tail appearance in the output beam. By adopting a novel intracavity heatspreader sandwich approach it was predicted that the overall parallelism present in the cavity might be improved provided the right orientation of the components was achieved. In addition, this diamond sandwich configuration should offer better thermal management and larger fundamental cavity modes leading to higher brightness. Unfortunately, within the timescale of this project the parallelism issue could not be solved.

Whilst it is clear that the millichip configuration proved superior to the extracavity heatspreader approach both in terms of maximum attainable output power and in terms of brightness, comparison between it and the intracavity heatspreader approaches is more difficult due to the issues with diamond parallelism. The maximum output powers of the different configurations provided similar output powers for 6W of absorbed power; however, the difficulties experienced with the parallelism prevented any meaningful experimental comparison in terms of brightness. It must be noted, however, that the key parameter holding back the intracavity diamond heatspreader work i.e. the parallelism is purely due to the immaturity of the processing procedures for diamond and these are to be expected to improve in the future as diamond becomes more widely used in optics and lasers. Parallelism specifications of less than 30 arcseconds would be desirable for the intracavity diamond microchip lasers and microchip lasers using the diamond “sandwich” configuration.

5.7 References

[1] M. Liao, R. Lan, Z. Wang, H. Zhang, J. Wang, X. Hou and X. Xu "10W continuous-wave Nd:$GdVO_4$ microchip laser" *Laser Physics Letters*, vol. 7, pp. 503-505, 2008.

[2] A. E. Siegman, “How to (Maybe) Measure Beam Quality”, Tutorial presented at *Optical Society of America Annual Meeting*, 1997

[3] J. J. Zayhowski, "Thermal Guiding in Microchip Lasers," *Advanced Solid State Lasers*, vol. 6, paper DPL3, 1999

[4] E. Hecht, “Optics”, 4th ed., Addison-Wesley publishers, pp. 405, 2002

[5] P. Millar, R. B. Birch, A. J. Kemp and D. Burns "Synthetic Diamond for Intracavity Thermal Management in Compact Solid-State Lasers" *IEEE Journal of Quantum Electronics*, vol. 44, pp. 709-717, 2008

6. Conclusions

The solid-state microchip laser offers a robust, compact source of laser light that has potential for mass production. The sub-millimetre cavity design allows for single frequency operation whilst with the addition of a second element in the cavity, Q-switched operation can be achieved as well [1]. High brightness, multi-watt operation in microchip lasers has yet to be achieved without resorting to slab geometries [2,3] or more complex quasi-microchip designs [4] which do not lend well to being mass produced.

The main challenges to increasing the output power whilst retaining good beam quality in microchip lasers is the fact that the fundamental cavity mode radius is controlled solely by the thermal lens. In conventional lasers, this is less of an issue because the cavity is more flexible and so matching the pump and fundamental cavity modes is easier; in microchip lasers, the cavity length of the monolithic or quasi-monolithic is essentially fixed once assembled and so the thermal lens that arises from the pumping process controls the fundamental cavity mode. The fundamental cavity mode radius of microchip lasers is typically of a similar size or smaller than the radius of the pump mode and it typically decreases as the pump power increases and the thermal lens strengthens. Hence, at higher incident powers [5], oscillation of higher order transverse modes occurs and leads to a deterioration in beam quality. In order to achieve better beam quality at higher output powers thermal management of the microchip laser is essential.

6.1 Heatspreader Approach

To achieve better mode overlap, the fundamental cavity mode must be tailored to be equal to or larger than the pump spot radius. One method to increase the radius of the cavity mode within a microchip laser is to reduce the strength of the thermal lens in the gain material by reducing the pump induced temperature rise.

Through use of a heatspreader bonded via liquid capillarity to the gain material, the temperature gradients within the gain material can be reduced. Chapter 2 of this thesis

examined three different heatspreaders materials – sapphire, SiC and diamond – using finite element analysis (FEA) to model the effectiveness of each in a microchip laser format. The modelling predicted that the diamond heatspreader would provide the best performance followed by SiC and then sapphire in the doped-dielectric and semiconductor disk laser (SDL) microchip formats examined; however, the modelling also indicated that the doped-dielectric microchip configuration considered would not exploit the superior thermally conductive properties of the diamond heatspreader. Indeed, for a 0.5mm thick Nd:YVO_4 microchip laser pumped with 8W of incident power in a pump radius of 50µm, the use of a diamond heatspreader gave a predicted temperature rise within the gain material that was only 0.6% lower than when a SiC heatspreader was assumed. The use of sapphire led to a 9K difference compared to diamond. By contrast, in the SDL format, the use of a diamond heatspreader resulted in temperature drop of 24%. The larger differential between the use of diamond and silicon carbide is predicted in the SDL case is due in large part to the fact the heat is deposited in the SDL in a very thin region (~1.6µm) close to the heatspreader. By scaling the thickness of the Nd:YVO_4 down to 12.5µm, keeping the absorbed power constant, it was found that the diamond heatspreader led to a predicted temperature drop of 5% less than the SiC case. This indicates that diamond can be more readily exploited as a heatspreader when bonded to materials that possess very thin gain regions. For doped-dielectrics this means that certain materials will be more suited to exploiting diamond as will be discussed in section 6.2.

The thermal lens in terms of a radius of curvature of the equivalent mirror of a Nd:YVO_4 laser was modelled for diamond and SiC heatspreaders using FEA data. For a pump spot radius of 50µm and at a gain thickness of 12.5µm, the use of diamond lead to a predicted radius of curvature drop of 55% resulting in a calculated rise in the fundamental cavity mode radius of 18%. As the thickness of the gain material was reduced, the maximum temperature rise difference between the diamond and SiC heatspreader models increased as did the difference between calculated fundamental cavity mode radii, demonstrating theoretically that diamond is the heatspreader of choice for doped-dielectrics both in terms of reducing the temperature gradients within the gain region and increasing the fundamental cavity mode radius for better mode matching at thinner gain thicknesses. It must be noted that

the FEA analysis did not take into account thermally induced deformation and stress due to time constraints in the project but it is likely that due its superior mechanical properties (see table 1.4.i in chapter 1 of this thesis) compared to SiC, diamond will have greater potential in this regard too, especially if thin pieces of gain material can be exploited..

Sapphire, SiC and diamond heatspreaders were experimentally examined in three-mirror and quasi-microchip cavities in chapter three of this thesis where the use of diamond lead to the highest output powers using 0.5mm thick Nd:YVO_4 as the gain material. The SiC material used displayed higher losses than the diamond heatspreader (approximately 7x higher), leading to lowered slope efficiencies and higher thresholds.

Both 1 and 3 atm. % doped Nd:YVO_4 was used in this chapter where it was found that the 1 atm. % doped material performed better. In terms of output coupling, between 7 and 9% transmission was found to lead to the best performance. The thermal lens in terms of a radius of curvature of the equivalent mirror produced in the gain region when diamond and sapphire heatspreaders are used was investigated and it was shown that sapphire produced the stronger thermal lens as would be expected, being approximately four times stronger than that experienced by the diamond heatspreader. Future work would need to be done to experimentally assess the thermal lens when using SiC but it is likely to be slightly stronger than that of diamond at these gain thicknesses according to the FEA analysis in chapter 2.

In chapter 5 an example of a multi-watt microchip laser (termed for the purposes of this thesis as a “millichip”) was investigated. This reproduced and extended work done by Liao *et al.* on an edge-cooled 0.5% atm. doped, 3x3x1.5mm long a-cut Nd:$GdVO_4$ crystal in an end-pumped microchip format without the use of a heatspreader [7]. An output power of 10.2W was reported. at an incident input power of 23.9W, in continuous wave operation at a pump spot radius of 260µm; however, no quantitative value was given for the brightness or beam quality of the laser. The work done in this thesis showed that for an output power of 3.5W

at an absorbed power of 6.4W, an average M^2 over the two planes of the beam of 7.2 was measured for a pump spot radius of 114μm.

Microchip configurations incorporating extracavity and intracavity diamond heatspreaders were investigated, using 0.5mm thick Nd:YVO_4 as the gain medium. It was shown that for a 3 atm. % doped, 0.5mm thick Nd:YVO_4 laser bonded to a diamond heatspreader to provide face-cooling, 3W of output power could be achieved for an absorbed power of 6.2W at a pump spot radius of 69μm; the M^2 was measured to be 9.2. Whilst the output beam is not as bright as the beam produced by the millichip, the efficiency with respect to absorbed pump power and output powers (for a fixed absorbed power) are similar. By moving to an intracavity heatspreader approach it was predicted that the increase in cavity length provided by the intracavity diamond would serve to increase the fundamental cavity mode and allow for more effective mode overlap and hence better beam quality. The configuration was bonded together via liquid capillarity and the output power was measured to be 3W for 5.7W absorbed pump power; however the output beam profile displayed signs of a lack of parallelism between the outer surfaces of the microchip. Using Fizeau interferometry, this lack of parallelism was found to arise from the diamond heatspreader and it was apparent that the diamond parallelism did not match the manufacturer's specifications.

A third diamond heatspreader configuration was examined, where the Nd:YVO_4 was sandwiched between two intracavity diamonds which achieved 3W of output power for 5.9W of output power. It was postulated that the parallelism between the outer mirror-coated surfaces could be improved by arranging the two diamond heatspreader in such a way that their wedges cancelled one another out. This was tried multiple times but without success due to technical difficulties in aligning the samples. As a result, the output beam profile was also degraded in this case. Had the diamond parallelism of the diamond surfaces been better then higher beam quality would be expected due to the increased cavity length, and at higher input powers the diamonds should provide more effective thermally-induced stress management than the other heatspreader configurations [8].

6.2 Gain material choice

FEA analysis carried out in chapter 2 examined Nd:YVO_4, Nd:$GdVO_4$, Yb:KYW and a 1060nm InGaAs/GaAs SDL in a microchip format. The modelling predicted that the SDL suffered the lowest temperature gradients followed by the Yb:KYW, Nd:$GdVO_4$ and Nd:YVO_4 doped-dielectric material. The smaller fractional heat loading of the Yb:KYW ensured that it suffered lower temperature rises than the vanadates. It was noted, however, that the difference in material parameters in the literature gave rise to a 59% difference in temperature rise of when two different sets of parameters for the vanadates were examined. One set of parameters was chosen as the conditions under which they were measured in the literature most closely resembled the experimental conditions in this thesis. To improve the accuracy of the model for comparison with experimental data, the parameters could be experimentally measured for the crystals used in this thesis; however, the main purpose of the FEA analysis was to identify trends in the data.

The maximum temperature rise with respect to gain thickness at a constant absorbed power of 8W was modelled for Yb:KYW, Nd:$GdVO_4$ and Nd:YVO_4 microchip lasers bonded to a diamond heatspreader at pump spot radii of 50µm, 200µm and 500µm. The gain crystal thickness was varied from 12.5µm to 1.5mm. For any combination of pump spot radius and gain material thickness, the Yb:KYW material suffered the lowest temperature rise compared to the vanadates. This is a direct result of the smaller fraction of the absorbed pump power converted to heat in Yb:KYW. At a pump spot radius of 50µm it was observed that for each gain material, a peak in the maximum temperature rise occurred for a gain thickness of twice the pump spot radius. The peak was still observable for the vanadates in the 200µm pump spot radius case but the temperature rise plateaued in the Yb:KYW. This temperature plateau was observed for all crystals at a pump spot radius of 500µm. It was reasoned that at 50µm pump spot radius, the microchip lasers were operating in a similar manner to a classic rod lasers in terms of heat extraction for the larger thicknesses – with significant radial heat flow in the laser gain material. At a pump spot radius of 500µm, however, the lasers were operating in something more akin to the thin disk regime over

most of the range of thicknesses considered, with axial heat flow predominant. This gives rise to the different forms of the variation in maximum temperature with thickness for different pump spot radii. From this information gain thickness optimisation can be derived in order to provide more effective thermal management by operating microchip lasers in the thin-disk regime. Whilst gain materials such as Yb:YAG which have been commonly used in the thin-disk region, the low absorption and high threshold of Yb:YAG means that as much of the pump light as possible needs to be absorbed for efficient laser operation. Multi-pass arrangements have been devised that allow the Yb:YAG to absorb the majority of the pump light, however, these set-ups are typically complex and bulky and unsuitable for use in microchip lasers. Yb:KYW stands out as a potential gain material for use in microchip lasers in thin disk operation due to the higher absorption offered by the tungstates and the ability dope Yb:KYW to much higher levels than the vanadates [8.5]. This makes it attractive for use in microchip lasers that provide only two pump passes as the absorption is still reasonable for small thicknesses. An additional quality of Yb:KYW is its small quantum defect which leads to less absorbed power being converted to heating the gain region compared to the vanadates [9]. The thin-disk path offers a good route to lowering thermal lensing, increasing the likelihood of better beam quality at higher output powers.

Chapter 4 of this chapter examined Nd:$GdVO_4$ and a 1060nm InGaAs/GaAs SDL in a three mirror format to assess the suitability of these materials for future use in a microchip format. It was found that the available 10 quantum well structure 1060nm InGaAs/GaAs material produced an output power of 2.2W for 10.3W of incident power. Power scaling of the material revealed that 6.5W could be achieved at an input power of 35W before thermal roll over occurred. Although the tunability and the spectral coverage of SDL's are very impressive, it was decided that the available material would not suit a high power microchip laser due to the lower slope efficiencies and limited potential output power compared to the vanadates. 0.5mm thick, 1 atm. % doped Nd:$GdVO_4$ was examined and compared to 1 atm. % doped Nd:YVO_4 of the same thickness where it was found that the Nd:YVO_4 offered an output of 3.9W compared to the 3.5W achieved using Nd:$GdVO_4$. It was reasoned that the Nd:$GdVO_4$ growth processes – at least in the case of the crystals procured

for this work – have not reached the same stage of maturity as those associated with Nd:YVO_4 leading to a reduction in crystal quality and hence laser performance [10].

Finally, initial experiments incorporating Yb:KYW in a diamond "sandwich" configuration in a three-mirror cavity were undertaken. A 0.25mm thick, 10 atm. % doped sample of Yb:KYW was successfully bonded to two diamond heatspreaders. 1.9W of output power was achieved with an estimated slope efficiency with respect to absorbed pump power of 66% using a 2% transmitting output coupler. Further work would be required to optimise the set-up and to obtain an experimental measurement of the absorbed pump power.

6.3 Future work

Although a high brightness, multi-watt microchip laser was not achieved, much progress has been made towards this goal. What has emerged from this thesis is that the thin disk regime stands out as an advantageous region in which to work in order to minimise the thermal lens within the microchip laser and increase the size of the fundamental cavity mode. Whilst Nd:YVO_4 offers good output powers and efficiencies, it is not suited for working at very small thicknesses because at higher doping levels required to maintain efficient pump absorption, various parasitic effects exist that both reduce the laser efficiency and increase the fractional heat load. The ability to highly dope Yb:KYW and the absence of up-conversion and concentration quenching compared to the vanadates makes it attractive for use as a very thin gain material and the small quantum defect makes for more efficient thermal management. Whilst it will be necessary to carefully optimise the combination of doping level, material thickness and pump arrangements, the prospects for using Yb:KYW in a high power microchip laser format appear to be favourable.

The use of diamond for use as heatspreaders in microchip lasers has been demonstrated in extracavity and intracavity configurations for the first time. Diamond proved to be the best heatspreader material, although for applications where cost is a higher priority than

performance SiC might be the wiser choice given that the improvements in thermal management associated with moving to diamond are likely to be small in many cases.

For both SiC and diamond there are challenges of material supply. In the case of SiC, careful procurement and selection of material will be required to avoid the significant reduction in output powers associated with the use of SiC heatspreaders in this thesis. This was attributed to significant absorption loss. SiC has been successfully used intracavity in other lasers, however [11, 12]. This suggests that a detailed programme of characterisation is required to identify the most appropriate specifications for laser use.

In the case of diamond, the lack of parallelism between the faces of the disks, synthetic, single crystal, ultra-low birefringent diamond used in this thesis compromised the quality of the output beam. Element 6, the company that manufactures the diamond, believes they can now meet a parallelism specification of less than 30 arcseconds, which the work done in this thesis suggests is likely to be sufficient to remove this obstacle. The availability of this diamond would mean that the diamond “sandwich” microchip configuration will be achievable and future work would entail examining Yb:KYW in this format. The combination of the thin-disk approach and the diamond heatspreader approach would allow for greater power scaling and better beam quality, bringing the goal of achieving a multi-watt, high brightness microchip laser closer to fruition.

6.4 References

[1] J. J. Zayhowski, "Microchip Lasers," *Optical Materials*, vol. 11, pp. 255-267, 1999

[2] C. Yin, L. Huang, M. Gong, P. Yan, Q. Liu, and F. He "A novel compact side-pumped bonded microchip laser" *Laser Physics Letters*, vol. 4, pp. 584-587, 2007.

[3] O. Konoplev, A. A. Vasilyev, A. A. Seas, A. W. Yu, S. X. Li, G. B. Shaw, M. A. Stephen, and M. A. Krainak, "Multi-Watt Average Power Nanosecond Microchip Laser Design Scalability Approaches," in *Advanced Solid-State Photonics*, paper ATuB16, 2010.

[4] T. Suzudo, M. Hiroi, Y. Higashi, Y. Satoh, Y. Sato, H. Ishizuki, T. Taira, and Y. Furukawa, "9.6-W cw Green Output from Diode Edge-Pumped Composite Vanadate Microchip Laser with Small Packaged Volume," *Advanced Solid-State Photonics*, paper WD4, 2008.

[5] A. J. Kemp, R. S. Conroy, G. J. Friel, and B. D. Sinclair, "Guiding effects in Nd:YVO_4 microchip lasers operating well above threshold," *IEEE Journal of Quantum Electronics*, vol. 35, pp. 675-681, 1999.

[6] ISO 11551: test method for absorptance of optical laser components," (International Organization for Standardization, Geneva, Switzerland, 1997)

[7] M. Liao, R. Lan, Z. Wang, H. Zhang, J. Wang, X. Hou and X. Xu "10W continuous-wave Nd:$GdVO_4$ microchip laser" *Laser Physics Letters*, vol. 7, pp. 503-505, 2008.

[8] P. Millar, R. B. Birch, A. J. Kemp and D. Burns "Synthetic Diamond for Intracavity Thermal Management in Compact Solid-State Lasers" *IEEE Journal of Quantum Electronics*, vol. 44, pp. 709-717, 2008

[9] M. Hildebrandt, U. Bunting, U. Kosch, D. Haussmann, T. Levy, M. Krause, O. Muller, U. Bartuch, and W. Viol, "Diode-pumped Yb:KYW thin-disk laser operation with wavelength tuning to small quantum defects ", *Optical Communications*, vol. 259, pp. 796-798, 2006

[10] P. Millar, A. J. Kemp, and D. Burns, "Power scaling of Nd:YVO_4 and Nd:$GdVO_4$ disk lasers using synthetic diamond as a heat spreader," *Optics Letters*, vol. 34, pp. 782-784, 2009.

[11] G. A. Newburgh, A. Michael, and M. Dubinskii, "Composite Yb:YAG/SiC-prism thin disk laser," *Optics Express*, vol. 18, pp. 17066-17074, 2010.

[12] N. Schulz, J. M. Hopkins, M. Rattunde, D. Burns, and J. Wagner, "High-brightness long-wavelength semiconductor disk lasers," *Laser & Photonics Review*, vol. 2, pp. 160-181, 2008.

Acknowledgements

There are several people who I would like to thank for assisting me in the course of my PhD and the first person I should thank is Alan who has provided me with lots of helpful advice and guidance on microchip lasers as well as jokes about stingy Fifers. I must thank Patsy for helping me bond diamond and for introducing me to the notorious “Bird Song” which will haunt me for ever more. I’d like to thank Alex for his help and advice on SDL matters and for entertaining conversations in the Pot Still. I need to thank Vasili for showing me some handy new tricks for aligning lasers. The rest of the solid-state laser group (past and present) need crediting too for their useful advice, fruitful discussions and witty banter. These are: David, John-Mark, Gareth, Walter, Nils, Gerald and Sean.

Not mentioned above is Peter Roth who I must thank alongside Schlosser, Johnny, and Johannes for being excellent mates and putting up with my inane ramblings at the Todd’s and for putting up with my eclectic musical tastes. Someday I will organize that damnable curry night!

There are many other people at the Institute of Photonics who I must thank for various reasons: Paul Thomson, Paul Hynd, Lisa, Sharon Kelly, Lynda, Tim, Ewan, Stephane, Yujie, Yanfeng, Daniele, Line, Loyd, Elliot, Sharon Vetter, Alicja and Fiona. I’m grateful to Simon Poland, David Elfström and Chris Griffen for the 5-aside football and nights out in the pub. I’m very appreciative towards Lynne for answering lots of my questions before and after joining the IoP, and also towards Antony Smith for his ever-present chirpiness and enthusiasm!

My parents deserve a big “thank you” too for the support they have shown me and finally I must acknowledge Kim for putting up with me throughout the experimental and writing up phases of my PhD. As I write this she is undertaking a PhD of her own; I only hope that I can be as great to her as she has been to me.

Cheers,

Rolf